



HAL
open science

3D and 4D printing of high performance continuous synthetic and natural fibre composites for structural and morphing applications

Guillaume Chabaud

► **To cite this version:**

Guillaume Chabaud. 3D and 4D printing of high performance continuous synthetic and natural fibre composites for structural and morphing applications. Materials. Université de Bretagne Sud, 2020. English. NNT : 2020LORIS563 . tel-03217124

HAL Id: tel-03217124

<https://theses.hal.science/tel-03217124>

Submitted on 4 May 2021

HAL is a multi-disciplinary open access archive for the deposit and dissemination of scientific research documents, whether they are published or not. The documents may come from teaching and research institutions in France or abroad, or from public or private research centers.

L'archive ouverte pluridisciplinaire **HAL**, est destinée au dépôt et à la diffusion de documents scientifiques de niveau recherche, publiés ou non, émanant des établissements d'enseignement et de recherche français ou étrangers, des laboratoires publics ou privés.

THESE DE DOCTORAT DE

L'UNIVERSITE DE BRETAGNE SUD

ECOLE DOCTORALE N° 602

Sciences pour l'Ingénieur

Spécialité : « Génie des matériaux »

Par

Guillaume CHABAUD

3D and 4D printing of high-performance continuous synthetic and natural fiber composites for structural applications and morphing.

Impression 3D et 4D de composites à hautes performances renforcés par des fibres continues synthétiques ou naturelles pour des applications structurelles ou de morphing.

Thèse présentée et soutenue à Lorient, le 16 Octobre 2020

Unité de recherche : IRDL UMR CNRS 6027

Thèse n°563

Rapporteurs avant soutenance :

Nadia Bahlouli, Professeur, Icube Université de Strasbourg

Masahito Ueda, Associate-professor, Nihon University Tokyo

Composition du Jury :

Président :	Yves Grohens	Professeur, IRDL, Université Bretagne Sud
Examineurs :	Nadia Bahlouli	Professeur, Icube Université de Strasbourg
	Amandine Celino	Maître de Conférences, GeM, Université de Nantes
	Fabrizio Scarpa	Professor, ACCIS, University of Bristol (UK)
	Jérémie Soulestin	Professeur, IMT Lille Douai
	Masahito Ueda	Associate-professor, Nihon University Tokyo (JP)
Dir. de thèse :	Antoine Le Duigou	Maître de Conférences-HDR, Université Bretagne Sud
Co-dir. de thèse :	Mickaël Castro	Maître de Conférences, Université Bretagne Sud

Remerciements

En tout premier lieu, je souhaite remercier chaleureusement mes directeurs de thèse, Antoine Le Duigou et Mickaël Castro, sans qui cette thèse n'aurait pas été possible. Merci de m'avoir encadré durant ces trois ans, merci pour votre aide et votre soutien !

Un grand merci à Nadia Bahlouli, Amandine Celino, Yves Grohens et Jérémie Soulestin d'avoir accepté d'être membres du jury. Many thanks as well to Fabrizio Scarpa and Masahito Ueda for agreeing to be part of my jury.

Je remercie également les membres de l'IRDL pour leur aide et leur disponibilité, notamment Antoine Kervoelen, Françoise Peresse, Hervé Bellegou, William Berckmans, Edouard Gheslain, Anthony Magueresse, Thomas Pierre, Thibault Colinart, Vincent Keryvin, Samuel Réquillé, Camille Goudenhooff, ainsi qu'au reste de l'équipe de l'IRDL pour leurs nombreux conseils et aides apportés tout au cours de ma thèse.

Je remercie les différentes personnes de CompositIC et Irma pour leur accueil, leur aide technique et scientifique tout au long de ma thèse, notamment Romain Bevan, Antoine Barbé, Kevin Henry, Clément Denoual, Yves-Marie Corre, Morgane Deroiné ainsi que toutes les autres personnes de IRMAtech et CompositIC.

Je remercie également Mael Arhant et Peter Davies pour leur accueil au sein de l'Ifremer de Brest ainsi que de leurs contributions au cours de ces travaux.

Je souhaite également remercier les membres du jury du concours SAMPE France, Philippe Briant, Charlotte Salaun et Jérôme Brouard de m'avoir donné l'opportunité de participer au SAMPE Europe, ce qui fut une expérience très enrichissante.

Je remercie également l'ensemble des doctorants de l'Université Bretagne Sud, plus particulièrement mes collègues de bureau Victor, Lucile, Delphin, Samuel et Camille, pour la bonne humeur toujours de mise et les bons moments passés dans le cadre du travail ou en dehors.

Enfin, un grand merci à ma famille et mes amis pour vos encouragements et votre soutien durant ces trois ans malgré la distance, vos visites en Bretagne et également, parfois, vos conseils.

Scientific contributions

Contests:

Second position at the French SAMPE Chapter, selection for the International Students Seminar Chapter, SAMPE Europe 2019

Participation at the 34th International Students Seminar, SAMPE Europe 2019

Accepted publications:

G. Chabaud, M. Castro, C. Denoual, A. Le Duigou, “Hygromechanical properties of 3D printed continuous carbon and glass fibre reinforced polyamide composite for outdoor structural applications,” *Additive Manufacturing.*, vol. 26, pp. 94–105, 2019.

DOI: <https://doi.org/10.1016/j.addma.2019.01.005>

A. Le Duigou, **G. Chabaud**, F. Scarpa, M. Castro, “Bioinspired Electro-Thermo-Hygro Reversible Shape-Changing Materials by 4D Printing,” *Advanced Functional Materials.*, vol. 29, pp. 1–10, 2019. DOI: <https://doi.org/10.1002/adfm.201903280>

Publications under review:

A. Le Duigou, **G. Chabaud**, R. Matsuzaki, M. Castro, “Tailoring the mechanical properties of 3D printed continuous flax/PLA biocomposites by controlling the slicing parameters”, *Composites Part B*, 2020.

International conferences:

G. Chabaud, M. Castro, A. Le Duigou, “3D and 4D printing of continuous carbon fiber composites: from structural applications to morphing structures”, SAMPE Europe 2019, 2019 (poster).

National conferences:

G.Chabaud, M.Castro, A.Le Duigou, “Impression 3D et 4D de matériaux composites à fibres de carbone continues : des applications structurelles au morphing de structures”, 21ème édition des Journées Nationales sur les Composites, 2019.

G.Chabaud, M.Castro, A.Le Duigou, “Impression 4D de matériaux composites multi-stimulables pour le morphing de structures”, 24ème édition du Congrès Français de Mécanique », 2019.

Table of contents

Glossary

General introduction	1
-----------------------------------	---

Chapter 1: State of the art in 3D/4D printing of continuous fiber-reinforced (bio)composites: achievements and future outlooks	10
---	----

1. General presentation of 3D printing and Fused Filament Fabrication	12
1.1. Principle of 3D Printing.....	12
1.2. Glossary and definitions of 3D printing.....	13
2. Overview of current research on 3D printing of thermoplastic materials with Fused Filament Fabrication (FFF)	15
2.1. Presentation of FFF process for pure thermoplastics and current limitations ..	15
2.2. Parametric studies on 3D printed parts for the improvement of mechanical properties	17
2.2.1. <i>Influence of printing parameters</i>	18
2.2.2. <i>Influence of slicing parameters</i>	20
3. 3D printing of fiber reinforced composite materials.....	22
3.1. 3D printing of discontinuous fiber-reinforced composites	23
3.2. 3D printing of continuous fiber reinforced composites.....	28
3.2.1. <i>Overview of the mechanical characterization of 3D printed continuous fiber reinforced composites</i>	33
3.2.2. <i>Current limitations in 3D printing of continuous fiber composites</i>	41
3.2.3. <i>Future outlook on the optimization of 3D printing of continuous fiber reinforced composites</i>	43
4. 4D Printing of synthetic materials.....	50
4.1. 4D printing of polymer and composite materials.....	52
4.2. Humidity as a motor of actuation	60
4.3. Future outlook on the optimization of 4D printing of fiber reinforced composites.....	63
5. 3D and 4D printing of natural fiber reinforced composites	68
5.1. Natural fiber specificities for 3D printing	68
5.2. Filament production	71
5.3. 3D printing of natural fiber composites	72
5.4. Future outlook on the optimization of 3D printing of natural fiber reinforced composites.....	76
5.5. 4D printing of natural fiber reinforced composites.....	78
5.6. Future outlook on the optimization of 4D printing hygromorphic (bio)composites	84
6. Bibliography summary.....	87

Chapter 2: Materials and Methods	90
1. Material selection.....	91
1.1. Synthetic continuous fiber reinforced composites.....	91
1.2. Flax continuous fiber reinforced biopolymer composites	91
2. Manufacturing by 3D printing.....	92
2.1. Synthetic continuous fiber composites.....	92
2.2. Printing of continuous flax fiber reinforced composites.....	94
3. Mechanical characterization	95
3.1. Tensile tests on single fiber and composites.....	95
3.1.1. <i>Tensile tests on synthetic fiber</i>	95
3.1.2. <i>Tensile tests on synthetic-fiber reinforced composites</i>	95
3.1.3. <i>Tensile tests on flax-fiber reinforced composites</i>	96
3.2. Characterization of interlaminar properties of synthetic continuous fiber composites.....	97
3.3. Three-point bending characterization	99
4. Analysis of the microstructure.....	100
4.1. Optical microscopy.....	100
4.2. Scanning Electron Microscopy (SEM).....	100
5. Hygroscopic conditions and seawater aging.....	100
5.1. Specimen storage in various humidity chambers.....	100
5.2. Seawater-aging of 3D printed composites	101
5.3. Moisture sorption measurement.....	101
5.4. Hygro-expansion measurement.....	101
6. Measurement of the actuation of hygromorphic composites based on continuous carbon fiber and continuous flax fibers, and electro-thermo-hygromorphic composites based on continuous carbon fiber.	102
6.1. Description of the environmental conditions for actuation	102
6.2. Electrical stimulus generation.....	102
6.3. Measurement of the actuator curvature	103
7. Thermal characterization of the composites	104
7.1. Differential Scanning Calorimetry (DSC)	104
7.2. Thermogravimetric analysis (TGA).....	104
7.3. Thermal expansion measurement	104

Chapter 3: Mechanical and hygromechanical properties of continuous carbon and glass fiber composites.....105

1. Microstructure description.....	107
1.1. Filament microstructure description	107
1.2. Cross-section description	107
1.3. In-plane description	111
2. Mechanical characterization	114
2.1. Longitudinal and transverse characterization	114

2.2.	Evaluation of interlaminar properties with Double Cantilever Beam (DCB) tests.	118
2.2.1.	<i>Mode I delamination resistance behavior</i>	119
2.2.2.	<i>Comparison of critical strain energy release rates with literature values</i>	121
3.	Evolution of mechanical performances under exposure to wet environment and accelerated seawater aging	124
3.1.	Sorption behavior and hygroscopic expansion	124
3.1.1.	<i>Moisture uptake and hygroscopic expansion in humid environment</i>	124
3.1.2.	<i>Evolution of water uptake and hygroscopic expansion during seawater aging</i>	127
3.2.	Evolution of tensile behavior under different moisture conditions	130
3.3.	Influence of seawater aging on flexural properties of 3D printed composites	133
	Conclusion	137
Chapter 4: Bio-inspired reversible electro-thermo-hygro reversible shape-changing materials by 4D printing		140
1.	Concept of 4D printed electro-thermo-hygromorphic structural composite materials	142
2.	cCF/PA6-I:PA6 bilayers as hygromorphic actuators	145
3.	cCF/PA6-I:PA6 bilayers as electro-thermo-hygromorphic actuators	148
4.	Influence of the print pattern on the electro-thermo-hygro actuation of the cCF/PA6-I:PA6 bilayers	154
4.1.	Influence of the printed pattern on the electro-heating	156
4.2.	Influence of the printed pattern on the electro-thermo-hygromorphic actuation	159
	Conclusion	165
Chapter 5: Tailoring the mechanical properties of 3D printed continuous flax/PLA biocomposites with slicing parameters		167
1.	Production of continuous filaments of flax/PLA biocomposites and description of the microstructure	169
1.1.	Production of continuous filament of flax/PLA biocomposites by co-extrusion process	169
1.2.	Microstructure of the continuous filament of flax/PLA biocomposites prior to printing	170
2.	Influence of Layer Height (LH) on the mechanical properties of printed cFF/PLA composites	171
3.	Influence of Trip Number (TN) and Interfilament Distance (ID) on the mechanical properties of printed cFF/PLA composites	175
4.	Influence of Layer Number (LN) on the mechanical properties of printed cFF/PLA composites	180

5. Influence of raster angle / fiber orientation on the mechanical properties of printed cFF/PLA composites.....	185
Conclusion	188
Chapter 6: 4D printing of hygromorphic biocomposites with continuous flax fiber/PLA: toward compliant mechanism.....	190
1. Design of hygromorphic biocomposites	192
2. Material selection.....	195
3. Control of the stiffness with variation of the architecture by controlling the interfilament distance	200
4. Compliant mechanism with localized bending actuation.....	204
Conclusion	207
General conclusion	209
Perspectives	213
References	219

Glossary

μ-CT	Micro-computed Tomography	MCC	Modified Compliance Calibration
ABS	Acrylonitrile Butadiene Styren	MFR	Mass Flow Rate
AFP	Automated Fiber Placement	NASA	National Aeronautics and Space Administration
ASTM	American Society for Testing and Materials	NFC	Natural Fiber Cellulose
ATL	Automated Tape Laying	P2VP	Poly(2-vinylpyridine)
BAAM	Big Area Additive Manufacturing	PA	Polyamide
BOPP	Biaxially Oriented PolyPropylene	PA6-I	Polyhexamethylene isophthalamide
CAD	Computer Aided Design	PAAM	Poly(acrylic acid co-acrylamide)
CBT	Corrected Beam Theory	PBS	Polybutylene Succinate
cCF/PA6-I	3D printed continuous carbon fiber polyhexamethylene isophthalamide matrix	PC	Polycarbonate
cFF/PBS	3D printed continuous flax fiber polybutylene succinate matrix	PCL	Poly(ϵ -caprolactone)
cFF/PLA	3D printed continuous carbon fiber polylactic acid atrix	PEDOT:PSS	Poly(3,4-ethylenedioxythiophene):poly(styrenesulfonic acid)
cGF/PA6	3D printed continuous carbon fiber PA6-I matrix	PEEK	Poly-ether-ether-ketone
CHE	Coefficient of Hygroscopic Expansion	PEGDA	Poly(ethylene glycol) diacrylate
CMC	CarboxyMethyl Cellulose	PEKK	Poly-ether-ketone-ketone
MFA	MicroFibril Angle	PETG	Polyethylene glycol
CTE	Coefficient of Thermal Expansion	PHA	Polyhydroxylalcanoate
DCB	Double Cantilever Beam	PLA	Polylactic acid
DSC	Differential Scanning Calorimetry	PNIPAm	Poly(acryl acid-co-N-isopropyl acrylamide)
EBM	Electron Beam Melting	POM	Polyoxymethylene
FDM	Fused Deposition Modeling	RH	Relative Humidity
FFF	Fused Filament Fabrication	ROM	Rule Of Mixture
G_{ic}	Critical Energy Strain Rate	SEM	Scanning Electron Microscopy
HBC	Hygromorphic Biocomposites	SLA	Stereolithography
HEPA	Hygroexpansive Electrothermal Paper Actuators	SLS	Selective Laser Sintering
ID	Interfilament Distance	SMC	Shape Memory Composites
IFSS	InterFacial Shear Strength	SME	Shape Memory Effect
ILSS	InterLaminar Shear Strength	SMP	Shape Memory Polymer
ISO	International Organization for Standardization	STL	Standard Tessellation Language
LCA	Life Cycle Analysis	TCP	Toner Coated Paper
LCE	Liquid Crystal Elastomer	TGA	Thermogravimetric Analysis
LH	Layer Height	TN	Trip Number
LN	Layer Number	TPU	Thermoplastic Polyurethane
LOM	Laminated Object Manufacturing	VAS	Volume Average Stiffness
LT	Layer Thickness	VSC	Variable Stiffness Composites

General introduction

The concept of additive manufacturing refers to technologies that aim to produce three-dimensional objects with the addition of matter layer-by-layer. Additive manufacturing is a promising technology that allows precise control of the trajectory of deposition and thus the architecture and properties of the materials. This concept is opposed to “subtractive manufacturing” where matter is removed from an object to create the desired shape (for example: milling, drilling, slitting...).

Automation of composite manufacturing is a great challenge, but not so new, as the Automated Fiber Placement (AFP) and the Automated Tape Laying (ATL) technologies have been widely used in aeronautic sector since the late 1980s. These technologies allow the placement of tapes (from 3 to 100 mm) to efficiently build custom laminates, layer-by-layer, with planar or curved geometry. ATL systems are normally mounted on horizontal gantries or vertical columns because of the high mass of the head. ATL systems follow accurately predefined trajectories with good reproducibility, thus eliminating layup errors that could occur during manual laying. However, this process is limited to a simple design with small variations in curvature. The AFP technology aims at laying down fibers tapes on the surface of a mold thanks to a robotic head with 7 or 8 mobile axis and allows to manufacture structures with more complex shapes than ATL. However, these technologies are restrained to a large scale with a minimum tape length of 100 mm and is prohibitively costly which limits their applications to industrial fields.

The 3D printing process is a generic branch of additive manufacturing and aims to build a three-dimensional object from a computer-aided design (CAD) model layer-by-layer under computer control. 3D printing was born in 1986 when Chuck Hull issued the patent “Apparatus for production of three-dimensional objects of stereolithography” and commercialized the first 3D printing device called SLA-250. In 1988, another 3D printing method was patented by Scott Crump and commercialized by Stratasys in 1992. This process is trademarked under the name Fused Deposition Modeling (FDM™), also called Fused Filament Fabrication (FFF). This technology is based on the melting of a thermoplastic filament through to a heated nozzle and the layer-by-layer deposition of the molten polymer. Nowadays, this process has become the most widely spread 3D printing technique thanks to its easy use and the low cost of FFF 3D printers compared to other techniques such stereolithography (SLA), selective laser sintering (SLS), inkjet printing; selective laser melting (SLM), electron beam melting (EBM), laminated object manufacturing (LOM), etc...

During the last decades, 3D printing has overcome many innovations regarding the material availability and the improvement of technical performances (accuracy, reproducibility, process speed...). Between years 2000 and 2010, initiation of the *Reprap* project at the university of Bristol (UK) and the expiration of FDM patent from Stratasys® led to large open-source movement that significantly reduced costs. The RepRap (Replicating Rapid prototypes) project is an initiative that aims to develop open source 3D printers capable of printing most of its own to enable the democratization of 3D printing technology by FFF. All these features allow 3D printing to spread for private consumers and companies. According to a report published by the International Data Corporation (IDC) in January 2019, global spending on 3D printing (materials, hardware, software and services) estimated that 3D printing market may reach \$13.8 billion in 2019 and \$22.7 billion in 2024 with an annual growth rate of 19.1 %. 3D printing market size forecast in the five years according to various analysts is displayed in Figure 0.1.

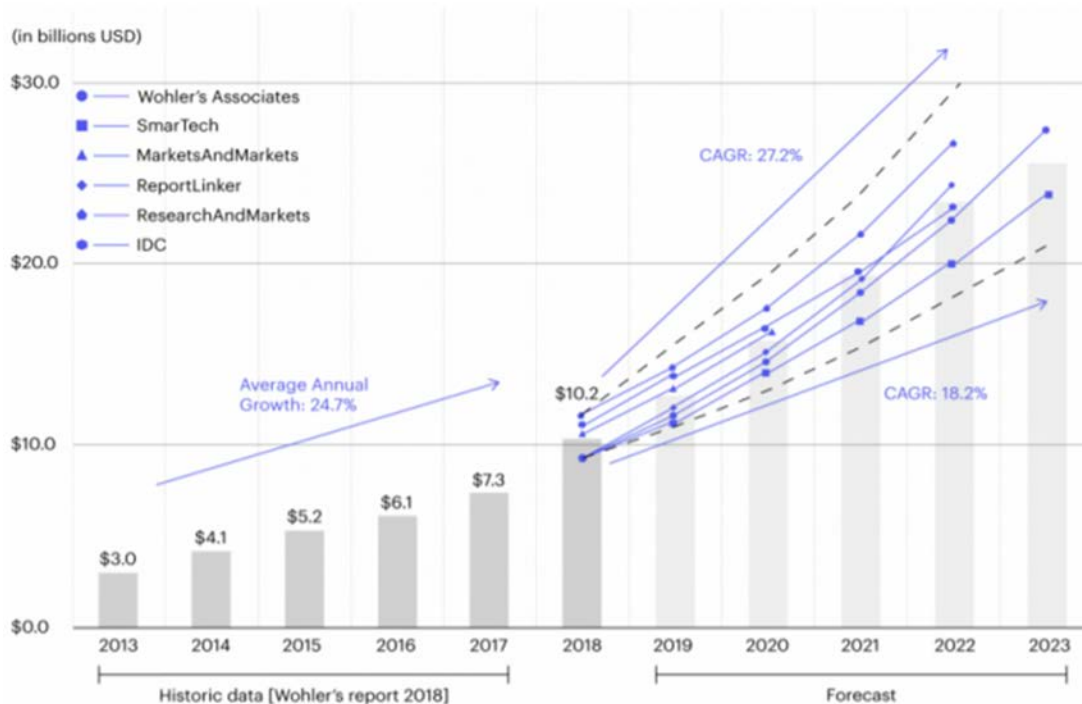


Figure 0.1: 3D printing market size according to Wohler's report (2018) and forecast of 3D printing market size until 2023 according to various market analysis.

Nowadays, 3D printing technology has become a disruptive innovation and has found many applications (automotive, aerospace, medical, robotics, building, food industry, marine engineering...). The maritime field, within the Framework of the Sailing Valley in Lorient, is currently researching high performance structural parts, especially for ocean racing, with complex design and

sufficient manufacturing reproducibility. To this end, companies such as Avel Robotics (<https://fr.avelrobotics.com/>), SEAir (<https://www.seair-boat.com/fr/>) or Coriolis Composites (<https://www.coriolis-composites.com/>) are working directly or indirectly on the manufacture of hydrofoils for ocean yachting race by AFP. Marine engineering should also lead to severe conditions such as those experienced in ocean expeditions or marine transport, where it is difficult to quickly repair materials or bring in spare parts. Thus, 3D printing offers an encouraging solution where printed materials also offer high mechanical performance and durability.

The main interest of 3D printing compared to the traditional manufacturing process is the ability to produce final parts in fewer steps, which speeds up the production process and leads to lower manufacturing costs. Moreover, it offers the possibility to accurately control material architecture (fiber orientation for composite materials, material location, infill structure). Compared to AFP and ATL technologies, 3D printing allows to automatically manufacture small-scale structures without design limitations. For maintenance applications, 3D printing is transportable under outdoor conditions and is suitable for the manufacture of spare parts.

However, the most widespread 3D printing technique, FFF of thermoplastic materials, nowadays has certain limitations. In first instance, 3D printing of thermoplastic polymer is limited for the production of prototypes, trial products or toys due to moderate mechanical properties and a poor understanding of the relationship between process, microstructure and properties. Because of its potential, the applicability of 3D printing to the manufacture of high mechanical performance parts is a major objective of industrial manufacturing.

One of the solutions to improve mechanical properties is the development of short fiber reinforced polymer filaments. The fibers such as carbon, glass or natural fibers significantly improve mechanical performance, reduce warping and offer a higher dimensional stability. This improvement has enabled, for example, the development of Big Area Additive Manufacturing (BAAM). This technology was used to print a full-scale car body at the 2014 International Manufacturing Technology Show in Chicago, as well as a full-scale boat, the 3Dirigo, printed at the University of Maine in 2019. Nevertheless, 3D printed composites have moderate mechanical properties compared to conventional manufacturing processes. Consequently, short fiber-reinforced filaments cannot be used in structural applications.

In 2014, R. Matsuzaki et al. were among the first to investigate the addition of continuous fibers in 3D printed composites to develop high performance materials. Their “in-nozzle impregnation”

technology has overcome the performance of short fibers composites and is today extensively studied. Next, industrial 3D printers capable of printing continuous fibers reinforced composites were commercialized, *i.e.* the *MarkOne*[®] and *MarkTwo*[®] from Markforged[®] (released in 2016) and the *Composer*[®] from Anisoprint[®] (released in 2019) (Figure 0.2).



Figure 0.2: Photography of *MarkTwo*[®] from Markforged[®] (left) and *Composer*[®] A3 from Anisoprint[®] (right).

An increasing number of companies are now working on the development of 3D printers capable of printing continuous synthetic fiber such as 9T Labs[®] and Desktop Metal[®] which are developing solutions for 3D printing of very high performance composites with very high fiber content (60 % vol.) and low porosity (< 1 %) for structural applications. Other company such as Arevo[®] and +Lab[®] are also working on 6 axis 3D printers, which combine AFP with 3D printing, to develop continuous fiber-reinforced structures of complex shapes. The stimulating potential of this technology and the performance of the associated composites has yet to be fully understood.

Beyond improving the mechanical performance of 3D printing composites, Skylar Tibbits from the Massachusetts Institute of Technology proposed the term of 4D printing in 2013. 4D printing is : “ (...) takes multi-material 3D printing to deposit multiple materials and add a capability of transformation to printed parts which are able to transform from one shape to another shape directly on their own (...)”. 3D printing capabilities are used in 4D printing to print multi-materials with precisely adjusted architecture to develop pre-programmed self-assembly structures. Hence, 4D printing makes it possible to obtain a self-assembled structure, self-repairing materials and adds multi-functionality to printed structures. Transformation properties of 4D printed parts are triggered by external stimulation, e.g. water, temperature, light or mechanical actuation. Many fascinating applications can be imagined with the help of 4D printing, especially for self-assembled structures. For example, one could imagine self-assembled buildings, many applications in the space industry could be targeted (deployment of solar panels or antennas without energy input, improvement of the transportation system for the International Space Station, etc...).

As a result of the current environmental situation described by the Special Report on Global Warming of 1.5°C published by the Intergovernmental Panel on Climate Change in 2018 that now well established (except for some climatosceptic), the way in which materials and structures are designed and manufactured is expected to change. Therefore, the selection of materials must be made with care and mechanical performance is not the only parameter to be promoted. Thus, local sourcing, renewability, low energy to be produced and finally end of life management are, among other things, the key parameters for conducting an eco-design approach. Manufacturing should induce low energy consumption and reduce waste.

In this way, natural fiber-reinforced composites and additive manufacturing are a relevant alternative to synthetic counterparts manufactured by conventional processes. Flax fibers like other bast fibers used to reinforce plant stems, have high stiffness and a strength-to-density ratio that is competitive with the properties of glass fibers. The Life Cycle Assessment (LCA) has also shown that flax fibers have a moderate environmental impact compared to glass. However, due to short-term research (around 20 years), compared to synthetic composites, biocomposites are still lagging behind in terms of technological maturity but also in terms of basic understanding. 3D/4D printing is an incredible opportunity for biocomposites to develop for the first time on the same time scale as their synthetic counterpart 3D printing of natural fibers composites.

The development of 3D and 4D printing is progressing together with the optimization of design tools such as topological or parametric optimization. NASA has recently identified a synergistic effect to combine 3D printing and biomimicry through the possibility of manufacturing complex architectures. An increasing number of articles reflect this trend (Figure 0.3).

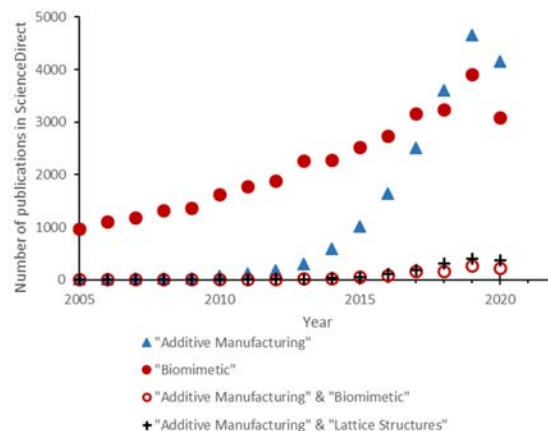


*Figure 0.3: Number of publications for the period 2005-2020 in biomimicry and additive manufacturing
(Adapted from Du Plessis et al, Additive Manufacturing, 2019).*

The latter is now described by standards ISO_PRF_18458; ISO_PRF_18459 and could be done in two ways: Bottom-up (or Biology influencing design) with biological push approach and Top-Down (Design looking to biology or Problem-Driven Biologically Inspired Design) with an engineering driven approach.

Bottom-up is defined as: identifying a particular characteristic, behavior or function in an organism or ecosystem and translating that into human designs.

Top down approach is defined as: *“Defining a human needs or designing problem and looking to the ways other organisms or ecosystems solve this”*. Top-down approach of biomimicry has offered a new opportunity to overcome current material properties in terms of crack resistance, stiffness to weight ratio, damping and adaptability (morphing). In addition, this approach enables to turn the drawbacks of the materials into new functionalities. For example, natural fiber composites suffer from moisture which limits their use in outdoor semi-structural applications. Inspired by hygromorphic biological actuators such as the pine cone, Hygromorphic Biocomposites have been developed since 2015 by Le Duigou et al. as new multifunctional smart materials and combine the paradigm of biomimicry with eco-design. These materials are capable of changing shape autonomously in response to changes in humidity due to the anisotropic hygroscopic expansion of the natural fibers (fiber-dominated actuation) and their asymmetrical architecture. Autonomous morphing (or meteo-sensitive) included in a frugal design is a real advantage when aiming for low maintenance and extreme environment. However, market field of natural fibers based printable filaments is today limited to few products such Woodfill from Colorfabb (Polylactic acid filled with 30 % wt. of wood flour), Laywoo-D3 from Lay Filaments (Polylactic acid (PLA) filled with 40 % wt. of wood fibers) or Starflax® 3D from Nanovia® (PLA filled with flax fibers) for example. Moreover, non-open access 3D printers, only able to print their own materials (such MarkTwo® from Markforged® or Composer® from Anisoprint®), restrain further development.

To overcome current limitations, the objective of this thesis work is to provide more in-depth knowledge on the relationship between the 3D and 4D printing manufacturing process, the resulting microstructure, the mechanical and hygro-mechanical behaviors for two types of high performance composite materials.

Figure 0.4 present a schematic overview of this thesis work. The methodology is applied on continuous “off-the-shelf” synthetic fiber (Carbon, Glass) and on flax fiber composites produced on this occasion. Structural or semi-structural applications and morphing structures are targeted. First of all, the principle of 3D printing is exposed while a glossary and a global definition will be proposed.

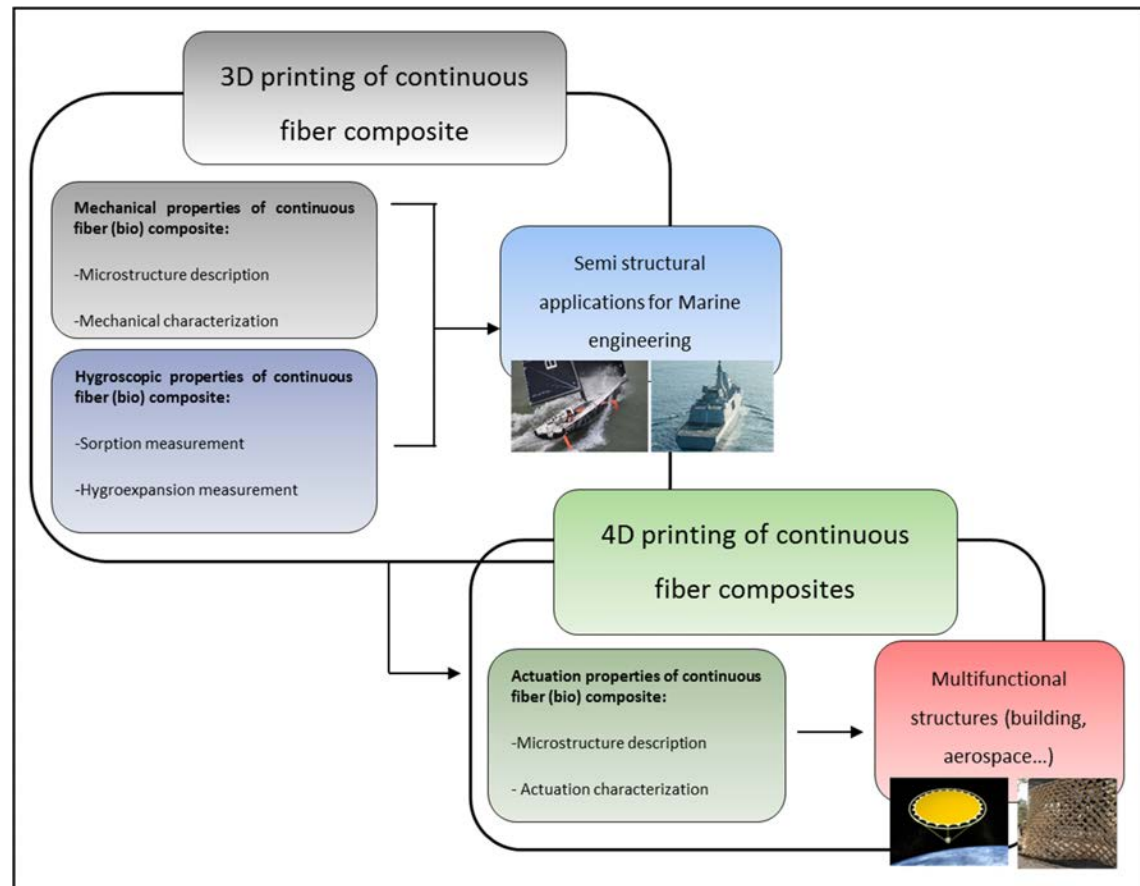


Figure 0.4: Schematic overview of thesis work.

Then, in Chapter 1, a literature review on 3D printing of thermoplastic composites is performed with a focus on the 3D printing of continuous synthetic and natural fiber composites. This overview of current advances in 3D printing of composite materials is presented alongside work on conventional manufacturing and other additive manufacturing technologies such as Automated Fiber Placement (AFP) and Automated Tape Laying (ATL). On this purpose, the mechanical performance reached with 3D printed continuous fiber composites is discussed as well as current limitations and process improvements. Then, the 4D printing technology for polymer and composites materials is described and current research trends are presented for synthetic and natural fiber composites with regard to architecture and material optimization.

In Chapter 2, the different materials, experimental techniques and measurement protocols used in this study are presented and described. A first part is devoted to the selection of materials. A second section presents the 3D printing process. A third section presents the mechanical characterization methodology (tensile test, three-point bending and out-of-plane characterization). The fourth section displays the imaging techniques used to describe the composite microstructure. The fifth part shows the environmental conditioning used to evaluate the evolution of mechanical performance with respect to moisture or sorption. The sixth section describes the 4D printing procedure for continuous carbon fibers composites and continuous flax fibers composite with hygromorphic and electro-thermo-hygromorphic actuation and the last section presents the thermal characterization of the composites.

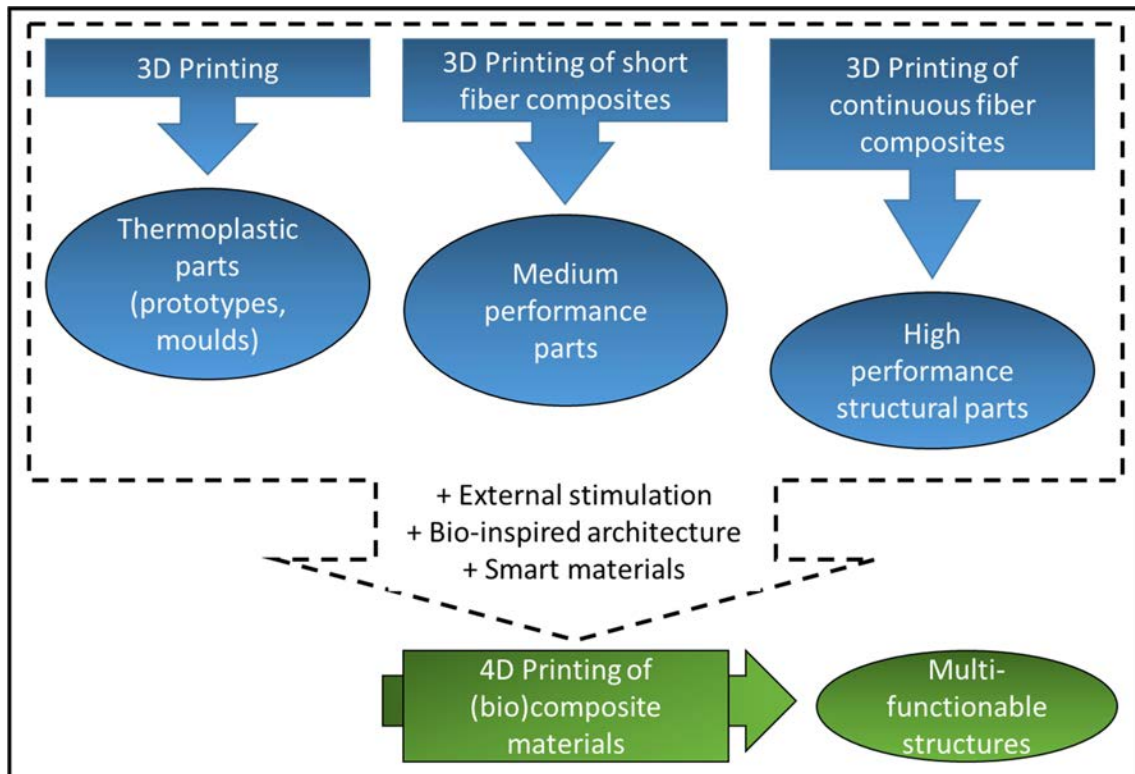
In Chapter 3, the mechanical characterization of two continuous fiber composites, carbon and glass fibers reinforced PolyAmide (PA) composites manufactured with a commercial 3D printer is shown. The relationship between the microstructure of the composite (voids, fibers orientation, printing strategy and edge effect) and mechanical performance is investigated by the means of three mechanical characterizations; tensile test in the fibers direction (longitudinal properties), tensile test perpendicular to fibers direction (transverse properties) and measurement of out-of-plane properties through Double Cantilever Beam (DCB) tests. Properties are discussed and compared to those of conventional manufacturing to establish a baseline for 3D printing with continuous fiber composites. As the polyamide matrix used is well-known for its chemical composition induced hygrosensitivity, moisture and water-induced properties are evaluated to identify i) their durability in wet environment and seawater conditions for marine applications and ii) their potential of matrix-dominated hygromorphism for smart 4D printed devices following biomimicry top-down rules.

In Chapter 4, following the hygromechanical properties of printed continuous carbon fibers/polyamide composites, the design and development of a new paradigm of bio-inspired 3D/4D electro-thermo-hygromorphic actuators is presented. First, passive or autonomous hygromorphic behavior is characterized experimentally by following the evolution of responsiveness (curvature amplitude) and reactivity (curving kinetic) of asymmetric composites in various humid environments. Then, this study focuses on the control of moisture content and desorption kinetics within continuous carbon fibers/PA using a combination of electrical, thermal and hygroscopic stimuli. The applied current, thermal distribution, moisture content and the resulting actuation (amplitude and kinetic) are monitored. Finally, the influence of the printed pattern on the resulting actuation is studied and discussed.

Chapter 5 is based on the development of novel continuous flax yarns biocomposites based on Polylactic acid (PLA) using a customized 3D printer with tailorable properties. The multiscale investigation of 3D printed flax yarns reinforced biopolymer is carried out by studying the relationship between the slicer parameters (Layer height, interfilament distance...) on the microstructure and the resulting mechanical performance. Mechanical properties are discussed and compared to conventionally manufactured biocomposites (Injection molding or thermocompression).

Finally, chapter 6 presents 4D printing of continuous flax fiber (cFF) biocomposites with PLA and PBS matrices. The objective is to design and manufacture fiber-dominated Hygromorphic BioComposites. The design methodology is examined in terms of the use of 4D printing. Then, the selection of materials is presented in terms of matrix stiffness and strain with the characterization of the hydroelastic properties of cFF/PLA and cFF/PBS. Stiffness control with a local and progressive architecture of the cFF/PBS composite is investigated following the bending responsiveness and the reactivity given by the different interfilament Distance (*ID*). Finally, compliant (hinge-type) mechanisms are printed and tested. The last part of this manuscript is a general conclusion and perspectives to highlight the main achievements of this work and to discuss future studies and improvements.

Chapter 1: State of the art in 3D/4D printing of continuous fiber-reinforced (bio)composites: achievements and future outlooks



This first chapter aims to present a state of the art on 3D printing of thermoplastic materials with Fused Filament Fabrication (FFF) with emphasis on synthetic and natural fiber reinforced composites for structural and morphing applications. Hence, after a general presentation of 3D printing technology with an exhaustive glossary, a description of FFF with thermoplastic materials is done to highlight the moderate mechanical performances. To overcome this drawback, two solutions are detailed, one focused on process parameters optimization and one on the material scale where the addition of reinforcing fibers is investigated. Two categories of reinforcing fibers are presented and discussed here, discontinuous and continuous fibers. The benefits brought by these fibers to 3D printed thermoplastic by FFF are displayed with an emphasis on the mechanical performances linked to the microstructure. This literature review provides a better understanding of the relationship between mechanical performance and microstructure and identifies the improvement required for 3D printed composites to reach structural applications.

However, in the composite industry there is a need to develop multi-functional composite materials. In this context, 4D printing (3D printing materials with time-dependent properties triggered by an external stimulus) has emerged in the late years. Section 4 describes 4D printing of polymeric and composite materials, summarizing the materials and stimulation investigated in the literature as well as the current limitations. This section also presents an overview of the future prospects for 4D printing of composite and polymeric materials.

Section 5 of this chapter details the literature research on 3D and 4D printing of natural fiber-reinforced composites. There is a growing interest in natural fibers in the composite industry. Indeed, they possess high specific strength (competitive to glass fibers properties) and a lower environmental footprint. Consequently, a growing number of research teams are now working on natural fiber-reinforced composites for 3D printing and these works are presented in this chapter. Moreover, natural fibers have shown great potential for designing multifunctional materials through the study of hygromorphic biocomposites (composites reinforced with natural fibers able to modify its shape in response to humidity) and, consequently, the addition of natural fibers in 4D printed structures is a promising new research trend.

1. General presentation of 3D printing and Fused Filament Fabrication

1.1. Principle of 3D Printing

3D printing principle is divided in five major steps. First, a numeric file is generated thanks to a numeric model developed by Computed Aid Design (CAD) that represents the desired part. CAD model can be generated thanks to two methods: design of the part with a CAD software or with a digitalization technique such 3D scanner. Numeric model is then generated in a file; most common used format is STL (Standard Tessellation Language) invented by the company 3D system which commercialized the first stereolithography (SLA) 3D printer [1]. Thus, STL file is uploaded in a software dedicated to 3D printing named slicer. This software slices the model layer-by-layer and defines the printing pathway for each layer and generates a G-code file. G-code is a language for computerized machine tools which summarizes all engine instructions (path to follow, how fast to move, which motors are required, etc...). Then, the 3D printing begins with the layer-by-layer built up of desired part. Depending on printing techniques and on part complexity, post-treatment may be required (polishing, chemical treatment to remove support; etc...). These 3D printing steps are summarized in Figure 1.

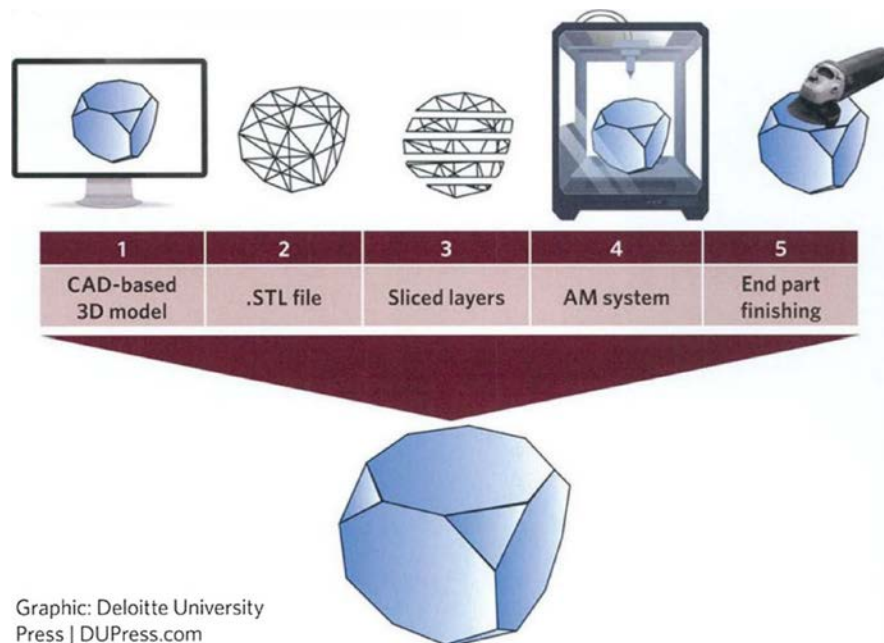


Figure 1 : 3D principle divided in 5 major steps [2].

1.2. Glossary and definitions of 3D printing

Fused Filament Fabrication process:

During printing, a polymer filament is brought to an extruder head by means of drive wheels. The extruder head is composed of driving wheels which pull the filament through a liquefier, a heating resistor which aims to heat the filament above its glass transition temperature (if it is an amorphous polymer) or above its melting temperature (if it is a semi-crystalline polymer). This liquefier heats up an extruder nozzle where the molten polymer flows. The extruder head moves along X and Y directions (Figure 2) and deposits beads (extruded filament) following a raster (printing pattern defined prior printing). The bead is deposited in a heated build plate (or bed) placed on a building platform. When a layer is over, the building platform (or the extrusion head depending on 3D printer model) move vertically to let the extrusion head print the following layers until finishing the part [3].

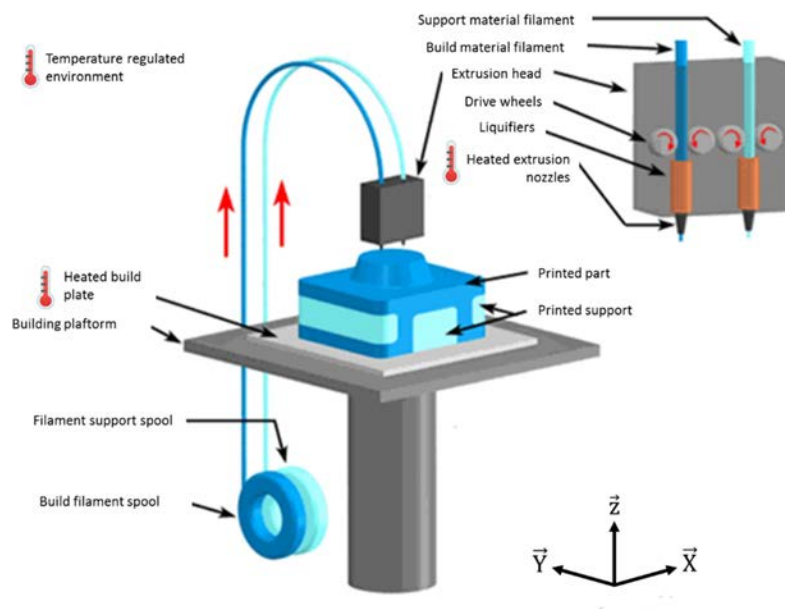


Figure 2 : Schematic representation of FFF process showing the components of a 3D printer by FFF. Adapted from [4].

The following section aims to describe the main slicing and printing parameters used in 3D printing. The slicing parameters are related to the architecture of the material, while the printing parameters are related to the 3D printer itself. Figure 3 shows a schematic representation of these parameters.

Slicing parameters:

- Layer Height (LH) refers to the distance between the nozzle and the building platform of the printed layers.
- Raster/Air gap or Interfilament Distance (ID) refers to the distance between the center of two printed beads within a same layer.
- Raster Angle (RA) refers to the angle between nozzle trajectory during printing and the axis X.
- Raster/Bead width is the width of deposited material. Small values lead to a lower production time and material amount while high value allows to print stronger parts.
- Building orientation refers to the part orientation on the build platform with respect to X, Y, Z axes (Figure 3.b).
- Infill percentage is the percentage of matter within the printed structure.
- Infill pattern represents the trajectory of printed beads. In the literature, two patterns are used, i.e. concentric (Figure 3.c) and isotropic pattern (Figure 3.d).

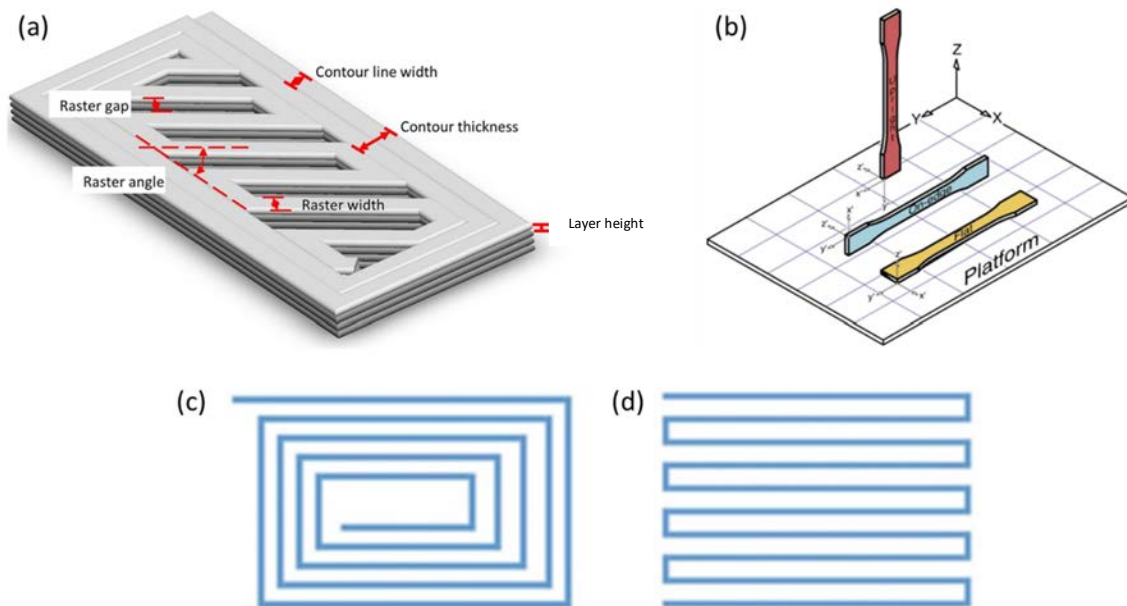


Figure 3 : Schematic representation of FFF process parameters (a), building orientation (b), concentric (c) and isotropic (d) infill pattern [1], [5].

Printing parameters:

- Heated plate (or bed) temperature is the temperature of the plate where printed beads are deposited.
- Nozzle temperature is the temperature of extrusion nozzle and, therefore, material extrusion temperature.
- Deposition/Printing speed refers to the speed of printer head during printing process.

2. Overview of current research on 3D printing of thermoplastic materials with Fused Filament Fabrication (FFF)

2.1. Presentation of FFF process for pure thermoplastics and current limitations

Among the many 3D printing technologies, the most common method for printing polymers is Fused Deposition Modelling (FDM), also known as Fused Filament Fabrication (FFF), a trademarked material extrusion process patented by *Stratasys* in 1992 [6], [7]. In FFF, the thermoplastic filament is melted through a heated nozzle and the viscous polymer is deposited layer-by-layer onto a build plate where layers are fused together and, once solidified, create the final part [8]. This process is almost fully automatized, making this technology suitable for mass production. One of the main interest of FFF technology is its ability to precisely control the microstructure of the printed part and to locally control its properties (porosity, density and orientation) [9]. However, in order to shift FFF from the prototype stage to end products, a number of improvements are required [10]. These improvements are: a greater variety of available polymeric materials, a process improvement for better dimensional reliability, improvement in surface finish and finally, enhanced mechanical properties. As described in several articles, the mechanical performance of 3D printed parts is lower than their conventionally manufactured counterparts [11]–[13]. Masood et al. [12] observed that PolyCarbonate (PC) printed with FFF process exhibits tensile strength in the range of 70-90 % compared to injection molded PC parts . Similarly, Ahn et al. [11] studied Acrylonitrile Butadiene Styrene (ABS) and found that the tensile strength of FFF printed samples was 26 % lower than that of injection moulded samples.

Different strategies were investigated in the literature to improve the mechanical performance of FFF printed parts. The first one is the modification of the formulation of printable filaments through the addition of reinforcing fibers. This point will be discussed further in the section 3 of this chapter. The second strategy is to optimize printing and slicing parameters.

In 3D printed parts by FFF, the lower mechanical properties are mainly due to insufficient bonding strength between printed beads within and between printed layers, leading to poor interlayer strength as well as poor interbead cohesion and the creation of porosity. The adhesion between the printed layers is governed by the interdiffusion of polymer chains between the printed layers [14]. The formation of a bond between the printed layers and the adjacent beads in printed parts is similar to the process of welding polymer interfaces where similar physical mechanisms (*i.e.* reptation) are involved [15]. The formation of the bond interface is schematized in Figure 4 where the cross-section of the bead is idealized as circles.

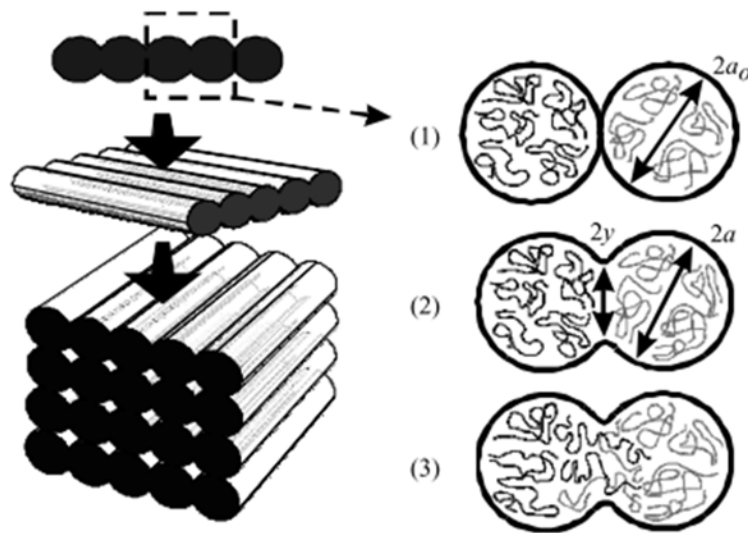


Figure 4 : Schematic illustration of bond formation between adjacent beads. When beads are in contact (1), a neck between these beads is created (2). This neck formation occurs because of the establishment of interfacial molecular contact by wetting. After establishment of connection between the beads, interdiffusion of polymer chains occurs across the interface (3) and after extensive interdiffusion of polymer chains, a randomization is reached between the beads [10].

This mechanism of bond formation is driven by the thermal energy applied to the extruded material, the contact time and pressure between the printed beads. Bellehumeur et al. [16] described this phenomenon and evaluated it qualitatively through thermal modeling and sintering experiments. They showed that printing parameters such as extrusion temperature and filament size play a role in the growth of the neck of the bonding zone (Figure 4). However, complete bonding does not take place because the FFF process cannot maintain a high temperature long enough for complete bonding. Consequently, as mentioned previously, printed parts exhibit lower out-of-plane and transverse cohesion as well as lower mechanical performance than their conventionally

manufactured counterparts. Hence, key parameters for improving the mechanical properties of 3D printed thermoplastic parts are the enhancement of the interbeads and interlayer properties.

2.2. Parametric studies on 3D printed parts for the improvement of mechanical properties

In the literature, numerous studies have focused on the influence of printing parameters on the mechanical properties of 3D printed thermoplastic parts, especially with regard to tensile tests.

Popescu et al. [17] divided the parameters of the FFF process into two categories :

- Printing parameters – extruder temperature, bed/plate temperature and environment temperature, flow rate, deposition speed.
- Slicing parameters – raster angle, layer height, raster width, interfilament distance, infill percentage, infill pattern.

All these parameters are linked to the quality of bead bonding described above, which determines the mechanical performance of the parts printed by FFF [18]. Figure 5 describes the main printing and material parameters that govern the quality of the parts as well as the sintering of the beads during 3D printing process. The viscosity and surface tension of the material dictate the flow characteristics in 3D printing, which is also driven by the temperature conditions.

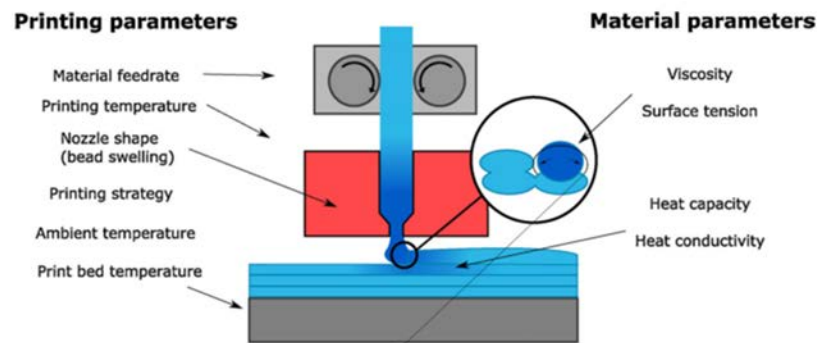


Figure 5 : Main printing and material parameters influencing part quality and bead sintering [19].

For example, Zhao et al. stated that rheological behavior plays a significant role in the 3D printing process as low viscosities at high shear rates are required for easy low energy extrusion, but high

zero-shear viscosities are also required for the extruded to retain its shape once being out of the nozzle and deposited [20].

The heat capacity and conductivity of the 3D printed polymer affect the temperature profile of the printed beads [19], [21]. The categories of slicing and printing parameters are discussed extensively in the following sections.

2.2.1. Influence of printing parameters

During the printing process, different heat exchanges occur, by convection with the environment and by conduction between adjacent beads, the printer bed and the nozzle that leads to various and complex thermal state [22]. The temperature and cooling conditions therefore influence the level of crystallinity of the polymer, the bonding of the beads and thus the mechanical properties [8]. For example, Aliheidari et al. [23] studied ABS and showed through Double Cantilever Beam tests, that higher extrusion temperature leads to a higher delamination resistance and therefore a better interlayer adhesion. Consequently, increasing the nozzle temperature enhances the mechanical performance of the part, but too high a nozzle temperature can lead to material degradation and deformation of the structure, leading to dimensional inaccuracy [24]. During cooling, shrinking and residual stresses develop in the printed layer because of the temperature gradient within the part, which may cause delamination or warping [25]. Sun et al. [10] studied the temperature profile of a printed ABS bead as a function of the number of printed layers (15 and 30 layers). On this purpose, the authors placed a thermocouple on the heated plate to record the temperature profile of the first layer. Thanks to this method, they studied the influence of nozzle temperature and environment temperature on the temperature profile. The results are shown in Figure 6.

The authors showed that the temperature of the first layer rises periodically with each additional layer printed and then decreases rapidly as the nozzle move away from the thermocouple. The study of the influence of the process parameters (Figure 6.b, c) shows a minimum temperature (lower limit) increase, which means that the first layer undergoes the thermal influence of the other printed layers. Moreover, the nozzle temperature seems to have less of an influence on the temperature profile than the environment profile. Indeed, the authors did not measure a significant effect of increasing nozzle temperature, whereas a 20 °C increase in environment temperature (50 °C to 70 °C) leads to an increase in the minimal temperature (average of the lowest temperature reached at each deposition pass) from 73 °C to 87 °C.

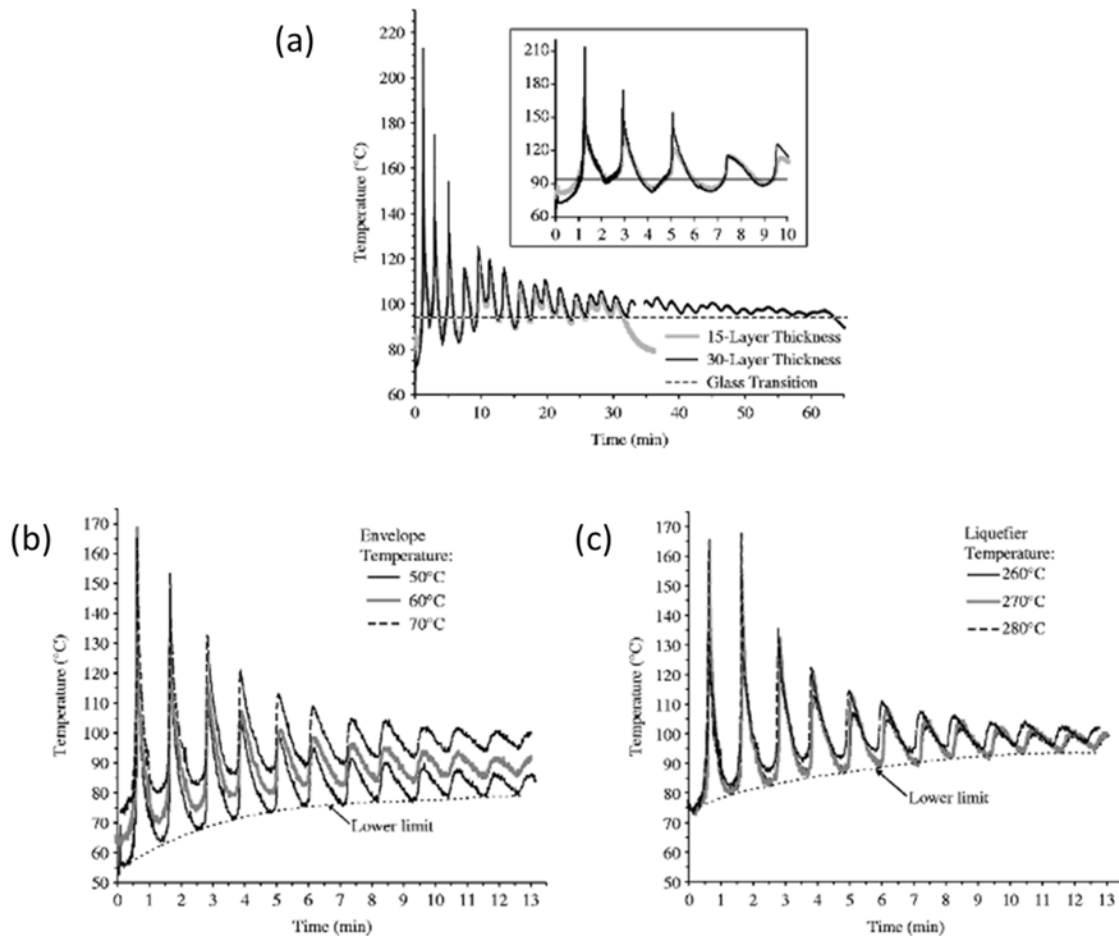


Figure 6 : Influence of the number of layers on the temperature profile of first layer (Temperature nozzle = 270 °C and environment temperature = 70 °C) (a). Influence of environment temperature on the temperature profile of first layer (Nozzle temperature = 270 °C) (b). Influence of nozzle temperature on the temperature profile of the first layer (Environment temperature = 70 °C) (c) [10].

Several articles aimed at modeling the temperature profile in the printed bead to better understand the influence of bead bonding and cooling on internal stresses considering various assumptions and analytical models [26]–[28]. Costa et al. [29] studied the heat transfer during cooling of ABS beads. They have taken into account all physical contacts between the bead and the 3D construction in order to estimate the quality of the bond between printed beads and the evolution over time of the temperature of the beads. They demonstrated that the lower the extrusion temperature, the lower the adhesion between beads. They also showed an influence of ambient temperature with more areas of poor-adhesion at ambient temperature.

The printing speed also plays a major role on the mechanical performance of 3D printed parts, on the printing time and therefore, on the production cost. A higher speed rate allows the reduction of printing time but causes a drop in tensile properties [30], [31]. Ning et al. [31] attributed this drop to a lower contact time at the nozzle temperature between adjacent beads for higher velocity rate. Consequently, the printed beads are exposed for a shorter period of time to the heated nozzle and interdiffusion of the polymer chain is not promoted; leading to a lower quality of inter-bead and interlayer bond and affecting the mechanical performance.

2.2.2. Influence of slicing parameters

The influence of raster orientation is a slicing parameter widely studied in the FFF research [32]–[34]. The raster angle is defined as the angle between the X-axis of the 3D printer and the deposited bead (Figure 3.a). Literature studies indicate that a raster angle of 0° ensures better tensile strength. For example, Lanzotti et al. [21] studied PLA and observed a decrease in mechanical performance when the raster angle increases, with a 20 % difference between 0° and 90° in regard of the ultimate tensile strength. El-Said et al. [35] assigned this difference to the anisotropy of the printed parts. During the processing, polymer chains tend to align themselves along the raster axis [36] which explains the strongest properties in that direction. Moreover, as the raster angle becomes higher, the interbead interfaces are loaded, which negatively affects the tensile properties. In their study, analysis of fracture path for different raster angles (0° , 45° and 90°) revealed that the inter-bead bonding plays a major role in the tensile test (Figure 7).

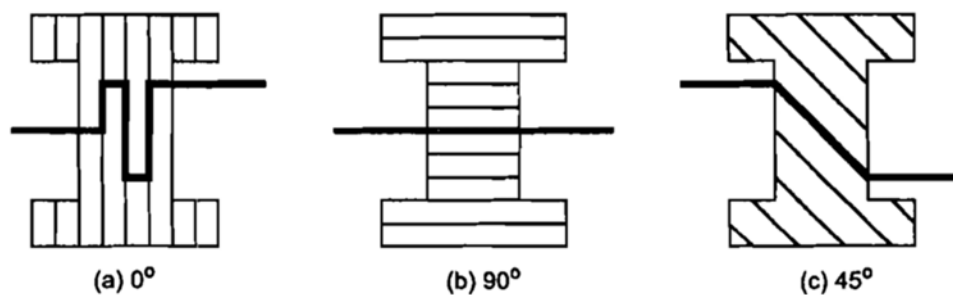


Figure 7 : Schematic representation of the rupture geometry on 3D printed samples varying raster angle. For a raster angle of 0° , the break occurs within the printed beads and at the interface between the beads. For raster angles of 45° and 90° , the specimen breaks at the interface between the beads. For 45° and 90° , the bonding between adjacent beads plays a more important role in the load transfer than for the 0° raster angle similarly as happens for fibers reinforced composites [35].

As mentioned above, the bonding between the beads is the weakest link in the printed part and leads to a decrease in mechanical properties as the raster angle increases.

In the literature, slicing parameters are considered to be the most influential process parameters on printing quality as they are directly related to the microstructure of the material. The most significant influencing slicing parameters are: layer height, infill percentage and air gap or interfilament distance [17]. These parameters are critical for the quality of the bonding strength, the porosity content and, consequently, for the mechanical performance of the 3D printed parts.

-Layer Height is widely studied in the literature and research teams observed that optimal tensile strength of polymer is reached with minimal layer height [37]–[39]. Sood et al. [40] studied ABS and attributed the highest tensile strength for the thinnest layers to a normal pressure driven molecular diffusion between the adjacent beads and layers (interdiffusion mechanism). Hence, during the 3D printing process, considering higher number of layers for a constant sample, the part undergoes more heating and cooling cycles that promote molecular diffusion between printed layers.

Zhang et al. [41] created a model to simulate the FFF deposition process and predicted residual stresses and distortions of ABS parts as a function of the process parameters (layer height, raster width and printing speed) and selected the layer height as the most influential parameter. The authors simulated the evolution of maximum first principal stress as a function of layer thickness, raster width and printing speed and observed a higher stress accumulation for a greater layer thickness, leading to distortion of the part, a degradation of the inter-bead bond strength and reduction of the mechanical properties.

- Infill and related interfilament distance are linked parameters. They have a direct influence on mechanical strength, dictating the contact area between adjacent beads in the X and Y directions (Figure 2) and therefore the bond strength. A lower infill percentage speeds up the 3D printing process, reduces the use of materials and therefore costs [13]. The infill percentage is controlled by the interfilament distance parameter which represents the distance between the printed beads (Figure 2). The higher the interfilament distance, the lower the infill density and, consequently, the porosity content increases and the number of connections between adjacent beads also decreases, resulting in lower mechanical performance [42]. In the literature, optimal mechanical performance is observed with a slightly negative interfilament distance (infill over 100 %) which physically means that the printed beads overlap, implying low porosity content [43]. Figure 8 shows the evolution of

cross-section surface of a 3D printed ABS part over infill density evolution, showing a qualitative decrease of porosity content when infill percentage increases.

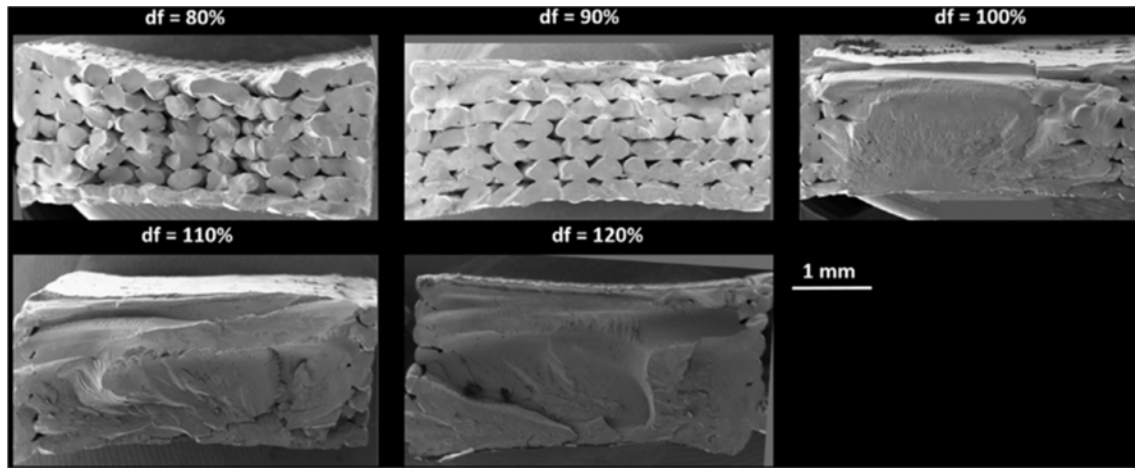


Figure 8 : Scanning Electron Microscopy images of cross-section of 3D printed ABS parts with several infill percentage [43].

Finally, the mechanical performance depends on the slicing and printing parameters which is often felt as negative points. However, the mechanical properties are adjustable through the control of the process parameters giving more degree of freedom to the designer.

It must be kept in mind that the mechanical performance of 3D printed parts remains lower than their conventionally manufactured counterparts. In order to overcome this major issue, several research works have focused on the 3D printing of composite materials through the addition of reinforcing fibers in the printable filament.

3. 3D printing of fiber reinforced composite materials

The addition of reinforcing fibers in printable filaments follows two strategies. The first one is the addition of discontinuous fibers to improve mechanical performance, reduce warping during printing and increase dimensional stability [14]. The second is the addition of continuous fibers used to greatly improve mechanical performance. In the following section, both strategies and the respective studies are presented and discussed.

3.1. 3D printing of discontinuous fiber-reinforced composites

To the best of our knowledge, the first literature research which aimed at reinforcing FFF printed parts with discontinuous fibers was conducted by Zhong et al. in 2001 [44]. In this research, the authors aimed to develop a printable filament made of ABS reinforced with short glass fibers using a twin-screw extruder. The authors observed an improvement of mechanical performance with the addition of glass fibers (+140 % between pure ABS feedstock and ABS reinforced with 11.4 % vol. of short-glass fibers) but also a strain reduction. Strain was improved thanks to addition of plasticizer and compatibilizer. Following this research, several teams have worked on the addition of fibrous reinforcement such as carbon nanotubes [45], [46], graphene [47], [48] or carbon/glass short fibers [31], [49], [50].

Actually, 3D printing of discontinuous fiber-reinforced polymer composites shows several advantages compared to neat thermoplastic 3D printed parts.

First, mechanical performances are improved by the addition of short fibers. Ning et al. [49] showed that the addition of 4.5 % vol. of short carbon fibers improved the tensile strength (+24 %) and the modulus (+27 %) compared to neat ABS. Love et al. [51] showed that the addition of 8 % vol. of short carbon fibers to ABS leads to an increase in tensile modulus (+630 %) and tensile strength (+144 %). Jiang et al. [52] investigated the addition of carbon fibers to three different matrices (ABS, polylactic acid (PLA) and polyethylene glycol (PETG)). The authors investigated three fibers fraction, i.e. 10.5 % vol.; 9.4 % vol. and 14.3 % vol. for ABS, PLA and PETG; respectively. The authors measured a strong increase in tensile strength (+211 % for ABS-based composites, +164 % for PLA and +314 % for PETG) and tensile strength (+33 % for ABS-based composites, +14 % for PLA and +48 % for PLA). Carneiro et al. [53] showed that addition of glass fibers to polypropylene (PP) leads to an increase of 30 % and 40 % for the modulus and the ultimate tensile strength, respectively. These results are displayed in Figure 9.

Second, the introduction of fibers leads to a lower coefficient of thermal expansion which reduces the thermal strain gradient during 3D printing and therefore limits warping during the process [51], [54]. Finally, short fibers made it possible to achieve greater geometric precision and subsequently improve the surface appearance of the printed structures [51]. Greater dimensional stability allows to develop new fields of application such the Big Area Additive Manufacturing (BAAM) [55], [56] where large scale structures are printed like a boat at the university of Maine [57].

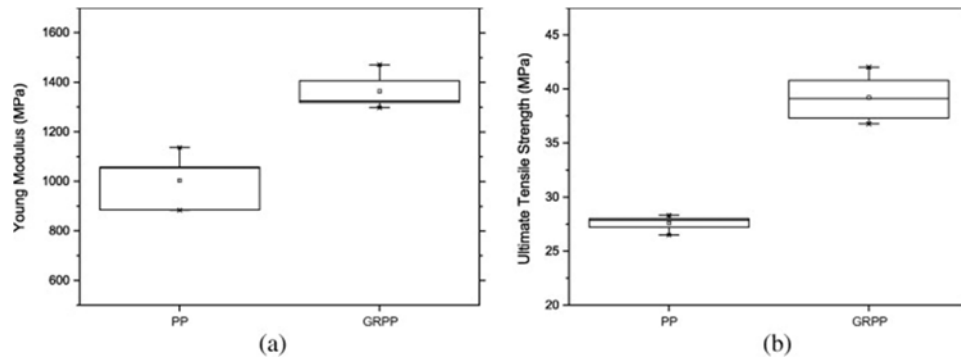


Figure 9 : Tensile modulus (a) and ultimate tensile strength (b) of samples 3D printed with pure polypropylene (PP) and polypropylene reinforced with 17.6 % vol. of glass fibers (GRPP) [53].

As with thermoplastics, the 3D printing of short-fiber reinforced composites is strongly dependent on the process parameters [31]. As discussed in the previous section, the most influential parameters are raster angle, layer height, interfilament distance. In 3D printing of short fiber composites, fiber type, content, orientation, aspect ratio (L/d), and fiber/matrix interactions also play a major role on mechanical performance.

Tekinalp et al. [50] used Bay and Tucker's method [58] to characterize the fiber orientation in the FFF process and compared it to compressed molded samples. The authors demonstrated that 90 % of discontinuous fibers in FFF are oriented along the printed path while samples elaborated by compression molding exhibit a more homogeneous fiber distribution. Mulholland et al. [59] studied the evolution of fibers orientation in relation to filament extrusion and FFF printing for PA6 matrix reinforced with 20 % vol. of short copper fibers (500 μm long and 30 μm width). They observed that after the extrusion process, the fibers are preferentially oriented in the direction of extrusion and that this orientation is maintained during the printing process with a slight decrease of fibers orientation from 80 % to 68 %. Garcia et al. [60] modeled the evolution of fibers orientation within the nozzle with Moldflow[®]. Material modeled is a Thermocomp RC004SXS made by SABIC Innovative Plastics US, LLC filled with 20 % vol. of discontinuous carbon fibers. A representative example of model representation is displayed in Figure 10. In this Figure, red color corresponds to a fibers orientation in the Z direction near 1 while blue areas represent a fibers orientation near 0. This model shows that fibers tend to align in the section reduction of nozzle head due to higher shear stress [54] and decrease of die swell acting perpendicular to shear flow.

As described in the literature, tensile properties are maximized when the samples are oriented in the direction of stress [61]–[63]. Thus, filament extrusion allows the short fibers to be oriented in the

direction of the filament. The fiber orientation is maintained during the 3D printing process, and then control of the fiber orientation in the printed structure is possible by controlling the raster angle.

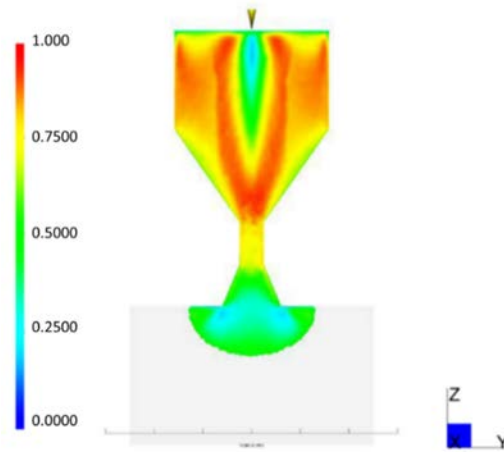


Figure 10 : Representation of short carbon fibers orientation tensor in Z direction within a printer nozzle [60].

Another parameter that dictates the mechanical performance is the influence of fiber length. Ning et al. [49] studied the influence of carbon fiber length on the tensile properties of ABS-based composites and observed higher tensile modulus and tensile strength for longer fiber length (150 μm instead of 100 μm) but observe no change in yield strength. The decrease in tensile modulus and tensile strength with a shorter fiber length is well-known for conventionally manufactured short-fiber composites and is explained by lower fiber efficiency [64], [65]. Moreover, a minimal fiber length, namely the critical L_c fiber length, is defined in the Kelly model and shown in Equation 1 where r_f is fiber radius, σ the composite tensile strength and τ_i the interfacial shear strength between matrix and fiber. When the length of the fibers is greater than L_c , the fibers act as a reinforcement with sufficient load transfer to the fibers, but when the of the fibers is less than L_c , the load transfer is not sufficient and matrix/fiber debonding occurs at the interface during the tensile test.

$$L_c = \frac{r_f \sigma}{\tau_i} \quad \text{Equation 1}$$

However, in 3D printing, the length of the fibers is limited by the extrusion process used to manufacture the printable filament, which causes long fibers to break. Moreover, the length of the fibers is limited by the viscosity of the filament: A longer fibers length leads to a higher filament viscosity, which makes the 3D printing process more difficult due to the clogged nozzles.

The volume content of fibers in the printable filament affects the mechanical performance of 3D printed structures; the higher the fiber content, the higher the mechanical properties. However, this increase becomes less significant for fibers content above 20 % wt. (15 % vol.) as displayed in Figure 11.

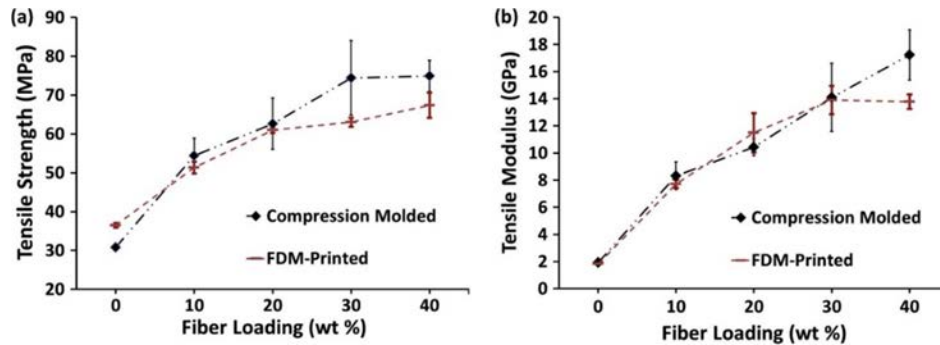


Figure 11 : Effect of fiber content and preparation process on (a) tensile strength and (b) tensile modulus of ABS/CF composites [50].

Ning et al. [49] observed the same results, but also noted the appearance of porosity with increasing fiber content, as shown in Figure 12.

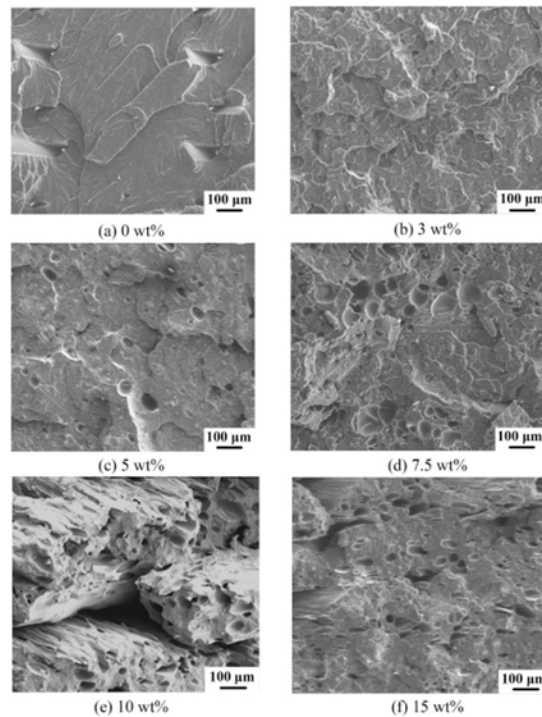


Figure 12 : Scanning Electron Microscopy observation of fracture surface of ABS/CF samples after tensile testing showing an increasing of porosity content for higher fiber content [49].

Consequently, there seems to be an upper-limit of fiber content for short fiber-reinforced composites, where the mechanical properties drop due to the appearance of un-impregnated areas, which affects the void content and induces a decrease in mechanical properties. Moreover, it is now well-stated that it is not possible to print filaments with a volume fiber content higher than 30 % vol. because of processability issues such as a nozzle clogging due to the excessive viscosity of the filaments and nozzle shear stress too low to extrude processed filament [5]. Figure 13 summarizes the tensile properties found in the literature for short fibers composites elaborated by FFF compared to pure thermoplastic printed parts and short fiber composites elaborated by conventional processes.

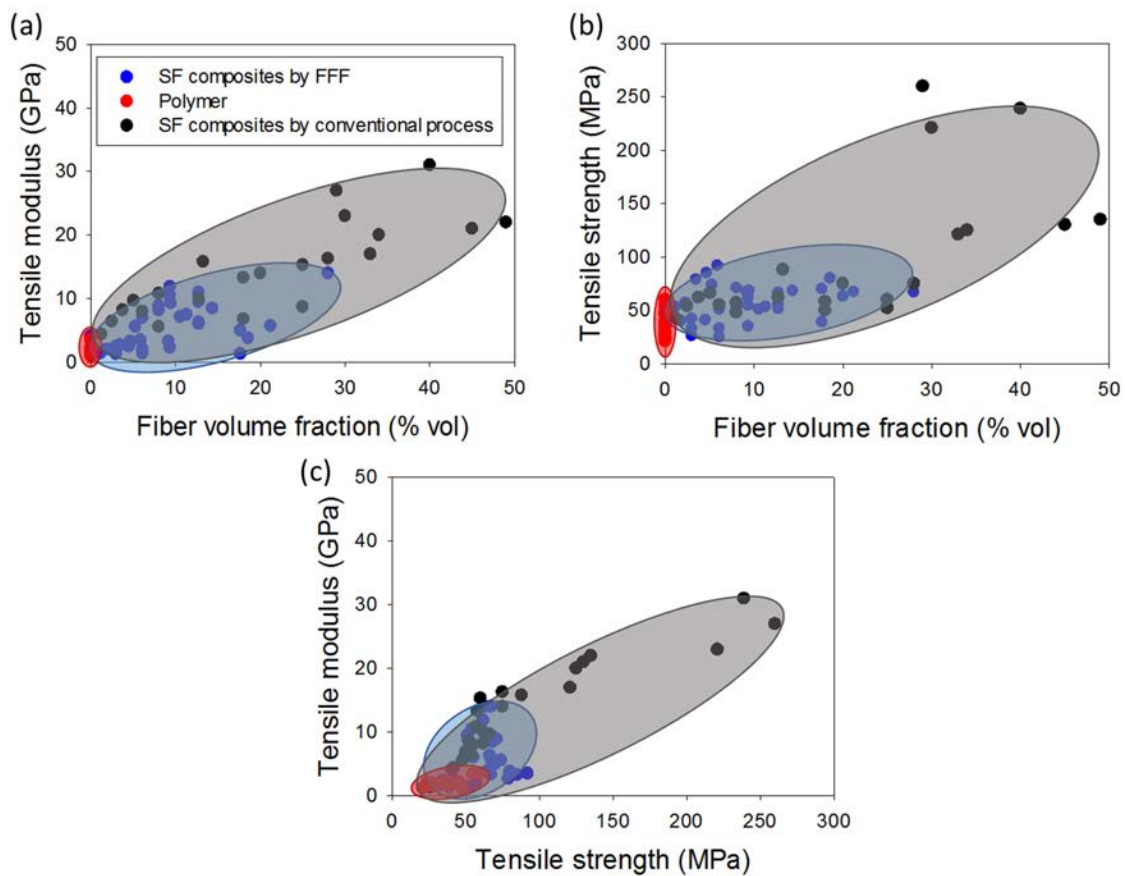


Figure 13 : Literature review on the tensile properties of short fiber based composites manufactured with 3D printing. Evolution of tensile modulus (a) and tensile strength (b) as a function of volume fiber content; tensile modulus as a function of tensile strength (c)

[46], [49]–[53], [56], [61], [63], [64], [66]–[76].

In conclusion, the addition of short fibers in printable filaments improves the mechanical performance of 3D printed structures compared to pure polymer 3D printed structures and

considerably reduces the warping of parts, opening up new field of applications for 3D printing. Moreover, for similar volume fiber fraction, the tensile strength of short-fibers 3D printed composites lays in the same range as that of conventionally manufactured short-fibers based composites. However, a higher fiber fraction (50 % vol.) is attainable thanks to conventional process that provides a wider range of tensile properties. However, mechanical performances remain too low to target structural applications because only a limited amount of short fibers can be incorporated into the printable filament.

3.2. 3D printing of continuous fiber reinforced composites

Today, the automation of the continuous composite manufacturing process is necessary for several industries (aeronautics, aerospace, automotive, marine engineering, energy...) in order to address productivity and reproducibility issues, but also to reduce costs [8], [77], [78]. Consequently, 3D printing of continuous fibers composites is a formidable research topic, with an increasing number of research articles and patents as shown in Figure 14. Figure 14 reports the published patents based on 3D printing technology (a) and continuous fibers-reinforced 3D printed composites (b) since their invention based on the Google Patents search engine [1].

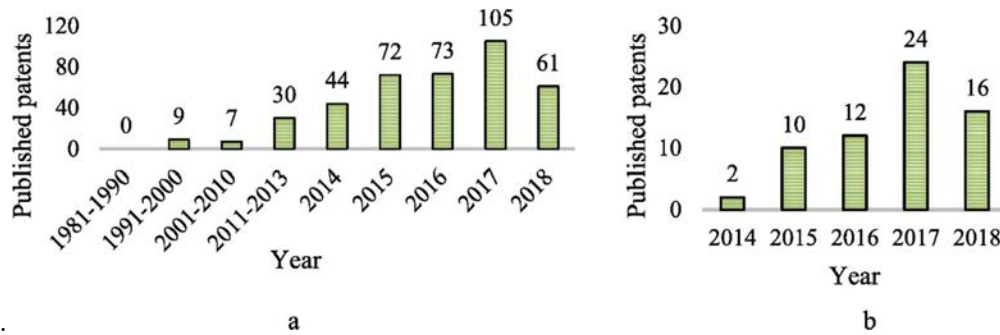


Figure 14 : An overview of publish patents evolution regarding 3D printing (a) and 3D printing of continuous fibers composites (b) since their invention [1].

Actually, the development of high performance 3D printed continuous fibers composites follows other additive manufacturing process such as filament winding, Automated Tape Laying (ATL) or Automated Fibers Placement (AFP). Among these processes, AFP shows various similarities with 3D printing of continuous fibers composites. In AFP, a pre-impregnated tape made of unidirectional fibers tows is placed on a mold by means of a robotic arm with a short manufacturing time and excellent reproducibility. Contrary to ATL process (75-300 mm), AFP allows to deposit on curved structures due to thinner tapes (3.2-12.7 mm) and the ability of this technology to individually

control and cut fiber tapes as a function of required trajectory, thus it facilitates the manufacturing of complex parts (Figure 15).

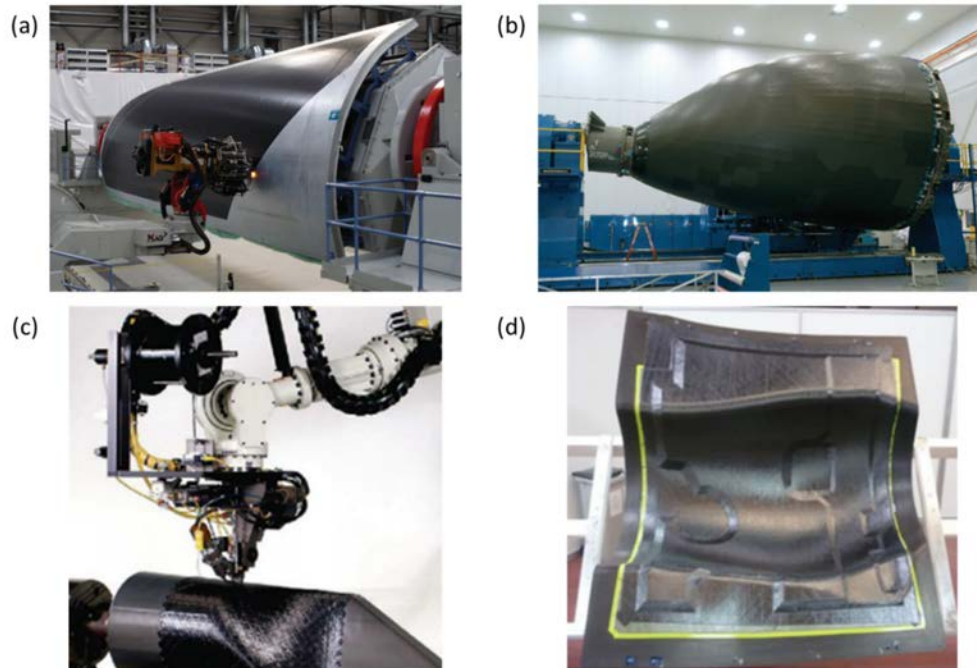


Figure 15 : Example of carbon fibers-based composites structures elaborated by AFP for aerospace industry. (a) Fuselage panel from A350 XWB (Premium AEROTECC GmbH); (b) Boeing 787 nose; (c) helicopter tail boom processes by Automated Dynamics' XT fibers placement robot; (d) complex geometry part of Airbus A318 [79], [80].

However, AFP has several limitations which are known and controlled but unavoidable. The first is a limited radius of curvature which causes defects such fiber misalignment, local buckling (steering effect) and pull-up. Blom et al. [81] studied carbon fibers reinforced epoxy composites and found that the minimum radius of curvature to avoid fibers buckling is 635 mm for tapes 3.175 mm wide. The second typical defect with AFP is the presence of a gap or overlap of tapes due to a variation in the draping angle. That leads to the appearance of porosities or fibers-rich areas creating stress concentrations in the structure and negatively affecting mechanical performance [82], [83].

However, fiber tapes cut and optimization of deposition trajectories allows to minimize gaps and overlaps. The cuts occur perpendicularly to the fiber tapes, resulting in the appearance of gap and overlap with triangular shape depending on chosen trajectory of the fiber. A coverage of 0 % indicates that a tow is cut off as soon as one edge of the tow reached the boundary of the adjacent course, leading to triangular areas without tapes. When a 100 % coverage parameter is used, which

is the case where to are cut as soon as one tow have passed the boundary curve, small overlaps are created.

Finally, a minimum tape length (between 63 and 152 mm) is required by the process which prevents the manufacturing of small size parts. 3D printing of continuous fiber composites overcomes some of these limitations and prints smaller angles and smaller parts due to the lower stiffness of the filaments compared to AFP tapes, resulting in a smaller printable radius curvature at the edge of the part. As a matter of fact, Matsuzaki et al. [84] evidenced a minimum radius of 5 mm with continuous carbon fibers/PA composites.

3D printing has however a low productivity due to the moderate printing speed (100 mm/min maximum) compared to AFP (60 m/min maximum). Hence, the AFP process is suitable for large-scale manufacturing while continuous 3D printing is more suitable for small and intricate parts which is complementary. Moreover, 3D printing is less restrictive and more affordable than AFP technology. Indeed, while MarkTwo® from Markforged® costs 20 000 €, most AFP engines costs about 1 M€. Last point but not the least is also the cost of materials. Today it is significantly higher for 3D printing of continuous fiber composites than for AFP tapes. For example, Markforged® company sells polyamide coated continuous carbon fibers at 1970 €/kg, glass fibers at 870 €/kg and Kevlar fibers at 1470 €/kg while AFP material costs between 50 € and 300 €/kg for carbon fibers based tapes depending on the nature of the polymer.

There are different strategies for 3D printing composite materials with continuous fibers, such as modifying the print nozzle to ensure that the initially dry fibers are impregnated by the matrix inside the printing head (during printing) [85]–[89]. With the latter technology, two feeders are available, one for the thermoplastic matrix and one for the dry fibers. A schematic representation of this printing process is shown in Figure 17.a. When the nozzle is heated, the thermoplastic is melted and impregnates the dry fibers before being deposited on the build plate. This technology makes it possible to create parts with a stiffness gradient by varying the flow rate of the thermoplastic matrix and thus the fiber volume content [90]. However, this process leads to moderate impregnation of the fibers by the thermoplastic matrix, resulting in high porosity content and layers delamination [85]. The low impregnation is due to the low shear pressure in the print nozzle. Moreover, a short impregnation time limits the impregnation of the fibers.

The second strategy is to develop “ready-to-print” pre-impregnated continuous fiber-reinforced filaments [91]–[95]. In the literature, ready-to-print filaments are commonly manufactured by co-

extrusion process. Hu et al. [93] manufactured continuous filament composed of a carbon bundle (1000 carbon fibers) coated with PLA matrix (Figure 17.c). The author's process is composed of a single screw extruder which melts the PLA and a heating pipe where a continuous carbon fiber bundle is heated to keep the fibers dry and warm to promote impregnation of the fibers by the PLA matrix. The molten polymer is squeezed into the carbon fiber bundle thanks to a nozzle head and continuous carbon fibers based filament is cooled in water to be solidified and dried by a blower. Another widely studied process is based on pultrusion of commingled yarns [92], [96]. In this process, the commingled filament is heated and consolidated in a heating die and a traction system drives the filament to a spool. Thanks to this process, manufacturers claim to have produced filaments with a high fiber content (50 % vol.).

The literature description of Markforged® continuous fibers based filament shows that there are limitations to the production of continuous fibers based filaments production: a heterogeneous fiber distribution leading to fiber and matrix-rich areas as well as a heterogeneous filament shape which might induces defects in printed composites (Figure 16).

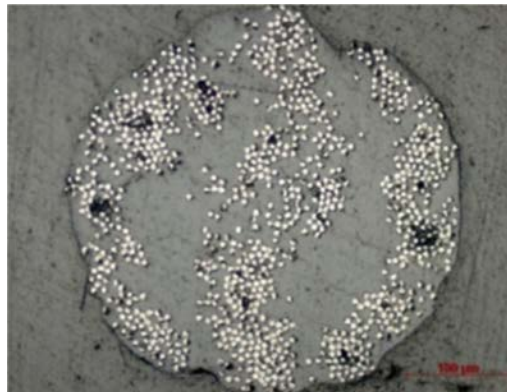


Figure 16 : Cross-section of continuous carbon fibers filament from Markforged® [19].

However, fiber impregnation is optimized during the extrusion or pultrusion processing of the filament and the filaments before printing exhibit a low porosity content of about 2 %. This strategy was adopted by Markforged®, which commercialized in 2014 the first industrial printer capable of printing continuous fibers reinforced composites. A schematic representation of this printing process is shown in Figure 17.b and a picture of MarkOne® 3D printer is shown in Figure 17.d. This 3D printer is composed of two nozzles, one for the pure thermoplastic and the other for the continuous fibers (carbon, glass or Kevlar) coated with a thermoplastic matrix.

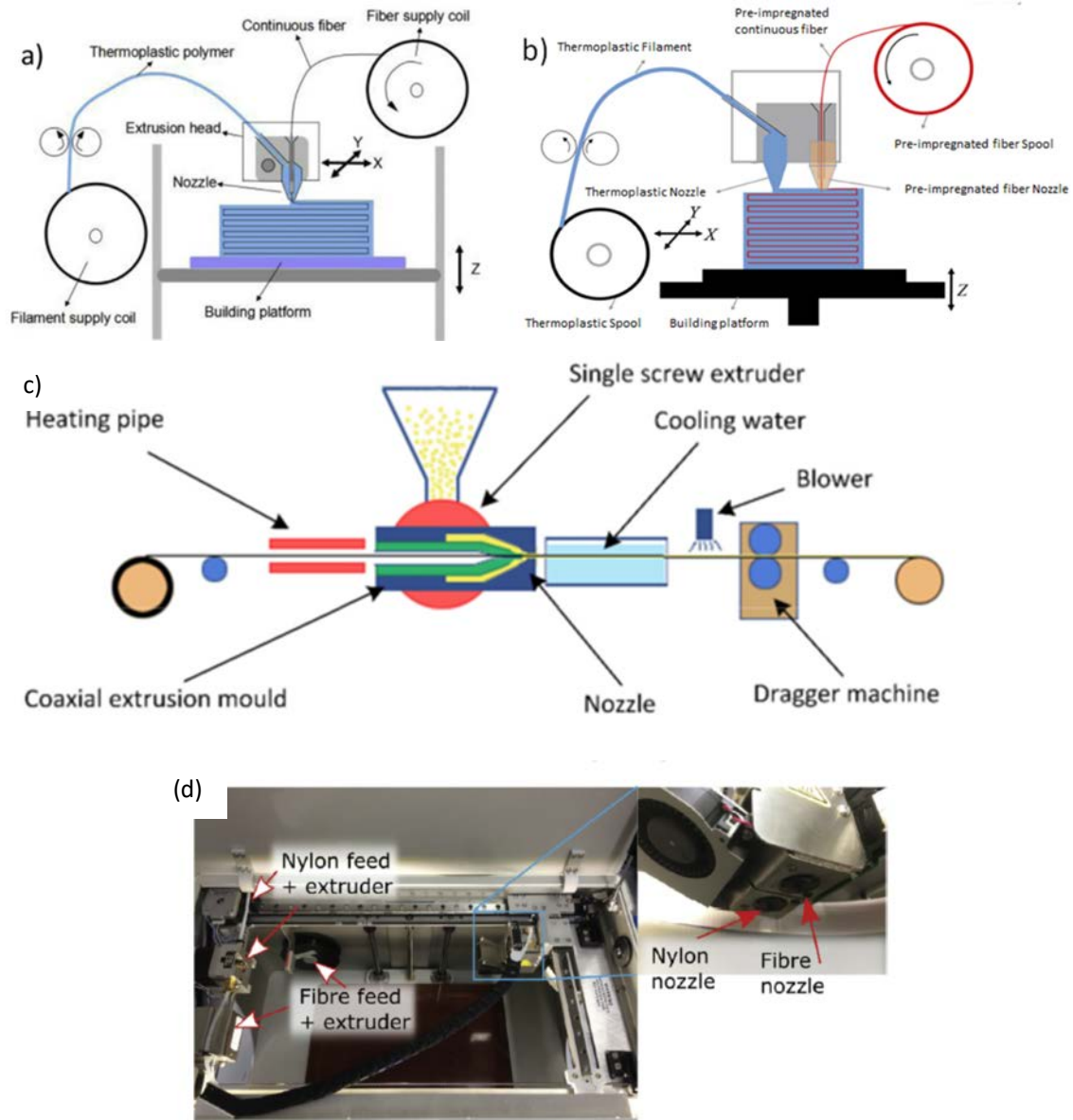


Figure 17 : Schematic representation of the FFF in-nozzle process (a) [95] and dual-nozzle printing with ready-to-print continuous fibers reinforced filament (b). Manufacturing process of ready-to-print filament based on continuous carbon fibers reinforced PLA (c). Overview of the MarkOne® printed from Markforged® with the dual nozzle system to print Nylon (PA6) filament and fibers-reinforced filament (d) [19], [93], [97].

An increasing number of research teams have worked on the mechanical characterization of 3D printed parts with Markforged® (MarkOne® or MarkTwo®) [19], [89], [90], [98]–[104] and highlighted several limitations : Impossibility to adjust the fiber content , restriction of processing parameters that limits process improvement, high void content after printing, limited control of fibers trajectory on the web interface Eiger.io which prevents control of material architecture, low material

availability (limited to Markforged® filaments composites of pure polyamide, short carbon fiber reinforced polyamide and continuous carbon, glass and Kevlar fibers reinforced polyamide filaments) and, finally, prohibitively high material cost [90]. To overcome the drawbacks of Markforged® devices, one trend is to develop one's own 3D printers based on the printing strategies shown in Figure 17 [85], [86], [88], [91], [105]. Unlike Markforged® printers, these printers are open and can print a wide range of thermoplastic materials with customized fiber content. Illustration of customized 3D printers able to print continuous fiber composites are shown in Figure 18.

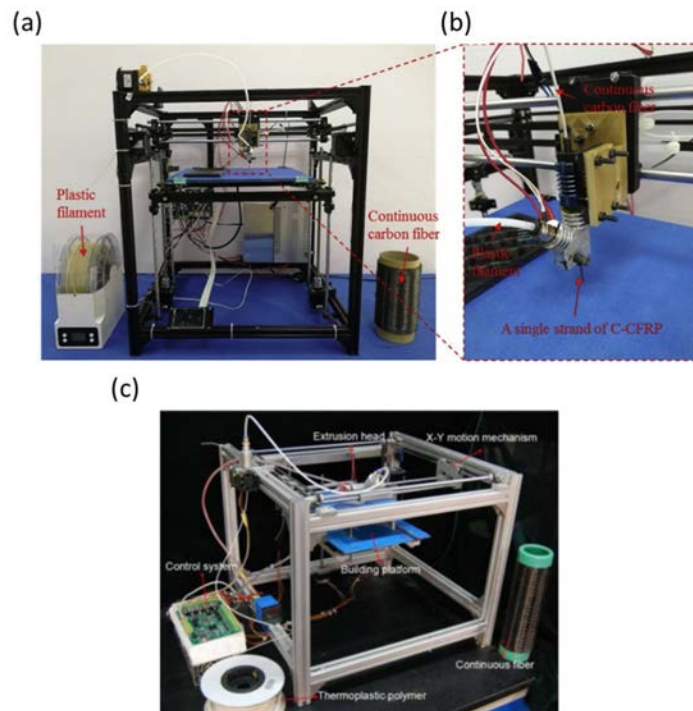


Figure 18 : Image of experimental set-up for FFF fabrication continuous carbon fibers reinforced parts (C-CFRP) (a,c) with a focus on the co-axial extrusion head structure (b) [88], [105].

The next section presents an overview of the mechanical characterization of 3D printed continuous fibers reinforced composites, showing their potential for structural applications.

3.2.1. Overview of the mechanical characterization of 3D printed continuous fiber reinforced composites

Most of the studies in the literature focused on the evaluation of the tensile properties of 3D printed composites. A wide range of mechanical performance is noticed in the literature due to the use of

different printers, different printing or slicing parameters (infill, fibers orientation, layer stacking) as well as different printed materials. A literature review of mechanical properties of continuous fibers based 3D printed composites is displayed in Figure 19.

As observed in Figure 19 the tensile modulus increases linearly (from 15 GPa to 80 GPa for carbon fiber based 3D printed composites and from 5 GPa to 25 GPa for glass fiber based composites) as well as tensile strength (from 150 MPa to 800 MPa for carbon fiber based 3D printed composites and from 200 MPa to 500 MPa for glass fiber based composites) with increasing fiber content (from 5 % vol. to 50 % vol.), showing the interest of continuous fiber printed structures for structural applications.

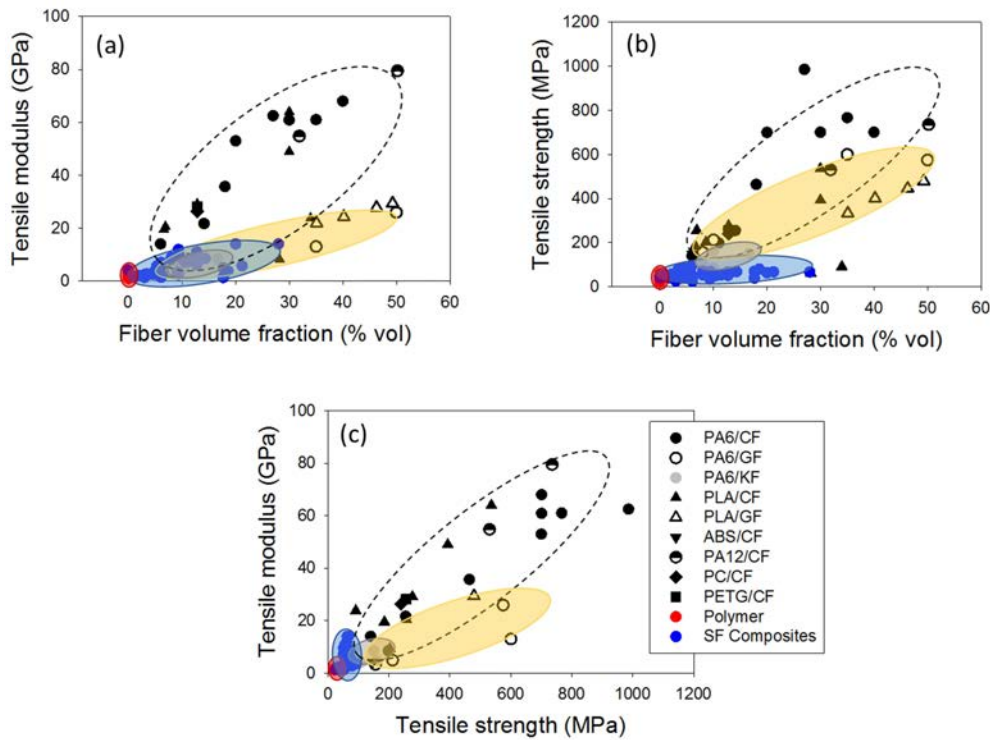


Figure 19 : Literature review on the tensile properties of continuous synthetic fibers based composites manufactured with 3D printing. Evolution of tensile modulus (a) and tensile strength (b) as a function of volume fibers content; tensile modulus as a function of tensile strength (c) for various polymer matrix (polyamide 6 (PA6), polylactic acid (PLA), acrylonitrile butadiene styrene (ABS), polyamide 12 (PA12), polycarbonate (PC) and polyethylene glycol (PETG)) and various fibers nature (carbon fibers (CF)(black ellipse), glass fibers (GF) (yellow ellipse) and Kevlar® fibers (KF)(grey ellipse). Comparison with pure 3D printer polymer (red ellipse) and short fiber (SF) 3D printed composites (blue ellipse)

[19], [45], [46], [49]–[53], [56], [63], [66]–[71], [85], [86], [88]–[91], [95], [98]–[100], [102], [104]–[112].

However, the results are widely dispersed due to the different process parameters and printers used. While the polymer matrix seems to influence tensile modulus and strength only slightly, a strong difference is observed with the variable nature of the fibers. Hence, carbon fiber reinforced composites exhibit higher tensile modulus and strength than glass and Kevlar fibers due to inherent properties of carbon fibers [90], [100]. Compared to short-fiber composites elaborated by 3D printing, continuous-fibers based composites show higher tensile strength and modulus (Figure 19). For example, Yamawaki et al. [91] worked on PA6 reinforced with continuous carbon fibers and obtained samples with an ultimate tensile stress of 700 MPa at a volume fibers content of 20 % and a tensile modulus of 53 GPa. In this way, these authors obtained parts with an ultimate tensile strength 8.6 times higher using a lower fibers content than printed short fiber-reinforced composites. Moreover, while mechanical performance improvement of short fiber reinforced composites is limited by the lower volume fiber range (between 0 and 30 % vol.) possible with these short fibers; higher fiber fractions are reached with continuous fibers based composites (until 50 % vol.).

However, 3D printed continuous fiber composites have lower mechanical performances compared to their conventionally manufactured counterparts [88], [107], [113], [114]. He et al. [107] compared the mechanical performances of 3D printed continuous carbon fiber PA6 composite materials with continuous fiber reinforced composites produced by compression molding process with a volume fibers content of 35 % vol. They also studied the microstructure of the composite through micro computed tomography (μ -CT) analysis to quantify internal porosity and void distribution. The authors noticed a void content of approximately 12 % and failure mechanism associated with poor fibers-matrix interface combined with porosity between adjacent beads. μ -CT analysis combined with mechanical characterization showed that void content principally affects transverse tensile strength, flexural strength and interlaminar adhesion. Yang et al. [88] compared the mechanical performance of 3D printed ABS continuous fibers composites with that of the same injection-molded composite and observed a 33 % higher tensile strength for conventionally manufactured composites compared to 3D-printed ones. The authors attributed these results to poor impregnation of the matrix in the fibers with significant fibers pull-out. However, the tensile performance of 3D printed composite materials is of the same order or better than the properties of lower density aluminum, suggesting a potential application for structural parts.

Thus, the moderate mechanical performances of 3D-printed continuous fiber composites is induced by the microstructure of the printed parts, namely porosity between the printed beads and printed

layers [111] (Figure 20). Those porosities act as stress-concentrators and play a role in the fracture mechanism by promoting early failure and debonding between adjacent beads and layers [90]. For the in-nozzle-impregnation process, studies have reported fiber pull-out within layers indicating a poor fiber-matrix interface due to a poor fiber impregnation [86].

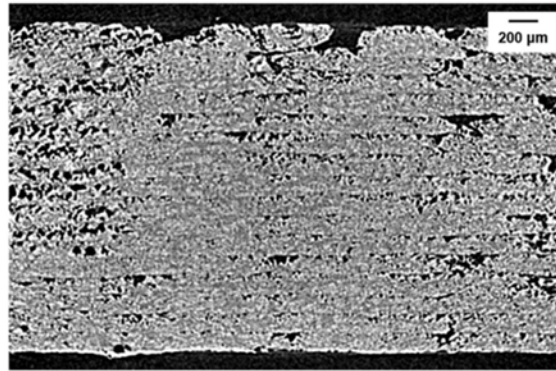


Figure 20 : Typical morphology of carbon fibers/PA6 3D printed composites by micro-computed tomography showing porosity content in 3D printed composites [111].

The orientation of the reinforcing fibers and printing path play a crucial role in the mechanical performance of 3D printed composites. The most studied printing orientations are 0° , 90° and $\pm 45^\circ$ with the longitudinal axis of the sample. One has to keep in mind that fibers and printed beads have similar orientation. However, beyond the effect of fiber orientation that leads to various composite damage, the orientation of printing path adds another scale of damage. Thus, when the printing path is different from the longitudinal axis, the inter-bead interface starts to be loaded and the mechanical properties evolve drastically. The hierarchical interface can be considered (Fiber/matrix and bead/bead) in the same way as pure thermoplastic printed composites (Figure 7).

Justo et al. [100] evidenced the high anisotropic properties of printed composite structures with a transverse strength 58 times lower than the longitudinal strength and a tensile modulus 23 times lower compared to longitudinal modulus for continuous glass fibers reinforced polyamide composites. The transverse modulus was 1.13 GPa while transverse strength of 9.84 MPa. The continuous carbon fibers/polyamide composites had a transverse strength 35 times lower than the longitudinal and a transverse modulus 15 times lower [102]. The transverse modulus was 3.97 GPa and a transverse strength of 19 MPa.

Transverse properties and especially strength may limit their use for structural applications. However, a high anisotropy of the parts might be used as an advantage in the design of the parts

because it allows to control the properties of the local structures. Basically, the transverse properties of composites are influenced by the transverse properties of the fibers, the fibers/matrix interface properties, the properties of the matrix and the heterogeneities and defects of the composites. In 3D printed composites the interbeads interface produces an additional effect. He et al. [107] observed the transverse fracture surface of carbon fiber reinforced PA6 composites and noticed fiber/matrix debonding and interbead interfacial fracture (Figure 21). The presence of porosity at the interface between the printed beads, resulting in a small contact area between adjacent beads to transfer the stress load and act as a defect that facilitates crack propagation.

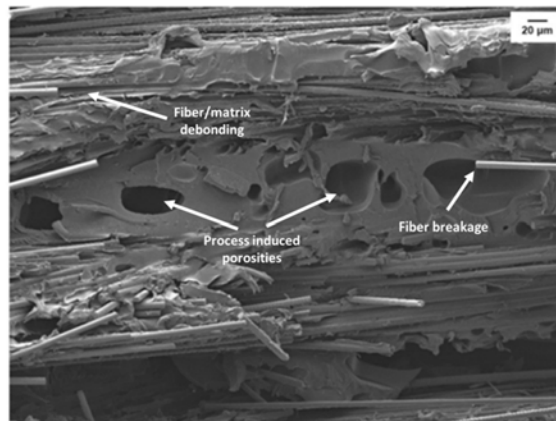


Figure 21 : Typical fracture surface of transverse tensile specimen made of continuous carbon fibers/PA6 composites oriented at 90° [107].

Similar observations were made for a printing orientation within $\pm 45^\circ$ of the longitudinal axis. With this fiber configuration, shear stress is generated in the composite sample. In the same manner as in the transverse tensile tests, the in-plane shear tests are highly dependent on the interface between the beads. However, contrarily to the transverse tensile tests, the continuous fibers are slightly loaded in shear, thus shear strength is slightly higher (between 30 and 70 MPa) than transverse tensile strength (between 9 and 20 MPa). Blok et al. [19] observed a shear strength of about 31.2 MPa and a shear modulus of 1.7 GPa for continuous carbon fibers printed composites while Justo et al. [100] measured a shear strength of 67.7 MPa for and shear modulus of 0.88 GPa for continuous glass fibers reinforced composites.

Consequently, composites based on continuous fiber have a high mechanical anisotropy with longitudinal properties between 20 and 60 times greater than transverse properties. This specificity has to be considered in the design of structural parts but also allows the design of structures with variable stiffness thanks to the control of the anisotropy by the FFF process.

In addition to the tensile properties, the flexural properties of 3D printed composites has been extensively investigated in the literature. A literature review of the flexural properties of continuous fibers 3D printed composites is shown in Figure 22.

The nature of the polymer seems to have a slight influence on the flexural properties as well as fiber nature; indeed, 3D printed composites reinforced with continuous glass fibers lay in the same range as those reinforced with continuous carbon fibers. However, only scarce data are available for these materials and further investigations should be done in the literature.

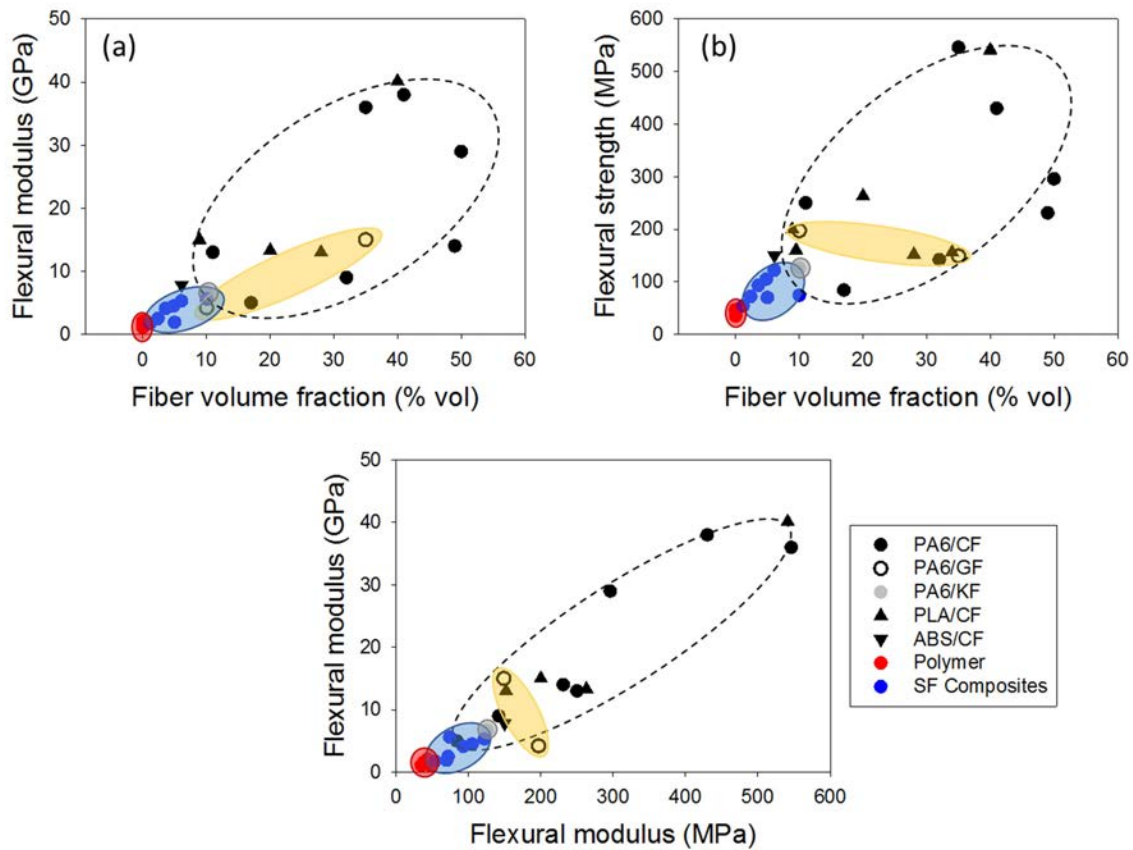


Figure 22 : Literature review on the flexural properties of continuous synthetic fibers based composites manufactured with 3D printing. Evolution of flexural modulus (a) and flexural strength (b) as a function of volume fibers content; flexural modulus as a function of flexural strength (c) for various polymer matrix (polyamide 6 (PA6), polylactic acid (PLA), acrylonitrile butadiene styrene (ABS) and various fibers nature (carbon fibers (CF)(black ellipse), glass fibers (GF)(yellow ellipse) and Kevlar® fibers (KF)(grey ellipse)). Comparison

with pure 3D printer polymer (red ellipse) and short fibers (SF) 3D printed composites (blue ellipse) [31], [66], [69], [86], [88], [90], [93], [99], [106], [107], [109], [115]–[121].

The addition of continuous fibers obviously improves the flexural properties compared to neat 3D printed polymers [88] and compared to short fiber reinforced composites printed with the FFF process. Heidari-Rarani et al. [109] measured a flexural strength of 152 MPa and a flexural modulus of 13 GPa for continuous carbon fiber reinforced PLA composites. Goh et al. [90] studied PA6/carbon fiber composites as well as PA6/glass fiber composites printed with Markforged® and measured a flexural modulus of 38 GPa and 15 GPa for carbon and glass fibers, respectively.

As for the tensile characterization, high fiber fractions are reached (around 50 % vol.) for continuous fibers based composites compared to short fiber 3D printed composites (10 % vol. in the literature) with a linear increase as the fiber content by volume raises. However, the flexural characterization of short fiber 3D printed composites is only limited to few articles and review of tensile test properties of short fibers based 3D printed composites showed that the fiber volume fraction in short fiber composites manufactured by FFF is limited to 30 % vol. Yang et al. compared the flexural properties of continuous carbon fibers/ABS composites elaborated by 3D printing and injection moulding and measured a similar flexural strength for both materials with similar fibers content (127 MPa for 3D printed part and 140 MPa for injection molded part) [88]. Hence, 3D printed composites exhibit similar flexural properties than composites elaborated with conventional manufacturing process.

Goh et al. [90] observed crack propagation during 3 points bending tests and noticed that the crack is initiated at the top of the studied sample where carbon fibers undergo high compressive stresses. The failures start in this area because of the low compressive strength of carbon fibers [122]. Finally, the composite breakage occurs from the bottom layer where the fibers undergo tensile stress and propagate in the remained intact layers. This breakage mechanism is illustrated in Figure 23.

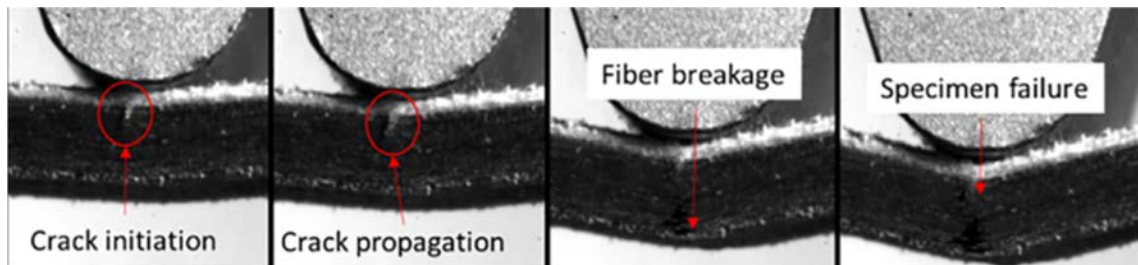


Figure 23 : Image sequence of flexural test captured using high speed camera showing the evolution of crack propagation and the resulting failure of the part [90].

Araya-Calvo et al. [115] evidenced that the flexural properties of 3D printed composites are strongly dependent of fiber volume fraction, the printing orientation and the pattern of printing (concentric or isotropic, Figure 2). Higher flexural strength and modulus are reached for increasing fiber content as shown on PA6/carbon fibers with a flexural modulus and strength of 14.3 GPa and 231.1 MPa, respectively for a volume fraction of 48.9 % vol. while continuous carbon fiber fraction of 17 % vol. lead to a flexural modulus and strength of 5 GPa and 84 MPa, respectively. Higher flexural strength is observed for samples printed with a concentric shape than for an isotropic shape [99].

Li et al. [106] showed that the fiber-matrix interface plays a critical role in the flexural strength of 3D printed composites. For this purpose, the authors chemically modified the carbon fibers and observed a 186 % increase of flexural strength between neat carbon fibers and modified carbon fibers based PLA composites.

Due to the lack of pressure applied during the printing process, the interlayer properties of 3D printed composites are considered to be the main limitation of 3D printed structures. The interlaminar properties, i.e. InterLaminar Shear Strength (ILSS) of the parts made by FFF are often characterized by short-beam tests because they require little material and are easy to perform. For instance, Liu et al. [95] have characterized continuous carbon fibers reinforced PA6 composites and measured a low ILSS, about 20 MPa, compared to epoxy-based composites used conventionally in industry (ILSS \approx 100 MPa). The use of a sizing agent on carbon fibers led to strengthening of the interlayer properties by promoting the interlaminar shear strength about 42.2 %. Caminero et al. [123] investigated the influence of synthetic fibers (carbon, glass and Kevlar[®]) and printing parameters (layer height and volume fiber fraction) on the ILSS of 3D printed PA6 reinforced composites. Carbon fiber reinforced composites showed better interlaminar strength (22 MPa) compared to Kevlar[®] (14 MPa) and glass fibers (14 MPa) because of the weak impregnation of Kevlar[®] and glass fibers by the PA6 matrix.

Nevertheless, several studies have shown the limitations of this test, especially for thermoplastic-based composites [124] where, in the compression zone, fiber failure and indentation may occur prior to delamination, thus invalidating the results. In addition, the heterogeneous loading promotes strain concentrations [125]. It has to be noted that this test also failed to properly describe the effect of singularities induced by the AFP process on the out-of-plane properties of carbon/epoxy composites [80]. To overcome this drawback, Iragi et al. [101] measured the interlaminar bond strength of continuous carbon fibers/PA6 3D printed composites and the critical energy strain rate

through Double Cantilever Beam (mode I) and end notched flexure test (mode II). The authors measured a fracture toughness of 2 kJ/m² and 1.59 kJ/m² for mode I and mode II characterization, respectively, which is significantly lower than for continuous carbon fiber polyamide based composites elaborated by hot compression molding [114], [126]. Poor mechanical properties are attributed to manufacturing defects such as voids between printer layers, inhomogeneous fiber distribution and insufficient fiber impregnation.

3.2.2. Current limitations in 3D printing of continuous fiber composites

First of all, the high porosity content due to the lack of compaction acts as structural defect and is responsible for the weaker mechanical properties of 3D printed structures compared to their conventionally manufactured counterparts. Moreover, continuous fibers enable higher mechanical performances to be achieved than discontinuous fibers, but processing becomes more difficult and induces manufacturing defects, especially at the edge of the part [84], [127]. Figure 24 shows the processability and performance evolution with continuous and discontinuous fibers.

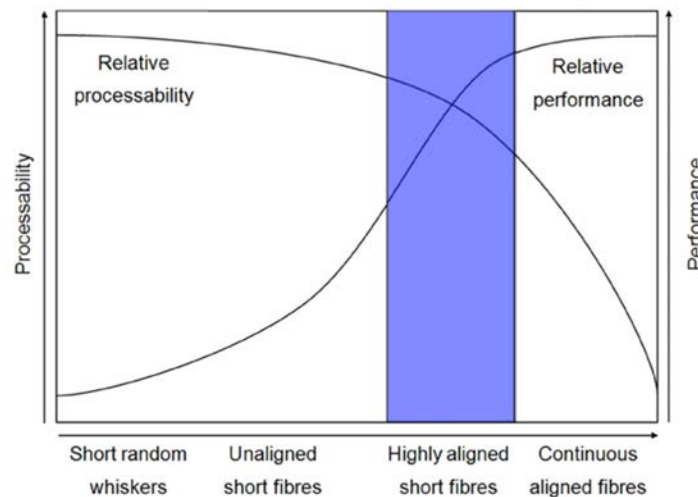


Figure 24 : Impact of fibers architecture on processability and performance [128].

The most widespread 3D printer, i.e. MarkTwo® from Markforged®, is today closed and limited to PA6 based composites, which today prevents new investigations into the formulation of composites. Moreover, these materials have prohibitive costs and unknown property change with aging under outdoor conditions.

In Markforged® 3D printed structures, a relationship exists between structure geometry (i.e. thickness) and the fiber volume content. For example, van der Klift et al. aimed to design parts with 35.7 % vol. of fiber content with 6 and 4 layers of pure PA6 and continuous carbon fibers, respectively [98]. However, in Markforged® printers, the pure PA6 layers and walls are always adjusted to ensure good part cohesion and surface appearance, so that dimensional structure lead to an increase in the volume of continuous fiber while the volume of pure PA6 is almost constant. Consequently, thicker samples lead to samples with higher fiber content. This may be taken into account in the design process. Indeed, if constant stiffness is considered, that should be a drawback as thinner areas have a lower fiber content and may thus act as weak points in the structure. However, if taken into account in the design, it would be possible to tune and tailor fiber content very accurately by following complex specifications [98].

Finally, some improvements are required with regard to the tensile evaluation of continuous fiber based composites. For example, no literature researches was conducted for mechanical properties in the Z-direction. Environmental conditions are also rarely discussed in the literature despite the known sensitivity of most of the polymers used, i.e. PA6, to moisture uptake. Moreover, because this technology is still in its infancy, no standard deals with mechanical characterization of continuous fibers based composites. However, as described by Kabir et al. [1], few standard are in development by combined efforts of ASTM and ISO: ISO/ASTM DIS 52903 “Standard specification for material extrusion-based AM of plastic materials” and ISO/ASTM NP 52905 “Non-destructive testing of additive manufactured products”. In the literature, the mechanical evaluation of 3D printed composites follows same standard as conventionally manufactured composites. However, specificity of 3D printing such as printing path should be taken into account in the development of new standards. Dickson et al. [99] carried out tensile tests on dogbone samples for different materials (polyamide reinforced with carbon, glass and Kevlar continuous fibers) and noticed that the failure of the samples occurs at the shoulder of the dog bone (Figure 22). The authors modeled the parameters of a tensile test on a specimen using the Autodesk® simulator. The resultant stress gradient illustrated on Figure 25 shows that high compressive stress is generated in this area leading to early breakage of tested specimen. Consequently, the design of parallelepipedic samples with end-tab at the ends of the specimen is recommended for tensile characterization of 3D printed composite structures and commonly used in the literature for tensile characterization of continuous carbon fiber 3D printed composites.

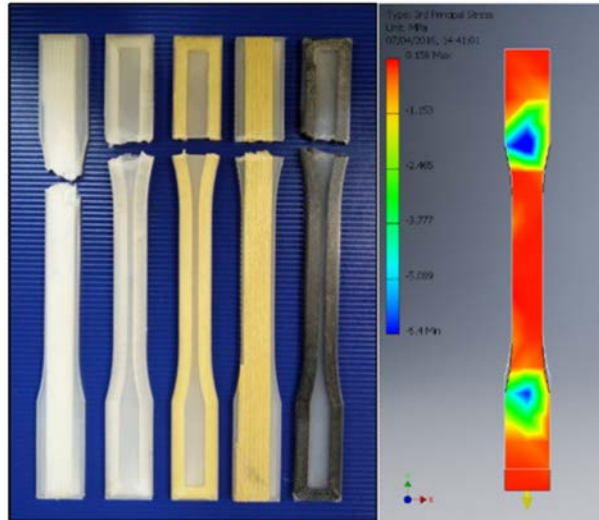


Figure 25 : Photography demonstrating specimen failure in the shoulder region of dog-bone samples during tensile tests (left). Finite Element Analysis of a tensile specimen showing compressive stresses present at the sites of failures (right) [99].

Thus, the next section will focus on the research work concerning the optimization of the 3D printing process with continuous fibers with regard to processing defects and material availability.

3.2.3. Future outlook on the optimization of 3D printing of continuous fiber reinforced composites

Nowadays, the 3D printing process needs to fill the gap with conventional manufacturing techniques such as AFP, Vacuum infusion or Resin transfer molding. To this end, several works are ongoing on the manufacturing process, the availability of materials and the prediction of mechanical properties in order to control and minimize printing defects and optimize the printing process.

Among the process optimizations, several studies focused on the post-consolidation of 3D printed structures. For example, Yamawaki et al. [91] applied a hot pressing treatment (270 °C at 0.2 MPa during 10 min) to continuous carbon fiber reinforced PA composites and measured a 42 % improvement in tensile modulus and a 49 % in tensile strength. The authors attributed this improvement to a reduction in voids content and also to better intermolecular diffusion compared to the 3D printing process. He et al. [107] measured the porosity content of printed composites and measured an improvement in porosity from 12.5 % to 5.9 % when a hot-press treatment was applied to the sample. A cross-sectional view of continuous carbon fibers printed composites with and without a compression stage is shown in Figure 26.

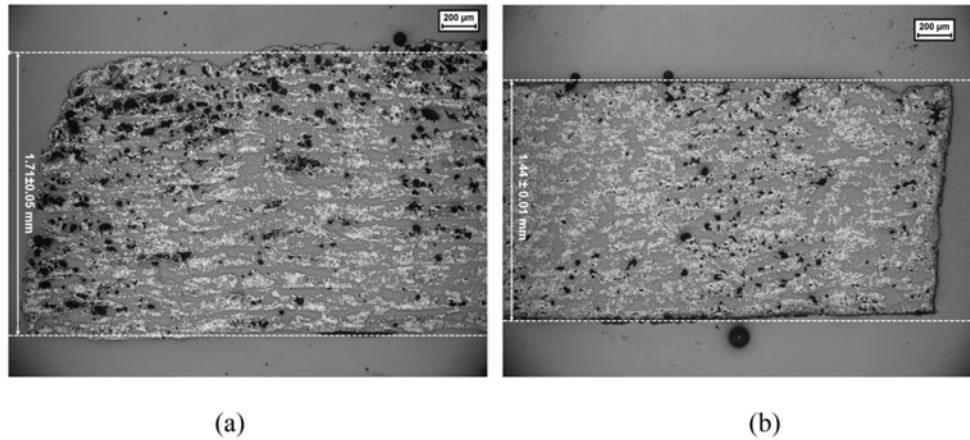


Figure 26 : Microscopic view of cross-section of 3D printed CF/PA6 composites without (a) and with (b) compression molding [107].

Mei et al. [97] investigated the influence of the hot-press on the mechanical properties for different temperatures, pressures and hot press times. The authors observed greater mechanical strength at higher temperature, pressure and manufacturing time due to improved polymer interdiffusion. However, the hot-pressing process changes the geometry of the sample and thus negatively affects the accuracy of the print.

Consequently, some authors have worked on improving the printer head to enhance in-situ impregnation and part consolidation while maintaining dimensional accuracy. Various improvement strategies are available in the literature. For example, Parandoush et al. [129] developed a printing head equipped with a compaction roller and a laser, which heats the beads during the printing process of continuous glass fibers reinforced polypropylene composites. The pressure brought by the compacting roller and the heat provided by the laser promoted molecular diffusion between the printed layers and consequently the microstructure of these printed parts showed good interfacial diffusion without porosity. The authors measured the adhesion of the layer by T-peel and lap shear strength test and the mechanical performance through tensile test and 3-point bending tests and showed mechanical performance as high as that of conventionally manufactured composites. Same results were found by Omuro et al. [110] who studied the influence of a compaction roller on the tensile and flexural strength of 3D printed continuous carbon fiber reinforced PLA. The authors noticed a significant improvement in mechanical performance but also observed delamination in the three-point bending test indicating poor adhesion between the layers.

Several other strategies were investigated to improve fibers/matrix interface. Qiao et al. [130] investigated ultrasound-assisted 3D printing in order to improve the wetting of the fibers for carbon

fibers reinforced PLA composites. Prior to printing, the carbon fibers are immersed in resin solution and the resin bath is subjected to ultrasonic waves that help impregnate the fibers bundles. The authors noticed that the ultrasonic treatment modified physically the fiber/matrix interface through resin agitation, dispersion stirring, impact etching and wetting. Hence, they measured a 34 % improvement in tensile strength compared to untreated composites.

Li et al. [131] induced micro-wave heating in printing process in order to enhance the mechanical strength and also to speed-up the continuous fibers printing process. Micro-wave heating allowed the printed structure to be heated evenly and thus reduced internal stresses in 3D printed parts. The authors noted a reduction in temperature heterogeneity, an improvement in tensile strength with a higher printing speed.

Liu et al. [132] investigated continuous fiber impregnation in combination with a micro-screw extruder directly implemented in the printer head. Polymer pellets were extruded by micro-screw and the extruded polymer fed an impregnation mold where the fiber bundle is tensioned and guide by rollers to the outlet die. A schematic illustration of this printing process is presented in Figure 27. In the same way than in-nozzle impregnation, this printing technique allowed the control of the fiber volume fraction with extrusion speed. The authors investigated the impregnation of continuous carbon fibers by nylon (PA12) matrix and noticed a low porosity content (2.62 %) for high fiber content (50.2 % vol.). Very high tensile properties were reached with a tensile strength of about 773 MPa and a tensile modulus of 85 GPa.

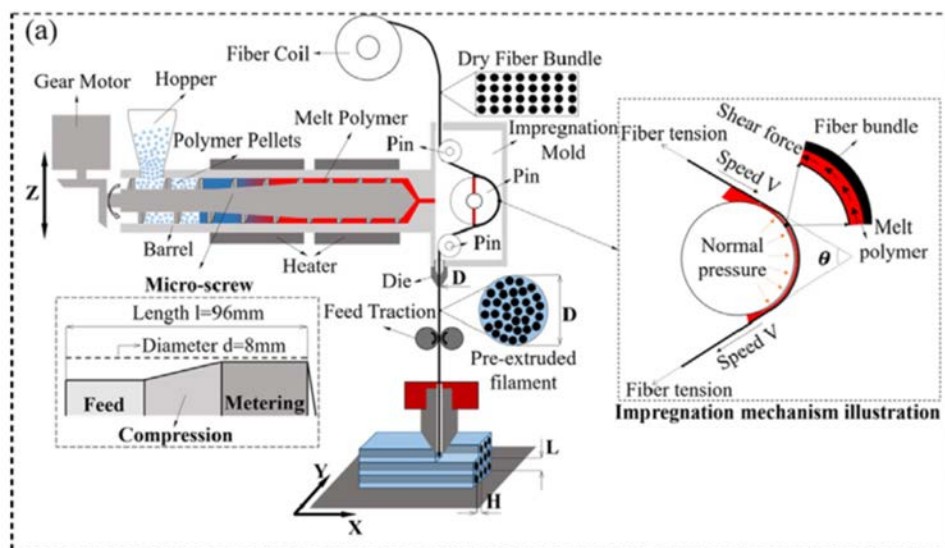


Figure 27 : Schematic illustration of micro-screw in-situ extrusion based 3D printed continuous carbon fibers PA12 composites [132].

Even though thermoplastic polymers are widely studied in the literature for 3D printing of continuous fibers reinforced composites, some research teams investigated the 3D printing of thermoset based composites. Thermoset reinforced composites are widely used in aeronautic industry due to their high specific performance, good corrosion resistance and good fatigue performance. For this purpose, Hao et al. [133] studied the 3D printing of thermoset composites. In the manufacturing process, the fibers bundle was impregnated in an epoxy pool and is thus fed into the extruder die. Mechanical performance was improved compare to short fibers composites and was in the same range as thermoplastic printed composites. However, in the literature thermoset matrix in 3D printing is mainly used in dual-materials printing with the addition of thermoplastic resin.

Azarov et al. [134], [135] aimed to pre-coat continuous carbon fibers with a thermosetting resin prior to in-situ thermoplastic impregnation. The authors claimed that dual-matrix composites aimed to take advantage of both thermoset and thermoplastic matrices where the thermoset improved the impregnation of the continuous fibers and the thermoplastic resin provided good inter-bead impregnation. The authors reached a tensile modulus of 44 GPa and a tensile strength of 511 MPa which is in the same range as other 3D printed technologies. This printing innovation was used to develop new commercial 3D printed able to print continuous fibers composites, namely Composer from Anisoprint®. The question of recyclability should be however raised.

Nowadays, the number of commercially available 3D printers capable of manufacturing continuous fibers reinforced structures is increasingly growing, based on various technologies. Desktop Metal® markets 3D printed fiber that aims to replicate AFP technology at the office scale (called μ -AFP) and uses continuous fibers reinforced tapes instead of filaments [136]. The manufacturer claims that this engine can be used to manufacture a wide range of thermoplastic matrix (PA6, poly-ether-ether-ketone (PEEK), poly-ether-ketone-ketone (PEKK)) reinforced with continuous carbon or glass fibers. 9T Labs® developed Red Series®, an all-in-one solution for 3D printing of continuous fibers based composites composed of Fibrify software able to quickly design optimal fibers trajectories and a 3D printer engine composed of two moduli. One is dedicated to continuous fibers 3D printing (Build modulus) and one on advanced post-processing (Fusion modulus) where pressure and heat treatment (400 °C at 20 bar) are applied to the printed structure, resulting in part with very high fiber content (60 % vol.) and low porosity content (< 1 %). The current materials available are PA12 and PEEK reinforced with continuous carbon fibers [137].

In order to broaden the design possibilities and improve the properties of the interlayer of 3D printed composites, some companies have worked on the manufacturing of robotic arms able to print in “real 3D”, i.e. printing in any direction. Arevo® aims also to combine 3D printing and AFP with a printing head mounted on multi-axis robot making possible printing in any space orientation [138]. This process consists of depositing pre-impregnated continuous carbon fiber tapes compressed by a roller laser-heated onto the build plate. Thanks to this process, Arevo® aimed to print a full bike frame. Continuous Composite company developed a new engine using a printing head mounted on 7-axis industrial robot [139]. Within printed head, the dry fibers are coated with a photo-curable thermosetting resin cured during the printing process thanks to an energy source. +Lab developed Atropos, a 6-axis robotic arm able to print continuous carbon and glass fibers thermoset composites [140].

In the aerospace industry, high quality polymers with high thermal resistance and high mechanical performance are required. However, the processing of PEEK composites requires a higher temperature (380 °C for nozzle temperature, 100 °C for build plate temperature) than that of other thermoplastic resins and consequently requires greater efforts than for other thermoplastics. However, higher ambient temperatures cause significant shrinkage and crystallization of the PEEK resin, leading to poor inter-layer performance. Stepashkin et al. [141] evaluated the micro-structure of 3D printed PEEK composites and observed the formation of porosity and micro-cracks in the structure due to the lack of impregnation combined with the internal stress mentioned above. However, the authors successfully printed continuous fiber reinforced PEEK composites although they believe that improvements are required. Meng et al. [142] studied the inter-layer adhesion of PEEK-based continuous 3D printed composites and aimed to reduce the interlayer delamination through laser treatment. The authors showed an improvement of interlayer adhesion through laser treatment and the use of a low-viscosity resin.

Recent research has focused on the addition of novel reinforcing fibers, especially natural fibers. This research will be discussed in the section 4.4.

In addition to process improvement, several works have been carried out on numerical studies to predict the mechanical behavior of 3D printed samples as a function of material properties and printing parameters. Numerical studies can be divided into two categories, namely the prediction of the mechanical properties and the optimization of the filament trajectories (i.e. fiber direction). A study by El Abadi et al. [143] has developed numerical models to predict elastic properties through Volume Average Stiffness (VAS) of 3D printed structured manufactured thanks to Markforged®

printers. Wang et al. [105] have developed a mechanistic model to predict tensile modulus and strength of continuous fiber reinforced composites by taking into account the volume of the impregnated fibers, the gap ratio and the fiber orientation. The predicted properties were closed to the experimental strength of printed structures with an error between 5 to 10 %. The authors noticed that further improvements are needed regarding the influence of fiber volume content on impregnation to make the model more accurate. Moreover, the influence of sample geometry and thickness on the fiber content should be taken account, as discussed earlier.

The optimization of printing trajectories is a major field of investigation in the literature today. The first work on fiber trajectories was performed by Brooks et al. [144] in the case of an optimized pulley. The topological optimization carried out with static finite element stress analysis has made it possible to obtain high mechanical performance with minimum use of continuous fibers, thus minimizing production costs. A schematic view of this study is displayed in Figure 28.

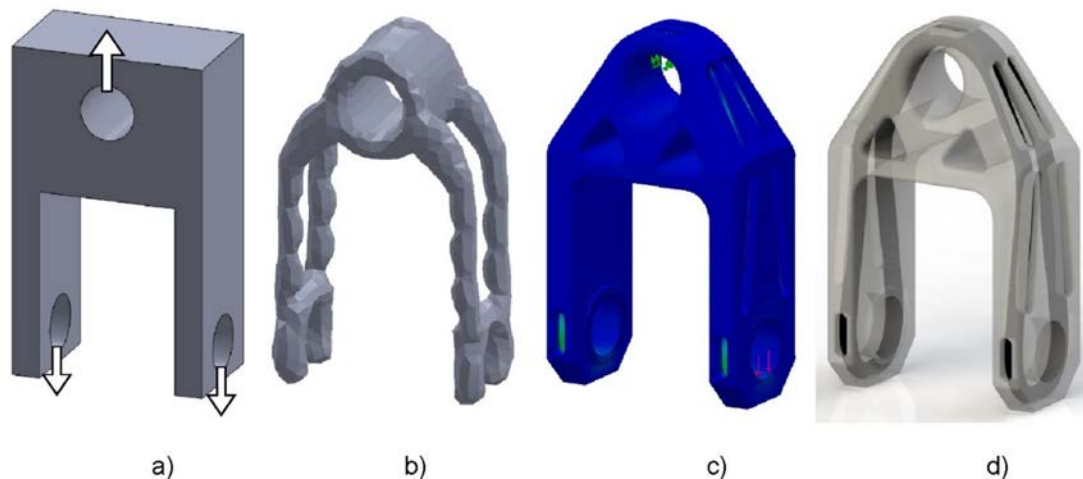


Figure 28 : Evolution of a pulley design from left to right : a) volumetric design space, b) topological optimization, c) finite element analysis of fibers reinforced part, d) final iteration after first physical tests [144].

Li et al. [145] succeeded, through topological optimization, in producing light-weight structures with reduced stress concentration zones.

Work on fiber orientation or printing trajectory is targeted to produce variable stiffness composites (VSC). Recent studies were performed on composites reinforced with curved printing path (Figure 29) where fibers orientation was optimized using genetic algorithms [87], [146], [147].

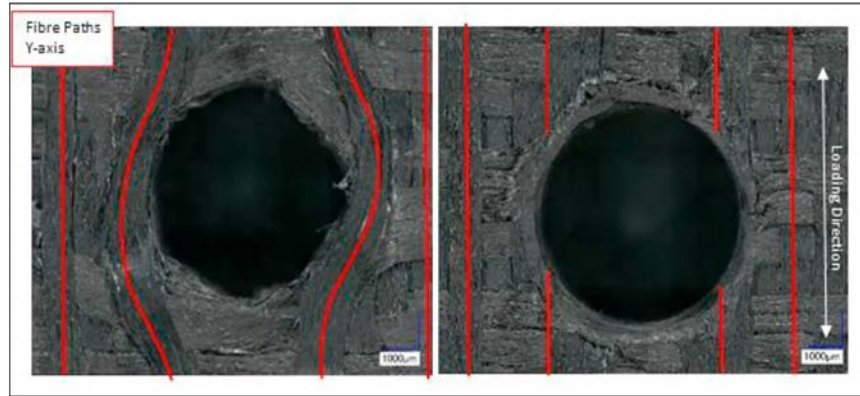


Figure 29 : Fibers pathing around a 6 mm hole feature and fibers path in straight woven section (red lines indicate fibers path and placement [148]).

Compared to constant-stiffness composites, these structures display a lower stress concentration, higher load-bearing capacities and higher stiffness to weight ratio [149]–[151]. Malakhov et al. [152] have developed a finite element method based on composites with variable fiber volume fraction and stiffness that takes into account the distance between fibers and changes in fibers direction to precisely optimize the fibers trajectory. The authors compared an optimized fiber deposition with a simple rectilinear fibers deposition and noticed a 3.2-fold decrease in the stress concentration factor around a central hole. Hence, they showed it is possible to manufacture composite parts with internal geometric discontinuities without degradation of mechanical properties. Sugiyama et al. [153] optimized the trajectory of the curved line to design 3D printed continuous fibers reinforced composites with variable fibers volume fraction and stiffness and compared them to composites with constant stiffness. The path of the filament (and the fibers) in the VSC follows the predetermined stress lines and is curved near the hole with a minimum radius of curvature equal to the radius of the hole as schematized in Figure 30.

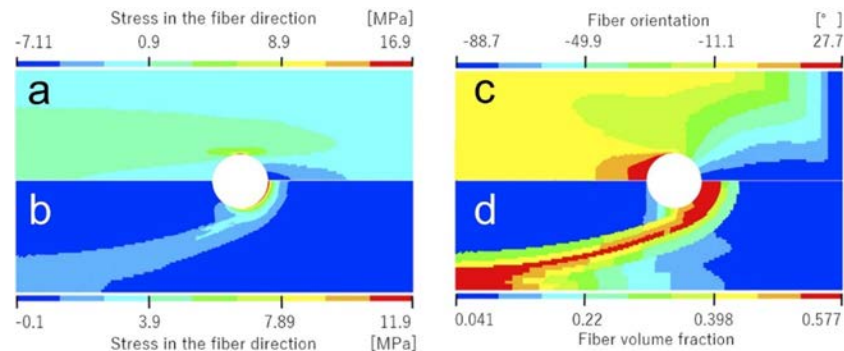


Figure 30 : Stress distribution fields in the fibers direction for a unidirectional (a) and a variable volume fraction (b) layer. Fibers orientation (c) and volume fiber fraction dispersion (d) obtained from the optimization [153].

Their work showed the potential of 3D printing to precisely tune the stiffness of composites thanks to the distribution of the fiber trajectory. Beyond mechanical purpose Variable Stiffness Composites can also be interesting for the design of structural actuators [154]–[156] where the stiffness gradient leads to an anisotropic shape change. Multifunctional materials capable of sensing, actuating and self-adapting to extremal stimuli, as do biological structures does (plants for example), are now showing a growing interest in the composite community. 3D printing, while allowing the precise adjustment of the structure architecture to design a pre-programmed structure, has evolved into what is known as the 4D printing concept.

4. 4D Printing of synthetic materials

Recently, multifunctional materials have gained interest in the industry, especially for structures capable of changing their shape during their lifetime. In this context, researches have been carried out to develop 4D printing technology. 4D printing combines 3D printing technology and the use of smart materials with time-dependent properties that are triggered when an external stimulus (temperature, moisture, light, pH, mechanical actuation...) is applied [157]–[159] as schematized in Figure 31.

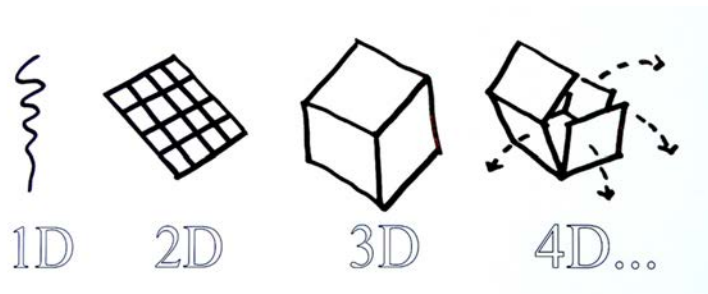


Figure 31 : Illustration of 4D printing concept showing 3D printed structures able to modify their shape during their lifetime in response to an external stimulation [160].

Among the properties of programmable materials, the most studied is the ability of the material to self-deploy, allowing the development of autonomous actuators such as deployable solar panels, self-deployable robots or responsive building skins [161]–[163] (Figure 32). There is currently a great interest in the environmentally-driven actuation to design stand-alone deploying systems with low maintenance, cost, and low energy consumptions without the addition of a control center.

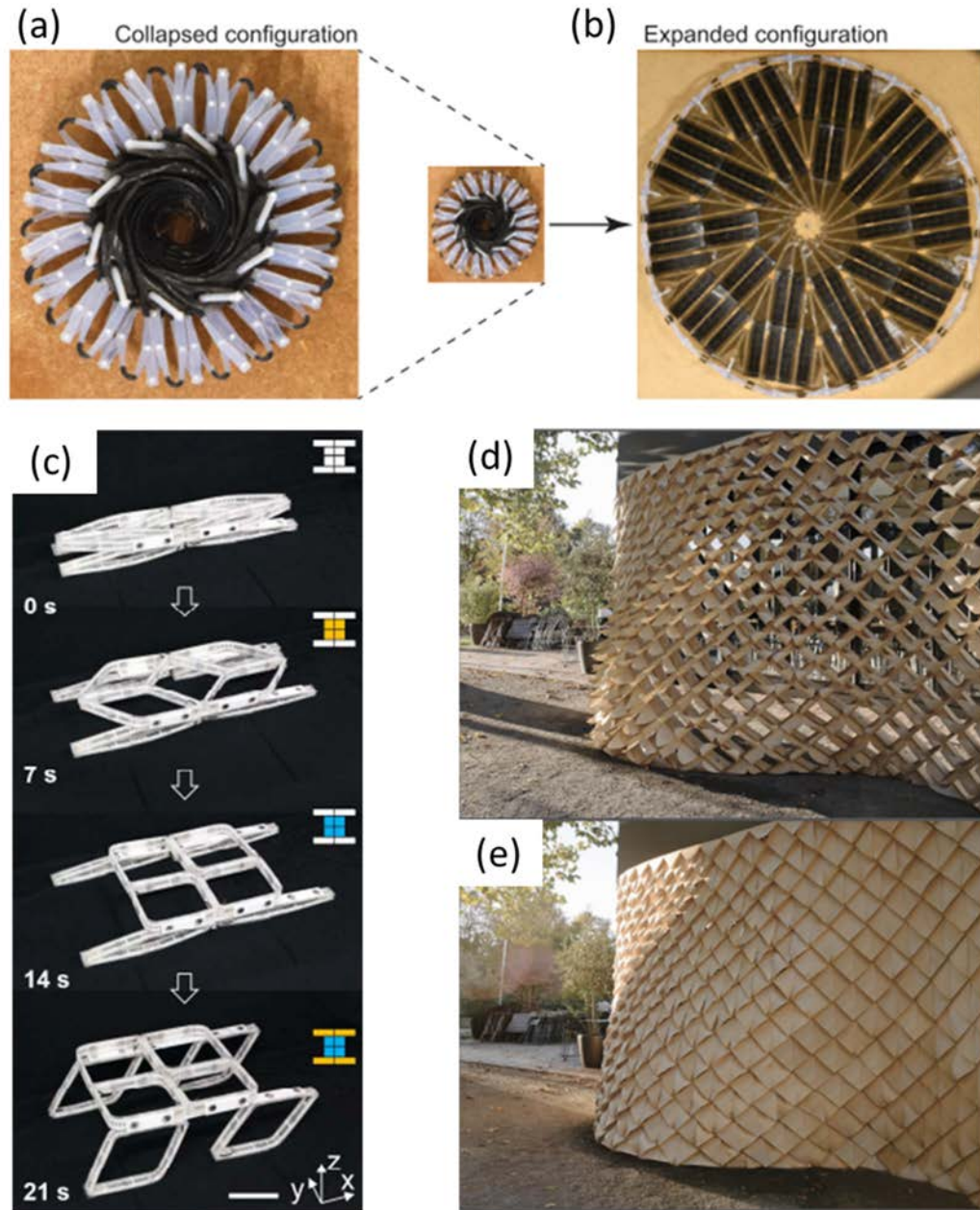


Figure 32 : Photography of self-deployable structures. Self-deployable solar panel from collapsed configuration (a) to deployed configuration (b) actuated thanks to shape memory polymer. Self-assembly DeployRobot deployment from a folded state to a deployed state (c). The center body of the robot is first deployed, and then the legs are state to a deployable state. Robot is composed of circular neodymium magnets and acrylobutadiene styrene fibers embedded in polyvinylchloride matrix. Architectural building skin meteosensitive using hygroscopic qualities of wooden veneer as a naturally produced constituent within weather responsive composite systems able to open in dry environment (d) from a fully closed state (e). [161]–[163].

4D printing makes it easier to manufacture smart materials with embedded functionalities through the ability to create complex architectures and design pre-programmed structures [164]. For materials capable of shape-changing, there are currently two types of stimulus-responsive materials: shape-changing materials that react spontaneously to stimuli and shape memory materials that return to their shape after external actuation [160], [165]. Today, Shape Memory Polymers (SMP) have been widely investigated to develop self-deployable structures in various fields. For example Zarek et al. [166] studied 4D printing in medicine to develop endoluminal medical devices to replace tracheal stent. Lin et al. [167] have developed a concept of self-deployable reflectors for the space industry.

The following section provides an overview of 4D printing of polymeric materials and their related composites.

4.1. 4D printing of polymer and composite materials

Plant structures exhibit various mechanisms which might be used as sources of inspiration in 4D printing through the biomimicry approach [168]. Biomimicry aims to study natural structures and mimic them in order to provide sustainable solutions to human technological problems [169]. Approaches to the design of bioinspired structures are divided into two categories: top-down and bottom-up approaches. The bottom-up approach aims at identifying a behavior or function of interest in a biological system and translating it into human design. One of the well-known biomimetic products developed using this approach is the Lotusan[®] paint which is based on the self-cleaning function of *Nelumbo nucifera* leaves [170]. Oppositely, in a top-down approach, human needs or technological issues are identified and solutions are sought in organisms or ecosystems with a technology-pull approach. An interesting case about this approach is the design of façade-shading system Flectofin[®] which is a hinge-less flapping shading derived from the deformation principle found in the bird-of-paradise (*Strelitzia reginae*) flower during pollination by birds [171]. Schematic representations of top-down and bottom-up approaches in biomimicry are shown in Figure 33.

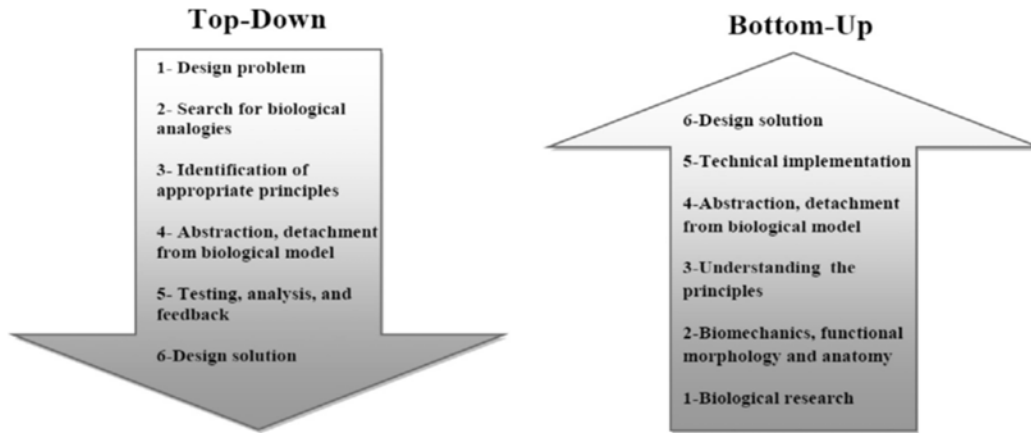


Figure 33 : Schematic representation of top-down (answer to a technical issue with a solution found in biological system) and bottom-up approaches (biological properties translated to human design) [172].

Recently, biomimicry has gained interest to design autonomous actuators using 4D printing. Plant movements are divided into two categories depending on their spatial and temporal scales and are based on water transport. Some systems exhibit rapid and large-scale movements based on elastic instabilities, such as *venus flytrap* [173] (60 % of total displacement occurs in 0.1 second) [173]. When a prey touches the inner surface of the Venus flytrap leaf, water flows between the inner and outer faces of the plant leaf, creating changes in volume, buckling of the lobes and thus the closure of the flytrap [174] (Figure 34.a,b). Oppositely, plant systems such as pine cones [175]–[177] or wheat awns [178] exhibit small-scale and slow movements (a few hours) based on water transport in their hygroscopic tissues, leading to changes in volume. For example, the scales of the pine cones are closed in case of high moisture content and open in case of dry conditions, allowing the plant to spread its seeds depending on the climatic conditions (Figure 34.c,d) [177], [179]. These structures are composed of two connected layers (one active and one passive) (Figure 34.e), i.e. a bilayer architecture where each tissue has a specific architecture with differential elastic and swelling properties. When the system is submitted to environmental variation (temperature or moisture), the differential swelling between the layers results in curvature [180].

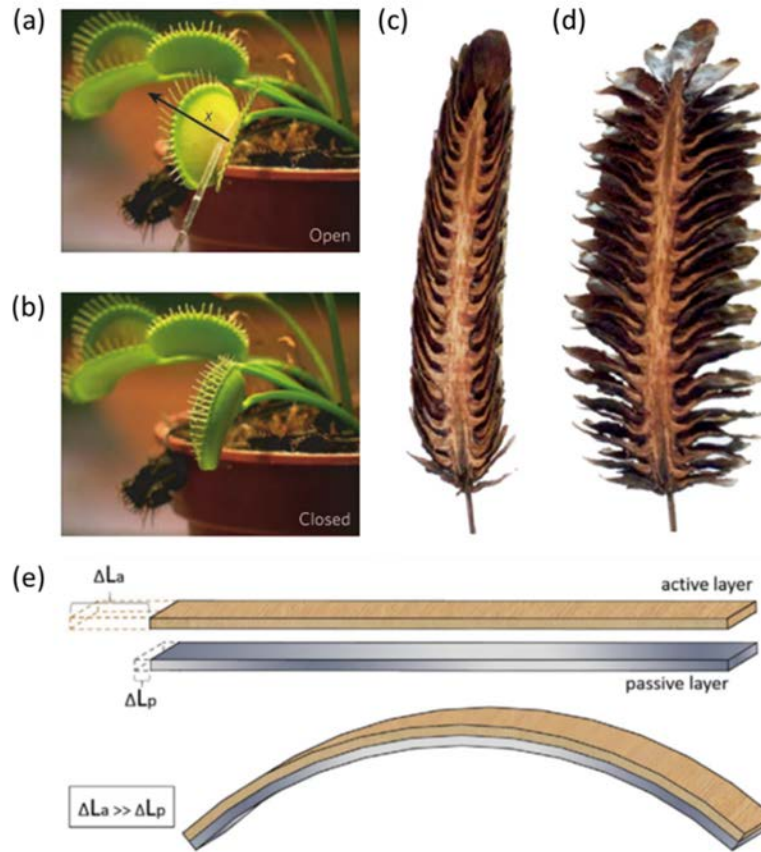


Figure 34 : Venus flytrap in its open (a) and closure (b) states. After the prey touches the inner surface of the open leaf, water flows between inner and outer surface of leaf changing its curvature in the x direction (a). Pine closed at high moisture content (c) and open at low moisture content (d) to allow seed dispersal. Principle of bilayer structure based on differential expansion (i.e. shrinkage or swelling) of active (ΔL_a) and passive (ΔL_p) layers (e) [163], [181], [182].

Bilayer actuation behavior (Figure 34.e) is currently basically well described by an adapted bimetallic theory derived from the thermo and hygro-elastic properties of each layer [177], where the curvature $\Delta\kappa$ is expressed by Equation 2 and 3:

$$\Delta\kappa = \frac{\Delta\beta \cdot \Delta M \cdot f(m,n)}{t} \quad \text{Equation 2}$$

$$f(m,n) = \frac{6(1+m)^2}{3(1+m)^2 + (1+mn)\left(m^2 + \frac{1}{mn}\right)} \quad \text{Equation 3}$$

With $m = \frac{t_p}{t_a}$ where t_p and t_a are the passive layer and the active layer thicknesses, respectively. Here, the active layer is considered as the swelling phase, while the passive layer is the non-swelling phase

which is used to bring stiffness to the assembly. Then $n = \frac{E_p}{E_a}$ where E_p and E_a are the longitudinal tensile moduli of the wet passive and active layers, respectively. $\Delta\beta$ is the differential hygroscopic expansion coefficient between the active and passive layers. ΔM is the difference in moisture content within the material between the test environment and the storage condition. Finally, t is the total thickness of the sample (active and passive layers).

Shape-changing materials operate differently because it is the external stimulus that triggers the transformation of their original shape, subsequently, the transformation is reversed when the stimulus is removed. Therefore, the material can be considered to oscillate between two states of equilibrium without the need for an external force, allowing multiple transformation cycles. The direction and amplitude of the movement are pre-programmed into the material structure through the architecture. For example, Ding et al. [184] designed 4D-printed SMP materials that were intended to be triggered in a single step after printing. They worked with a 3D polyJet printer that projects ink droplets of vitreous SMP (VeroClear) at room temperature combined with an elastomer (Tango+) with a bilayer structure. Both polymers exhibit a large difference in stiffness below the glass transition temperature of the SMP (Young modulus of about 1 GPa for the SMP and 1 MPa for the elastomer). When the printed structure was heated, the difference in Coefficient of Thermal Expansion (CTE) between the vitreous SMP and the elastomer caused an asymmetrical expansion between the layers and, in response, the printed structure bent. Above the T_g of the SMP, the Young's modulus and CTE of SMP and the elastomer were very close, so that when the structure is cooled down, the laminate retained its actuated shape. Van Manen et al. [183] developed PLA-based structures with tuned infill pattern to control the folding behavior. When structures are subjected to temperatures above the glass transition temperature, the structural layers exhibit different combinations of directional strains which lead to an out-of-plane deformation. The authors used this sequential stacking to develop various self-deployable origami structures (Figure 35).

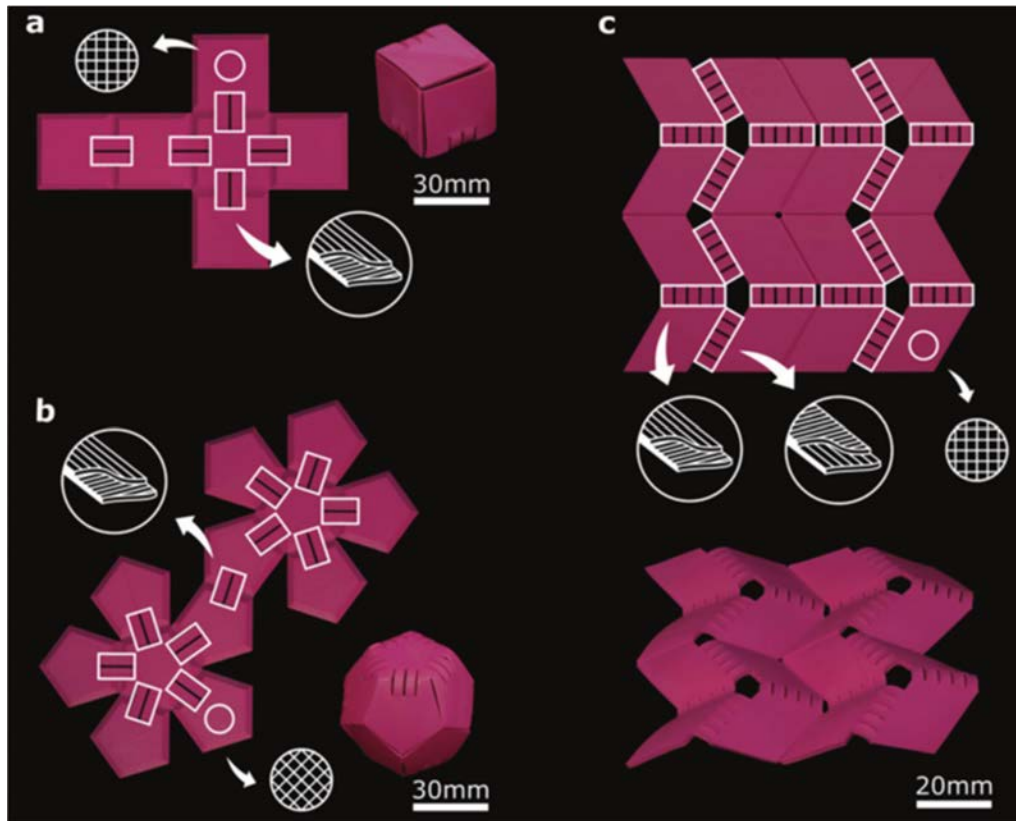


Figure 35 : Self-bending elements (annotated in the figure as white rectangles) connect the semi-passive panels of origami structures composed of PLA. (a) A flat printed construct, consisting of 6 square panels connected by a thin layer to preserve the integrity of the structure, is folded into a cubic box upon activation. The printing patterns of the active bilayers and semi-passive panels are shown schematically. (b) Using the same method, a self-folding dodecahedron folds into its 3D shape. (c) The well-known Miura-ori folding pattern was printed and activated using two different types of self-bending elements (with different bending directions). The initially flat structure made of four Miura-ori units transforms its shape to the desired folded state upon activation [183].

Because autonomous environmental actuators are often slow and non-controllable, some research teams have used electro-heating to develop new actuators with faster and more controlled actuation (Figure 36). Electro heating induces rapid and homogeneous heating within the structure depending on the nature of the material and the electrical input power [184].

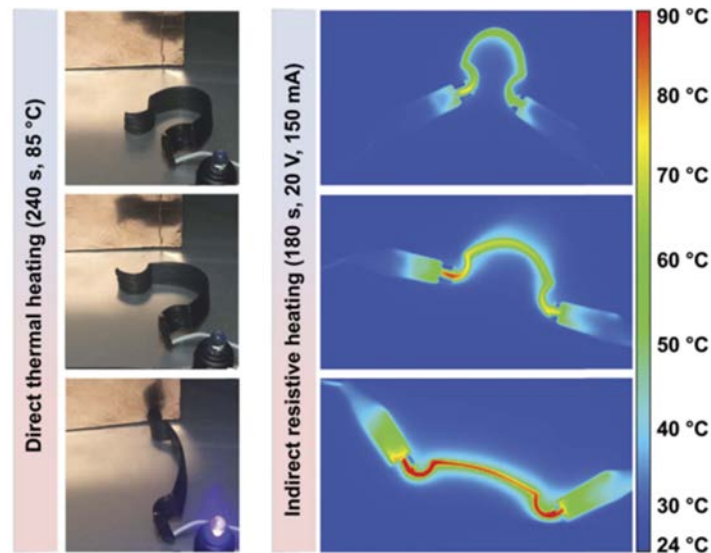


Figure 36 : Actuation of 4D printed composites (epoxidized soybean oil and bisphenol F diglycidyl ether blend filled with carbon nanofibers) actuated thanks to an external thermal heating (85 °C) from the programmed shape to the printed shape after 240s (left). Thermal images obtained with an infrared camera where structures are heated from a power source of 20V, 150 mA induces the shape change from the programmed shape to the printed shape after 180s [185].

Yang et al. [184] used the electrically conductive behavior of carbon fibers to trigger thermal actuation by electro-heating. To this end, the authors evaluated the electro-thermal effect of the conductive carbon fibers embedded in a PEEK and a PLA matrix. The electrically induced heating allowed to quickly reach a temperature high enough to trigger the thermal expansion of the polymer. Asymmetric lay-up converts thermal expansion of each layer in bending actuation (7 mm for carbon/PLA and 10 mm for carbon/PEEK). These materials had good recovery properties, but at temperatures above T_g , the carbon/PEEK actuators underwent irrecoverable deformation due to recrystallization when temperatures dropped below T_g .

Among 4D printed polymer materials, the most commonly used smart materials are shape memory polymers and associated shape memory composites (SMC). As described by Salimon et al., “*shape memory effect (SME) is a specific mechanism of the thermodynamically favorable process of transition from a metastable state (temporary shape) to a stable state (permanent shape)*” [186]. These states are separated by an energy barrier that can be overcome by an energy input brought by external stimulation (heat, light, electric stimulation, chemical modification, etc...). Temperature-

sensitive SMP materials are based on their properties that evolve above and below the glass transition (T_g) and melting temperature (T_m).

SMP materials are the most studied materials in the field of 4D printing thanks to their amplitude of response (responsiveness) and their quick response (reactivity) due to the instantaneous and homogeneous effect of temperature on the properties of the polymers. Many polymers are considered SMP but PLA is today the most studied polymer in 4D printing due to the availability of the filaments. For example, Zhang et al. [187] demonstrated the potential of PLA as SMP printed with FFF. They printed a tubular preform and applied compressive stress while heating the structure to reach an intermediate shape and maintained this stress while cooling. The structure was then heat above its T_g and recovered its initial shape with a recovery time between 120 and 240s depending on printing parameters such raster angle, recovery temperature or wall thickness.

These properties are interesting for sequential folding and were widely investigated in the literature for several material ranges. Generally, sequential folding is combined with localized compliant mechanism equivalent to hinges. Figure 37 shows mechanism of hinges (black area) which aim to move rigid panels (grey areas).

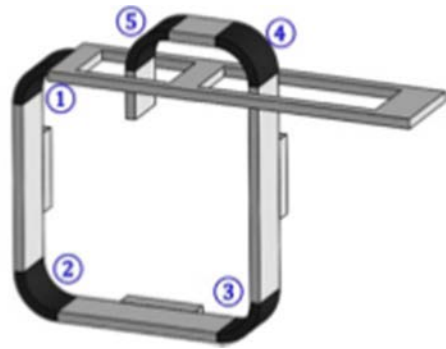


Figure 37 : Schematic representation of interlocking SMP (VeroWhite and Tangoblack) component made of flexible hinges (black areas) and rigid panels (grey) [188].

Ge et al. [189] aimed to develop 3D printed smart hinges from SMP materials capable of folding and creating a 3D structure from a 2D flat pattern. The materials used in this study were flexible composites composed of glassy polymer fibers embedded in an elastomeric matrix. The glassy polymer fibers exhibited shape-memory behavior and the coating matrix remained in the rubbery state in the temperature range (between 15 °C and 60 °C) while the fibers underwent a glass transition. In order to activate the shape memory effect, the structures were deformed at 60 °C where the fibers were above T_g and a stress was applied in the structure while cooling to 15 °C.

When the sample was heated to 60 °C, it recovered its shape. An illustration of the folding process is shown in Figure 38. The folding angle is governed by the stress applied to hinge structure as well as by the hinge gap [190]. Moreover, the stiffness of the structure and therefore the stacking sequence controls the load-bearing capacity of the 4D printed hinges and its recoverability [191]. Finally, the nature of the materials has made it possible to design multimaterial 4D printed SMP structures with mismatched thermal strains, allowing to create time-dependent shape recovery structures [192].

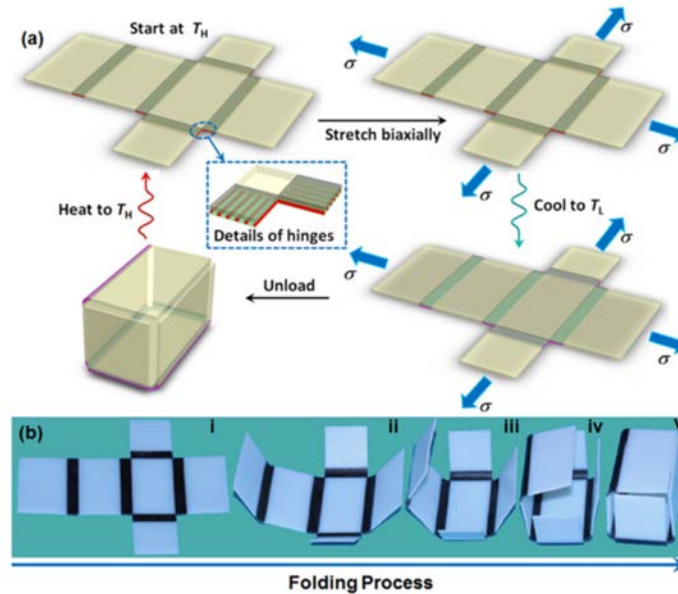


Figure 38 : A self-folding opening box manufactured with SMP composites hinges connecting inactive plates with a schematic view of the thermomechanical actuation pathway (a) and photographs of the tested specimen recovering its shape from the flat to the 3D box (b) [189].

In addition to the temperature, other external stimuli can be provided to actuate the 4D printed structures. Yang et al. [193] developed photo-responsive 4D printed actuators based on SMP filled with carbon black with good photo thermal conversion efficiency. In this study, a pre-deformed shape was achieved using the usual SMP actuation pathway. After the irradiation of light, carbon black generates heat by absorbing light and reaches a temperature of about 35 °C. After 160 s of illumination with the intensity of sunlight, the authors managed to fully actuate their structure. Similarly, Hubbard et al. [194] used light to induce local shrinkage in the hinges area of a 2D planar structure to create a 3D structure. However, light is often an indirect stimulus and actuation is limited to SMP with a low glass transition temperature.

4.2. Humidity as a motor of actuation

Humidity, often considered as a drawback in composite materials, is a promising actuation stimulus, especially for self-folding hydrogel-based micro-actuators [195], [196]. These materials capable of modifying their shape in response to water sorption are called hygromorphic materials. These materials are inspired by biological hydraulic actuators (pine cone, wheat awn, wild carrot...) and mostly exhibit a bilayer microstructure with asymmetric elastic and hygro-expansive properties between the layers (Figure 40.e). For example, Raviv et al. [197] combined a 2 GPa stiff polymer with UV-curable hygro-sensitive acrylated monomers. When exposed to water, the cross-linked acrylated absorbs water molecules and becomes a hydrogel with a large increase in volume (+200 %). The stiffness and hygroexpansion gradient between the rigid polymer (2 GPa) and the hydrogel (40 MPa) organized in a asymmetric lay-up forces the structure to bend with a maximum folding angle of 120°. The authors demonstrated the capability of this material in another study [198] where they printed a proof-of-concept with various transformation of complex shapes such as octahedrons, curved surfaces or self-joining lines as shown in Figure 39.



Figure 39 : 4D printing of cross-linked hygro-sensitive hydrogel and rigid plastic insensitive to water. Demonstration with self-folded lines with customized angles (a), transformation of flat surface to a 3D octahedron (b) and curved surfaces (c) [198].

According to Liu et al. [199], 4D printed hydrogel can be divided into three groups: pure hydrogel, hybrid hydrogel and hydrogel composites. In pure hydrogel actuators, the shape-change is brought by a differential cross-linking within the structure. When the hydrogel is immersed in water, the cross-linking gradient causes an anisotropic swelling responsible for the actuation. Kirillova et al.

[200] and Huang et al. [201] have developed self-folded hydrogel with differential cross-linking by the different light absorbance in the structure. When immersed in water, the structure underwent a differential swelling and took a stable tubular shape.

Hybrid hydrogels are structures composed of two or more types of hydrogels. The different hydrogels phases present a different swelling amplitude and responsiveness speed. During exposure to water, each hydrogel swells depending on its own properties, resulting in a strain mismatch and dynamic shape change. Naficy et al. [202] have developed a printable ink composed of linear hydrophilic polyurethane combined with photocurable monomers. Polyurethane provided the rheological and mechanical properties required for 3D printing, while photocured monomers provided hydrophilic network that adjusts the elastic properties and water swelling. Shape changing is then tailored by the properties of the materials (length of molecular chains, photosensitive monomer concentration, nature of polyurethane chain) and printing parameters. Similarly, Zheng et al. [203] printed a hydrogel fibers-based structure with a high response speed using two hydrogels of different reactivity, namely poly (acrylic acid-co-acrylamide) (PAAM) and poly(acrylic acid-co-N-isopropyl acrylamide) (PNIPAm). The structure of the gel was composed of a nonresponsive gel layer and a hybrid gel made of PAAM combined with PNIPAm fibers. The hydrogel structure gets an anisotropic distribution of swelling and stiffness and when the structure is exposed to water or a saline solution, the part is curved in a programmed way such as cylinder helices or tubes with a control of the alignment of the gel fibers.

Baker et al. [204] developed a Miura-Ori origami structure based on a trilayer structure consisting of a polyurethane hydrogel core and two polyurethane elastomer skins. Bilayer hinges made of the same materials (polyurethane hydrogel and elastomer) are introduced into the structure and are designed to bend when the hydrogel is hydrated. By increasing the length of hinges, the authors observed that the bending angle increased linearly from 30° for a 1 mm long gap to 135° for a 5 mm long gap. Thickness ratio also plays a role in the actuation angle. The location of the bilayer in the structure also affected the angle of actuation and, consequently, the authors successfully designed various complex origami structures from a 2D flat shape. One example is displayed in Figure 40.d where a flat design becomes a 3D deployed structure (Figure 40.e) after immersion in water.

Mao et al [205] have also developed a SMP “Grey60”/Elastomer “Tangoblack” or “Verowhite”/hydrogel actuator that enables the combination of moisture and temperature to trigger actuation while providing a higher level of stiffness for the material system. The hygroscopic actuation of the hydrogel was influenced by the evolution in stiffness of the SMP with the

temperature. The overall actuation of this hydrogel/SMP is however not fully controllable and the reactivity is still rather low (10-20h) for a complete actuation cycle. Liang et al. [206] developed calcium-ion cross-linked alginate-based hydrogel filled with hydrogel microfibers that actuate (bending) due to a mismatch in hygroscopic strain between the hydrogel and the microfibers upon dehydration. By manipulating the arrangement and orientation of the microfibers, the authors aimed to control the actuation and thus various different shapes were obtained.

Despite this, hydrogel materials have moderate mechanical performances, which is why the authors investigated the addition of reinforcing fibers or particles to create hydrogel-based composites. Fibers or particles promote the anisotropic properties and their orientation control the shape-change. Gladman et al. [207] have developed a novel ink made from NanoFibrillated (NFC) Cellulose embedded in an Acrylamide matrix. During the printing process, the cellulose fibers were oriented by shear force in the nozzle. In general, NFCs, due to their high crystallinity, do not swell but rather control the direction of actuation as in organic plants [208]. For the first time, they have pre-programmed complex actuation through localized swelling anisotropy that yields multiple shape-changing domains (Figure 40). In Figure 40.a, the $0^\circ/90^\circ$ stacking is studied and the petals tend to bend as they close. In Figure 40.b, the stacking is $45^\circ/-45^\circ$ and the petals twist when exposed to moisture.

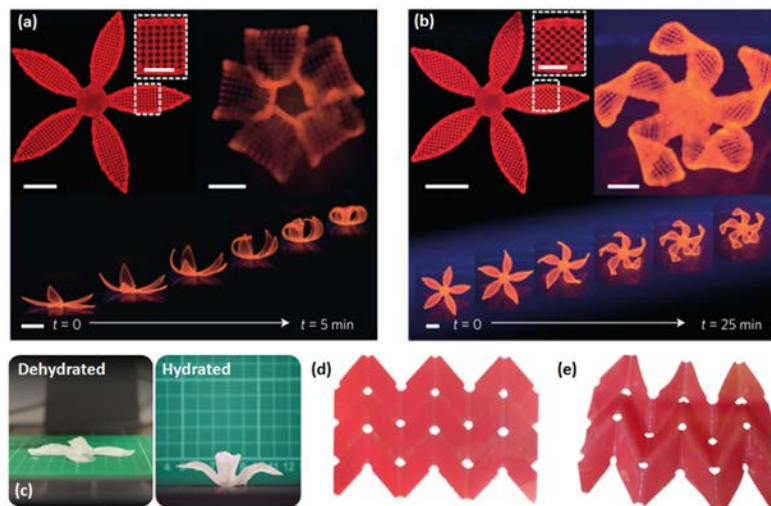


Figure 40 : Complex flower morphology composites with localized $0^\circ/90^\circ$ bilayers (a) and $45^\circ/-45^\circ$ stacking made of soft acrylate filled with cellulosic fibrils (b). Actuation of petal architecture with a sodium carboxymethyl cellulose (CMC-Na/CMC) filled with cotton derived pulp linters (c). Actuation of an origami-fold pattern composed of polyurethane hydrogel core and polyurethane skins from dry state (d) to wet state (e) [196], [204], [207].

Mulakkal et al. [196] have developed a carboxymethyl cellulose (CMC) filled with cellulose pulp fibers ink for 4D printing. Rheological properties, stability and swelling potential were investigated as well the unfolding of petal architecture (Figure 40.c). The actuation is based on a strain mismatch in petal thickness due to physical changes in the configuration of the cellulose (hornification, i.e. irreversible loss of fibers swelling ability after the wet/dry cycle due to a biochemical modification [209]).

However, unlike temperature-actuated structures, hygromorphic materials have a moderate actuation speed, limited by the kinetics of moisture transport, which is diffusive as opposed to temperature, or by the actuation of light. In addition, moisture related actuation is influenced by relative humidity, which is difficult to control manually. These points may constitute bottlenecks in technical applications where actuation control and fast responses are required.

4.3. Future outlook on the optimization of 4D printing of fiber reinforced composites

Unlike polymers, that are thermally activated by the presence of a stimulus, hygromorphic materials are activated hygroscopically, but are also temperature-dependent. As a result, few studies have focused on the control of hygromorphic behavior by external thermal stimulation. For instance, some research teams have used light as a way to control hygromorphic behavior. To this end, Chen et al. [210], [211] have developed a bilayer made with toner-coated paper (TCP) and biaxially oriented polypropylene (BOPP) with a precise pattern printed using laser technology (Figure 41).

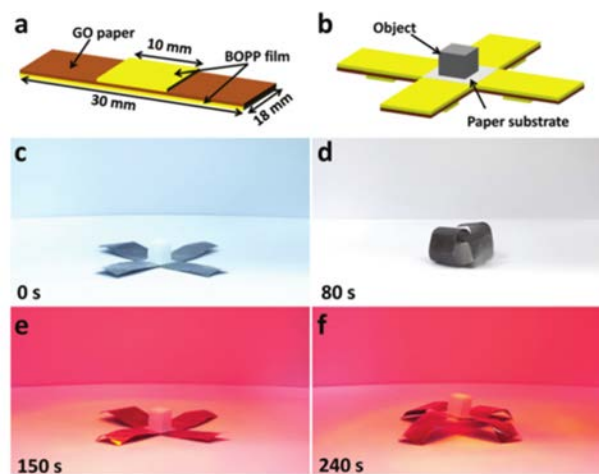


Figure 41 : Schematic representation of 4D printed robot made of graphene oxide and biaxially oriented polypropylene (a,c). Optical photo showing the protection mode of the intelligent robot responding to humidity (d). Optical photo showing the intelligent robot

responding to near infrared light (e). Optical photo showing the weightlifting mode of the intelligent robot responding (f) [211].

The authors observed a maximum curvature amplitude variation of about 2.1 cm^{-1} for light actuation and -1.3 cm^{-1} for moisture actuation. The light actuation mechanism is based on the conversion of light into thermal energy by the black toner. In order to reach the maximum amplitude of curvature, the authors irradiated the sample with a high light power (550 Mw.cm^{-2}) which led to local temperature of $70.4 \text{ }^\circ\text{C}$. This actuator behaved in a dual-mode actuation mechanism: temperature and hygroscopic actuations with temperature strains and hygroscopic strain controlled by temperature-driven desorption.

The hygroexpansive properties of the conductive papers have been combined with electricity-driven actuation [212], [213]. When electrical energy was applied to the structure, electrical heating caused rapid desorption of moisture, which *in fine* modified the curvature of actuation. To highlight this behavior, the authors studied samples stored at 15 % and 85 % relative humidity (RH) (Figure 42).

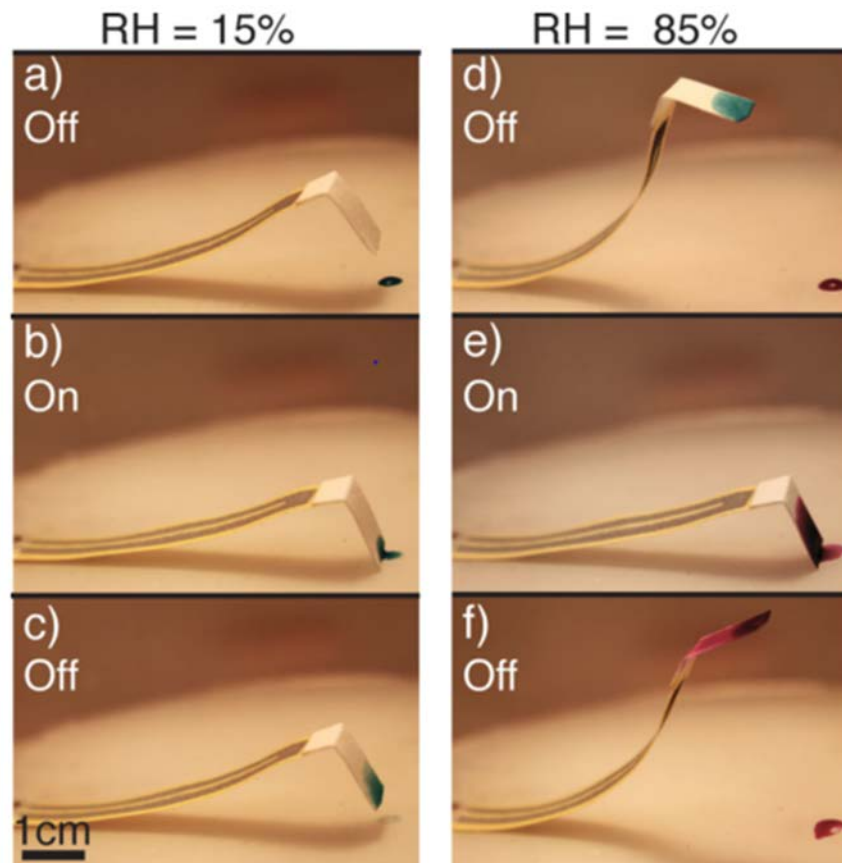


Figure 42 : Time-lapsed photographs Hygroexpansive Electrothermal Paper Actuators (HEPAs) embedded with conducting polymer (PEDOT:PSS) actuated at room temperature

at RH = 15 % (a-c) and RH = 85 % (d-f) with an electric stimulation ($P = 1\text{ W}$ and $I = 1.5\text{ mA}$) [212].

The experiment started at 15 % RH and an electrical current was applied to the paper ($P = 1\text{ W}$ and $I = 1.5\text{ mA}$); the water was evaporated from the paper and the actuator moved down until it reached a blue droplet. The authors increased the relative humidity to 85 % RH and the actuator bent with a greater amplitude of curvature. When the authors switched the power back on, the speed of the drying process was not affected by the increase in relative humidity. Moreover, they showed that the speed of actuation and recovery was neither affected by the RH content nor by the electrical power. However, electropaper has shown that its applications are limited to small-scale prototypes and that it can only be used in non-harsh environments because of its poor mechanical performances in wet environments.

Most smart materials such as SMP or the hydrogel based hygromorph used in 4D printing suffer from a lack of actuating force or load bearing ability, which limits their applications [214]. Akbari et al [191] propose to combine SMP with a flexible elastic hinge that stores elastic strain energy during programming and releases it during actuation to increase the recovery force. Reinforcing the stiffness and strength of hinges with stiff reinforcing fibers embedded in a polymer strategy is also a relevant option to yield high deformation accuracy [215], [216].

To control the orientation or direction of actuation, one solution is to control the anisotropic properties of the material by means of oriented reinforcing fibers. Gladman et al. [207] controlled the actuation curvature of a 4D printed sample by orienting stiff cellulose fibrils embedded in an acrylamide matrix. The effectiveness of the actuator is based on the control of the local fiber orientation to induce swelling and elastic anisotropy within the structure. As mentioned in section 3.1, short cellulose fibers are preferably oriented in the printing direction and the printed architecture has an anisotropic stiffness (longitudinal modulus = 40 kPa while transverse modulus = 20 kPa) and swelling (10 % in longitudinal direction and 40 % in transverse one). By controlling the printed architecture, the authors aimed to create mesoscale bilayers with oriented curvature through filament deposition and anisotropy combined with variation of printing parameters such as hatch spacing or interfilament distance. Schmied et al. [217] designed a structure inspired by the leaf of *Dionaea muscipula* based on epoxy resin reinforced with aluminum platelets. The orientation of the aluminum platelets is driven by a magnetic field and aims at locally modifying the stiffness of the structure. The 4D printing process is based on the difference in orientation of the aluminum platelets between the structural layers which induces an anisotropic thermal strain and allows to control the desired pre-strain. Two stacks were investigated, $[0^\circ/90^\circ]$ and $[45^\circ/-45^\circ]$, to create bending and

twisting actuation and create a multi-stimulable structure with fast shape reconfiguration that mimics the *venus fly-trap* mechanism. However, the 3D printing process orientates a limited fraction of the fibers during the process and the anisotropy of the structure is therefore incomplete. Continuous fibers should be preferred to discontinuous ones because of the difficulty in correctly aligning shorts fibers [191], [214], [216], [218]. However, since the orientation of the continuous fibers can be controlled more accurately, the shape of the structure could be easily programmed. With this in mind, some authors have worked on 4D printing of continuous reinforced composites.

For instance, Wang et al. [215] studied 4D printing of continuous fiber reinforced composites. The deformation of the laminate is triggered by a differential CTE between the continuous carbon fibers and the embedding matrix. The authors demonstrated that the angle between continuous fibers bundles dictates the amplitude of the curvature, while the bisector of the angle between two fibers bundles controls the shape of the curvature. Indeed, each layer exhibit different CTE vector that depend on the fiber's orientation. Consequently, modifying the orientation of the fibers leads to the expansion and the resulting bending actuation. Therefore, the deformation of the structure is directly programmable thanks to the fiber distribution and a complex shape as well as a multi-curvature are accessible as shown in Figure 43 where the obtained 3D structures are shown with their 2D flat pattern. In order to optimize fiber orientation and trajectory, Tian et al. [219] developed a fiber trajectory model and were able to predict the shape and amplitude of curvature as a function of the printed pattern. The authors studied the same structures as Wang et al. and the model used is based on the bilayer theory which aims to obtain an amplitude of curvature as a function of temperature, layers thickness and composite stiffness.

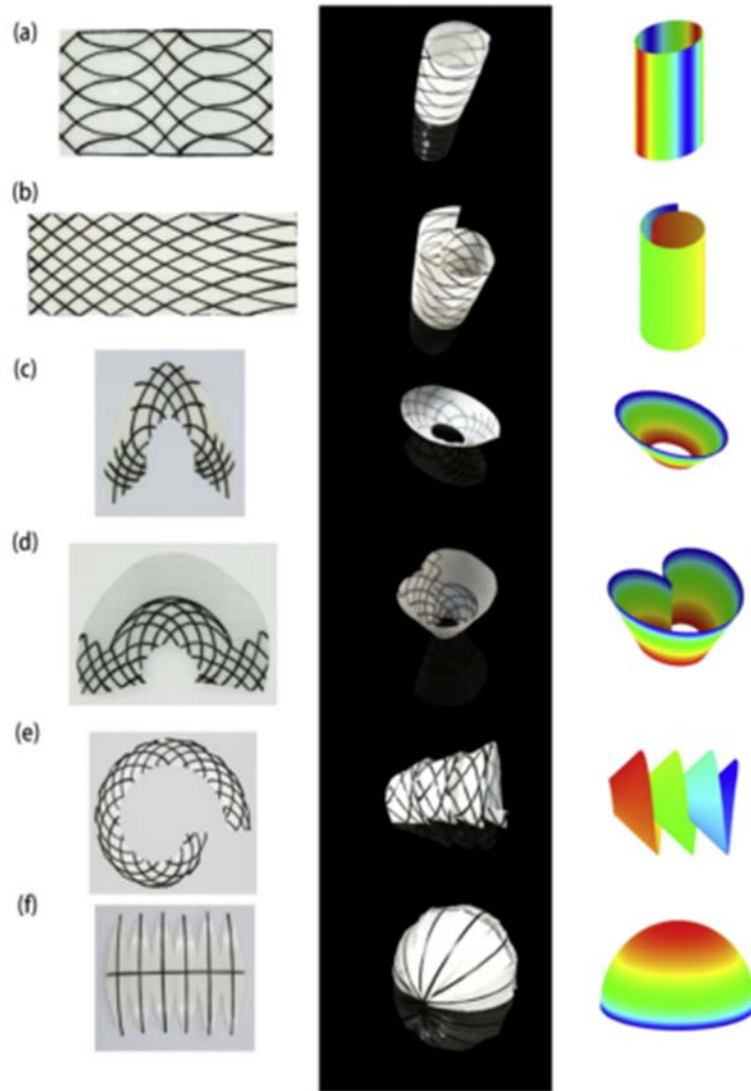


Figure 43 : Required shape of a) and elliptical cylinder, b) an Archimedes spiral cylinder, c) an elliptical cone, d) a heat-shaped cone, e) an involute helicoidal surface, and f) a hemisphere made of PA6/continuous carbon fibers composites [215].

Hoà [220] used 4D printing of continuous fibers composites to design self-deployable leaf springs with structural mechanical properties. The authors used AFP to lay a continuous carbon fibers coated with an epoxy matrix. These layers are manufactured with different fibers orientations ($0^\circ/90^\circ$) to ensure an anisotropic swelling during curing cycles to configure the shape of the structure to design curved beams. In another study, the authors used the same process to design a twisted structure with two different stacking [$0/30^\circ$] and [$0/45^\circ$] for solar energy concentrators, actuators, etc [221]. The curvature configurations were evaluated by measurement and numerical prediction with finite element model and the authors were able to obtain a good agreement between the numerical and experimental measurement.

5. 3D and 4D printing of natural fiber reinforced composites

5.1. Natural fiber specificities for 3D printing

Natural fibers are now well established as a relevant reinforcement in composites because of their mechanical properties [222] combined with their low density compared to glass fibers (between 1.35 and 1.55 for flax fibers and around to 2.66 for glass fibers) [223]. They also have a moderate environmental impact [224] and a cleaner end-of-life management. Natural fibers mechanical properties are strongly linked to their hierarchical microstructure (Figure 44.a) and their biomechanical composition (cellulose, hemicellulose, pectin, lignin and water). Table 1 summarizes mechanical properties and biochemical composition of various natural fibers used in 3D printing. The mechanical performance of natural fibers also depends on their role in biological architectures. For example, bast fibers bring mechanical stability to the plant (hemp, flax...) and exhibit higher mechanical performances (stiffness and strength) than fruit fibers (coir, coconut...) which are dedicated to energy dissipation [225]. Indeed, their secondary cell-wall controls the overall hygro-mechanical properties thanks to the cellulose MicroFibril Angle (MFA [226], [227] the interactions between the components of the natural fibers [228] and their overall composition.

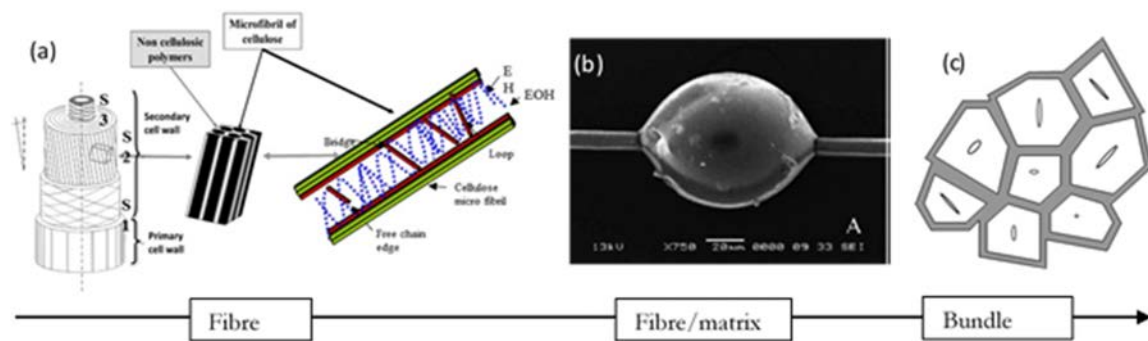


Figure 44 : Different scale of natural fibers composites, (a) cell-wall interface, (b) fiber-matrix interface and (c) fiber-fiber interface [229]–[231].

This complex and hierarchical architecture as well as the interactions between natural fibers components imply a complex non-linear behavior [232], [233] transposed to natural fibers based composites [234]–[237] which makes it difficult to assess the stiffness of composites. Consequently, Shah et al. [234] recommended evaluating the tensile modulus of natural fibers based composites in a range of strain between 0.05 % and 0.1 % and also after 0.4 % strain when the change in stiffness of the composite is limited.

The hierarchical architecture of natural fibers also leads to multi-scale interfaces, for example single fibers are often assembled into a bundle thanks to pectin cement (Figure 44.c, diameter of bundle \approx 200-400 μm and diameter of single fibers \approx 20 μm). The scale of the fiber bundle is typically referred to as “technical fibers” in the literature. Consequently, compared to conventional fiber-based composites, natural fiber composites have multiple interfaces, from cell-wall component interfaces (Figure 44.a) to cell-wall layers (Figure 44.a) to the fiber/matrix (Figure 44.b) and fiber/fiber (Figure 44.c) interfaces into the bundle.

Thus, compared to synthetic fibers, the surface properties of natural fibers are more complex. Natural fibers surface can be assumed to the primary cell-wall (Figure 44.a) and; for single flax fibers, this primary cell-wall is composed of low-crystallized cellulose, hemicellulose and pectin. However, the exact distribution and quantity in the cell wall is still unknown, only the overall biochemical composition of flax fibers is known (Table 1). Consequently, for all natural fibers, the surface of the fibers is not well-understood as well as their compatibility with the polymer matrix.

Fibers	E (GPa)	σ (MPa)	Cellulose [%]	Hemicelluloses [%]	Lignin [%]	Pectins [%]	MFA (°)	Ref.
Flax	46-85	600-2000	64-85	11-17	2-3	1.8-2.0	10	[228][238]
Jute	24.7-26.5	393-773	61-75	13.6-20.4	12-13	0.6 \pm 0.6	7-12	[239][240] - [242][238][225]
Kenaf	11-60	223-930	45-57	21.5	8-13	3-5	7-12	[239][29,32][245]
Coir	3.44-4.16	120-304	32-46	0.15-0.3	40-45	3-4	30-49	[239][246][238][225]
Cotton	3.5-8	287-597	82-99	4	0.75	6	30-40	[247][248]
Wood	15.4-27.5	553-1500	38-45	19-39	22-34	0.4-5	5-45	[249][250]
Bamboo	10-40	340-510	34.5-50	20.5	26	<1	2-10	[247]
Harakeke	14-33	440-990						[251]
Hemp	14.4-44.5	270-889	55-90	4-16	2-5	0.8-8	6.2-11.2	[252][253][254]

Table 1 : Mechanical and biochemical composition of various natural fibers used in 3D printing.

However, they exhibit specificities such as inherent defects, variability in terms of mechanical performance [255] and sensitivity to heat and moisture due to their complex polysaccharide composition. The most common processes applicable to natural fibers today are extrusion, injection molding, thermoforming, film stacking and vacuum bag molding [246].

The condition of natural fiber bundles could be a concern when FFF 3D printing of natural fiber composites, by introducing an additional interface [256]. Indeed, the shear stress generated by the printing process is not high enough to properly separate the fibers bundles, which induces variability in the reinforcing effect in biocomposites. In the literature, proper fibers separation can be reached by chemical treatment such as retting [230] or by mechanical division or by a high shear stress process such as extrusion or injection molding [257], [258]. The bundle state also induces the formation of interfacial porosities due to incomplete impregnation, so the fiber bundle allows to reduce its porosity content and thus improves the mechanical performances of biocomposites [259], [260].

Natural fibers have specific characteristics that must be considered during the 3D printing process. They are sensitive to high temperatures (above 150 °C) because of the sensitivity of the polysaccharide components to temperature. High temperature and prolonged exposure have been shown to degrade their mechanical performance due to polysaccharide degradation, water evaporation and differential cell-walls shrinkage [237], [261], [262]. Yang et al. [263] observed the influence of fiber degradation in PLA/wood 3D printed composites where temperature increase from 200 to 230 °C resulted in a 10 % reduction in tensile strength and 5 % reduction in tensile modulus. However, in 3D printing, the filament is only exposed to high temperature for a short period of time due to the cooling of the part after printing. Guessasma et al. [264] noticed a significant cooling of the hemp/PLA printed part during printing. The authors noted a filament temperature close to 180 °C at the nozzle exit and a rapid cooling of the filament (≈ 10 seconds) to 40 °C. The polymer selection must be done accordingly in order to reduce the potential degradation induced on the cell-wall. Hence, most of today's current polymers printed with natural fibers are PLA, [265]–[267], ABS [265], [268], PHA/PLA [269], rPP [256] and PCL [270].

Unlike synthetic fibers, natural fibers have a high CTE and a high coefficient of hygroscopic expansion (CHE) due to their high sensitivity to water and low MFA (Table 2) [226].

	Carbon fiber	Glass fiber	Flax fiber	Polypropylene
Radial thermal expansion coefficient $\alpha_{f,T}$ ($10^{-6}/^{\circ}\text{C}$)	18 [271]	5 [271]	78 [272]	120 [273]
Radial hygroscopic expansion coefficient $\beta_{f,R}$ ($\epsilon/\Delta m$)	-	-	1.14 [274]	-

Table 2 : Thermal and hygroscopic expansion coefficient of different fibers and polymer.

As described by Le Duigou et al. [274], during thermal processing (extrusion or printing process for example), natural fibers shrink due to water desorption with an amplitude greater than thermal expansion. After cooling, the fibers and matrix undergo thermal shrinkage and after storage at 50 % RH, the fibers undergo a significant hygroscopic expansion due to moisture uptake. These steps are schematized in Figure 45. Consequently, changes in moisture content in the material throughout the printing process may be responsible for the state of stress at the fiber/matrix interface.

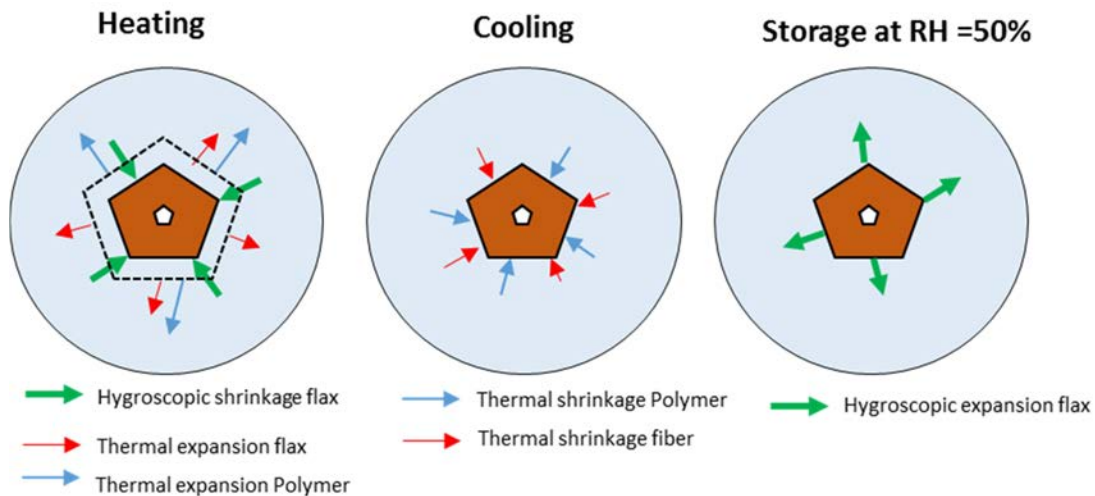


Figure 45 : Principal of residual stress generation at the plant/matrix interface during processing. The thickness of the arrow is proportional to the magnitude of the stress [274].

5.2. Filament production

The first step in 3D printing of natural fibers is the manufacture of the filaments, which plays a major role in the properties of the 3D printed structure (porosities, residual stress, mechanical or hygrothermal degradations). To this end, several works have been devoted to the extrusion of short natural fibers-reinforced filaments based on hemp fibers [266], [275]–[277], hemp hurds [278],

bamboo fibers and powder [279]–[281], coconut fibers [282], cotton fibers [283], wood fibers [265], [269], [284], wood pulp [256], [285], wood flour [286]–[289], Harakeke fibers [266], [275], [277] and waste macadamia nut shell [290]. The main issues concerning the development of a 3D printed natural fibers reinforced filament are porosity content and surface roughness. Tran et al. [270] studied the influence of cocoa shell waste content on filament roughness and noticed an increase in roughness with increasing fiber content (Figure 46).

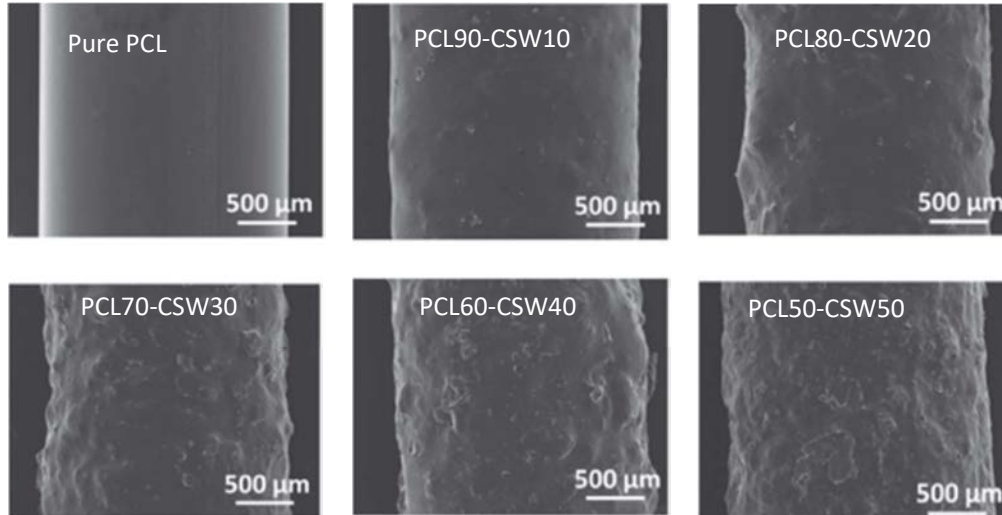


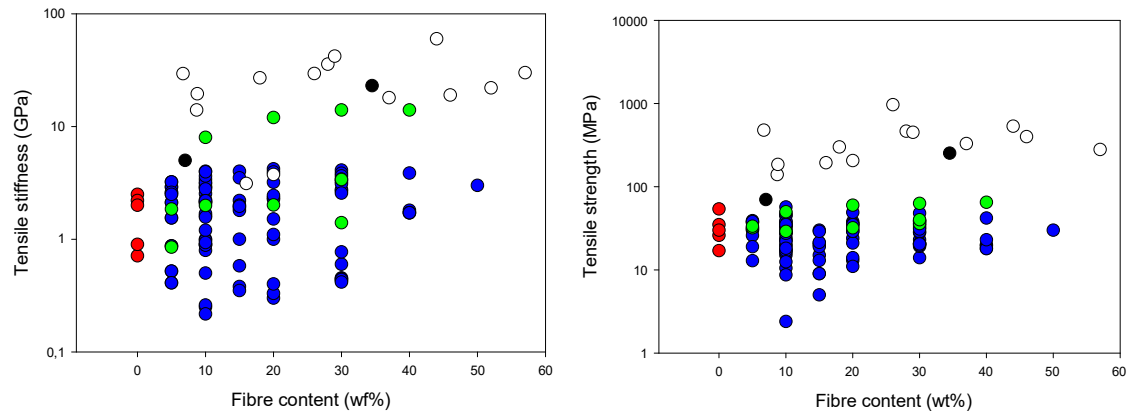
Figure 46 : Evolution of filament roughness with increasing fibers content with PCL/Cocoa shell Waste(CSW) [270].

As has been observed for synthetic fibers, a high fibers content induces greater porosity content and more difficult processability due to the prohibitive high viscosity of the filament. For example, with the addition of 10 % wt. of wood fibers, the porosity content increases to 27.1 % and to 47 % for 20 % of wood fibers [256]. Consequently, the fiber content of 3D printed composites based on natural fibers is between 5 % and 15 % wt.

However, Filgueira et al. [256] and Depuydt et al. [279] managed to produce a printable filament with low porosity (between 0 and 4 %) by modifying the extrusion process. Depuydt et al. applied a vacuum treatment at the end of the metering zone combined with a drying treatment in an air dryer that removed the porosity content.

5.3. 3D printing of natural fiber composites

In the literature data provided for natural fibers-reinforced composites, there is a wide dispersion due to differences in filament formulation (polymer and fiber nature, fiber content), printing and slicing parameters and mechanical tests.



Literature review is summarized in Figure 47.

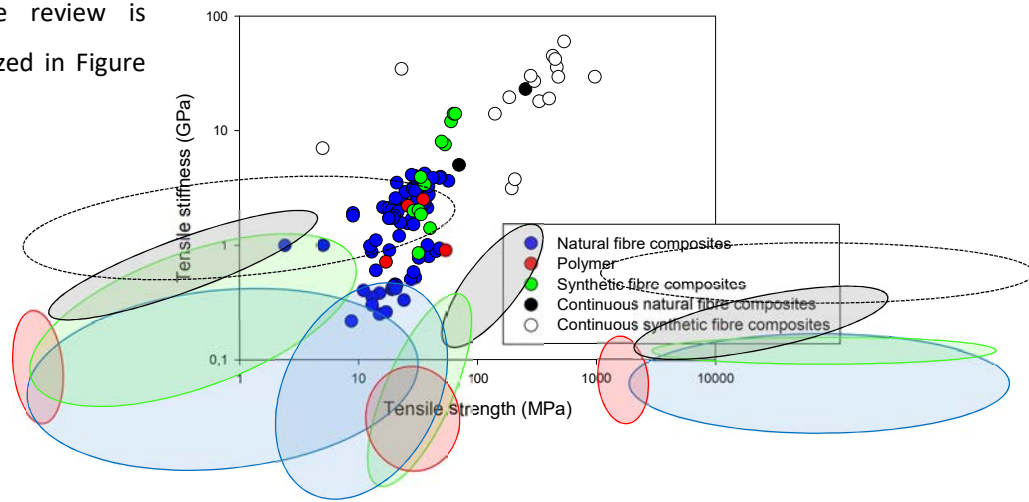


Figure 47 : Literature review on the tensile properties of natural fiber biocomposites manufactured with 3D printing. Stiffness (a) and strength (b) as function of fibers content; (c) Stiffness as a function of strength comparison with pure polymer, between short and continuous natural fiber composites [31], [50], [53], [85], [98], [99], [108], [112], [256], [264]–[266], [269], [270], [275], [277]–[279], [281], [282], [286], [289], [291]–[306].

As noticed for filament, in most studies, the addition of short natural fibers induces a decrease in tensile strength and a slight increase in tensile modulus. Safka et al. [282] have shown that ABS/Coconut biocomposites exhibits a slight increase in tensile modulus (+ 6 %) and a drastic reduction in strength (-50 %) and strain (-15 %) compared to neat ABS. Dong et al. [300] observed a reduction in tensile strength of about 60 %, a reduction in Charpy impact strength of about 55 % and finally a decrease in flexural modulus of about 60 %. Zander et al. [289] found that on PP filled with

10 % of wood flour, the increase in tensile modulus was 60 %, while the addition of cardboard fibers increased the tensile modulus by 20 % compared to pure PP. However, the authors also observed a decrease in tensile strength of about 7 % and 20 % for PP/waste paper fibers and on PP/cardboard fibers. Xiao et al [278] observed a reduction in tensile strength of about 20 % by mixing hemp hurds in a PLA matrix. Finally, Guessasma et al. [264], [303] highlighted a decrease in both stiffness and strength of PLA/Hemp and PLA/wood 3D printed composites compared to pure PLA with a large dispersion attributed to the natural variability of the natural fibers.

Based on the low added-value of short natural fibers, their reinforcing effect for 3D printed samples may be questioned. On the other hand, they are used as filler to reduce the proportion of polymer in order to reduce the price [301] and density [295] of the printing product, to bring a new design aspect (wood aspect, color,...) or to valorize biobased resources and waste.

The moderate mechanical performances of 3D printed natural fibers reinforced composites might be explained by several factors:

- Fiber content is limited to around 40 % wt. (30 % vol.) [50] and most research studies focus on fiber content between 5 and 15 % wt. As the fiber content increases, the viscosity of the filaments increases while the impregnation of the fibers decreases.

- A low length to ratio diameter (L/D) to manage the viscosity of biocomposites. However, due to the diameter of the filament (1.75 mm or 3 mm), natural fibers tend to agglomerate easily. In addition, too low an L/D ratio does not effectively transmit stresses to the fibers [307] and natural fibers tend to act more as stress concentrators than as reinforcements.

- The low mechanical properties of the natural fiber used. Natural fibers have different mechanical properties depending on their microstructure and biochemical composition. While bast fibers such as flax or hemp have high stiffness and strength for semi-structural applications, wood flour or coconut husks have mechanical properties inferior than that of bast fibers and could only be considered as revalued wastes from industry or agriculture.

- The porosity content is higher than fibers-reinforced composites, as shown in Figure 48. As with synthetic fibers, the appearance of porosity is due to the printing process (low compaction pressure, limited interdiffusion between printed beads) and limited impregnation of the fibers.

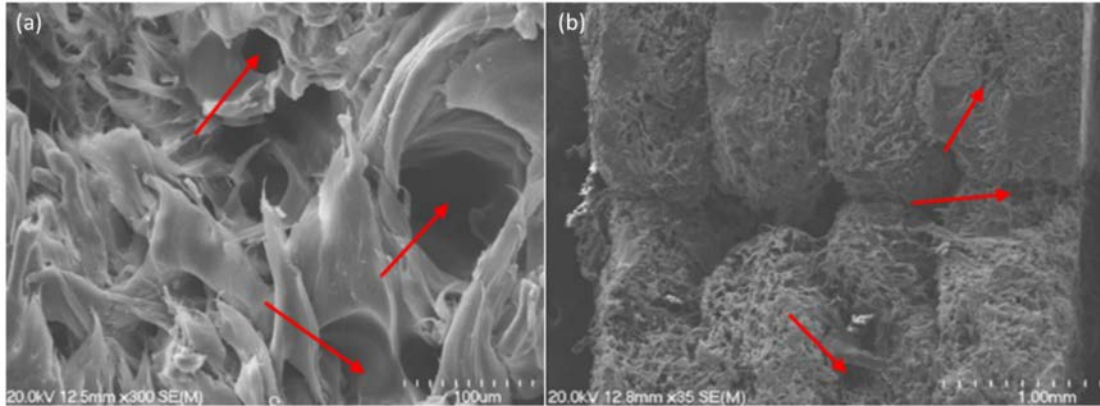


Figure 48 : Fracture surface of polypropylene/flax composites with 10 % wt. (a) and 30 % wt. (b) of short fibers showing excessive porosity and large gaps between printed beads and layers [275].

Consequently, the authors sought to improve the mechanical performance of 3D printed natural biocomposites through several methods. The first is the optimization of printing and slicing parameters that affect bead interdiffusion, fibers impregnation or porosity content. Higher printing temperature and lower layer height lead to better bead interdiffusion and better impregnation of the fibers. These improvements lead to higher mechanical performances [263], [303]. Guessasma et al. suggested that, wood-based biocomposites exhibit stable tensile properties over a range of 210 to 250 °C [303]. Yang et al [308] studied the extrusion temperature in the range of 200-230 °C and showed a slight decrease in tensile modulus (from 1.8 GPa at 200 °C to 1.7 GPa at 230 °C) and flexural modulus (from 1.9 GPa at 200 °C to 1.6 GPa at 230 °C) but an increase in compressive strength and internal bond strength whereas the compressive strength (+ 15.1 %) and internal bond strength (+24.3 %). The higher extrusion temperature showed better compatibility at the fiber/PLA interfaces and good adhesion between the extruded filament segments. Hemp/PLA biocomposites evidenced an increase in performance over the temperature range of 210 to 250 °C [303]. At low printing temperatures, the loss of tensile performance (around 20 %) is explained by a lack of cohesion between filaments.

A higher percentage of infill multiplies the tensile properties while a lower layer thickness leads to a better consolidation of the part and thus to better mechanical performance [304] [305]. Vigneshwaran et al. showed that the tensile strength of 3D printed wood fibers reinforced PLA composites shows a strong increase in tensile performances (tensile strength of 22 MPa and tensile modulus of 188 MPa for 90 % infill, tensile strength of 11 MPa and tensile modulus of 98 MPa for 30 % infill) [304].

5.4. Future outlook on the optimization of 3D printing of natural fiber reinforced composites

A promising strategy to improve the mechanical performance of printed composites has been explored in the literature and aims at printing continuous jute fiber/PLA by impregnating in the nozzle [62] continuous flax fibers/PLA pre-impregnated filaments [226]. Figure 49 shows the image of continuous jute fiber reinforced composites (Figure 49.a) and its fractured zone (Figure 49.b) and the fractured zone of flax (Figure 49.c) fiber reinforced 3D printed composites. The fracture zone of jute/PLA highlights incomplete wetting with a multiscale breakage (fracture of both coating matrix and jute fiber) while flax/PLA shows a mode of rupture typical of 3D-printed continuous fiber reinforced composites [67] with fibers breakage, matrix shear-rupture and transverse crack propagation.

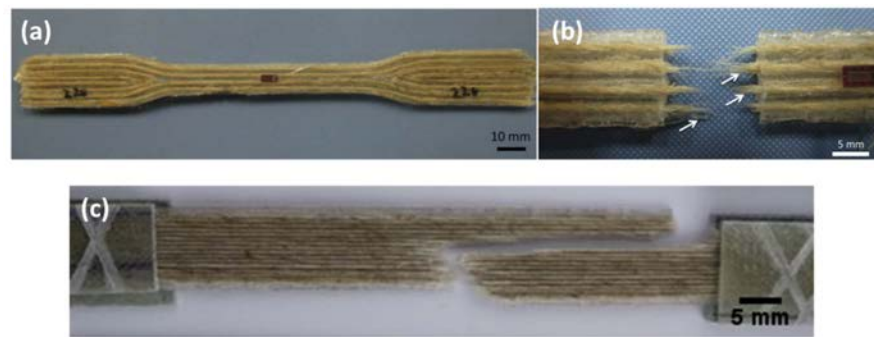


Figure 49 : Continuous jute fibers/PLA sample with in-nozzle impregnation (a) and fracture analysis (b). Continuous flax fibers/PLA printed samples with coated filament and fracture analysis (c) [62], [226].

Regarding mechanical performance, Matsuzaki et al. [62] studied PLA filled with 6 % vol. of continuous jute fiber and achieved a stiffness of 5.11 ± 0.41 GPa and a strength of 57.1 ± 5.33 MPa. Meanwhile, Le Duigou et al. [226] printed PLA reinforced with 30 % vol. of continuous flax fibers and measured a remarkable stiffness of 23.3 ± 1.8 GPa and a strength of 253.7 ± 15 MPa. The strong differences between these studies can be explained by a lower density of 68 Tex (g/km) for flax yarn and 500 Tex for jute yarn, which ensures a homogeneous distribution of the reinforcement in the composite and promotes a better impregnation of the fibers. Moreover, flax fibers have higher tensile properties than jute fibers (between 46 and 85 GPa for flax fibers and between 24.7 and 26.5 GPa for jute fibers [227], [228]) and a higher fiber content leads to superior mechanical performance. Finally, in comparison to 3D printed synthetic fibers-reinforced composites, flax fiber reinforced counterparts have lower stiffness and strength than to continuous carbon fibers [90], [98]. However,

their mechanical performances are in the same range as those of glass fibers-reinforced composites [108]. Consequently, application to semi-structural or structural applications where glass fibers reinforced composites are used can be achieved with lower density natural fibers reinforced composites.

Future strategies to reach higher performance for 3D printed biocomposites based on continuous natural fibers shall be realized at the material scale with the production of an optimized filament using a low twist, low linear weight yarn, as developed by Baets et al. [309]. The authors have shown that the performance of the composites decrease when the yarn is subjected to strong twisting due to a lack of fiber impregnation combined with fibers mis-orientation with respect to the load under mechanical solicitation. Commingled natural fibers/polymer yarn is also an interesting alternative to improve fiber impregnation during filament production and to facilitate printability. Finally, the selection of natural fibers is a very important factor to print high performance biocomposites based on natural fibers. The development of hybrid fibers formulations (natural and synthetic fibers) combined with the tailoring of fiber selection could make it possible to target structural or semi-structural applications.

Another way to improve the performance of 3D printed biocomposites is directly linked to the printing process with the development of customized and cost-effective processing devices. Recently, Zhao et al. [20] developed large-scale 3D printing of wood/PLA (Figure 50). This process achieves a high deposition rate (50 kg/h) as well as a high building volume ($\approx 27 \text{ m}^3$), thus reducing processing time and cost. To print parts with more intricate shapes, the authors have investigated the use of 6-axis printing configurations thanks to the AFP robot arm [310]. However, this process requires significant costs and may require additional steps (thermocompression) to reach structural mechanical performance.

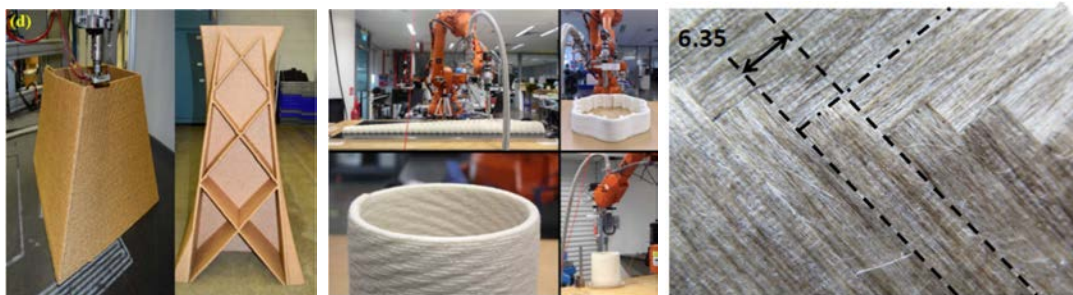


Figure 50 : Large scale printing process with poplar/PLA composite (a); chitosan/wood flour/cellulose composites (b,c). Adapted from [20], [310].

However, the use of the 6 degrees of freedom allows better control of the trajectory of the printed beads and thus precise monitoring of the microstructure and shape of the composites. These abilities should lead to opportunities to develop high-performance biocomposites produced using an automated process. For example, Baley et al. [310] developed a 37 % vol. PP/Flax biocomposite made by AFP, followed by thermal compression, with a tensile modulus (E_1) of 28.9 ± 1.9 MPa and a tensile strength of 183 ± 8 MPa. These values are similar to those of thermocompressed biocomposites but with the ability to accurately control the orientation and fraction of fibers, the lay-up thickness and the overall architecture.

5.5. 4D printing of natural fiber reinforced composites

As described in section 5.1, natural fibers are sensitive to moisture due to their chemical composition, which is one of their main drawbacks for structural applications, according to the majority of the literature [246]. However, their sensitivity to moisture also offers a promising way to develop the hygroscopically induced morphing, i.e. hygromorphing. This actuation mechanism is widely found in natural architectures such as pine cones (microstructure detailed in Figure 51) [175], [176], wheat awns [208] and other seed dispersal mechanisms [178].

Their architecture is based on a hierarchical bilayer microstructure where each tissue is composed of anisotropic fibers with different hygroscopic expansion properties. The hygroscopic mismatch between the layers of the natural actuator leads to an out-of-plane bending and thus to the release of seeds. Based on these observations, this natural mechanism is transferred to natural fibers composites to mimic this actuation functionality. Because natural fibers swell anisotropically when exposed to moisture, the use of an asymmetrical architecture allows to reproduce the mismatch in hygroscopic strain and induces actuation.

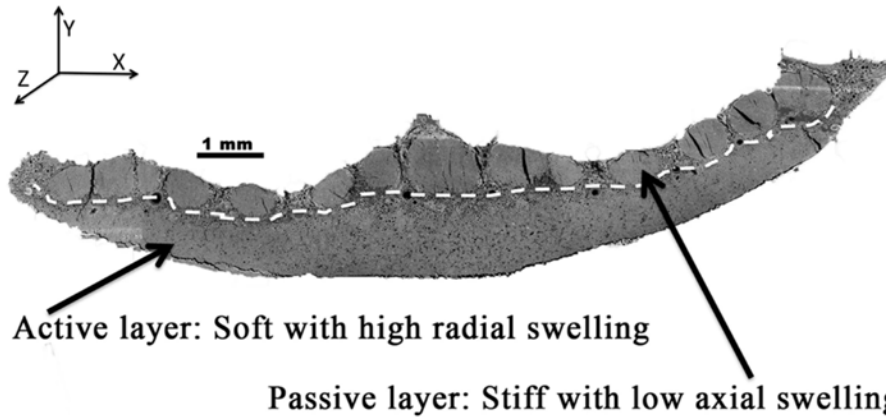


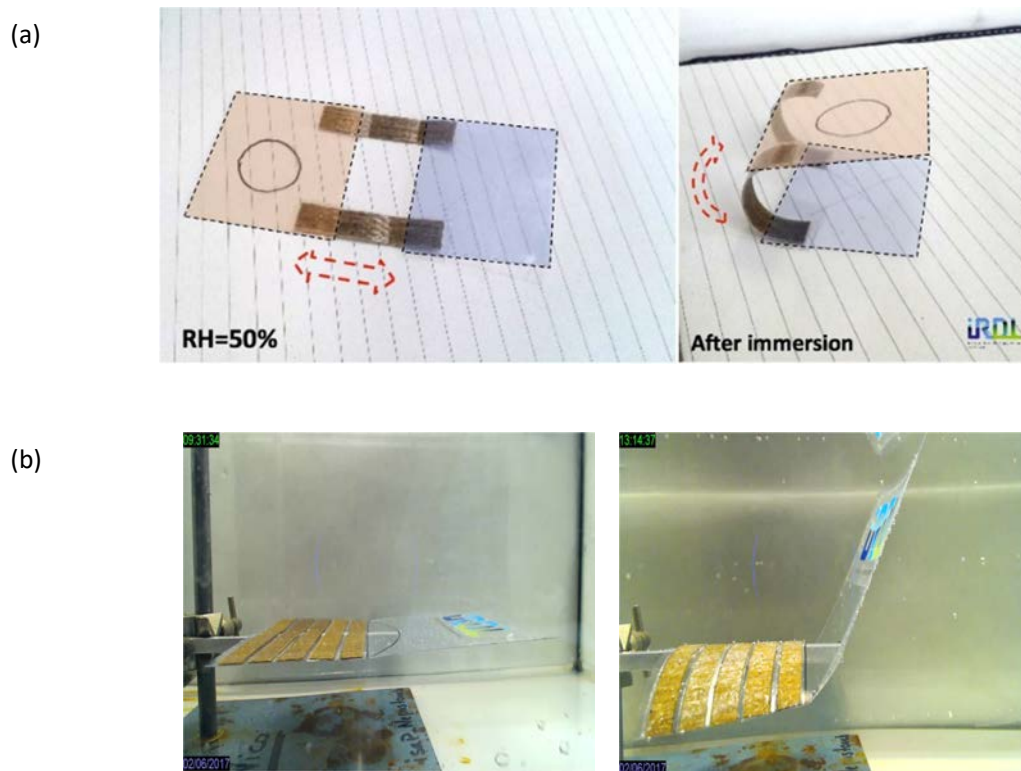
Figure 51 : Cross-section image of a pine cone scale highlighting a bilayer structure. Pine cone scale is composed of one passive layer of sclerenchyma fibers which provide stiffness (around 35 %) and one active layer of sclerids that provide strain (around 65 %). Hygroscopic swelling gradient between these layers force the scale to bend when it is exposed to dry environment [176].

Hygromorphic composites are inspired by biological structures such as the pine cone. The actuation of the pine cone is based on an anisotropic bilayer microstructure composed of anisotropic sclerenchyma fibers and sclerides. These fibers are organized in concentric cell-walls [175], [176]. The secondary cell-wall is composed of stiff cellulose microfibrils embedded in a hygroscopic hemicellulose/pectin matrix. The macroscale bilayer configuration of the pine cone scale results in a gradient of hygroexpansion between the two layers that forces the structure to bend when exposed to various humid environment. Similarly, in hygromorphic biocomposites, differential hygroscopic swelling is targeted to provide actuation bending. Several works have been performed on wood fibers [163], [312]–[315], spores [316], [317]) and natural fibers (flax, jute, coir, kenaf) reinforced polymer biocomposites named hygromorphic biocomposites [175], [176], [318], [319].

Hygromorphic biocomposites are a new approach that uses natural fibers and takes advantage of their sensitivity to moisture to trigger a natural reversible and autonomous actuation triggered by combining moisture and temperature gradient with significant strain or forces [176]. Their bilayer microstructure allows to control their responsiveness thanks to the swelling coefficient, the moisture content/moisture gradient and the structure stiffness of the thickness ratio of each layer [177], [320]. Moreover, their actuation potential can be directly controlled by the microstructure of the fibers (MFA and lumen size) as well as by their biochemical composition. Currently, most work on hygromorphic biocomposites used composites elaborated by thermocompression which yield to an initial flat geometry. The thermoplastic matrix allows hygromorphic biocomposites to be easily

thermoformed, allowing the structure to achieve complex shapes. Finally, at the end of their life, these materials are recyclable and potentially compostable.

Hygromorphic biocomposites have various potential applications as a deployable system or as actuators such as active hinges (Figure 52.a) that connect two rigid panels. Figure 61.a presents the evolution of a hinge-type Origami prototype in which a hygromorphic biocomposites is used as the active hinge and a PLA polymer is used as the passive facets before and after immersion in water. Hinge-less rectangular sheets with a curved crease pattern could yield a specific folding and create a 3D shape [321]. The two elements of the sheets are constrained by each other due to the curved line. Thus, a small uniaxial bending will force the thin shell element to bend with a reverse curvature. The exploitation of the anisotropic behavior of the HBCs and their placement on the backbone element during the planar state the generation of a continuous bending of this element during sorption (Figure 52.b, RH = 50 %). The forces and the moment are therefore transmitted through the crease to the adjacent face and trigger autonomous self-snapping. Smart materials are widely used in Kirigami structures to develop self-deploying structures as shown in Figure 52.c [322]–[324]. In this Figure, laser-cut hygromorphic biocomposites with different patterns provide flexural responses from a planar biocomposite sheet.



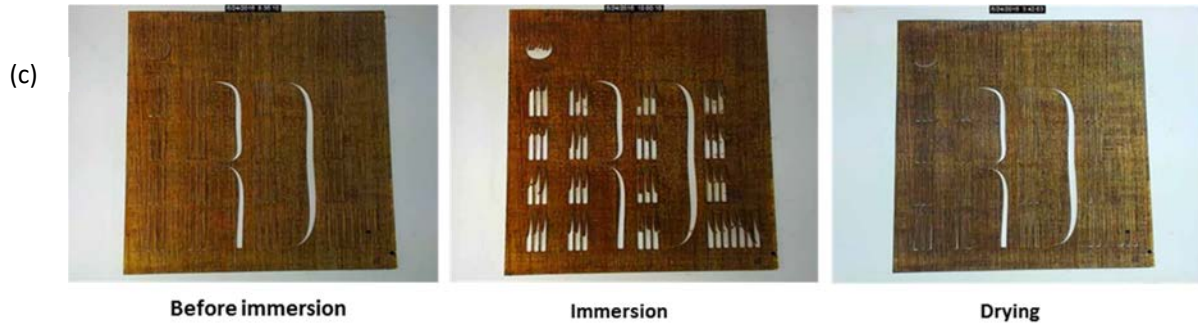


Figure 52 : Example of Hygromorphic BioComposites used as : a hinge type origami [319] (a) and a simple deployable structure based on curved line fold [319] (b), Kirigami design for HBCs: IRDL laboratory cut patterns [319].

In this context, 3D and 4D printing of hygromorphic biocomposites could be envisaged to precisely control hygromorphic architectures and therefore their actuation behavior. Actuation in 4D printed hygromorphic biocomposites follows two strategies: single-material printing (Figure 53.a,b,c) and multi-material printing (Figure 53.d,e,f).

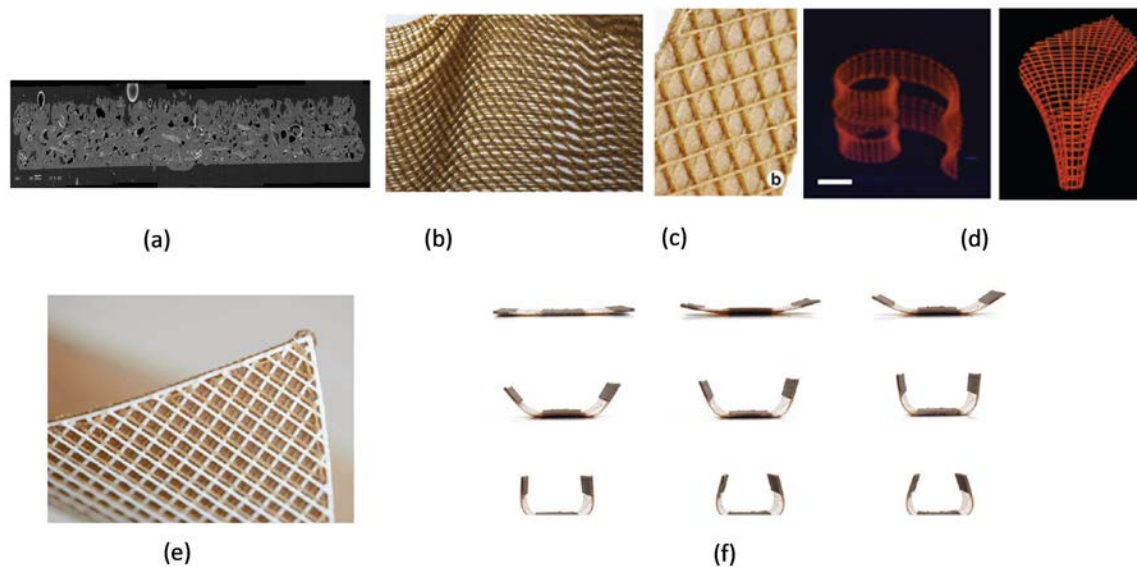


Figure 53 : Examples of 3D printed hygromorphic biocomposites architectures for monomaterial methodology (a-d) and multi-material methodology (e-f) [207], [216].

The monomaterial approach is based on the anisotropy of the material induced by the orientation of the fibers in the filament and the printing process. It assumes that the same printed material will have different mechanical properties and different coefficients of hygroscopic expansion in different directions. Generally, the stacking sequence follows an asymmetrical lay-up, i.e. a bilayer

microstructure. There are several ways to introduce an anisotropic swelling into the structure, such as the anisotropy of the fibers orientation in the bilayer, the porosity content, the number of printed layer and their thickness, the order in which the active and passive layers are printed and the Length/Width ratio [207], [216], [269]. $[0^\circ/90^\circ]$ and $[45^\circ/-45^\circ]$ stacking induce bending and twisting actuation, respectively [217].

The porosity content also plays a major role in the actuation of hygromorphs. Le Duigou et al. [269] investigated the amplitude and speed of the curvature as a function of different extrusion rates (100 %, 200 %, 300 %) which dictate filament overlap and, consequently, the porosity content (Figure 54).

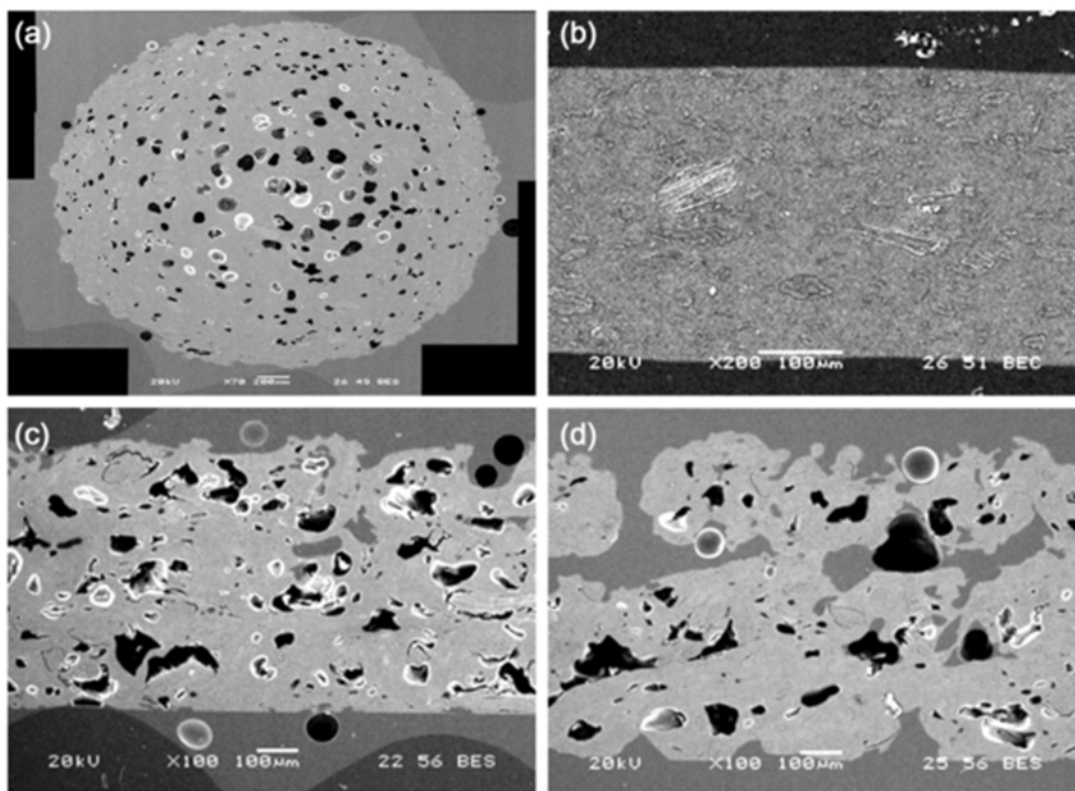


Figure 54 : Scanning electron microscopy observation of a raw filament (a), compressed printed samples (b) and samples printed with 100 % (c) and 200 % (d) extrusion rate leading to a raising of porosity content [269].

When the filaments overlap less, the porosity content increases from 14.7 % to 15.5 % and 21.8 % for 0° orientations. Porosity is reduced for samples printed at 90° with porosity content of 8.4 %, 11.1 %, 14 %. They noticed higher and faster water uptake at higher porosity content, resulting in faster actuation but with lower responsiveness (amplitude). The degradation of the bending amplitude with a low filament overlap (large interfilament distance) evidenced the role of interbead and interlayer

bond strength on the actuation mechanism. A study has also underlined the effect of fiber/matrix interface bond strength on actuation reliability of thermocompressed PP/Flax [318].

The porosity network has a considerable influence on the diffusion of water but, on the other hand, it reduces the hygroscopic strain and decreases the properties of composite material. The optimized answer is in Nature. Biological actuators such as pine cones, wheat awns and wild carrots [176], [314], [325] present hierarchically porous structures consisting of micropores (lumen) and nanopores located in the cell-wall that trigger water diffusion by capillary effect [326].

In these structures, the porosity network acts as a moisture diffusion pathway rather than a mechanical defect [319]. The work of Vailati et al. [327] pointed out that higher water sorption and greater responsiveness were reached when a diffusion path along the direction of the fibers was milled. For their part, Le Duigou et al. [319] studied the role of natural fibers on moisture uptake and hygroscopic swelling as a function of their internal porosity. The authors investigated flax, jute, kenaf and coir fibers with internal porosity of 0.10 ± 0.02 %, 6.40 ± 0.17 %, 13.80 ± 0.23 % and 39.10 ± 0.70 %, respectively. They observed faster moisture uptake at higher porosity content, but hygroscopic swelling is more influenced by the biochemical composition and the angle of the microfibril; hence pectin-rich fibers such as flax fibers therefore swells faster.

Interestingly, the content and distribution of porosity can be controlled by 4D printing parameters such as layer height, raster orientation and infill percentage. In the latter structures, filament spacing and surface-to-volume ratio play an important role. Gladman et al. [207] showed that water diffusion is promoted by increased filament spacing due to increased surface-to-volume ratio and increased porosity. The same observation was made by Vazquez et al. [328] who improved the reactivity and responsiveness of the wood/biopolymer hygromorph by increasing the distance between the printed beads from 1 to 1.5mm.

Another 4D design principle is based on multimaterial printing with a highly hygroscopic material and another material that is not sensitive. The design of the structure is also based on the bilayer lay-up, with particular attention to the interlaminar zone where the compatibility between the two materials must be good enough to avoid delamination [168]. In these structures, the hygroscopic material is oriented in a direction perpendicular to the desired angle of expansion while the inert material is printed parallel to the angle of expansion [207]. Moreover, the use of an inert polymer makes it possible to generate a high hygroscopic swelling gradient with high actuation amplitude and speed control [204].

5.6. Future outlook on the optimization of 4D printing hygromorphic (bio)composites

One of the next steps in 4D printing of natural fiber composites must first address the issue of materials, with a rigorous selection of materials. Hygrosensitive polymers (hydrogels, PA6,...) should also be used to achieve higher mechanical properties than hydrogel, while a low melting temperature polymer could avoid the thermal degradation of the natural fibers during the process. Finally, the low viscosity of the polymer could promote fibers impregnation and adhesion, which reduces the amount of porosity and degradation of the actuator over its lifetime. Then, the nature of the fiber (biochemical composition and microstructure) must be taken as a design parameter [319]. The volume fraction of the fibers must be optimized to promote the reactivity and responsiveness of hygromorphic composites. However, as already seen, the volume fibers content is limited to 30 % by the 3D printing process. As observed in section 3.2, the elaboration of 3D printed composites allows the introduction of a higher fibers content (50 % vol.) and is a promising alternative for 4D printed actuators.

Finally, the printing path. Correa et al [329] designed a wood-based composites with a double curvature through a paraboloid pattern. Wood-based composites are printed at 90° from the main axis to the center of the specimen and the angle changes to 10° for the lateral section. The representation of this wood-based hygromorphic composite is shown in Figure 55.

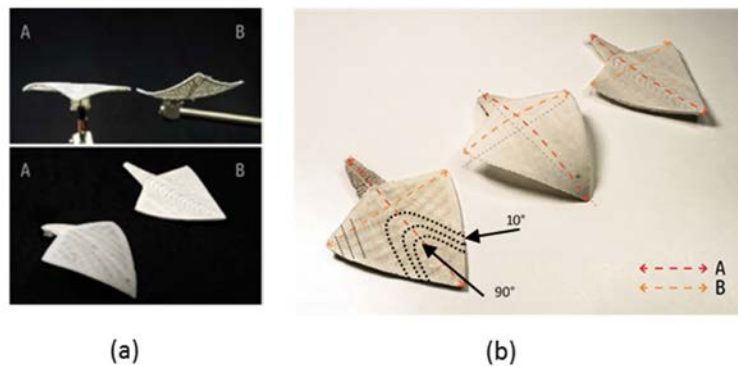


Figure 55 : Three viewing perspectives of wood fibers composite- responsive flap under various RH (a) and evidence of localized print path within the sample to induce a double curvature and multistep actuation (b) [329].

Further improvements are possible with regard to structural design with geometric amplification of the response. With 4D printing it is possible to achieve very complex structures such as

metamaterials. Metamaterials are structures whose properties are not found in nature due to their cellular architecture and their chemical composition [330]. For example, auxetic structures are programmable materials that have negative Poisson's ratio, which shows the advantage of shrinking or expanding in the transverse direction when deformed in compression or in tension, respectively (Figure 56) [331].

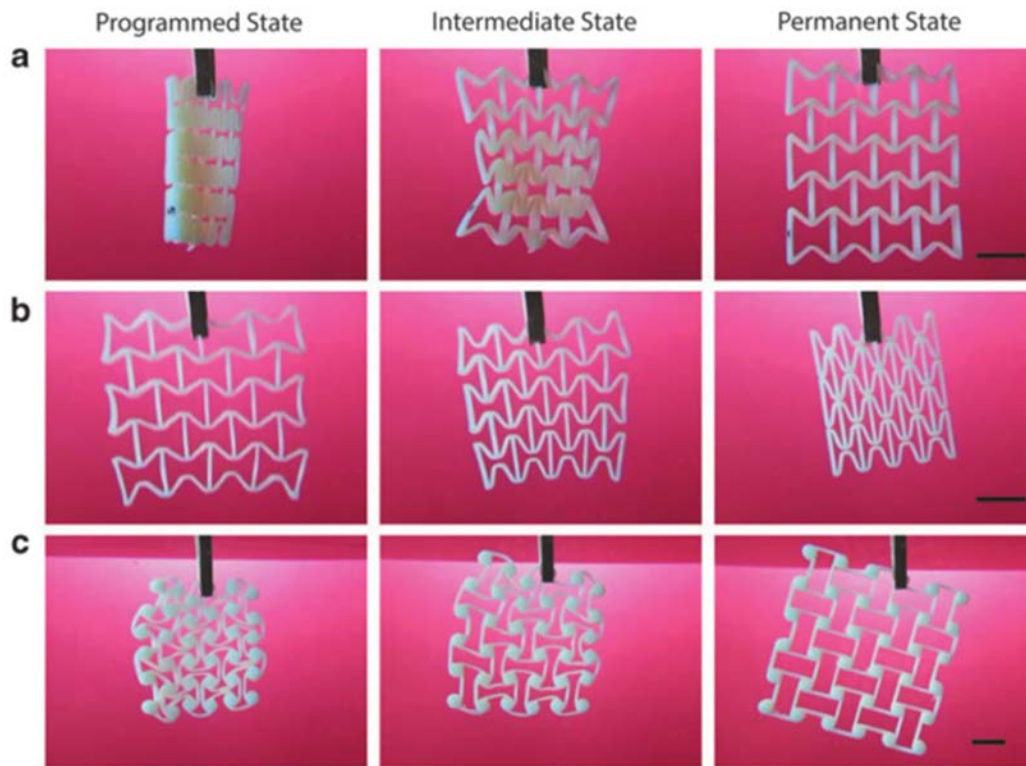
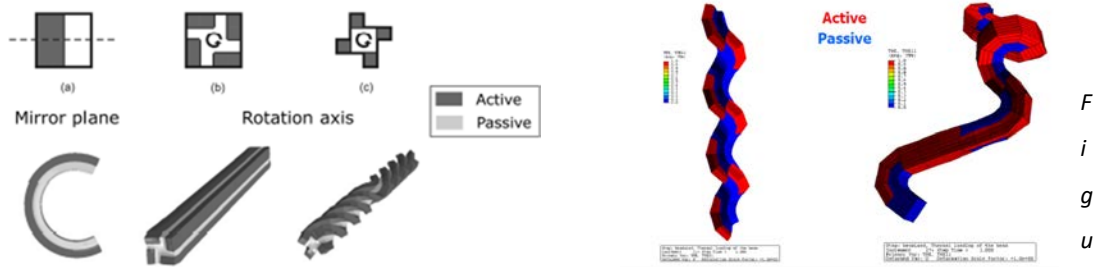


Figure 56 : Shape transformation of active structures printed with shape memory polymer, i.e. VeroWhite Plus RGD835. Structures are first stretched in water at 80 °C and programmed shape is fixed by cooling in a water bath at 5 °C (programmed state, left column). Return to original state is trigger thanks to an immersion in water at 80 °C (intermediate state and permanent state, middle and right column). Active auxetic structures: reentrant honeycomb expansion (a), reentrant honeycomb shrinkage (b), anti-tetrachiral honeycomb expansion (c). Scale bars represent 10mm. [331].

Turcaud et al. [332] have developed theoretical bending and twisting actuators based on architectural actuators by controlling the symmetry and distribution of hygromorphic materials in their initial geometry. Figure 57.a shows an extrudable cross-section with different patterns of actuation provided by the simulation with distribution of active and passive ingredients. Figure 57.b show the effect of material distribution on the control of the actuation of a slender beam.



re 57 : Simulated actuation patterns for several cross-sections with passive/active area ratio of 50:50 (left). Helical bending obtained by rotating the bending plane along the rod thanks to distribution of passive (grey) and active (white) regions [332].

Combined with rigid and inert materials, the 3D printed hygromorph can be placed to act as compliant system, i.e. hinges allowing to imagine a complex origami-like folding. Actually, the hinge can act as a fold (Figure 63.a). The use of the bilayer microstructure with multimaterial printing (nylon and wood biocomposites) on a dedicated area with a constant thickness ratio ($t_p/t_o = 1.5$) and variable width (9.5-27mm) (Figure 58) enabled to amplify the responsiveness from 98 to 161° due to a higher bending moment [216].

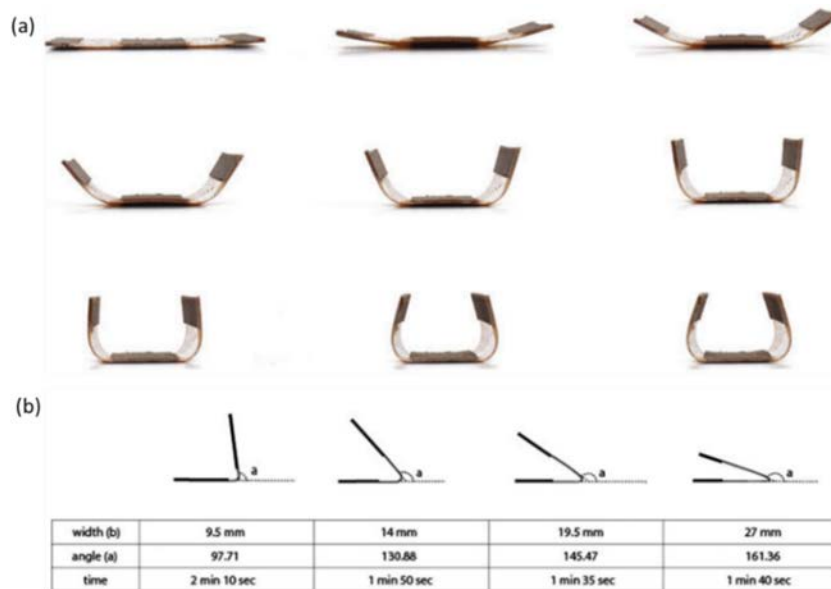


Figure 58 : A series of photographs showing a multimaterial printed wood composites composed of active hinges and rigid panels that self-transform into a flat sheet into a folded structure (a). Data table and section drawings with various hinges width b that lead

to various folded angle (from 98° to 161°) after being exposed to moisture (full water submersion at 20-25°C) (b) [207].

Kirigami 4D printed structures has also been used to improve the actuation of multi-material structures [333]. Multi-material 3D printing was used with the inclusion of swellable polyvinyl in stiff polyurethane resins cell-wall. In this case, isopropanol solvent-induced isotropic changes of the highly swellable material solvent resulted in an anisotropic volume change (+50 %) of the custom-designed cell. The periodic hierarchical microstructure allows anisotropic deformation of individual cells, resulting in unidirectional expansion/contraction of the cellular structure (Figure 59). The thickness of the cell wall, the rigidity ratio between the cell wall and the inclusion and topology modulated the responsiveness [334].

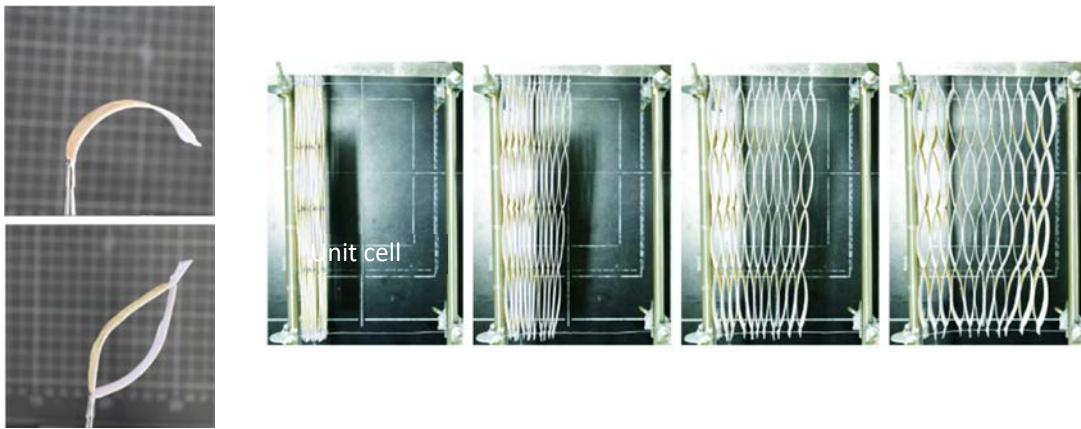


Figure 59 : Actuated Wood/paper bilayer and single unit cell (a), actuation of the bilayer cell concept from 0, 2, 4 and 16 hours at 95 % RH (b) [315].

6. Bibliography summary

3D/4D printing, e.g. based on Fused Filament Fabrication (FFF), is a disruptive technology that aims to produce final parts with complex shapes in a few steps and without any additional tools, thus reducing process cost and material waste. The addition of discontinuous fibers is intended to improve the mechanical performance of 3D printed parts and to provide greater dimensional stability, making it possible to print larger parts through Big Area Additive Manufacturing (BAAM). However, the mechanical performance of short fiber reinforced composites is not high enough for structural applications because the fiber content is limited by the printing process. As a result, 3D printing of continuous fiber composites has started to emerge.

The additive manufacturing of continuous fiber composites is widely used in the industry thanks to Automated Fibers Placement (AFP) or Automated Tape Laying (ATL). However, these techniques require very expensive equipment and do not allow the production of small parts due to a minimum tape length of 100 mm and geometrical constraints (radius of curvature). The 3D printing of continuous fiber composites is therefore a complementary technology to the latter and allows the manufacture of small parts for structural applications with potential applications in maintenance or prototyping. The identified authors of this topic in the literature have investigated the mechanical and microstructural properties of 3D-printed continuous fibers composites and have highlighted disadvantages such as high porosity content, low interfacial adhesion between the fibers and the matrix due to the lack of normal pressure during the printing process. Consequently, the mechanical properties are lower than those of conventionally manufactured composites. However, research teams have been working to improve the 3D printing process and have sought to develop high-performance printed parts with low internal porosity.

Currently, additional knowledge is needed to expand their potential in structural applications, especially for outdoor applications subject to moisture and temperature. **For these reasons, the relationship between printed-related microstructure and its properties with respect to temperature and humidity variation should be investigated (Chapter 3).**

In addition, in the context of marine engineering aimed at reducing maintenance in severe environment, the evolution of mechanical properties with the seawater environment is important but still lacking. Here **again, the relationship between the microstructure of the prints and their properties with respect to aging time needs to be investigated (Chapter 3).**

Beyond structural performance requirements, industry needs multi-functional materials, and 4D printing can be part of the answer. Research in 4D printing focuses primarily on thermally actuated shape memory polymers (SMPs) and hydrogels that are actuated by moisture variation. SMP materials have a controllable actuation with a high amplitude but require programming steps whereas hydrogels can be actuated directly after printing with a higher actuation amplitude than thermal actuators. However, hydrogels have poor mechanical performance in wet environments, which restrains their application outdoors. Moreover, actuation is dependent on external humidity conditions which are impossible to control and result in a slow response.

The development of 4D printed composites with shape-change and multiple stimuli should be done with the aim of physically controlling the moisture content within the material and *in fine* the actuation. Continuous fibers composites, their microstructure and related properties should be jointly investigated to expand the range of structural actuators (Chapter 4).

Natural fibers are now well established as a relevant reinforcement in composites because of their mechanical properties combined with their low density compared to glass fibers. They also have a moderate environmental impact and a cleaner end-of-life management. Thus, natural fiber biocomposites are increasingly being used in 3D printing but their mechanical properties are moderate due to insufficient fiber content, low L/d ratio, fiber type and porosity. To overcome these drawbacks, **further research should be conducted on high-performance printed biocomposites made from continuous natural fibers. In this respect, novel filaments should be produced and printability should be investigated. The latter concerns the influence of printing parameters such as layer height and interfilament distance on mechanical performance and actuation performance (Chapter 5).**

Moisture is one of the main disadvantages of natural fiber composite. Thanks to the paradigm of biomimicry, it is possible to transform this drawback into a novel functionality: moisture-induced morphing actuators or hygromorphic biocomposites. Their microstructure is inspired by that of hydraulic actuators such as pine cone scale. The differential hygroexpansion between the layers induced the curvature. Basically manufactured by thermocompression, **4D-printed hygromorphic biocomposites actuators will be designed, printed and tested to introduce new range of smart compliant mechanisms (Chapter 6).**

Chapter 2: Materials and Methods

The purpose of this chapter is to present and summarize the different materials and experimental methods used throughout the manuscript on 3D and 4D printing of continuous fiber-reinforced composites for structural applications and morphing structures.

The first part focuses on the description of continuous fiber filament materials, then manufacturing techniques are explained in a second part with emphasis on the production of flax/Biopolymer filaments.

Thirdly, the mechanical characterization and microstructural analysis of 3D printed composites are described.

Fourth, the hygroscopic and seawater aging conditions are described with related characterizations such as measurement of sorption and hygroexpansion.

The fifth section is based on the design, manufacture and characterization of hygromorphic biocomposites and electro-thermo-hygromorphic actuation of 4D printed continuous-carbon fiber and flax composites actuators.

The last section focuses on thermal characterization.

1. Material selection

1.1. Synthetic continuous fiber reinforced composites

Filaments, consisting of multiple strands of carbon or glass fibers coated with a polyamide matrix, are provided by Markforged®. Two filament spools are available during printing, i.e. one of neat PA6 filament and one of continuous carbon or glass fibers reinforced PA filament. The DSC analysis shows that the continuous glass fibers have been coated with PA6 while the polyamide used in the continuous carbon fiber reinforced filament is identified as a poly hexamethylene isophthalamide (PA6-I). In the following manuscript, we refer to the continuous carbon and glass fibers reinforced PA filaments (or printed composites) as cCF/PA6-I and cGF/PA6, respectively. The filaments supplied by Markforged® have a preset fixed fiber volume fraction measured by thermogravimetric analysis (TGA) (35 % vol. for carbon filaments and 39 % vol. for glass filaments). Filament diameters are $379.8 \pm 10.5 \mu\text{m}$ and $332.0 \pm 23.2 \mu\text{m}$ for cCF/PA6-I and cGF/PA6, respectively.

1.2. Flax continuous fiber reinforced biopolymer composites

Continuous flax yarns were provided by Safilin. The selected yarn was twisted (320 tpm) with a linear weight of 68 TEX (g/km). Polylactic acid Ingeo™ Biopolymer 3260HP (PLA) provided by NatureWorks® was used with the following rheological properties: MFR = 65 g/10min at 210 °C. Polybutylene succinate (PBS) Bionolle™ 3001 MD was used with the following rheological properties: MFR = 1.4 g/10min at 190 °C.

Continuous fiber coating was the process employed to make filaments with continuous fibers by extrusion coating. Flax fibers-reinforced Continuous filaments were manufactured thanks to a co-extrusion process. This process is schematized in Figure 60 :

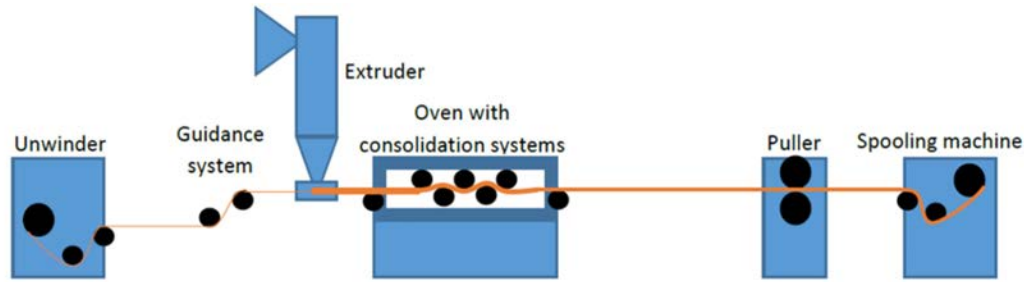


Figure 60 : Schematic representation of co-extrusion line used to developed the flax /biopolymer filaments.

Continuous flax yarn spool was placed on an unwinder and the yarn was brought to the extruder by means of a guiding system. This system was composed of a tensioner, guides and a furnace (heated at 125 °C) which aimed to remove residual water in the flax yarn prior to extrusion. Yarn was brought to the extruder head where melted biopolymer came to flax yarn with an angle of 45°. Before the process, PLA and PBS was stored at 60 °C under dry atmosphere to in order to remove water. The filament was then conformed by the extruder die (diameter = 0.6 mm). The coated filament was fed into a consolidation system made of 7 wheels of 20 mm diameter and heated in an oven. Finally, the filament was pulled to a winding machine where it was packed. A detailed experience plan has been done to optimize the quality of the filament. The results are presented in the section 1.1 of Chapter 5.

2. Manufacturing by 3D printing

2.1. Synthetic continuous fiber composites

The 3D printed used in this study is a MarkTwo® 3D printed provided by Markforged® (Figure 61) composed of a dual-nozzle extruder able to print pure polyamide (PA6) and continuous fibers (carbon, glass or Kevlar®) coated with polyamide matrix. MarkTwo® is driven by a web interface (Eiger.io) developed by Markforged®. Several printing parameters such nozzles temperatures, printing speed, layer height and extrusion feed rate are set by Markforged® and cannot be modified. Moreover, build plate is not heated and envelope temperature of 3D printed is not controlled.

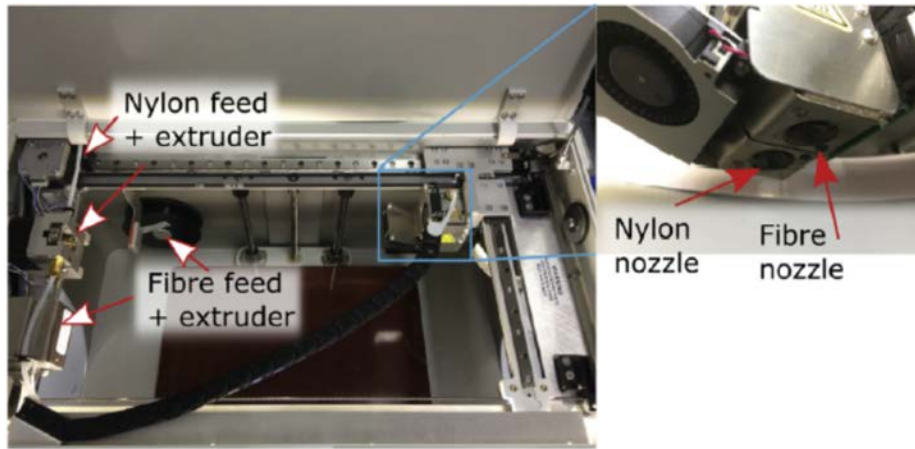


Figure 61 : Photography of Markforged® 3D printed showing PA6 extruder and continuous fibers extruder (left) with a focus on dual nozzle head (right) [19].

Note that a pure polyamide layer is always deposited on the bottom and on the top of each sample to avoid dismantling the part during printing [98], as well as the perimeter of each printed layer. This gangue-like coating is referred to as “Roof & floor layers” and “wall layers” and represents the number of layers deposited on the top, on the bottom and on the edge, respectively (Figure 62). The following printing parameters were used to prepare a rectangular specimen. The fill pattern is selected as rectangular, with a fill density of 100 %. To maximize the fiber volume fraction, “Roof & floor” layers as well as “wall” contour were set at 1.

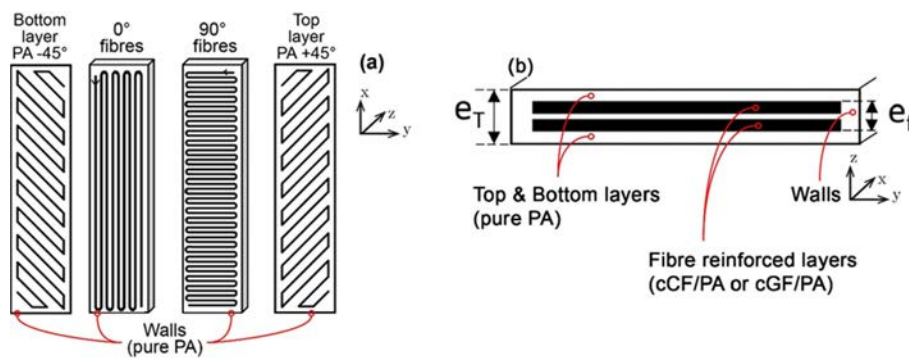


Figure 62 : Schematic views of (a) a continuous fiber reinforced printed part in (x, y, z) coordinate system, and (b) cross-section illustrating ‘Top & Bottom’ as well as reinforced layer sequence (e_T represents the total thickness and e_f the fiber reinforced layer thickness).

The printing speed of fiber filament is estimated around 14 mm/s. This speed is slow regarding other FFF 3D printed but for 3D printing of continuous fiber composite, printing speed has to be slow enough to avoid bead-pull out from the plate. Furthermore, a slow printing speed induce a slower

cooling which promote interdiffusion between printed beads and enhance transverse and interlaminar properties of printed parts. The thickness of the continuous carbon, glass fiber printed layers and pure PA-6 were set at 0.125, 0.1 and 0.2mm, respectively.

2.2. Printing of continuous flax fiber reinforced composites

Currently, the Markforged® MarkTwo® printer does not accept customized materials, while the ability to change its settings is also limited. Thus, the development of the original filament has to be done in conjunction with the development of the printer. Thus, a Prusa® MK3S printer has been modified to enable printing of continuous flax fiber composites (Figure 63).

First of all, the printer nozzle was replaced by a Markforged® flat-head nozzle with an aperture diameter of about 1.4 mm. The purpose of the flat-head nozzle is to drive and compress the filament during the process. To control the cooling rate and improve printing accuracy, a second fan cooling device is settled near to the nozzle. However, the second fan was not activated when printing the first layer in orders to ensure good adhesion between the heated bed and the printed bead. A preliminary Z-calibration was carried out before printing using a sheet of paper (thickness = 100 μm). The printer was controlled by the Pronterface® software.

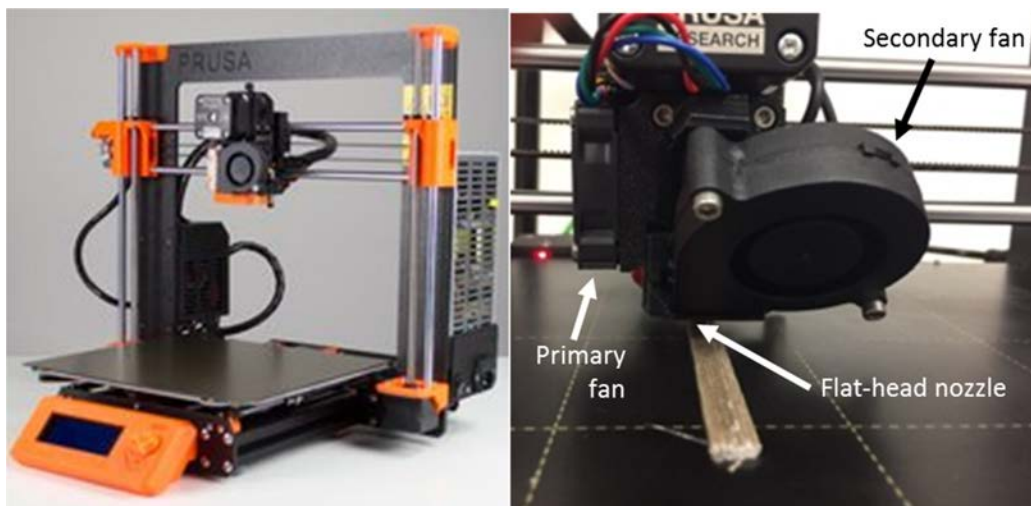


Figure 63 : Photography of Prusa® MK3S 3D Printer (left) with a focus on modified printing head (right).

The printing speed was set to 6 mm/s. In order to accelerate the deposition speed, bead pull-out occurs at the edge of the part. The selected printing parameters are shown in Table 3.

Table 3 : Printing parameters used for continuous flax/PLA composites.

Process parameter	PLA	PBS
<i>Set parameters</i>		
Nozzle temperature (°C)	195	135
Bed temperature (°C)	60	Ambient
Infill (%)	100	100
Second fan cooling rate (%)	0 (First layer) 100 (Other layers)	100 (First layer) 100 (Other layers)
Printing speed (mm/s)	6	6
<i>Studied parameters</i>		
Layer thickness (mm)	0.1/0.2/0.3/0.4/0.5	0.1/0.2/0.3/0.4/0.5
Bead width (mm)	0.4/0.6/1	0.6
Number of layer	1/2/3/4/5	5
Bead orientation (°)	0/90	0/90

3. Mechanical characterization

3.1. Tensile tests on single fiber and composites

3.1.1. Tensile tests on synthetic fiber




The tensile properties of single carbon and glass fiber were characterized according to ISO 11566. Beforehand, reinforced filaments were first immersed in a 98 % formic acid solution to dissolve the PA matrix and extract the individual fibers [335]. Afterward, single fibers were then bonded to a paper supports with a gauge length of 10 mm [259] and cross-sectional diameters were measured at three points along the fiber under an optical microscope. Finally, tensile tests were carried out with an MTS Synergie RT/1000 tensile machine using a 2 N capacity load cell at 23 °C and 50 % RH with a crosshead speed of 1mm/min. For each batch, 50 samples were tested.

3.1.2. Tensile tests on synthetic-fiber reinforced composites

Tests on samples were performed in accordance with ASTM D3039. The sample dimensions were 100 mm x 15 mm x variable thickness, in order to obtain a variable fiber volume fraction. Indeed, the

fiber volume fraction is controlled by the fiber thickness e_f and the overall thickness e_T . This may be a significant disadvantage because the properties of the material will depend on the geometry of the sample. For this purpose, three configurations were used for each material as summarized in Table 4.

Table 4 : Printing configuration illustrating the stacking sequence, total thickness, fiber volume fraction and number of carbon or glass fiber reinforced layers.

Printing configurations	Total thickness (mm)	Fiber volume fraction (% vol.)		Number of fiber reinforced layer(s)	
		Carbon	Glass	Carbon	Glass
	0.5	12.9	21.5	2	3
	1	22.6	28	6	8
	2	30	33.1	14	18

The total thickness of the sample (including the PA coating) was taken into account to calculate the tensile strength. Due to the high anisotropy induced by the continuous fiber reinforcement, two patterns were printed following the x and y axis, i.e. in order to evaluate the longitudinal and transverse mechanical properties. Polyamide/glass composites end tabs were glued to the sample with Loctite 406. The mechanical behavior of the longitudinal carbon fiber was measured on an Instron 8803 test machine with a 50 kN capacity load cell and Kyowa KFGS-10-120-C1-11 strain gauges. The crosshead speed was set at 1 mm/min according to ASTM D3039. Tensile modulus was calculated in a deformation range between 0.025 % and 0.1 %. Samples were stored at room temperature (23 °C) and 50 % Relative Humidity (RH) and tensile tests were performed at same conditions to monitor water content in tensile samples. However, there is no standards that address the characterization of printed composites.

3.1.3. Tensile tests on flax-fiber reinforced composites

MTS Synergie RT1000 tensile machine was used with an extensometer to measure the strain and calculate the elastic modulus. The tensile modulus E_1 is determined within a range of strains between 0.05 and 0.1 % according to the procedure suggested by Shah et al. [234], a second modulus E_2 is evaluated on the constant strain range (> 0.4 %). The tensile strain rate was set at 1 mm/min, and five samples were systematically tested for each determination. End tabs made of epoxy/glass composites were glued to the sample with Loctite 406. Samples conditioning prior test and tensile tests were performed at room temperature (23 °C) and 50 % Relative Humidity (RH).

3.2. Characterization of interlaminar properties of synthetic continuous fiber composites

Two categories of samples were studied in this work, one where the polyamide walls were preserved and the other where the polyamide walls were removed by careful mechanical drilling. The machine used for this process is a OT25040FG milling-drilling machine from OTMT with an 8 mm wide milling cutter.

According to ISO 15024, the samples were 20 mm wide, 120 mm long and 6 mm thick. In order to minimize the deflection of the arm during the DCB test; the thickness of the specimen was calculated using Equation 4 (according to ISO 15024) where $2h$ represents the sample thickness, G_{IC} the critical energy strain rate, a_0 the initial crack length and E_{11} the longitudinal tensile modulus of studied material.

$$2h < 8.28 \left(\frac{G_{IC} a_0^2}{E_{11}} \right)^{1/3} \quad \text{Equation 4}$$

A 25 μm thick polyimide film was introduced throughout the printing process to create a 60 mm long pre-crack at mid-thickness. The thickness of the insert film had to be adapted to the 3D printing process. Indeed, 10 μm thick aluminum and PTFE films, meeting the test standard, were tested in a first step, but because of the low temperature and low pressure during the 3D printing process, the printed bead did not adhere to the insertion film despite the use of several types of adhesives (glue and lacquer). Thus, a 25 μm thick polyimide film was used. This film allowed a correct printing, thanks to a good adhesion between the bead and the insertion film. In the literature, studies have shown that G_{IC} values at the crack onset decrease as the thickness of the insertion film decreases to a threshold thickness of about 15 μm [336]. However, the thickness of the insertion film does not affect the G_{IC} values during propagation. Thus, the results of these tests can be used to better

understand the relationship between FFF and the interlaminar bond strength induced during crack propagation, rather than accurately quantifying the critical strain energy rate at initiation.

The Double Cantilever Beam (DCB) test is schematized in Figure 64. In this test, a force P is applied to the specimen where a pre-crack has been introduced in order to promote crack propagation. The force induced a deflection δ leading to a crack propagation with a length a .

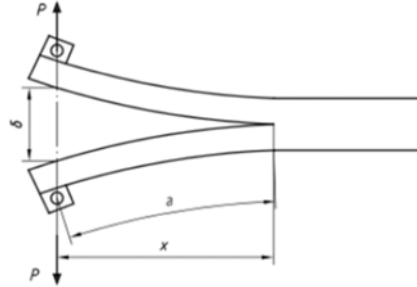


Figure 64 : DCB sample under load P leading to a displacement δ promoting a crack length with a length a (Figure from ISO 15024).

Tests were performed on an Instron 55661 test machine with a 1 kN capacity load cell and a crosshead displacement rate of 1 mm/min. Prior to delamination test, a pre-load was applied to the sample with the same crosshead speed up to a slight propagation over 2-3 mm. The specimens were then unloaded at a crosshead speed of 25 mm/min. The load was applied thanks to blocks glued to the DCB specimens with Araldite AW106. The onset and propagation of cracks were tracked using a Logitech HD Pro Webcam C920 camera with an acquisition speed of 30 frames per second. Prior to testing, the samples were stored at 23 °C and 50 % RH until they reached a constant weight, and the tests were performed under the same controlled conditions. Five replicates were tested for each material and results were arithmetically averaged.

In this study, data analysis was performed using both the corrected beam theory (CBT) proposed by Williams et al. [337] (Equation 5). Preliminary work compared these results with those obtained with the modified compliance calibration (MCC) proposed by Kageyama et al. [338] and no differences were observed. Therefore, only the CBT method has been presented in the present work. Two values were calculated, one at crack initiation from the thick insertion film, which is determined graphically as the onset of the non-linearity on the load-displacement trace, and a propagation value, which is the average of the G_{IC} values during crack propagation. The equations for to MCC model are presented in Equation 5 where P represents the load, δ is the displacement, b is the width of the

sample, a the crack length, Δ the y-intercept of a curve $(C/N)^{1/3} = f(a)$, F and N corrective terms associated respectively to the arm deformation over DCB test and the end-block strengthening (Equation 6, Equation 7)[339].

$$G_{IC} = \frac{3P\delta}{2b(a+\Delta)} \frac{F}{N} \quad \text{Equation 5}$$

$$F = 1 - \frac{3}{10} \left(\frac{\delta}{a}\right)^2 - \frac{2}{3} \left(\frac{\delta l_1}{a^2}\right). \quad \text{Equation 6}$$

$$N = 1 - \left(\frac{l_2}{a}\right)^3 - \frac{9}{8} \left[1 - \left(\frac{l_2}{a}\right)^2\right] \frac{\delta l_1}{a^2} - \frac{9}{35} \left(\frac{\delta}{a}\right)^2 \quad \text{Equation 7}$$

Where δ is the displacement, l_1 is the distance between stick blocks center and sample median plane, l_2 is the half of block width. These lengths are schematized in Figure 65.

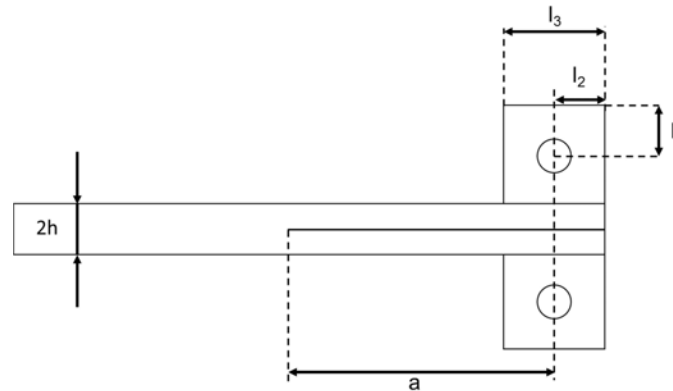


Figure 65 : Schematic view of DCB samples with end-block prior to delamination test.

If the factor F is less than 0.9, its impact is non-negligible on the G_{IC} calculation. The correction factor F was used for all measured crack lengths in order to take into account the deformation of the arm over the entire DCB test as well as the correction term N .

3.3. Three-point bending characterization

Three-point bending tests were carried out according to ISO 14125. The samples were printed with a span-to-depth ratio of 40 for cCF/PA6-I and 20 for cGF/PA6. Consequently, the dimensions of cGF/PA6 are 60 x 15 x 2 mm with a span length of 40 mm while cCF/PA6-I dimensions are 100 x 15 x 2 mm with a span length of 80 mm. Test speed was set at 1mm/min and was performed on a

MTS/Synergie 100. Samples were studied in laboratory conditions (23 °C and 50 % RH). Flexural stress was calculated thanks to Equation 8 where P represents load force, L span length, b sample width and h sample thickness.

$$\sigma = \frac{3PL}{2bh^2} \quad \text{Equation 8}$$

4. Analysis of the microstructure

4.1. Optical microscopy

The microstructures of the reinforced filament and printed parts were observed in optical microscopy (Olympus BX51) at different magnifications (x5, x10, x20). The samples were cut, coated with epoxy resin and finally polished with abrasive paper and diamond paste to obtain a clean and flat observation surface. For larger parts, a binocular microscope was used (Leica MZ16 binocular with 16:1 magnification and 840 LP mm⁻¹ resolution).

Image analysis was used with the ImageJ software to evaluate porosity and fiber volume content. A color threshold is applied to enhance the contrast between fibers, matrix and porosities. The images were then binarized and the amount of each element was finally calculated using the software. Ten images were used for each system.

4.2. Scanning Electron Microscopy (SEM)

Microscopic observations were performed by means of Scanning Electron Microscopy. The samples were sputter-coated with a thin layer of gold in an Edwards sputter coater and then inspected with a JEOL JSM 6460LV scanning electron microscope operated at an accelerating voltage of 20 kV. Macroscopic observations of the samples are made with a Canon digital camera DS126441 equipped with a macro lens Sigma 70-300 mm f/4-5,6.

5. Hygroscopic conditions and seawater aging

5.1. Specimen storage in various humidity chambers

The samples were first dried under vacuum (10 mbar) at 60 °C (Vacutherm VT6060 M from Thermo) until stable weight values were obtained. The samples were then stored in relative humidity (RH) chambers controlled by a saturated solution of potassium hydroxide (KOH), magnesium chloride (MgCl₂), sodium chloride (NaCl) and potassium sulphate (K₂SO₄) to achieve RH of 10 %, 30 %, 75 % and 97 % respectively. The specimens were also stored in a laboratory room at 50 % RH. All specimens were stored at room temperature (23 °C). The samples were used after reaching saturation, i.e. when the weight was stabilized.

5.2. Seawater-aging of 3D printed composites

The samples were first dried under vacuum (10 mbar) at 60 °C until stable weight values were obtained. The samples were then immersed in renewed and filtered natural sea water from Brest Estuary at 40 °C. Aging tests were performed at Ifremer in Brest. Three aging durations were investigated, 1 month, 3 months and 6 months after weight stabilization.

5.3. Moisture sorption measurement

Water absorption was determined on square samples (20 x 20 x 4 mm) where the mass gain was followed by periodic weighting thanks to a Fischer Scientific PAS214C balance (10⁻⁴ g). Prior to each mass measurement, water on the sample surface was removed with a paper towel. The mass gain is calculated thanks to Equation 9. The water content, $M(t)$ in % wt. of a sample is defined as shown in Equation 9 where M_0 is the initial water content.

$$M(t) = \frac{M(t) - M_0}{M_0} \quad \text{Equation 9}$$

5.4. Hygro-expansion measurement

Volumetric measurements were performed on three squares shaped (40 x 40 x 2 mm) glass and carbon printed composites with a Mitutoyo micrometer IP65 (0-25 mm of measurement range) at the same time as the mass measurement.

Volumetric measurements of the flax composites were done on three 70 mm X 25 mm printed biocomposite samples. Ten lines were drawn longitudinally and transversally to the fiber orientation, to ensure that the swelling measurements were always performed at the same location. The

measurements were done with a digital optical microscope (Keyence VHX-100, VHX-900 lens: VH-Z20W, VH-Z450).

6. Measurement of the actuation of hygromorphic composites based on continuous carbon fiber and continuous flax fibers, and electro-thermo-hygromorphic composites based on continuous carbon fiber.

6.1. Description of the environmental conditions for actuation

Continuous carbon fiber composites were initially dried and stored under various RHs: 10 %, 30 %, 50 %, 75 % and 97 %, respectively (described in 5.1) and at room temperature (23 °C). During storage, the samples were weighted regularly and the evolution of their curvature was measured.

The continuous flax fiber composites were immersed in deionized water at room temperature (23 °C). During storage, the samples were weighted regularly and the evolution of their curvature was measured.

6.2. Electrical stimulus generation

The electrical activation was performed thanks to an Agilent E31610A DC Power Supply generator. Two voltages were realized (15 V and 10 V) and a passive drying at 9 % RH was done in parallel. In order to apply a voltage to the sample, the printed actuator was placed on a support and held by metal clamps connected to the power generator (Figure 66). A silver paint was applied to the interface between the actuator and the clamp to improve electrical conduction. In order to follow the evolution of the mass during electro-thermo-actuation, a voltage was applied during 120 seconds to the sample. After this treatment, the samples were weighed and their curvature was registered.

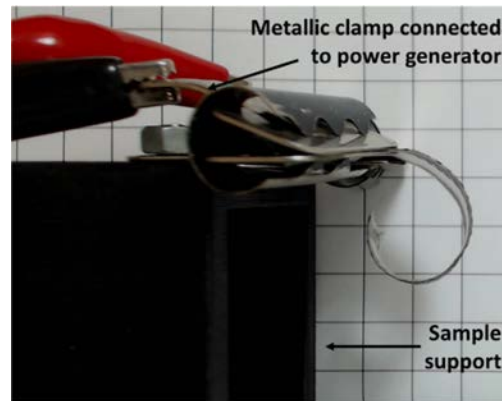


Figure 66 : Photograph of the actuator assembly with actuators placed on a support connected to power generator by means of metal clamps.

For each sample, the thermal distribution was observed with a FLIR X6580sc thermal camera while temperature was measured with a C.A 864 thermometer. The mass change was measured with a Fisher Scientific PAS214C balance (10^{-4} g).

6.3. Measurement of the actuator curvature

The curvature variation was tracked using the Logitech HD Pro Webcam C920 with an acquisition speed of 30 frames per second and image processing was performed using ImageJ 1.51j8 software (National Institutes of Health, USA). Curvature is measured by fitting the shape of the sample to a “circle” function. The bending curvature K is calculated using the adjusted circle radius r . The methodology for measuring the amplitude of curvature is shown in Figure 67.

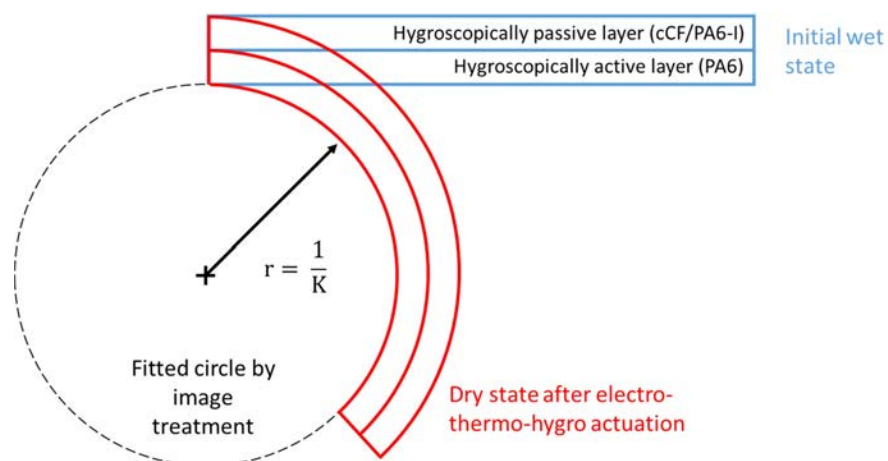


Figure 67 : Schematic representation of bending curvature measurement.

7. Thermal characterization of the composites

7.1. Differential Scanning Calorimetry (DSC)

Dynamic Scanning Calorimetry (DSC) was carried out to ascertain the nature of the polyamide in the printable filaments. A Mettler Toledo DSC3 Star® was used with the software Star® System. A first temperature ramp of 10 K/min was carried out from 25 °C to 350 °C to erase the thermal history. The samples were then cooled to -10 °C at 20 K/min, then a second 10 K/min temperature ramp of from -10 °C to 350 °C was performed to measure the thermal properties of the polymers (Glass transition temperature T_g , melting temperature T_m , crystallization temperature T_c and associated enthalpies).

7.2. Thermogravimetric analysis (TGA)

The fiber volume fraction was determined by thermogravimetric analysis according to ASTM D3171-15 and performed with a Mettler-Toledo Thermal Analysis instrument (STARe System). A 10 K/min temperature ramp from 25 °C to 400 °C was used and analyses were conducted under a nitrogen atmosphere.

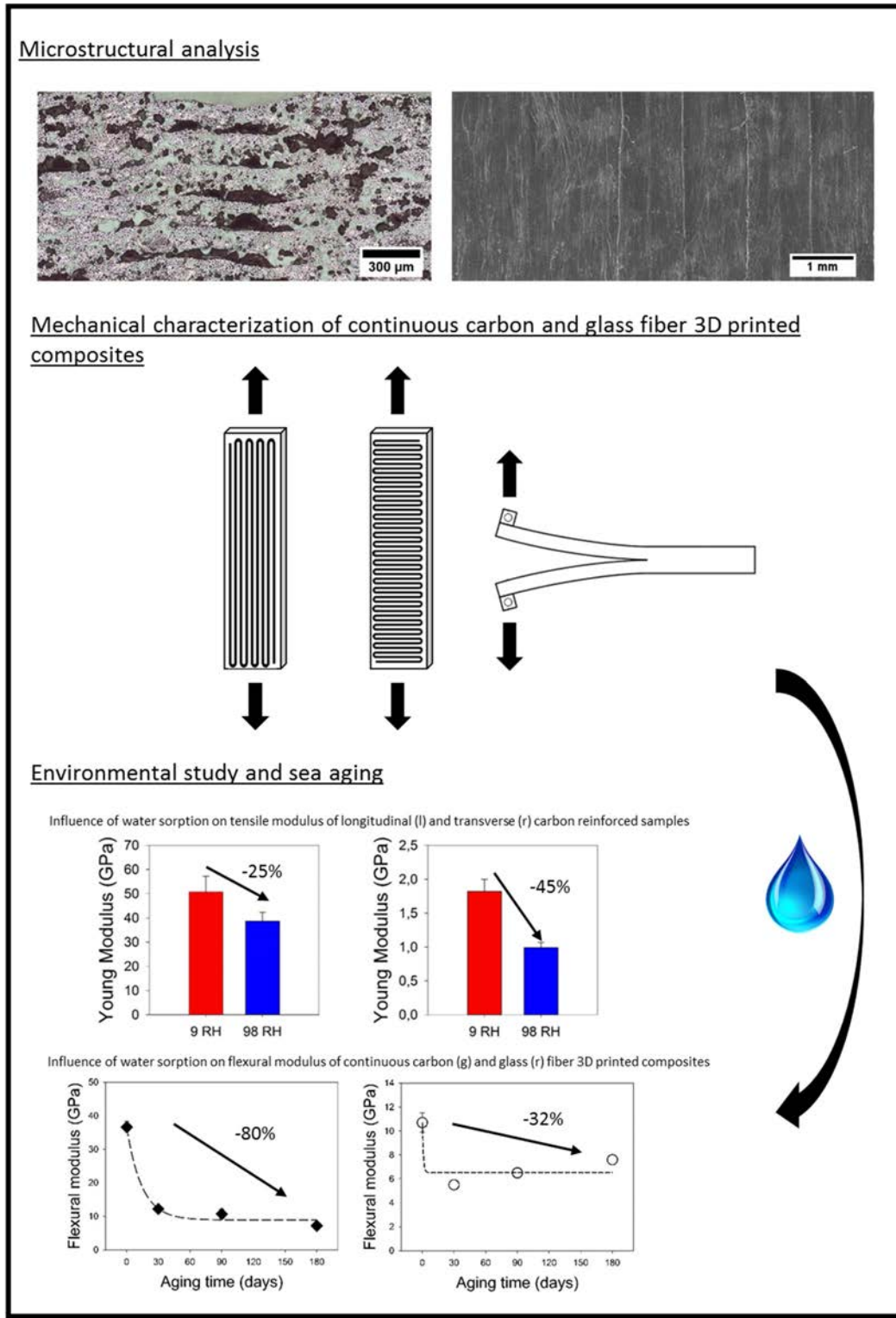
7.3. Thermal expansion measurement

Thermal expansion was measured on 10 x 10 x 10 mm sampled thanks to thermomechanical analysis (Q800 DMA) from TA Instruments. The samples were placed between two parallel plates and held with a blocking force $F = 0.1$ N. The samples were then subjected to a temperature ramp of 10 K/min from 25 °C to 200 °C and the thermal expansion ΔL on the temperature change ΔT was measured thanks to the displacement of one of the parallel plates. The coefficient of thermal expansion α is expressed by Equation 10.

$$\alpha = \frac{1}{L_0} \frac{\Delta L}{\Delta T} \quad \text{Equation 10}$$

Where L_0 represents initial sample length. Thus, the coefficient of thermal expansion was determined graphically as the slope of the curve $\Delta L/L_0$ against ΔT .

Chapter 3: Mechanical and hygromechanical properties of continuous carbon and glass fiber composites



For outdoor applications subject to temperature and moisture variations such as marine engineering (pulley, chandlery, propeller, submarine drones, marine turbine...), the sensitivity to moisture of the polymer matrix could limit their application, especially for PA6 used in Markforged® 3D printers. In addition, a microstructure effect (i.e. increased porosity, inhomogeneous fiber dispersion) also affects mechanical performance, moisture sorption, water transport in the material and a whole set of hygromechanical properties.

In this third chapter, a study on continuous glass fiber composites (cGF/PA6) and continuous carbon fiber reinforced PA composite (cCF/PA6-I) parts manufactured using a commercial 3D printer is carried out. First, longitudinal, transverse and out-of-plane mechanical behavior is investigated. For this purpose, three mechanical characterizations were performed: a tensile characterization for two raster angles (0° and 90°) to evaluate longitudinal and transverse properties and a double cantilever beam (DCB) to investigate the interlaminar resistance in mode I of 3D printed composites. A microscopic analysis is carried out to describe in detail the microstructure (coating wall for example), the defects induced by the printing process and its influence on the mechanical properties. The reinforcement mechanism is evaluated by comparing the properties of carbon and glass reinforced composites measured by tensile tests with the values obtained by back-calculation using the Rule Of Mixture (ROM).

Finally, in order to use these 3D printed parts in outdoor applications, an evaluation of sorption and swelling behaviors was done as well as mechanical responses under different moisture and seawater conditions.

1. Microstructure description

1.1. Filament microstructure description

Firstly, the microstructure of the as-received filaments was investigated through optical observations. Optical images of the filament cross-sections were acquired to investigate the pre-printing geometrical characteristics as well as the dispersion state of the fibers in the polymer matrix. Typical images are presented in Figure 68.

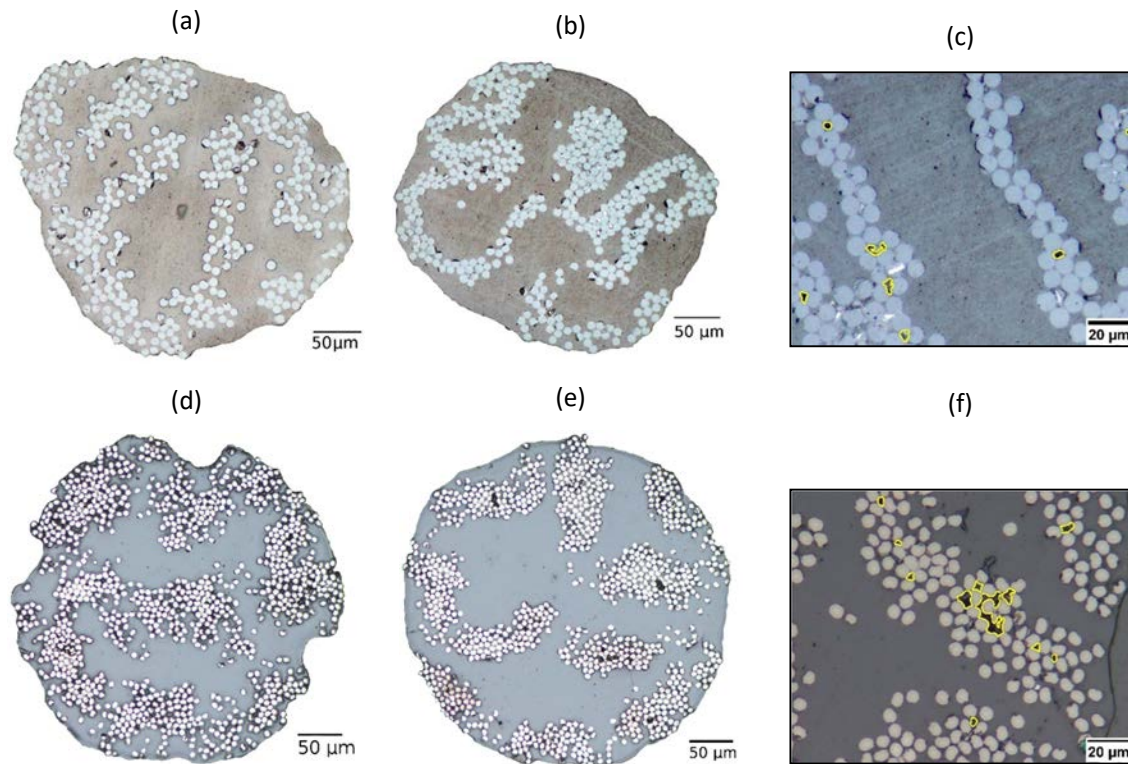


Figure 68 : Optical cross-sectional images of cGF/PA6 and cCF/PA6-I in the form of received filaments having (a and d) irregular outer boundaries, (b and e) regular circumference and (c and f) magnified views.

As shown in Figure 68.a, b and d, e; as-received filaments have irregular sections with an average diameter of 380 μm and 332 μm for cCF/PA6-I and cGF/PA6, respectively (Table 5). These variations may be due to the fiber coating process used to produce the filament. Moreover, the impregnated fibers are not homogeneously dispersed in the polymer matrix. Indeed, the fibers are agglomerated and not evenly spread in the filament, (almost reflecting the size and shape of the initial fiber yarn) resulting in very fiber-rich areas and, consequently, other very matrix-rich areas, thus limiting or

reducing the homogeneity of the subsequent printed part. Furthermore, as illustrated by the yellow dots in Figure 68.c and f, the filaments as-received also have matrix-free areas where the reinforcing fibers remain un-impregnated, implying internal porosity. These un-impregnated areas are more common in carbon filaments which exhibit 40 % higher internal porosity than glass reinforced filaments (Table 5). The profile of the carbon and glass fiber is similar, with an average glass fiber diameter of $8.8 \pm 0.5 \mu\text{m}$ and carbon fiber diameter of $6.9 \pm 0.7 \mu\text{m}$. Nevertheless, the diameters of the glass fibers are smaller than those of conventional E-glass fibers ($d \approx 20 \mu\text{m}$). Carbon fibers have been identified as TORAYCA® T300 tow by Van der Klift et al. [98] while glass fibers are assumed to be calcium aluminum borosilicate glass [340] due to their small diameter and tensile modulus (70 GPa).

1.2. Cross-section description

After the characterization of the filament, the microstructure changes induced by the process step were studied. Two planar areas are observed, a sectional view and an in-plane view along the (y, z) and (x, y) planes, respectively.

Figure 69.a, d shows some panoramic images of cross-sectional samples, for cCF/PA6-I and cGF/PA6, respectively. For both systems, large areas of recurring voids are present in both specimens. These images are magnified in Figure 69.b, e for the carbon reinforced samples and glass reinforced samples, respectively. The void areas result from a non-overlap between two adjacent printed beads, and correspond to inter-bead porosities accounting for the majority of the voids (around 85 % of global void content for cGF/PA6 and 60 % for cCF/PA6-I). For both composites, the interfilament distance is set at 0.9 mm in the slicer, as then cGF/PA6 filament exhibit lower diameter, the non-overlap zone is larger for cGF/PA6 samples and results in a higher inter-bead porosities content.

Other porosities are located between the layers as well as within each filament (intra-bead porosity). Porosities in the interlaminar zones are due to the absence of pressure and the inhomogeneous temperature field which reduce the efficiency of interdiffusion. Intra-bead porosities, especially for cCF/PA6-I, appear surprisingly in the printed beads. Several hypotheses can be raised, such as initial heterogeneity of filament diameter, lack of matrix wetting in fibers-rich areas or loss of a third component. Its origin still needs to be further investigated.

During the printing process, the filaments were flattened. Filaments $380 \mu\text{m}$ and $332 \mu\text{m}$ wide become layers $127 \mu\text{m}$ and $101 \mu\text{m}$ thick for continuous carbon and glass fibers polyamide

composites, respectively, which divides the initial filament size by 3. This flattening can significantly reduce intra-bead porosity.

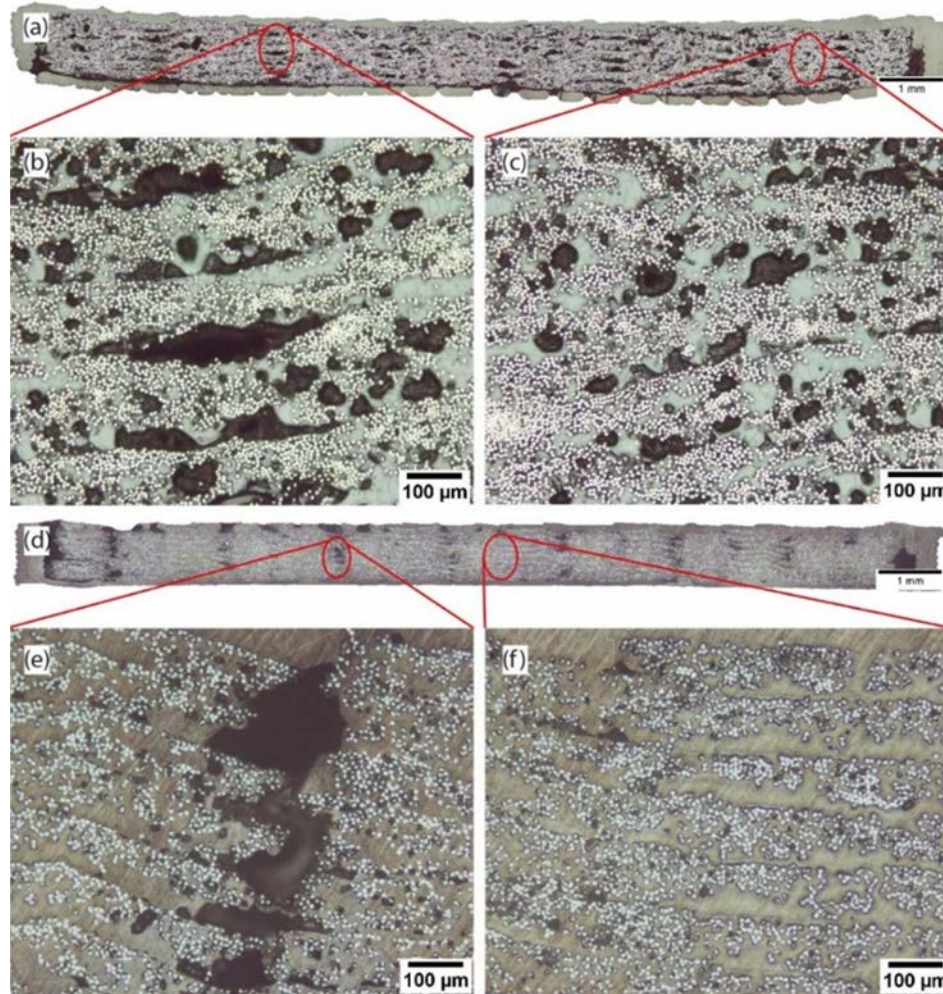


Figure 69 : Microstructure of cross-sectioned (a) cCF/PA6-I and (d) cGF/PA6 printed part under an optical microscope with magnification in the areas where the printed beads do not overlap for (b) cCF/PA6-I and (e) cGF/PA6 along with magnification in the areas of the printed beads of (c) cCF/PA6-I and (f) cGF/PA6 highlighting the intra and inter-bead porosities.

These different kinds of porosity therefore lead to a considerable increase in porosity during the printing process, reaching $15.1 \pm 0.4 \%$ for cCF/PA6-I parts and $12.3 \pm 0.7 \%$ for cGF/PA6 parts. The higher porosity for carbon-reinforced parts can be explained by the higher porosity of the filament. This higher intra-bead porosity can be observed in Figure 69.c, f. These defects are induced by the printing process and especially by the print trajectories that cannot be changed on this commercial printer.

Table 5 : Geometrical characteristics and porosity content for as received samples of cCF/PA6-I and cGF/PA6 filament and printed parts.

Sample		Filament diameter (μm)	Layer thickness (μm)	Porosity (%)
Filament	cCF/PA6-I	379.8 ± 10.5	/	1.85 ± 0.3
	cGF/PA6	332.0 ± 23.2	/	1.34 ± 0.13
Printed part	cCF/PA6-I	/	127.9 ± 22.7	15.10 ± 0.35
	cGF/PA6	/	100.8 ± 4.6	12.30 ± 0.65

During this printing process, at least one layer of pure PA6 is always applied on the top and bottom of the printed samples to ensure the cohesion of the part. Pure PA6 is also deposited on the perimeter of the sample and is referred to as “walls” (Figure 70). Consequently, when the number of top/bottom layers and walls is set to a single layer for example, when specimen geometry varies, the fiber content varies more than the PA6 content. Consequently, the volume fraction of the fibers and hence the properties of the composite depends on the geometry of the sample. In order to vary the volume fraction of the fibers, different thicknesses (0.5; 1; 2 mm) were printed and samples were prepared from which the polyamide coating was manually removed. Thus, for cCF/PA6-I, 0.5-mm thick samples correspond to 12.9 % vol., 1 mm is 22.6 % vol., 2 mm is 30 % vol. and finally, samples without a polyamide coating are 35 % vol. For cGF/PA6, 0.5-mm thick samples correspond to 21.5 % vol., 1-mm thick samples correspond 28 % vol., 2 mm represents 33.1 % vol. and, finally, samples without a polyamide coating exhibit 39 % vol.

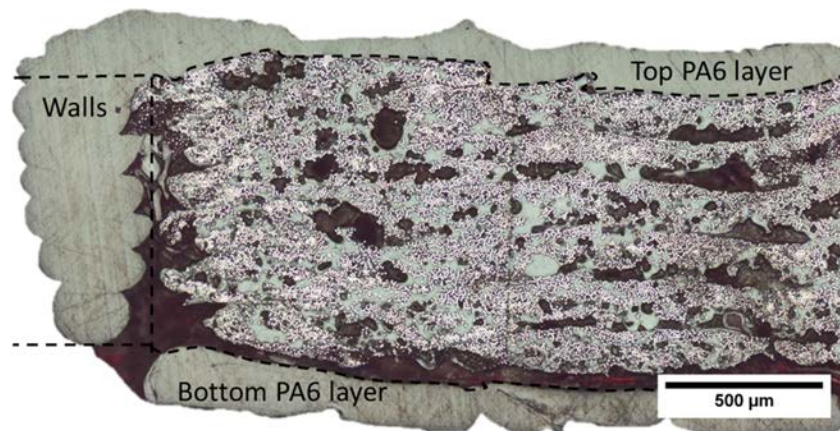


Figure 70 : Cross-sectional view of the cCF/PA6-I sample showing the upper and lower layers and the walls automatically added by the Eiger slicer.

1.3. In-plane description

In this section, a description of the microstructure in the plane is made. In-plane optical images of the cCF/PA6-I and cGF/PA6 samples are presented in Figure 71.a and c respectively.

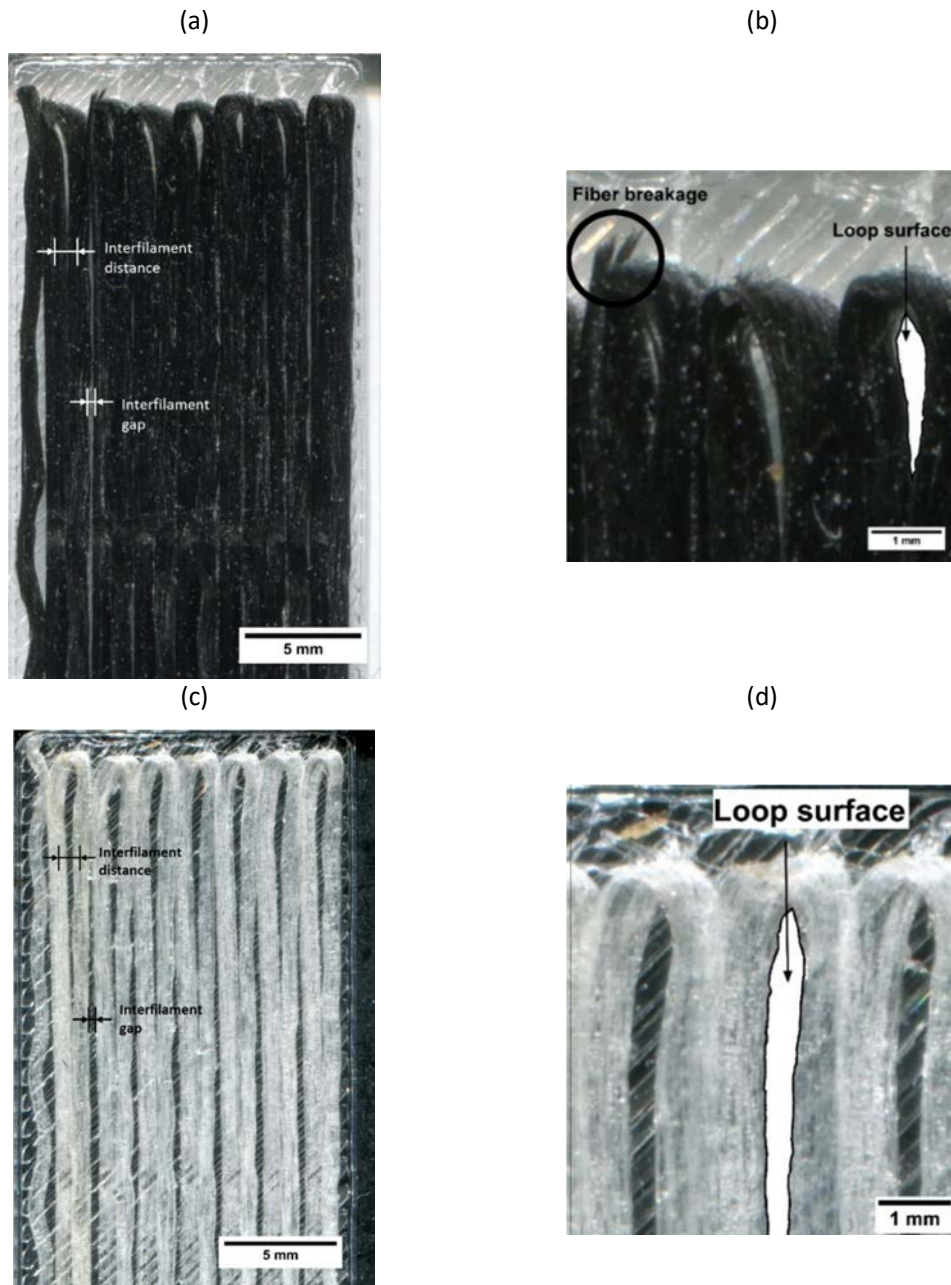


Figure 71 : Optical images of a single layer of printed filament (a, b) cCF/PA6-I and (c, d) cGF/PA6, with a higher magnification of their respective folding areas indicated in (b) and (d).

On these images, loops are created on the edge of the samples. These loops are due to the printing process; when the nozzle reaches the edge of the part, the printed head turns over, which folds back the printed beads, creating the loops. The radii of curvature of carbon and glass samples are measured at approximately 0.6 mm (Table 6). Folding induces stress concentration in the printed bead and causes local fiber breakage in carbon beads (Figure 71.b) due to their low toughness. This phenomenon is not observed for glass fiber composites (Figure 71.d). In addition, the folding of beads results in the formation of very fiber-rich and also resin-rich areas in the loop. The loop areas are different between carbon and glass reinforced samples (0.42 mm² for carbon and 1.04 mm² for glass) due to the different size of the filaments. Moreover, the samples of cCF/PA6-I and cGF/PA6 have a similar interfilament distance (Table 6) close to the preset value (0.9 mm), while the initial filament of cGF/PA6 is thinner than that of cCF/PA6-I. As a result, glass-printed parts have interfilament gaps (distance between the edge of printed beads) that are 3 times larger than carbon printed parts (0.31 mm for cGF/PA6 and 0.13 mm for cCF/PA6-I). Figure 71. also shows the bead overlap for cCF/PA6-I samples, which explains the lower inter-bead porosities for these samples. For cGF/PA6 samples (Figure 71.c), filament overlap is observed at each round trip (i.e. each 2 beads). This fiber trajectory is predefined by the Markforged® devices and cannot be customized to optimize the microstructure of the samples and thus their mechanical properties.

Table 6 : Geometrical characteristics of in-plane images of single layer cCF/PA6-I and cGF/PA6 printed parts.

Material	Loop surface (mm ²)	Interfilament distance (mm)	Interfilament gap (mm)	Curvature radius (mm)
cCF/PA6-I	0.42 ± 0,12	0.91 ± 0.09	0.13 ± 0.04	0.62 ± 0.07
cGF/PA6	1.04 ± 0,26	0.93 ± 0.08	0.31 ± 0.06	0.66 ± 0.06

Regarding the measurement of the interlaminar properties of cCF/PA6-I, two studies were carried out : One in which the walls were preserved in order to evaluate the composite properties in service and the other in which the walls (Figure 70) were removed by machine milling and drilling in order to evaluate the intrinsic properties of cCF/PA6-I. Optical observation was performed on the surface of the interlayer with and without wall coating to evaluate the geometries of the wall (thickness and surface) as well as the surface quality of the samples where the walls were removed. Images are shown in Figure 72.

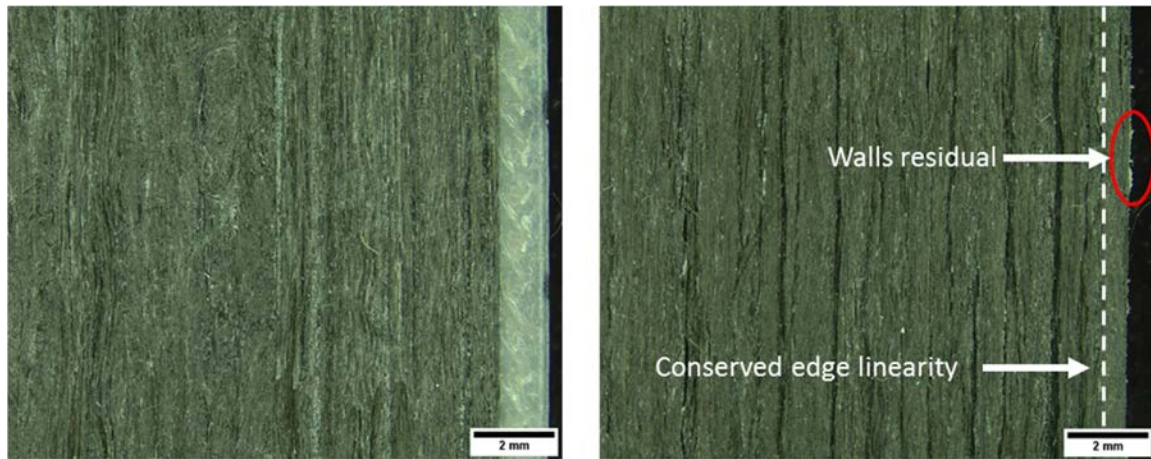


Figure 72 : Images of the sample surface for samples where the walls have remained (top) and the walls have been removed (bottom).

Optical observation of the sample surfaces reveals the coating wall. A wall thickness of approximately 1.33 ± 0.22 mm consists of pure PA6 and represents 13.2 % of the total delaminated surface of the 20 mm wide samples (Table 7). When the walls are removed by mechanical drilling, the linearity of the edge samples is maintained and the induced defects are observed in the sample. No damages are also observed on the sample surface and residues of PA6 remain on the sample surface.

Table 7 : Measurement of wall and sample width and percentage of walls surface in delaminated area.

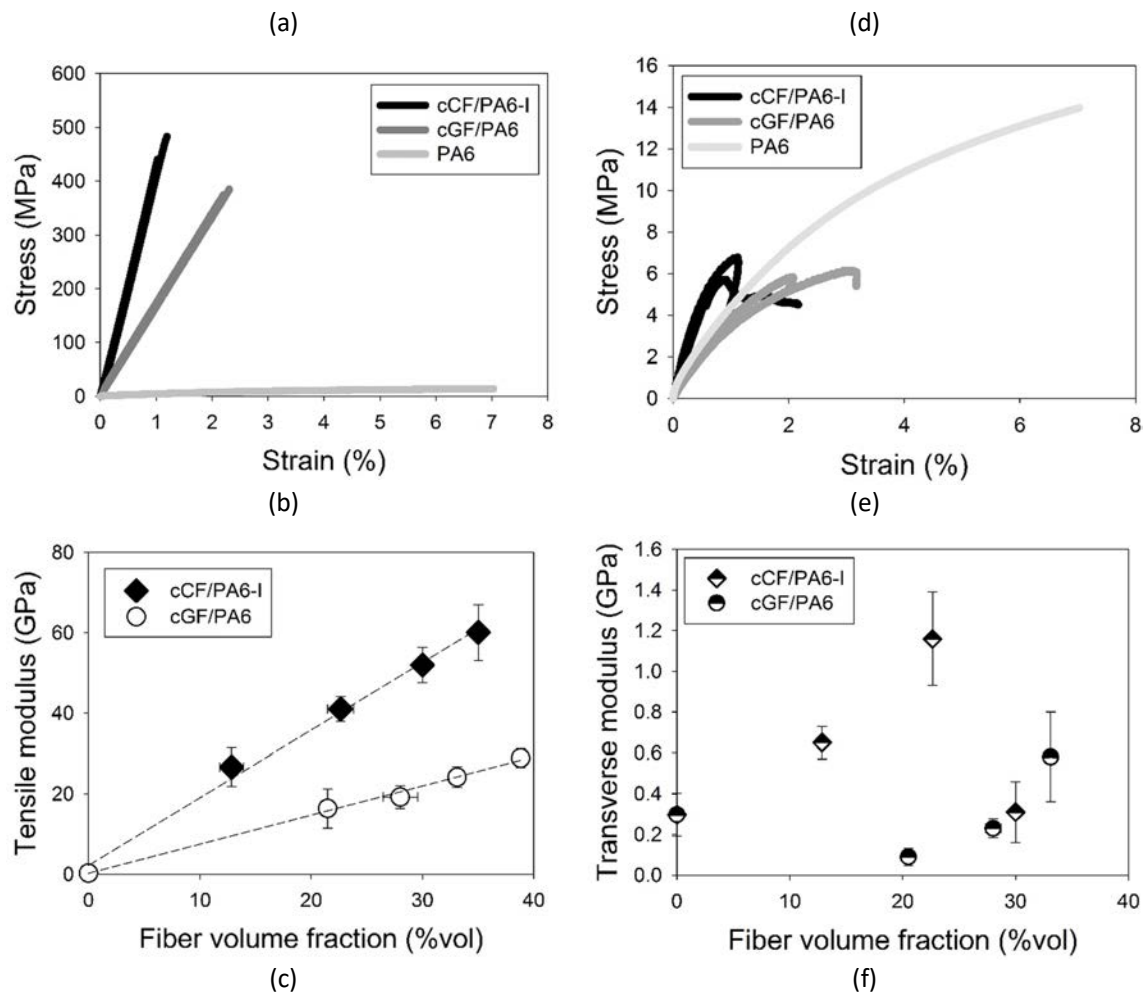
	Wall width (mm)	Sample width (μm)	Walls surface (%)
Remained walls	1.32 ± 0.22	20.02 ± 0.24	13.2
Removed walls		17.76 ± 0.21	

Hence, the printing process induces many defects that can be fairly compared to those observed in Automatic Fibers Placement (AFP). In the latter case, local misalignment, stirring (in-plane buckling) or overlapping of tapes are considered singularities rather than flaws, i.e. inherent in the process, which must be taken into account in the design/dimensioning process. Unlike AFP, the specific features of 3D printing of continuous fibers composites, such as the addition of coating walls and roof/top layers could affect the mechanical performance of 3D-printed-composites with Markforged® devices.

2. Mechanical characterization

2.1. Longitudinal and transverse characterization

In this section, an investigation of the tensile modulus and strength of neat PA6 matrix (as a reference), continuous carbon and glass polyamide printed parts in the longitudinal and transverse directions was carried out. For cGF/PA6 and cCF/PA6-I, mechanical tests are performed with variable fiber volume fractions (from 13 to 35 % vol.). The main results are summarized in Figure 73. Figure 73.a shows a typical stress versus strain curve for 1 mm thick specimens (22.6 % vol.). For both reinforced composites, the stress increases almost linearly with applied strain up to 1.1 % and 2.2 %, the point at which rupture occurs for carbon and glass, respectively, expressing brittle behavior. This behavior is similar to that observed in single fibers and indicates that the load is well transferred to the reinforcing fibers.



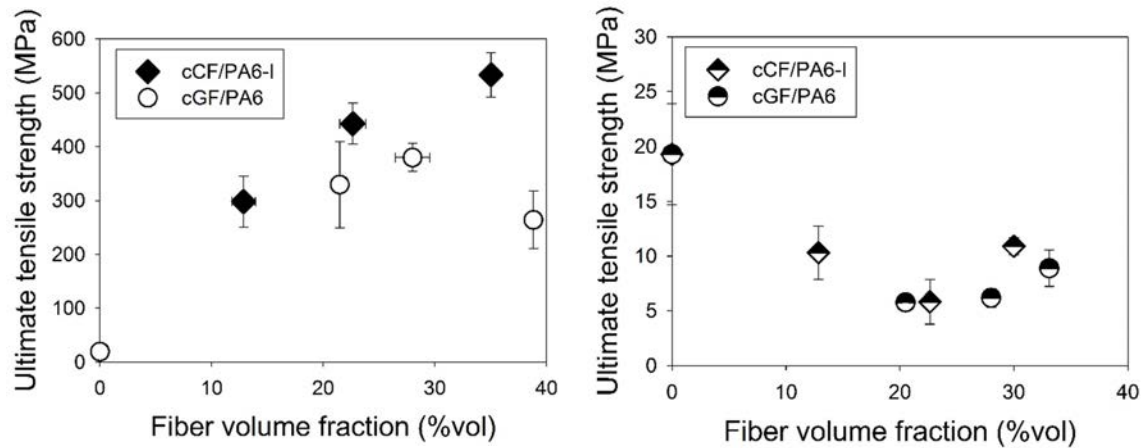


Figure 73 : Typical tensile stress vs. strain behavior of printed parts made of PA, cGF/PA6, and cCF/PA6-I tested in the (a) longitudinal and (d) transverse directions. Tensile modulus and strength of cGF/PA6 and cCF/PA6-I as a function of the volume content of fibers in the (b,c) longitudinal and (e, f) transverse directions, respectively.

For both types of fibers, the longitudinal sample breaks perpendicular to the load without necking, highlighting the brittle nature of the behavior (Figure 74.a) Moreover, debonding, delamination and matrix shear are present in both samples, but are more pronounced for cGF/PA6 (Figure 74.b). This difference can may be due to the microstructure effect with the greater interfilament distance for the cGF/PA6 samples which results in lower inter-bead cohesion.



Figure 74 : Optical images of fractured (a) cCF/PA6-I and (b) cGF/PA6 showing the mode of fracture for each sample that results in fiber breakage and debonding between printed beads.

Figure 73.b, c shows the evolution of tensile modulus and ultimate tensile stress as a function of fiber volume fraction for carbon and glass reinforced specimens. As expected, the modulus increases linearly with the carbon or glass fiber fraction. Actually, for cGF/PA6 with a fiber volume fraction

greater than 30 % vol., the mode of rupture (debonding between beads instead of fibers breakage) changes drastically and a lower ultimate tensile stress is observed.

Single-fiber tensile tests give values of 68 ± 7 GPa for glass fibers and 161 ± 10 GPa for carbon fibers for tensile modulus, which is slightly lower than the typical values for E-glass and carbon fibers. By applying a simple Rule Of Mixture (ROM) to these data and using the tensile modulus of polyamide measured by tensile tests ($E_{\text{exp PA6}} = 0.29 \pm 0.1$ GPa), it is possible to estimate the properties of the composite ($E_{\text{ROM cCF/PA6-I}} = 37$ GPa and $E_{\text{ROM cGF/PA6}} = 18$ GPa for $V_f = 22.6$ % vol. for cCF/PA6-I and $V_f = 21.5$ % vol. for cGF/PA6, respectively). It should be noted that the low modulus was measured for printed samples of pure PA6 samples with respect to data from the literature for classic manufacturing process. This observation is well known and has been evidenced in the literature for other polymers such as PLA and ABS [11], [71].

Moreover, the ROM can be modified to take into account the actual porosity content Φ (Equation 11) [341]:

$$E_c = E_{TH}(1 - \Phi)^2 \quad \text{Equation 11}$$

where E_{th} is the theoretical tensile modulus without porosity and Φ the porosity content. In this case, the experimental data are drastically underestimated compared to the ROM ($E_{\Phi\text{-ROM cCF/PA6-I}} = 26$ GPa and $E_{\Phi\text{-ROM cGF/PA6}} = 11$ GPa), which means that porosity has only a small influence on the longitudinal tensile modulus. This small influence of porosity on longitudinal tensile modulus is confirmed in the literature [342]–[344] for continuous epoxy-carbon fibers laminates manufactured by conventional processing routes.

The mechanical properties of the composites are greatly enhanced compared to pure PA6. Indeed, for 22.6 % vol., the ultimate tensile stress is 23 times higher and 19 times higher for carbon and glass, respectively, while the tensile modulus is 137 times higher and 63 times higher for carbon and glass respectively.

To evaluate the anisotropy of the material, an investigation of the tensile properties of the printed parts in the transverse direction was carried out. The results are reported in Figure 73.d-f. The typical behavior of cCF/PA6-I and cGF/PA6 (1 mm thick) for transverse specimens are shown in Figure 73.d and is compared to pure nylon samples as a reference. Hence, the stress increases linearly up to 0.6%

and 0.8 % for carbon and glass reinforced samples, respectively, and then plastic deformation occurs until rupture at 1 % and between 2 and 3 % for carbon and glass specimens, respectively. This behavior is characteristic of ductile behavior. This behavior is also illustrated in Figure 75, which gives a detailed view of the rupture mechanism in transverse profiles of carbon and glass samples.

For both materials, the breakage of the specimen is due to shear failure of the polymer coating, printed at 45° and at -45° to the longitudinal direction, for the upper and lower layer, respectively, and to the adhesive rupture between two adjacent beads (shown by Figure 75.b, e). Indeed, there is a little overlap between the beads, so that in tensile tests, two non-overlapping filaments move away from each other and, consequently, the tensile load is not transferred to the reinforcing fibers. Thus, the load is transferred to the polyamide coating (Figure 75.f), which explains the ductile behavior.

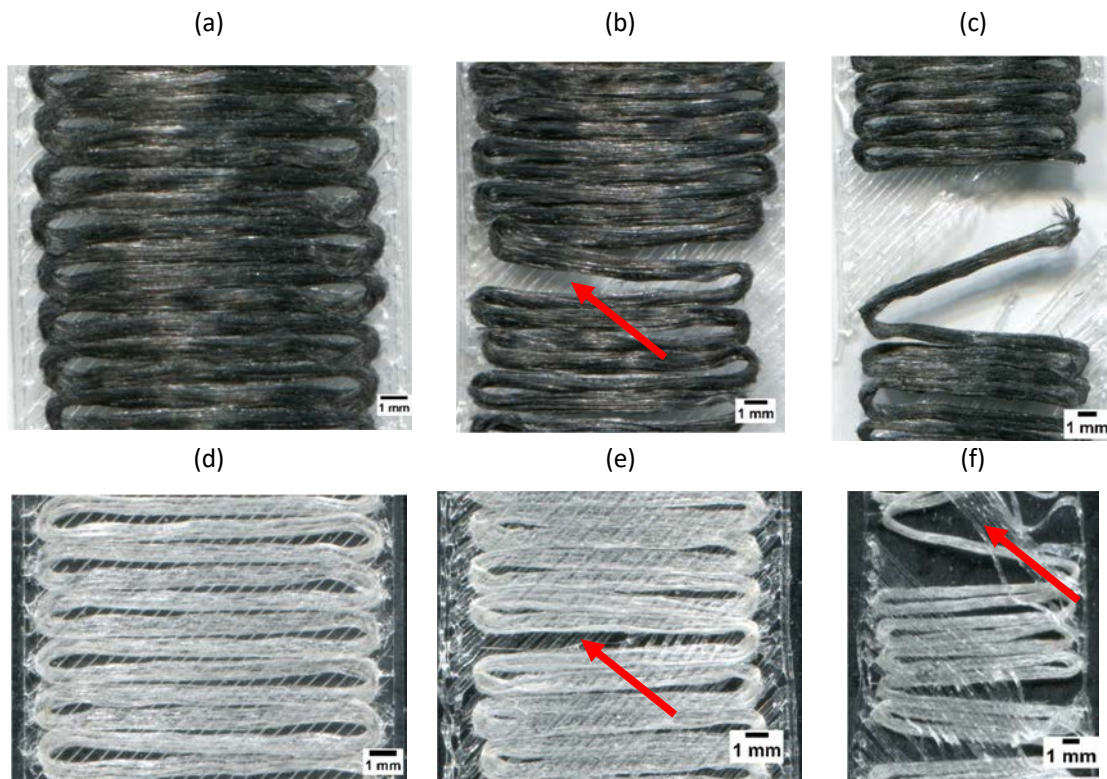


Figure 75 : Evolution of transverse sample profile during tensile tests for cCF/PA6-I (a,b,c) and cGF/PA6 (d,e,f) samples at different test strain; (a,d) representing the initial stage, (b,e) the portion at strain-at-break and (c,f) an excessive strain showing the unwinding and rupture of the printed bead.

This non-overlapping is also visible in Figure 75.c and f that show the result of excessive deformation applied to the material. For these samples, the polyamide coating breaks in shear and filament

unwinding is induced. For carbon samples, the rupture of the bead occurs in the folded area due to the initial failure of the fibers (Figure 75.b).

Figure 73.e and f represent the variation in transverse properties as a function of the fiber volume fraction. In contrast to the longitudinal samples, the transverse specimen exhibits different trends in modulus and strength, for both carbon and glass fiber composites. For modulus, samples of cCF/PA6-I exhibit an improvement with increasing fibers fraction, in contrast to cGF/PA6. In terms of strength, both cCF/PA6-I and cGF/PA6 show poorer properties than PA6 with a drastic reduction in stress at break ($\approx -70\%$) with the fraction of fibers. This trend can be explained by the weakness of the bead interface as well as by the presence of fibers that affect the strain field in the surrounding matrix, particularly when the fiber distribution is heterogeneous. In addition, the transverse and out-of-plane properties of laminates are very sensitive to defects, i.e. porosity content and location [345], [346].

The ratio between longitudinal and transverse properties (Anisotropic Ratio = AR) evolves with the type of fiber. For 23 % vol. fibers volume fraction, the AR in carbon samples is 32 for modulus and 70 for strength. For 21 % vol. fibers volume fraction and cGF/PA6, the AR is 160 for modulus and 56 for strength. Thus, the transverse properties are clearly a limiting factor, which can be further amplified by the printing process. These observations highlight the need for a carefully optimized stacking sequence before printing the laminate.

The application of an inverse Rule Of Mixture for cCF/PA6-I and cGF/PA6 ($V_f = 22.6\%$ vol. and $V_f = 21.5\%$ vol., respectively) and the use of a transverse modulus of 7 GPa for carbon fibers and 72 GPa for glass fibers [347] results in a large deviation between the calculated transverse modulus and the experimental values, in particular for cGF/PA6 (0.38 GPa for both $E_{ROM\ cCF/PA}$ and $E_{ROM\ cGF/PA}$). cCF/PA6-I show a measured transverse modulus of 1.03 GPa, while cGF/PA6 has a modulus of 0.19 GPa. This difference can be explained by the structural effect of the printed microstructure by which the PA6 coating contributes to the transverse behavior, but also the presence of porosity which disturbs the load transfer. Thus, the mechanical properties in the transverse direction cannot be predicted from the fiber volume fraction. In addition, the very poor properties in the transverse orientation of the printing is one of the most critical drawbacks of 3D printing of continuous fibers.

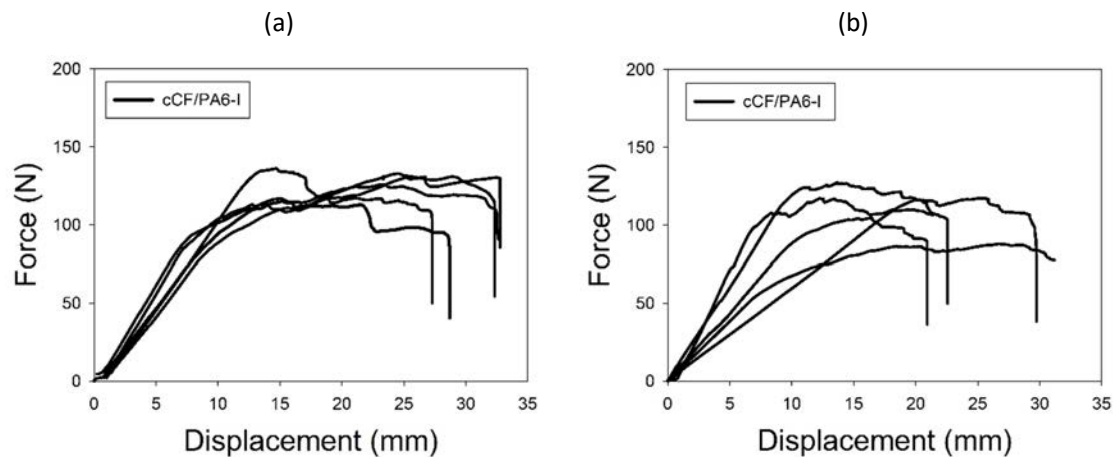
2.2. Evaluation of interlaminar properties with Double Cantilever Beam (DCB) tests.

The critical energy strain rate (G_{IC}) has been evaluated using mode I DCB specimens and the CBT method for both materials and a delamination fracture have been observed. The effect of adding a coating wall was investigated by a comparison sample with and without these walls.

2.2.1. Mode I delamination resistance behavior

The behavior recorded in the mode I DCB tests of the two printed composites with and without walls is presented in Figure 76.a and b, respectively. cCF/PA6-I samples with PA6 coated walls exhibit a delamination behavior where most samples show an increasing load after a quasi-linear section. This is typical of unstable crack propagation and ductile materials. As described by Treber et al. [348], the instabilities are due to heterogeneous composite toughness. When crack propagation reaches a region of high local toughness, the speed of propagation diminishes and the elastic energy is saved until an energy is released which causes a sudden crack propagation. In the literature, the unstable propagation in conventional composites is often explained by the fiber bridging the two arms of the specimen [349]. This mechanism is observed during delamination (Figure 76.c).

For cCF/PA6-I without wall samples, a steady decrease in load is observed in the delamination test for each sample reflecting stable crack growth [350], [351]. Hence, PA6 coating walls play an important role in the delamination behavior due to the higher toughness of the neat polymer compared to the 3D printed carbon composites. Moreover, cCF/PA6-I samples with coated walls shows a lower scatter than cCF/PA6-I samples without coated walls. This means that PA6 walls soften the delamination behavior of 3D printed composites, while samples without walls are more likely to be influenced by printing defects at the edge of the sample.



(c)

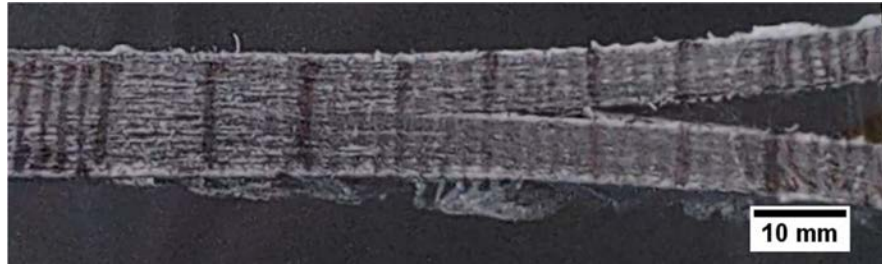


Figure 76 : Typical load-displacement curves for cCF/PA6-I with walls (a), without walls (b) and side view of cCF/PA6-I during delamination test.

Both wall and wall-less cCF/PA6-I samples exhibit a unique crack propagating between the delaminated layers, with no deviation of the delamination from the mid-plane, which is the simplest behavior found in unidirectional composites and confirms the opening (Mode I) delamination mode (Figure 76.c).

Figure 77 presents resistance-curves (R-curves) of the cCF/PA6-I printed composites representing the G_{IC} during crack initiation and propagation. The G_{IC} is calculated from the load-displacement curves, crack onset and propagation tracking using CBT method as displayed in Figure 77.

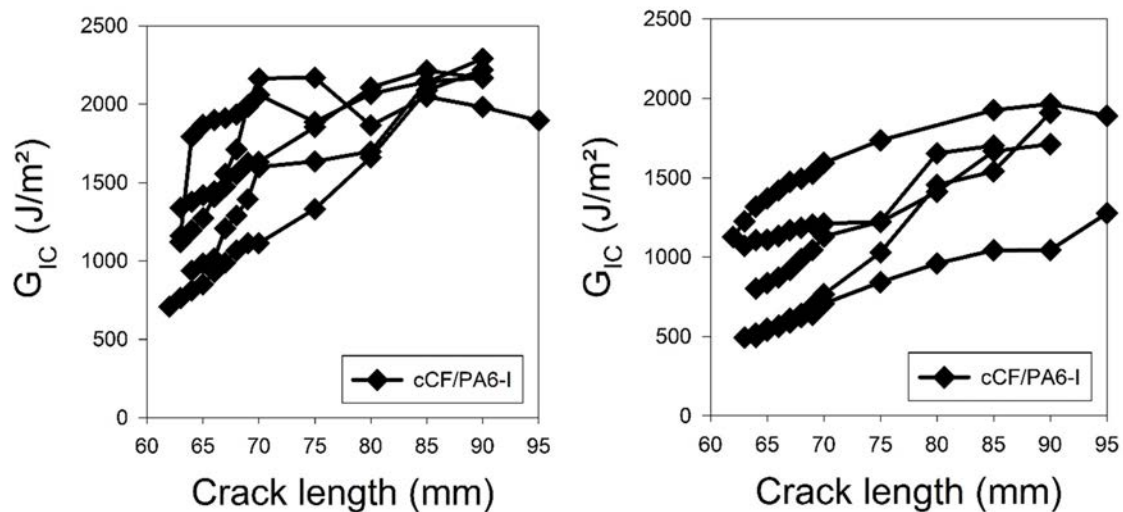


Figure 77 : R-curves for both cCF/PA6-I with (left) and without (right) coating walls for CBT data reduction method.

Considering the two printed configurations, an increase of G_{IC} values is observed with the progression of the crack. Figure 77 shows that the PA6 walls lead to higher average values of critical energy strain rates with a higher G_{IC} value for samples where the PA6 walls were retained compared to those where the walls were removed by mechanical milling.

2.2.2. Comparison of critical strain energy release rates with literature values

The average G_{IC} for the initiation and propagation steps calculated with CBT methods are summarized Table 8 for cCF/PA6-I. Initiation values are widely debated in the literature due to the defects in crack initiation and the definition of when initiation occurs [336]. Moreover, the values of the critical energy strain rate decrease as the starter film thickness decreases, but remain constant below a film thickness of about 15 μm [336]. Hence, the propagation values depend less on the mechanical test and are recommended in the standards to compare the evolution of the critical energy strain rate [336]. The measured values are compared with literature data provided for conventionally manufactured laminates (autoclave and hot press molding) and additively manufactured composites (AFP) and for various matrix polymers (Table 8).

Table 8: Measured delamination resistance of cCF/PA6-I printed parts and literature values referring to UD fibers/polymer composites.

Materials	Process	V_f (% vol.)	G_{IC} (init.) (J/m ²)	G_{IC} (prop.) (J/m ²)
cCF/PA6-I	FFF			
<i>With walls</i>		30	980 ± 250	1860 ± 346
<i>Without walls</i>		35	837 ± 262	1680 ± 207
CF/Epoxy [350]	Oven	51	250	500
	Oven	53	210	370
	Autoclave	53	290	320
	Autoclave	53	190	240
CF/Epoxy [80]	AFP	57	≈ 200	≈ 600
CF/PEEK [349]	Molded	-	1330	1540
	Molded	-	1275	2110
GF/PA6 [352]	Molded	30	-	≈ 1900

CF/PA [353]	Molded	55	-	1100
CF/PA [354]	Hot-press	-	-	2100

The microstructure of samples with walls has only a small effect on the resistance to delamination (+10 %). This can be explained by the higher fiber content reached for wall-less samples (35 % vol. and 30 % vol. for samples without and with coating walls, respectively) and by the toughness of PA6 walls which is much higher than the toughness of composite.

According to the values collected, the printed cCF/PA6-I composite exhibits competitive delamination resistance properties compared to CF/Epoxy composites manufactured by more traditional processing routes, while remaining lower than most thermoplastic PEEK carbon composites but in the same range as CF/PA. Thus, contrary to the negative *a priori* of the FFF process dealing with delamination properties, good interlaminar properties of cCF/PA6-I laminates are obtained thanks to complex dissipative mechanism. Several points can explain this trend:

- Ductile failure of the PA6-I matrix covering the carbon fibers. Figure 78.a and b show SEM images of delaminated surfaces for both cCF/PA6-I with and without walls (a, c) at two magnifications (x 20, x 200). For samples where walls are retained, plastic deformation of the PA6 coating is observed, confirming their contribution to toughness.
- cCF/PA6-I samples manufactured with the Markforged® printer have a lower fiber volume fraction than other processes, resulting in a prevalent matrix effect. Overall, the nature of the polymer matrix and its toughness play a major role in the interlaminar bonding strength of composites, as well as the fiber/matrix interfacial dissipative mechanisms (debonding and friction).
- Relatively low fiber/matrix interfacial shear strength. At high magnification (x200), carbon fibers have clean surfaces and fibers pull-out is observed. This is typical of low fiber/matrix interfacial bond strength and leads to adhesive failure with crack propagation along the fibers/matrix interface in delamination tests.
- An additional dissipative mechanism as cCF/PA6-I also experience inter and intra bead failures.
- Fiber bridging which induced numerous fiber breakage and unaligned fibers with the direction of delamination.

- Interfilament distance gap can be estimated to be about 0.13 mm Table 6 resulting in large in-plane porosities (Figure 78.g).

The initial diameter before printing is 380 μm for carbon-reinforced filaments and reaches 931 \pm 71 μm after printing. On similar materials, Goh et al. [90] quantified a 250 μm overlap between each round trip bead for cCF/PA6-I leading to very fiber-rich areas (Figure 78.f and g). These defects also referred to as “singularities” in the AFP field, are not specific to FFF [80]. The overlap and inter-bead porosity, only slightly affect the out-of-plane properties confirming the results on the interlaminar properties of the carbon/epoxy composites manufactured by AFP. Indeed, the singularities of the AFP greatly influence the transverse in-plane properties and compression properties but tend to increase the out-of-plane properties due to the crack blockage mechanisms [355]. Their location is not reproducible between printed parts, which leads to a variation in print quality and explains the scatter of the critical strain energy release rate values shown above.

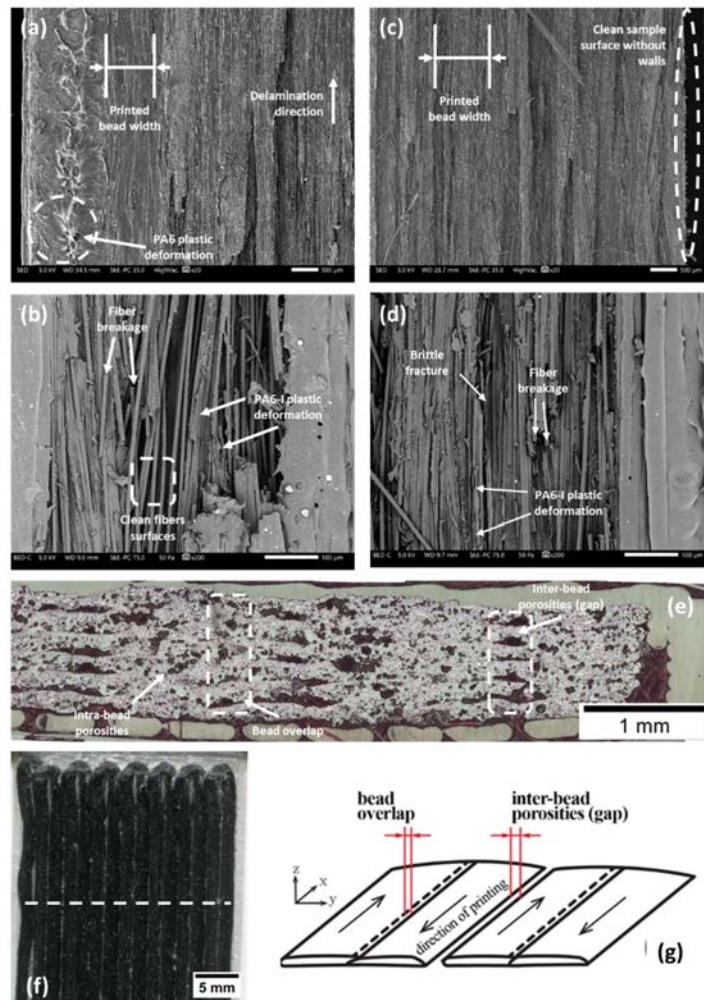


Figure 78 : Fracture surface of delaminated (a ,c) cCF/PA6-I and (b, d) cross-sectional view of (e) cCF/PA6- (observed under optical microscopy (magnification x10) and optical images of single printed layers of (g) cCF/PA6-I. (i) Schematic illustration of inter-bead porosity and overlap.

3. Evolution of mechanical performances under exposure to wet environment and accelerated seawater aging

Due to the well-known water sensitivity of the PA6 polymer, the mechanical properties are likely to vary in a humid environment as well as in outdoor applications. In this section, two studies were achieved. The first one aims at evaluating the evolution of hygromechanical properties (tensile, hygroexpansion, sorption) of 3D printed composites in humid environment for outdoor structural applications. To target applications in the field of marine engineering, a second study dedicated to accelerated seawater aging was performed. Initially, water diffusion and hygroscopic expansion over on water sorption at 40 °C were studied. As described by Davies et al. [356] on glass fiber reinforced polyester composite, it has been assumed that a 10 °C increase in temperature leads to a doubling of the diffusion rate, so 6 months of seawater aging at 40 °C corresponds to 2 years of seawater aging at 20 °C. Then, the influence of 6 months immersion in seawater on the flexural properties of the 3D printed composites was studied as well as the reversibility of the flexural properties after exposure to seawater aging and drying in 50 % RH at 23 °C.

3.1. Sorption behavior and hygroscopic expansion

3.1.1. Moisture uptake and hygroscopic expansion in humid environment

Figure 79 shows the change in moisture content (M) as a function of relative humidity for cGF/PA6 and cCF/PA6-I. The overall sorption behavior is similar between samples and can be well fitted by the Park model [357] expressed by Equation 12.

$$M = \frac{Ab_L a}{1+b_L a} + sa + \frac{K_c s^n a^n}{n} \quad \text{Equation 12}$$

where M represents the water content in the material, a the water activity, A the Langmuir capacity constant, b_L Langmuir affinity constant, s the Henry solubility coefficient, K_c the equilibrium constant for the cluster formation and n the number of water molecules per cluster [39].

As a result, moisture sorption by printed composites follows a three-stage sorption typical of porous materials, probably due to their high porosity. When water activity is low ($a < 0.1$), water sorption is driven by Langmuir sorption where water is absorbed by the free amide bonds. In the present study, the effect of Langmuir sorption is ignored due to the lack of data on water activity below 0.1, so the Langmuir parameters are set to 0. In case of high water activity ($0.1 < a < 0.6$), the sorption follows a linear fit according to Henry's law. Finally, at high water activity ($a > 0.6$), water clusters appear in the material according to a Flory-Huggins type sorption.

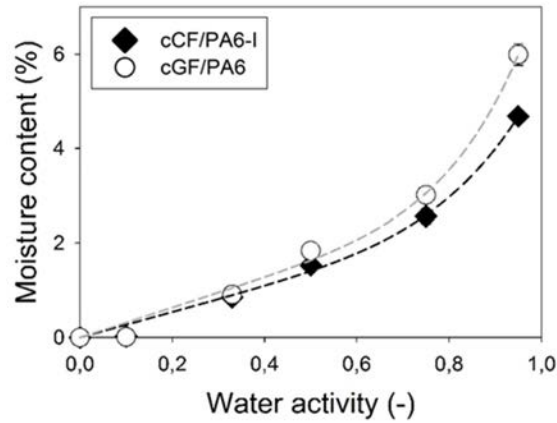


Figure 79 : Evolution of the moisture content of cCF/PA6-I and cGF/PA6 printed parts as a function of water activity (the dotted line represents the adequacy with Park model).

However, there is a slight difference in moisture content between the two systems. Indeed, at 98 % RH cGF/PA6 samples absorbed 30 % more water than their carbon counterparts despite their higher porosity (Table 5). A higher moisture content in glass samples can be explained by the different nature of the matrix. Indeed, the DSC analysis determined that the cGF/PA6 filaments had a glass transition temperature (T_g) at 50 °C and a melting temperature of 200 °C. The cCF/PA6-I filaments are composed of an amorphous polymer, with T_g at 135 °C, corresponding to polyamide 6-I. In the literature, PA6 absorbs more water (3 % at 50 % RH) than PA6-I (2 % at 50 % RH), resulting in a greater water uptake by cGF/PA6 [358]. One of the consequences of water sorption is the hygroscopic swelling. The swelling strains ε^h are calculated by equation 13 where θ^h is the hygroscopic swelling coefficient and M is the moisture content in the material.

$$\varepsilon^h = \beta^h M$$

Equation 13

The swelling of cCF/PA6-I and cGF/PA6 printed parts as a function of moisture uptake by the material are represented in Figure 80.a and b, respectively. Swelling is evaluated in directions (x, y, z)

depicting longitudinal, transverse and out-of-plane directions. Hygroscopic swelling increases monotonically with moisture content.

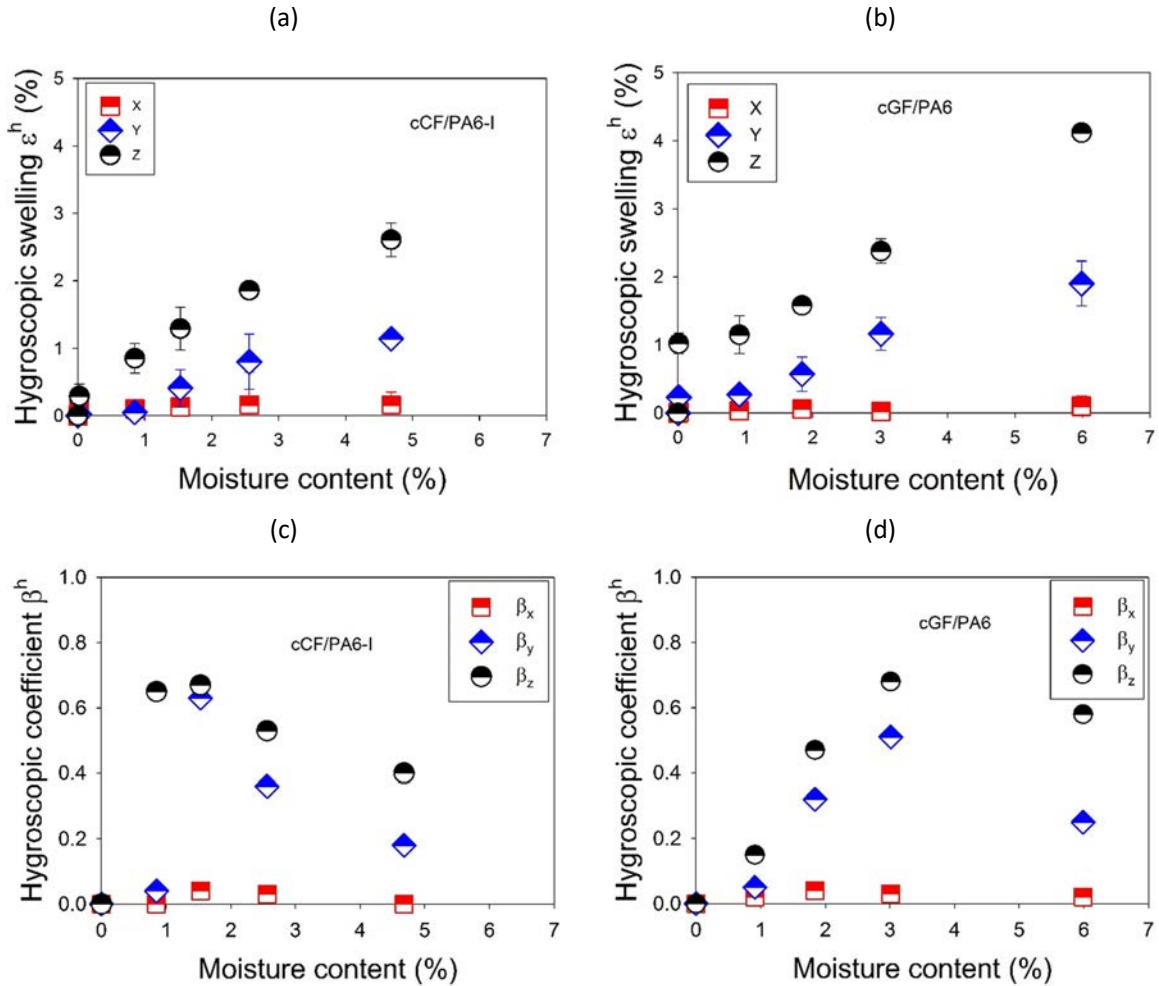


Figure 80 : Hygroscopic swelling of (a) cCF/PA6-I and (b) cGF/PA6 and hygroscopic coefficient β of (c) cCF/PA6-I and (d) cGF/PA6 in x, y and z direction as a function of moisture content after stabilization.

In the longitudinal axis (x), swelling is prevented by the stiffness induced by the orientation of the fibers. Transverse and out-of-plane directions exhibit a drastic difference in swelling properties, while the properties of the laminate properties are assumed to be transversally isotropic.

This phenomenon may be explained by the microstructure of the sample. Because of the non-overlapping areas between some printed beads in the transverse direction, and thus the higher

porosity distributed therein, swelling strains may not be transmitted efficiently with respect to the out-of-plane direction.

Porosities in the transverse direction may act as series connections, in which case all porosities will reduce induced swelling. Otherwise, the out-of-plane porosities will act as parallel connections, implying that the porosities have undergone hygroscopic swelling separately, resulting in less attenuation of the swelling.

Moreover, glass-fiber-reinforced show a greater hygroscopic swelling than carbon samples due to the higher water content and lower porosity in these samples. Based on equation 13, a linear relationship can be assumed between hygroscopic strain and moisture content. However, by plotting the slope, i.e., the hygroscopic coefficient β^h , against the moisture content of cCF/PA6-I and cGF/PA6, as shown in Figure 80.c, d, respectively, a reduction of β^h with moisture for cCF/PA6-I is observed, i.e., when free water transport occurs through the formation of clusters but also through voids. For cGF/PA6, β^h rises with moisture content up to 3 %, after which it decreases. The measured values of β^h are also compared with the literature. Several research teams have worked on various polymer matrices (epoxy, polyamide, etc.) with different treatments (storage in moisture-controlled chambers, immersion) [359]–[361]. These studies noted a linear increase in hygroscopic swelling as a function of moisture content indicating a constant hygroscopic coefficient despite the change in water content in the composite.

3.1.2. Evolution of water uptake and hygroscopic expansion during seawater aging

Figure 81 displays the change in moisture content for cGF/PA6 and cCF/PA6-I as a function of the square root of the conditioning time in seawater at 40 °C divided by the sample thickness. For cGF/PA6 composites, the moisture content follows a typical Fickian behavior where the moisture content raises linearly and reaches a plateau [362]. However, cCF/PA6-I composites do not follow Fickian behavior but also exhibit a moisture content that increases until a plateau is reached. cGF/PA6 appears to be water-saturated faster than cCF/PA6-I samples (24 days for cGF/PA6 and 41 days for cCF/PA6-I). The difference in sorption kinetic is probably due to the inter-bead porosity network observed for cGF/PA6 composites, which facilitates water diffusion by capillarity effect. In contrast to the relative humidity study, the maximum moisture content achieved for cCF/PA6-I is higher than for cGF/PA6 (12.3 ± 0.2 % and 10.0 ± 1.1 % for cCF/PA6-I and cGF/PA6, respectively). The higher water content for cCF/PA6-I can be explained by the higher porosity content. Indeed, in an

environmental study, it can be assumed that porosities play a moderate role because the water activity is not high enough to fill the porosities.

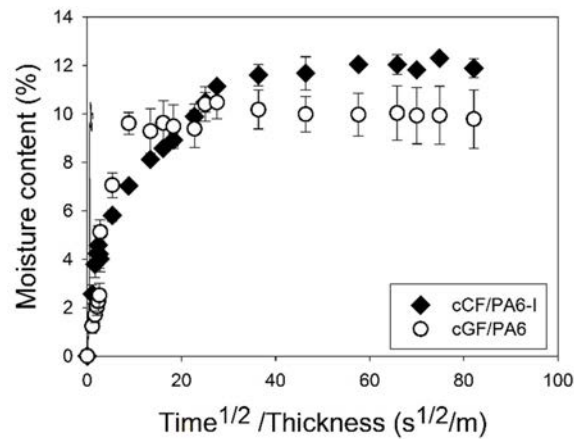
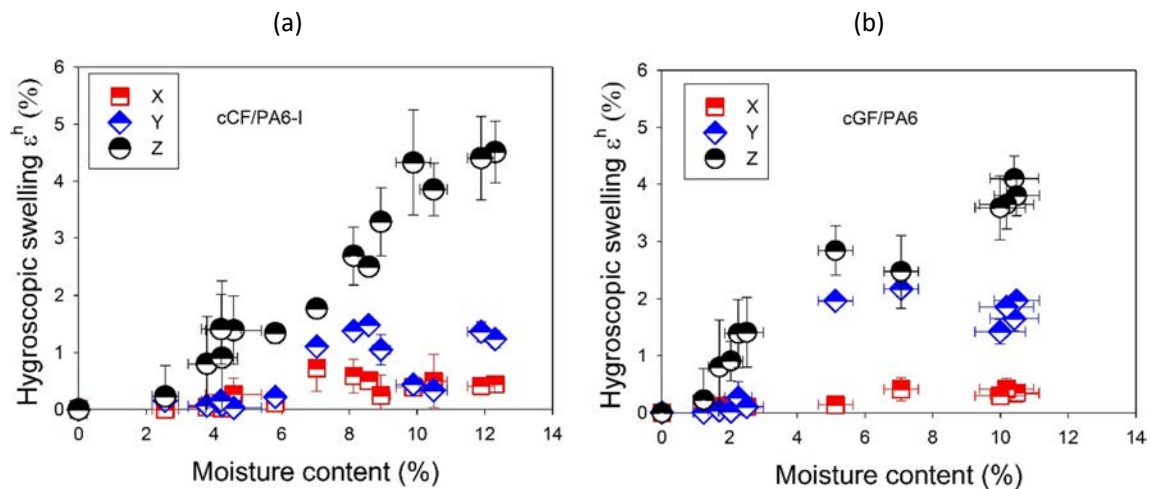


Figure 81 : Evolution of moisture content as a function of time square root divided by the sample thickness for cCF/PA6-I and cGF/PA6 samples immersed in seawater at 40 °C.

Water uptake leads to hygroscopic strains in the composite laminates. The swelling in (x, y, z) of the printed parts cCF/PA6-I and cGF/PA6 as a function of moisture uptake during seawater aging are shown in Figure 82.a, b. As in the environmental study, the hygroscopic coefficient (Figure 82.c, d) tends to vary as a function of moisture content for both cCF/PA6-I and cGF/PA6. However, by plotting the slope, i.e., the hygroscopic coefficient θ^h , against the moisture content of cCF/PA6-I and cGF/PA6 (Figure 82.c, d,) it appears that hygroscopic coefficient tends to vary as a function of moisture content for both cCF/PA6-I and cGF/PA6.



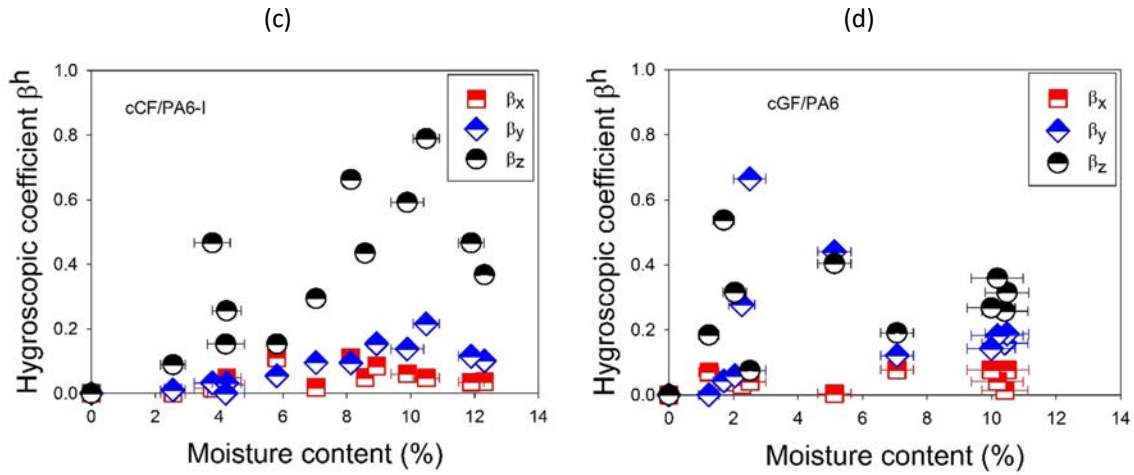


Figure 82 : Evolution of hygroscopic swelling (a, b) and hygroscopic coefficient (c, d) in x, y and z direction over moisture content for during seawater aging for cCF/PA6-I (a, c) and cGF/PA6 (b, d).

However, in the study of seawater aging, changes in hygroscopic properties are measured in transient regime, whereas they were measured after moisture content stabilization for the environmental study. Consequently, in order to compare the two sorption modes, only the values of the hygroscopic expansion coefficient after stabilization were taken into account (Table 9).

Table 9 : Average values of hygroscopic swelling in x, y, z directions for both cCF/PA6-I and cGF/PA6 composites after stabilization of moisture uptake.

	cCF/PA6-I	cGF/PA6
β_x	0.04 ± 0.01	0.05 ± 0.03
β_y	0.14 ± 0.05	0.17 ± 0.02
β_z	0.55 ± 0.18	0.30 ± 0.05

For cCF/PA6-I, the hygroscopic coefficient in the x- and z- directions for seawater aging were in the same range as the same coefficients for the environmental study (Figure 82.c). However, in the y-direction, the hygroscopic coefficient is lower for seawater aging compared to the environmental study (the minimum hygroscopic coefficient for the environmental study is $\beta_y = 0.20$). For cGF/PA6, only the hygroscopic coefficients in the x-direction are similar for seawater aging and hygroscopic swelling (Figure 82.d). For the y-direction, the minimum hygroscopic coefficient recorded is $\beta_y = 0.25$

while for the z-direction it is $\beta_z = 0.47$. It therefore seems that the swelling mechanisms are different from the seawater aging compared to the environmental study. This difference can be attributed to porosity network in cGF/PA6. In environment study, it can be assumed that water activity is not high enough to fill this porosity network, while during immersion these porosities are filled by seawater. Consequently, some of the water which diffuses into the composite material is located in the porosity network as free water and does not play a role in hygroscopic swelling. Hence, for a greater amount of water absorbed (up to 5 %), the hygroscopic swelling increases only sparsely, resulting in a lower hygroscopic swelling coefficient. The same observation was made by Gager et al. [363] on flax fiber/polypropylene composites where an increase in porosity from 5 % to 50 % did not lead to greater hygroscopic swelling but led to greater moisture uptake after storage at 98 % RH.

In order to better understand the influence of seawater aging on 3D printed composites, the evolution of hygroscopic swelling as a function of aging time was investigated (Figure 83). For both composites and in each direction, the hygroscopic swelling increased quickly (between 0 and 30 days) and then stabilized over the aging time.

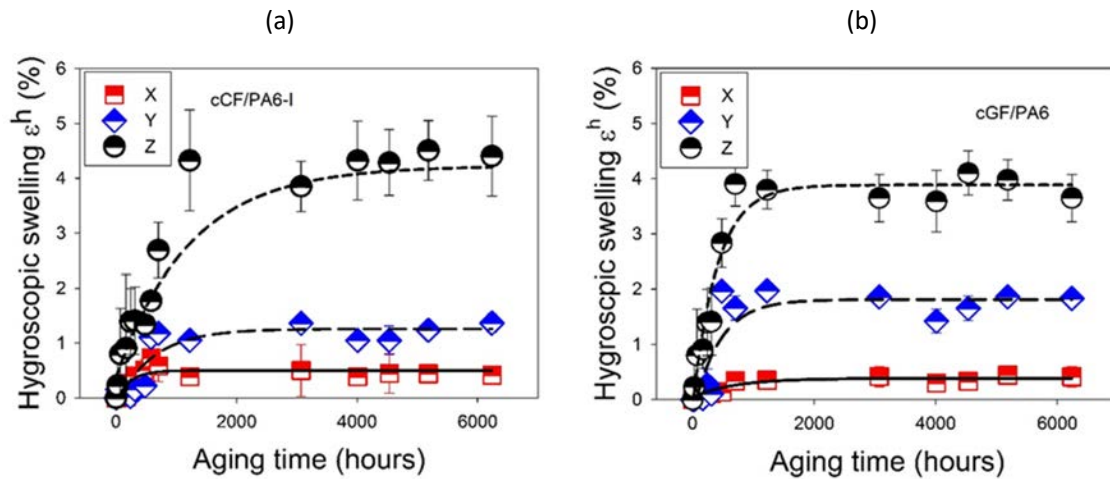


Figure 83 : Evolution of hygroscopic swelling in x,y,z directions during aging time for cCF/PA6-I(a) and cGF/PA6 (b) with exponential fit of the increase to the maximum (For cCF/PA6-I; $R^2 = 0.77$ in the X-direction, $R^2 = 0.82$ in the Y-direction, $R^2 = 0.95$ in the Z-direction while for cGF/PA6, $R^2 = 0.87$ in the X-direction, $R^2 = 0.82$ in the Y-direction and $R^2 = 0.94$ in the Z-direction).

3.2. Evolution of tensile behavior under different moisture conditions

Once a steady-state regime is reached under different moisture conditions (9-98 % RH), one can measure the longitudinal and transverse properties of continuous carbon and glass printed samples (Figure 84). The fiber volume fraction is set at 22.6 % vol. and 29 % vol. for cCF/PA6-I and cGF/PA6, respectively, for a thickness of 1 mm.

Moisture content conditioned by various environments leads to changes in the tensile properties of glass and carbon-printed composites. For carbon samples, the longitudinal tensile modulus and tensile strength depend on the fiber but are reduced linearly by approximately 25 % and 18 %, respectively, between 9 % RH and 98 % RH. The failure mode of cCF/PA6-I (not shown here) stored at 98 % RH showed more debonding than samples stored at 15 % RH. This difference in failure mode highlights the consequences of moisture-induced degradation, such as differential swelling between layers, which induces a weakening of the cohesion of the parts.

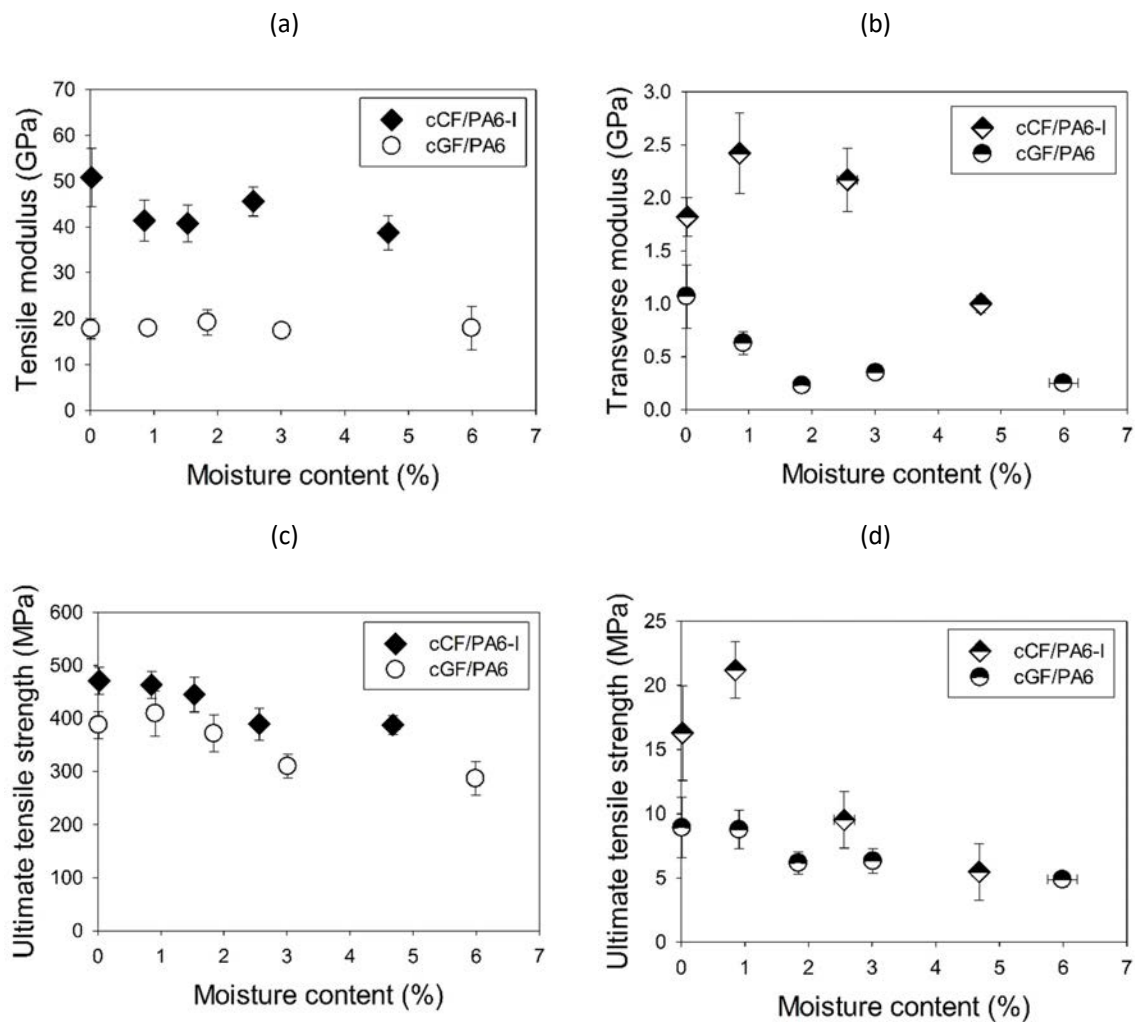


Figure 84 : Tensile modulus and ultimate strength of cCF/PA6-I and cGF/PA6 printed parts, respectively, in (a, c) longitudinal and (b, d) transverse direction after being moisture saturated.

Surprisingly, the cGF/PA6 tensile modulus is stable over a range of moisture variation despite the sensitivity of the PA matrix to moisture. Tensile strength decreases by 25 %. The slight decrease in cGF/PA stiffness could be explained by the microstructure in the plane; indeed, the non-overlapping in glass reinforced composites could reduce the consequences of hygroscopic swelling.

In addition, the sorption of water by the polyamide matrix induces a weakening of the matrix/fiber interface. Downes et al. studied the PA6/carbon interface and observed a decrease in IFSS (Interfacial Shear Strength) up to 40 % between tests processed at 0 % RH and at 90 % RH [364]. The reduction in fiber/matrix adhesion is due to the reduction in hydrogen interactions as well as change in the internal stress state in the interface region due to differential swelling between the fibers and the matrix [361]. The fiber/matrix interface is crucial for controlling the mechanical properties of composite materials. The degradation of the interface leads to a decrease in the mechanical performance of the composites.

The reversibility of the tensile properties is tested here after wetting at 98 % RH (until stabilization) and subsequent drying at 9 % RH. The two samples cCF/PA6-I and cGF/PA6 show full reversibility of stiffness and a slight reduction (-5 %) in strength, highlighting a predominant plasticizing effect of the polyamide matrix induced by moisture. A slight irreversible degradation could be attributed to the hygroscopic stress state within the materials, which is influenced by the heterogeneous distribution of the fibers between the printed layers and the differential hygroscopic properties between the components.

As shown in Figure 84.b, d, the influence of moisture content on transverse properties is very important. Water sorption considerably reduces the mechanical properties, but with different tendencies between carbon and glass fibers. Indeed, for carbon samples, transverse modulus and strength are reduced by about 45 % and 70 %, respectively, between 9 and 98 % RH. However, these trends are not monotonous and show a slight increase at low moisture content (< 1 %) and then a decrease. This may be due by the evolution of the state of stress at the fiber/matrix interface, which may be compressive due to a greater hygroexpansion of the polymer compared to the fibers. Above 1 % moisture content, reduced of fiber/matrix interactions and matrix stiffness can result in reduced transverse properties of the laminates. Further work is needed to confirm this hypothesis. Glass samples also show a reduction in transverse properties, but monotonically. Transverse stiffness and strength are reduced by 80 % and 45 %, respectively.

The reversibility of the transverse properties, measured after sorption-desorption cycles, shows that cCF/PA6-I has an irreversible reduction in strength of 40 %, while the stiffness is fully recovered. cGF/PA6 has an irreversible reduction in modulus (-65 %) and strength (-25 %).

Transverse properties are mainly controlled by the matrix and the performance of the fiber/matrix interface, but also by the microstructure of the composite. Although the plasticization of the polyamide matrix occurs again in this loading direction, the mechanical properties show an irreversible lowering which is mainly due to the microstructure of the printed samples as mentioned above (Figure 75). Indeed, inter-bead cohesion and weakening with increased moisture content are of paramount importance in relation to the fiber/matrix interface and the transverse properties of the reinforcing fibers (Figure 75). In addition, the polyamide coating influences the transverse behavior of the fibers and its moisture-induced degradation.

3.3. Influence of seawater aging on flexural properties of 3D printed composites

Once a stable water content value was reached, samples were left in seawater for 30, 90 and 180 days and flexural properties were measured. Three-point bending tests were used instead of tensile tests because of technical issue. Indeed, glue used to stick tabs on tensile tests is inefficient on wet surface and after immersion in water.

Figure 85 shows the evolution of the flexural behavior over 6 months of immersion (a and d), the evolution of the flexural strength (b and e) and the evolution of the flexural modulus (c and d).

The flexural behavior of cCF/PA6-I and cGF/PA6 printed composites shows a linear increase and a sudden drop in flexural stress caused by fiber breakage in the compression area. After water uptake, the flexural behavior retains the same shape with a lower slope and a lower maximal flexural strength.

Moisture uptake during aging in seawater for 6 months led to a significant change in the flexural properties of both cCF/PA6-I and cGF/PA6. For composites reinforced with continuous carbon fibers, the flexural strength and flexural modulus decreased by approximately 10 % and 80 %, respectively between the initial state and after 6 months of aging. The drop in flexural is observed following an exponential decrease ($R^2 = 0.98$). This form is linked to the evolution of water uptake which mainly occurs between 0 and 30 days of immersion and remains stable between 30 and 180 days.

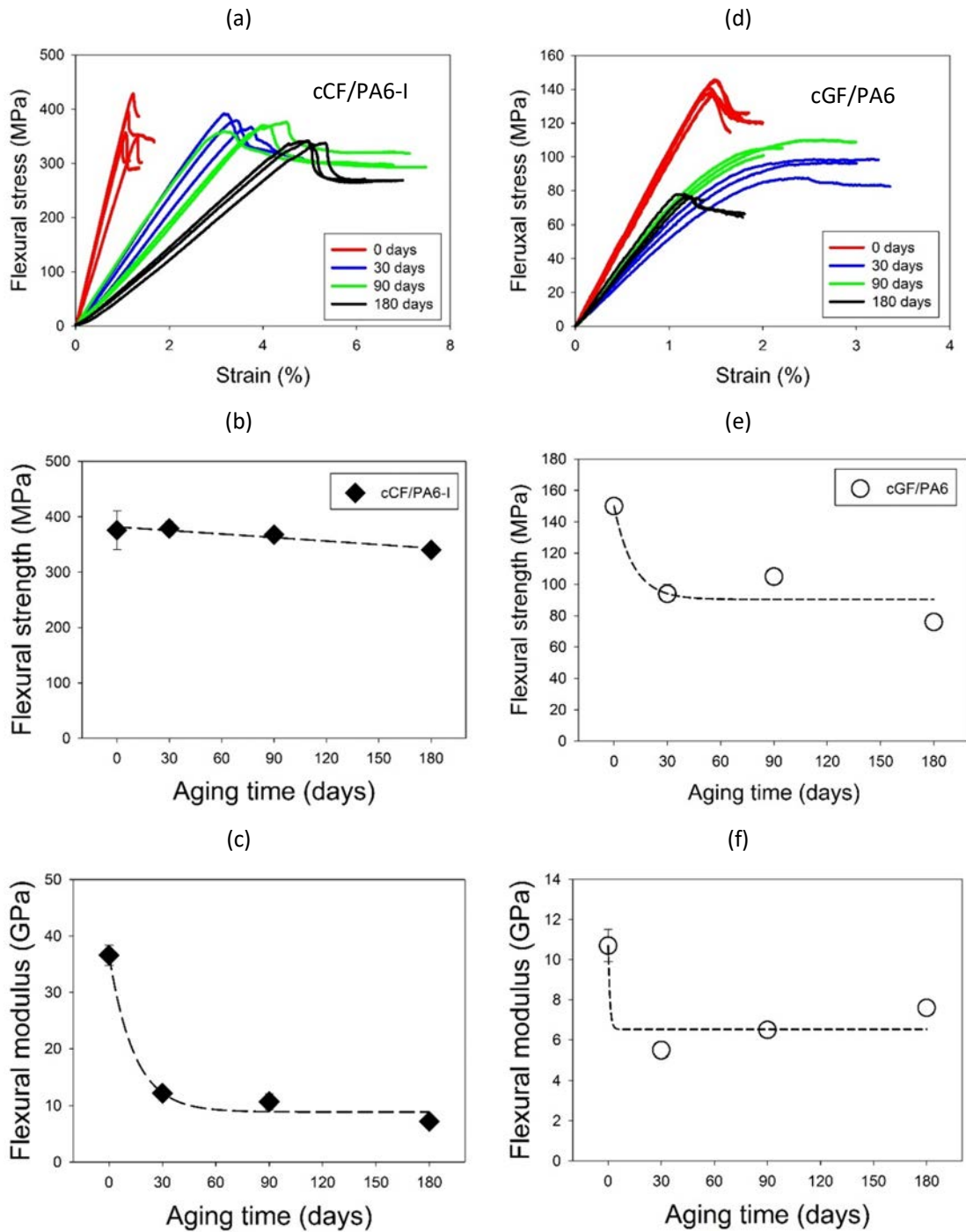


Figure 85 : Evolution in flexural behavior over aging time (a, d). Evolution of flexural strength over aging time (b, e) with a linear fit for cCF/PA6-I ($R^2 = 0.91$) and an exponential decay fit for cGF/PA6 ($R^2 = 0.92$). Evolution of the flexural modulus as a function of the

aging time (c, f) with an exponential decay fit ($R^2 = 0.98$ for $cCF/PA6-I$ and $R^2 = 0.86$ for $cGF/PA6$).

A similar observation is made for $cGF/PA6$ samples where a significant drop in flexural modulus and strength is observed between 0 and 30 days (-50 % and -32 % diminishing of flexural strength and modulus, respectively) and remains stable between 30 and 180 days after an exponential decrease in flexural strength and flexural modulus ($R^2 = 0.92$ for flexural strength and $R^2 = 0.86$ for flexural modulus).

To better understand the damages induced by seawater aging, a study was performed on the reversibility of flexural properties of 3D printed composites. On this purpose, a comparison is done with wet and dried samples after storage at 50 % RH at 23 °C until stabilization. Results are shown in Figure 86.

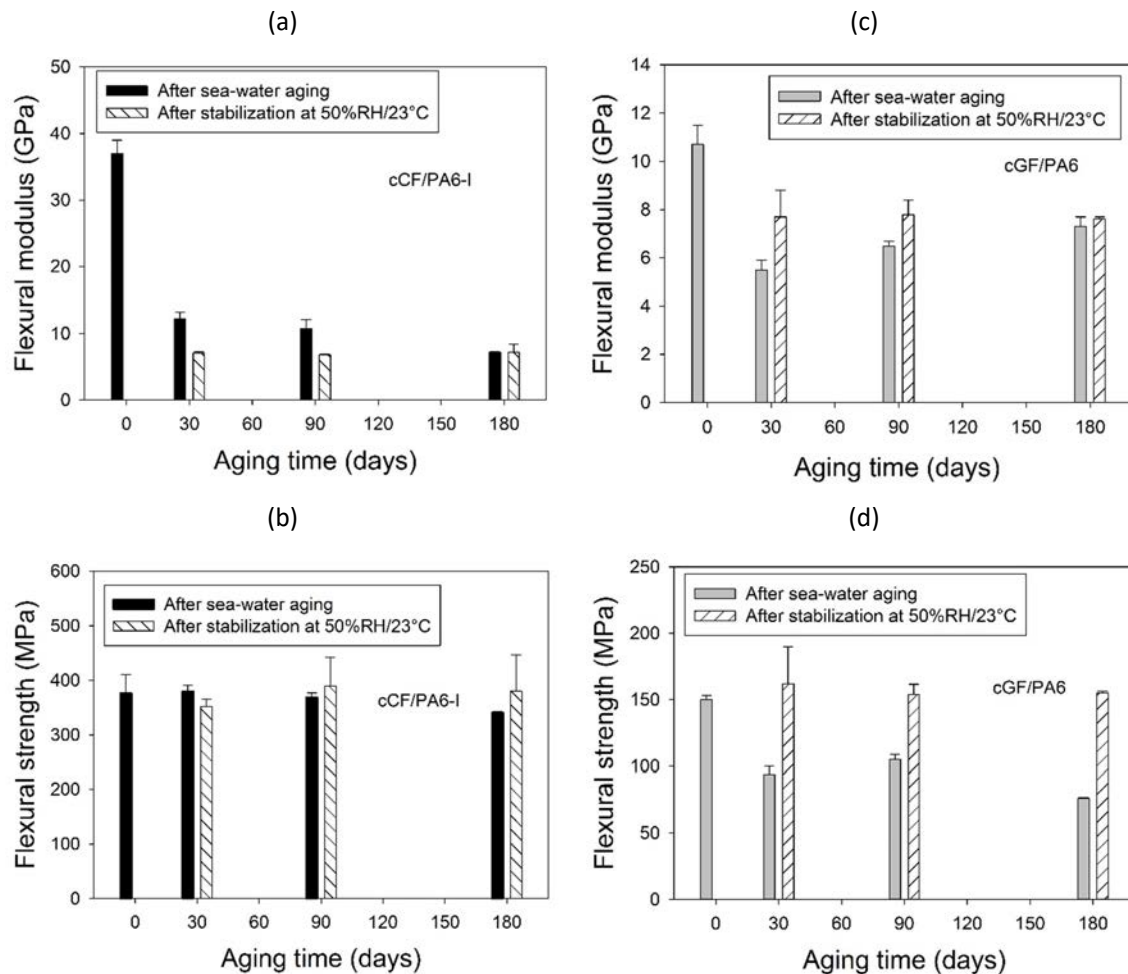


Figure 86 : Comparison of flexural stress (a, c) and flexural modulus (b, d) between samples where mechanical performances were measured after sea aging and samples where flexural performances were measured after stabilization at 50 % RH at 23 °C until stabilization for both cCF/PA6-I (a, b) and cGF/PA6 (c, d).

Unlike results found in the literature, e.g. Prabhakaran et al. [365] who observed an irremediable decrease in flexural modulus for continuous carbon/PA6 composites after 6 months in seawater aging at 60 °C and saturated at 50 % RH at 23 °C (-28 %). Here, for cCF/PA6-I, the flexural strength remains stable during aging in seawater. With regard to flexural modulus, drying does not allow to recover the initial properties even after a short aging duration (30 days) with even weaker properties after weight stabilization at 50 % RH at 23 °C. This result shows that irreversible damage to cCF/PA6-I occur during aging, altering the elastic properties rather than the fracture properties.

cGF/PA6 printed composites show rather stable properties with a seawater aging time of 6 months, which is very encouraging and makes them suitable for some marine engineering applications under severe conditions. Drying allowed cGF/PA6 to fully recover flexural strength but only 71 % of the flexural stiffness. Thus, cGF/PA6 composites exhibit a combination of reversible and irreversible degradation mechanisms, such as degradation of the fiber/matrix interface, which is a key parameter of the bending properties of the composite [86].

Seawater aging of cCF/PA6-I results are not straightforward and unusual regarding the seawater aging effect of composites. Usually, seawater aging leads to a decrease of mechanical strength (tensile or flexural) while the modulus undergoes only a slight decrease [113], [365]–[370]. Some hypothesis can be intended:

- PA6-I shows higher glass transition temperature than PA6, i.e. 135 °C versus 50 °C, respectively. As described by Arhant et al. [113], PA6 shows a significant decrease in glass transition temperature after water uptake until saturation (-12.1 °C). Thus, during seawater aging, PA6 is in the rubber state while PA6-I remains in the glassy state. During water uptake, due to greater chain mobility, cGF/PA6 will undergo greater matrix reconfiguration and potential stress release than cCF/PA6-I, while the cCF/PA6-I composite may be more susceptible stress-induced damage (differential swelling between components).

- As observed in section 2.2.2 of this chapter, a low fiber/matrix interfacial bond strength was stated for cCF/PA6-I promoting the non-reversible behavior of cCF/PA6-I after seawater aging.

- The desorption step was done at 50 % RH at 23 °C until stabilization to reach the initial environmental conditions for the two nature samples. As observed in the literature, a residual moisture content remains in the composite after drying [371], [372]. Consequently, the moisture content at 50 % RH at 23 °C is higher after desorption than in the initial state, which negatively affects the mechanical properties.
- As explained by Arhant et al [113], PA6 does not undergo hydrolysis after 6 months of seawater aging and DSC analysis showed that the glass transition temperature of PA6-I remains stable after drying. Hence, seawater aging did not induce hydrolysis of PA6-I.
- The porosity distribution varies greatly between cCF/PA6-I and cGF/PA6 composites, as observed in section 1.1 of this chapter. After drying at 50 % RH at 23 °C, cCF/PA6-I samples are thicker (+3.1 %) compared to the initial state while cGF/PA6 samples recover their initial thickness. One explanation is the expansion of porosities in the z-direction during seawater aging, caused by the hydrostatic pressure inside the water-filled porosities. This increase is more important for cCF/PA6-I because the porosities are mainly located in the interlayer areas, while the porosities of cGF/PA6 are located between the printed beads. Porosity expansion is confirmed by a decrease in density between the initial state and after drying at 50 % RH at 23 °C for cCF/PA6-I (-3.6 ± 0.3 %) and cGF/PA6 (-1.1 ± 0.2 %).

The main difference between cCF/PA6-I and cGF/PA6 being the nature of the polymer matrix and the distribution of porosities, deeper investigations should be carried on the seawater aging of PA6-I (evolution of mechanical properties and degradation), on the evaluation of fiber/matrix interface of cCF/PA6-I and cGF/PA6 and on analyses such as micro-tomography to better understand the role of the porosity network on water diffusion, stress state and induced damages.

Conclusion

3D-printed composites with discontinuous fibers are increasingly being studied, but their mechanical performance is still quite moderate. This explains why composites reinforced with continuous glass and carbon fiber have recently been considered in the literature and in the present chapter.

The printing process has been shown to achieve a high level of porosity, increasing the porosity level compared to filaments by a factor 8. The Inter-bead areas represent the main location of the

porosity. The turning back of the filaments, which obviously occurs during the printing process, also creates a singular microstructure that must be taken into account in the manufacture of the parts. These turn-backs also lead to heterogeneity in fiber content and a potential concentration of stress. The volume fraction of the fibers is currently limited and changes with the thickness of the sample due to the specific printing configuration. Thus, the fiber content of the printed parts depends on the geometry. In this chapter, an investigation of the mechanical properties of the carbon and glass specimens has been carried out. The longitudinal properties are influenced by the volume fraction of the fibers according to a typical Rule Of Mixture (ROM) where the properties of the fibers are evaluated by single tensile tests. Since the volume fraction of the fibers varies according to the thickness of the composite, predicting the properties of complex parts requires more detailed research. Even if the longitudinal properties are only slightly influenced by process-induced defects, the transverse properties are considerably impaired. Indeed, the inverse ROM does not match the experimental data. Transverse properties are currently a limiting factor for the development of 3D printed parts but also for the prediction of the properties. Due to the strong influence of the printing process, the studies have focused on the behavior of the printed part rather than on the material properties. Furthermore, it should be noted that there is no standard dealing with the characterization of continuous fibers composites manufactured by FFF.

In this chapter, the interlaminar fracture behavior of continuous carbon/PA6-I was studied by DCB mode I delamination tests with two printing configurations, with and without coating walls. It was interesting to note that the cCF/PA6-I composites tested here have interlaminar properties as high as those of conventionally manufactured composites. These observations are contrary to most claims in the literature. SEM observations of the microstructure and fracture highlight the presence of singularities such as overlap, intra and inter-bead porosities. These peculiarities, originating from the low pressure applied during processing and the geometry of the filaments, result in high porosity of the printed parts. In contrast to the in-plane transverse properties, these voids do not appear to alter the out-of-plane properties of the printed cCF/PA6-I composites. Overlaps may have a more negative impact on crack resistance properties than in-plane voids. Overlaps lead to an increase in local fiber content that reduces the energy required for crack initiation. In addition, the high local content of fibers creates very fragile areas that promote the propagation of unstable crack. Similarities can be found with composites manufactured by automatic fiber placement, highlighting the need for converging research paths on these topics.

The coating walls, inherent in the printing process result in higher delamination resistance for cCF/PA6-I composites caused by the higher interlayer toughness of the polymer wall. Greater scatter

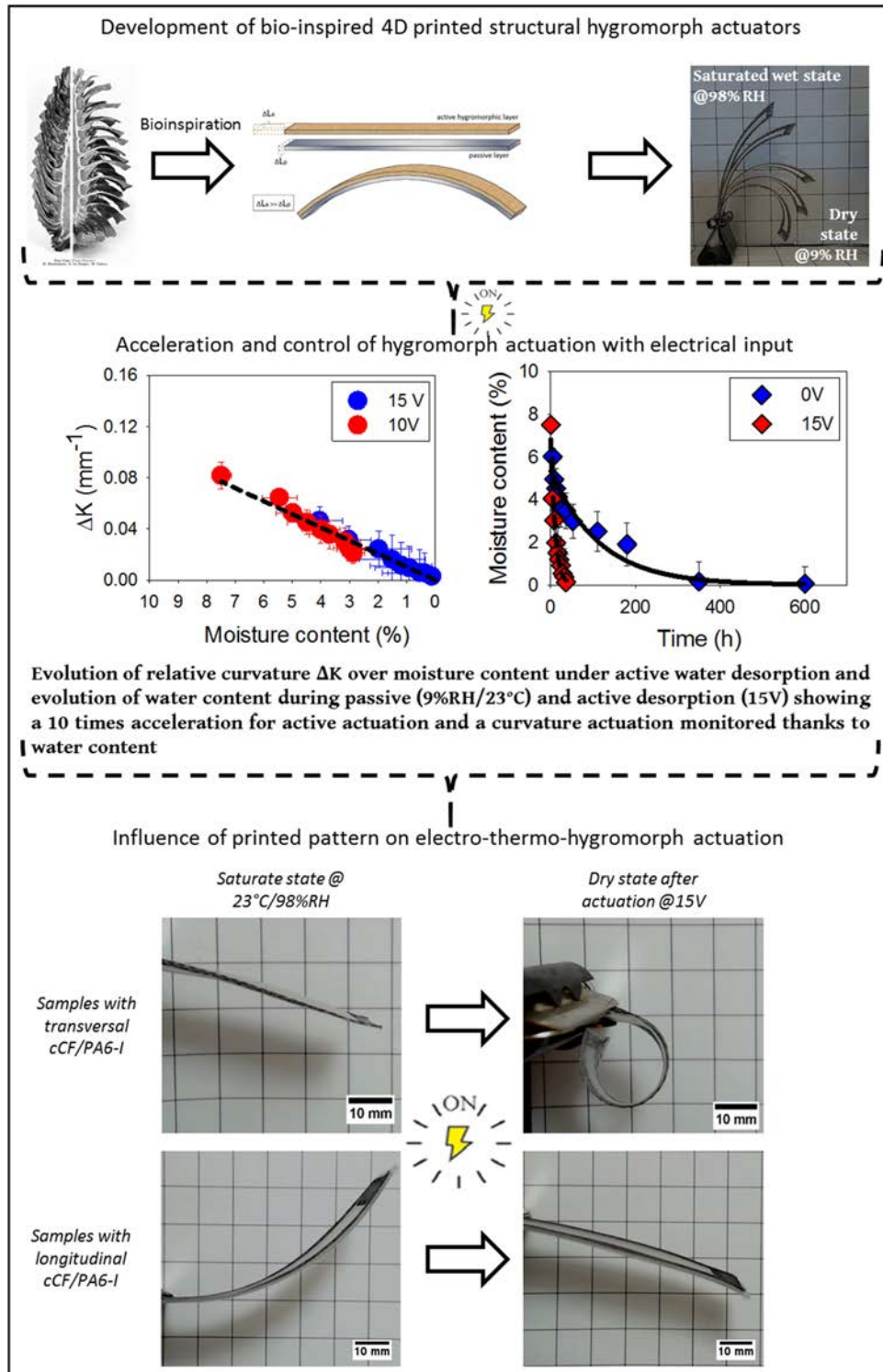
was also observed for coated samples due to an additional dissipation mechanism. Consequently, the interlaminar performance of 3D printed composites is highly dependent on the printing parameters. Further work should be undertaken to evaluate the effect of the printing trajectory (loop) on delamination properties.

In order to promote the use of these composites for outdoor applications and marine engineering, a study on the evolution of the mechanical performance of 3D printed composites in various moisture environments was carried out (9-98 % RH) and also on aging in filtered seawater at 40 °C for 6 months. Moisture sorption can lead to moisture contents of approx. 5-6 % for carbon and glass fiber composites and approx. 10-12 % when aging in seawater. In fact, moisture induces an orthotropic hygroscopic swelling influenced by the original microstructure (repeatable porosities, heterogeneous fiber distribution) of the composites as well as by the hygroscopic nature of the material. Finally, a reduction in longitudinal (-18 % and -25 % for tensile strength for cCF/PA6-I and cGF/PA6, respectively) and transverse tensile properties (-70 % and -45 % for transverse strength for cCF/PA6-I and cGF/PA6, respectively) is observed as well as a reduction in flexural properties (-10 % and -50 % for flexural strength for cCF/PA6-I and cGF/PA6, respectively) during seawater aging. As far as the environmental study is concerned, almost complete reversibility of longitudinal properties can be achieved, thus highlighting a main plasticization mechanism of the PA matrix. In the transverse direction, the degradation is only partially reversible, which reflects the drastic effect of the microstructure and the defects. With respect to seawater aging, an almost complete recovery is observed for cGF/PA6 composites after 6 months of aging at 40 °C, which corresponds to 2 years long aging at 20 °C, which is promising for their use in marine engineering applications. For cCF/PA6-I, the flexural strength is interestingly constant during seawater aging (-10 % of flexural strength drop), but the flexural stiffness decreases irreversibly after seawater aging (-80 % between the initial state at 50 % RH at 23 °C and after 6 month of sea aging and new stabilization at 50 % RH at 23 °C).

Several improvements are now needed for 3D printing of continuous fiber based composites and future work should be done on the development of customized composites with different types of polymers to prevent moisture uptake and enhance the durability of the composites. Work needs to be performed on the printing parameters in order to improve and to tailor the microstructure of 3D printed composites (reduction of porosity, customized fiber distribution to reduce differential swelling).

Finally, following the paradigm of biomimicry and 4D printing, the hygro-sensitivity of the polyamide matrix can be used as an advantage to develop new functionalities such as self-deploying structural actuators triggered by moisture variation.

Chapter 4: Bio-inspired reversible electro-thermo-hygro shape-changing materials by 4D printing



The present chapter introduces a novel concept of 4D printed continuous carbon fiber/Polyamide 6-I composite (cCF/PA6-I) printed thanks to a commercial 3D printer, i.e. MarkTwo® from Markforged®, which is commonly used for structural applications.

First of all, moisture-induced autonomous actuation (hygromorphing), with a biologically inspired bilayer microstructure is presented and discussed. In this study, the bilayers are made of one layer of cCF/PA6-I and one layer of pure PA6 and are referred to in the following section as cCF/PA6-I:PA6. Those printed cCF/PA6-I:PA6 bilayers are stored at different relative humidities (9 %, 33 %, 50 %, 75 %, 98%) to evaluate their autonomous hygromorphic behavior in terms of curvature.

Then, a novel concept of multi-stimuli responsive actuator, namely electro-thermo-hygromorphic principle, is described using similar materials. The effect of an electrical stimulus at different voltages (10 V and 15 V) applied to samples saturated at 98% RH is studied by analyzing the influence of electrical stimuli on the heating of materials by Joule effect, moisture content and actuation reactivity and responsiveness.

Finally, different printing patterns are evaluated to tune the actuation performance of the multi-stimuli responsive composite.

1. Concept of 4D printed electro-thermo-hygro-morphic structural composite materials

Polyamide and carbon fibers have been selected as components for the design of smart composite materials. The current actuation of 4D printed smart composites is mainly triggered by thermal expansion of the polymer and its Coefficient of Thermal Expansion (α) governed by thermal strains ϵ_{th} equations as shown in Equation 14:

$$\epsilon_{th} = \alpha \cdot \Delta T \quad \text{Equation 14}$$

Where ΔT is the temperature range applied during actuation. Here, hygromorphing is introduced through the moisture sensitivity of polyamide (PA6 and PA6-I) and the hygroscopic strains ϵ^h where CTE is substituted by the Coefficient of Hygroscopic expansion (CHE β) and ΔT by ΔM which is the variation in moisture content within the material. The CTE of polymers in the longitudinal and transverse directions is 3800 and 5000 times lower than the hygroscopic expansion (β^h), confirming their encouraging potential for actuation (Table 10).

Table 10 : Values of coefficients of thermal and hygroscopic expansion for cCF:PA6-I longitudinal, transverse, and for pure PA6.

Materials	α (10^{-5} K^{-1})	β (10^{-1} -)
cCF/PA6-I longitudinal	-	-
cCF/PA6-I transverse	4.9 ± 0.4	2.6 ± 0.3
PA6		3.4 ± 0.4

The orientation of the carbon fibers also affects the thermal and the hygroscopic expansions (Table 10). Although in the longitudinal direction of the fiber, the hygroscopic and thermal expansions are negligible, the coefficients α and β of the composites in the transverse direction assume the highest strain expansion potentials due to the anisotropy of the carbon fiber (cf Chapter 3: Mechanical and hygromechanical properties of continuous carbon and glass fiber composites).

This is therefore a critical parameter to design the microstructure of shape-changing composite materials made with thermally and/or hygroscopically active and passive materials. Continuous fiber composite materials and a 4D printing process were selected to tailor the orientation of the fibers

and consequently their stiffness, thermal and the hygroscopic anisotropy properties, that are key factors in promoting bending actuation.

The hygromorphic composite materials possess a bilayer microstructure inspired by the one of natural hydraulic actuators (pine cones for instance [168], [176]), printed with two layers having different hygro-elastic properties. The layer made with the continuous carbon fibers embedded in a PA6-I matrix is hygroscopically and thermally passive (i.e., with a low thermo-hygroexpansion). The printed cCF/PA6-I layer is used here as a mechanically resistant lamina with high stiffness against moisture. The other layer of pure PA6 matrix (Figure 87.a) is the hygroscopically and thermally active one.

The optimal stacking sequence for a maximal bending actuation is determined via bimetallic strip theory calculations [320] (Equation 2, 3). The model is based on the thickness ratio between active and passive layers and their hygroelastic properties [218]. An increase in thickness would geometrically increase bending stiffness and actuation force, but reduce the targeted morphing curvature. Hence, depending on the requirements and the application, a compromise should be found between the stiffness and responsiveness of the actuator. The differential hygroscopic expansion between the printed layers causes the hygromorphic composite to autonomously bend in various external humid environments (Figure 87.a).

An autonomous response with large responsiveness is produced (curvature variation about $0.088 \pm 0.011 \text{ mm}^{-1}$), however a slow response was also noticed due to the transitory and diffusive water transport within the material [373], [374]. This may limit the up-scaling of hygromorphic composite structures, and also limit their use for applications such as soft robotics, where passive actuation is less of a requirement than controlled actuation. To overcome this issue, a mechanism capable of actively controlling the moisture content and the resulting hygroscopic strains and therefore reaching a dedicated position of the shape-changing composite material has been elaborated. The concept is based on the work of Hamedi et al.,[212] who exploited the hygroscopic expansion in an electrically activated paper. A similar approach to develop electro-thermo-hygomorphs through 4D printing for structural and load-bearing composite materials has been used, rather than in soft solids such as paper. The electrical functionality is here embedded within the cCF/PA6-I:PA6 hygromorphic composites with the carbon fibers acting both as reinforcement and as an electrically conductive circuit. Tailoring the pattern of the carbon fibers makes it possible to control the stiffness distribution along the sample, i.e., its responsiveness and electrical conductivity, and thus finally, the reactivity. Fused Filament Fabrication (FFF) has been used here to construct the architecture of the electrical

circuit and the reinforcement. The layer containing the continuous carbon fibers is printed in a pre-optimized U-shape pattern to promote the electrical conductivity while maintaining a degree of freedom for the structure to actuate (Figure 87.a).

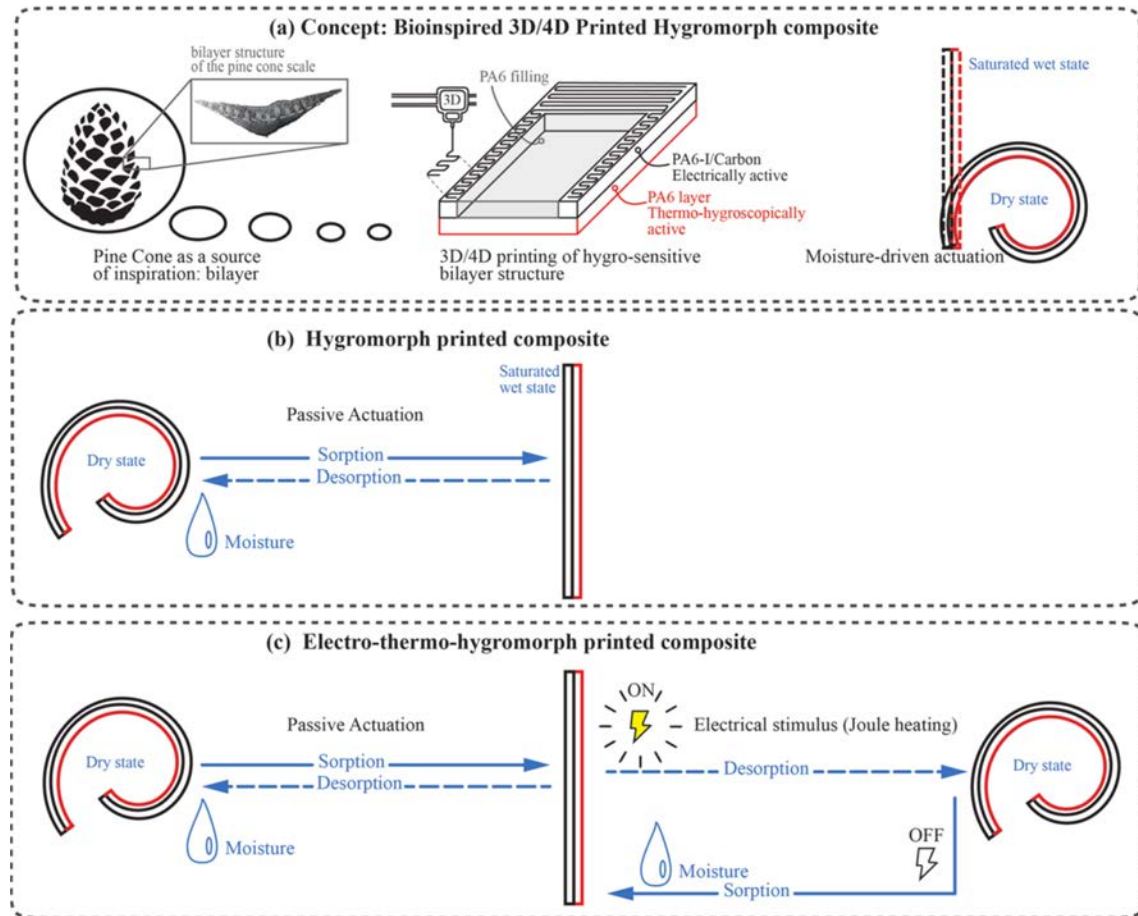


Figure 87 : a) Principle of hygromorphic composite materials. A pine cone actuator microstructure (inset: bilayer structure of the pine cone scale) is mimicked in a bilayer configuration. The materials are selected with at least one of them being moisture sensitive (the PA6 polymer in this case). 3D printing enables the manufacturing of complex architecture possessing various stiffness and electrical conductivity distributions. The variation of the relative humidity leads to moisture uptake and internal hygroscopic stress distributions within the bilayer and a resulting bending actuation. b) Initial state of the bilayer composite dried at 9 % RH and 23 °C, i.e., the composite is curved. Upon moisture sorption, the composite straightens. c) From dry to wet state the composite is similar to (b) in shape. At saturated wet state, an electrical stimulus leads to an increase of temperature by Joule effect. The moisture content then quickly reduces and allows controlling the actuation (return to dry curved state). When the electrical current is switched off, the temperature decreases and the moisture content increases, depending on the environmental RH at which the sample is exposed to. The material behaves as an autonomous and reversible hygromorphic actuator.

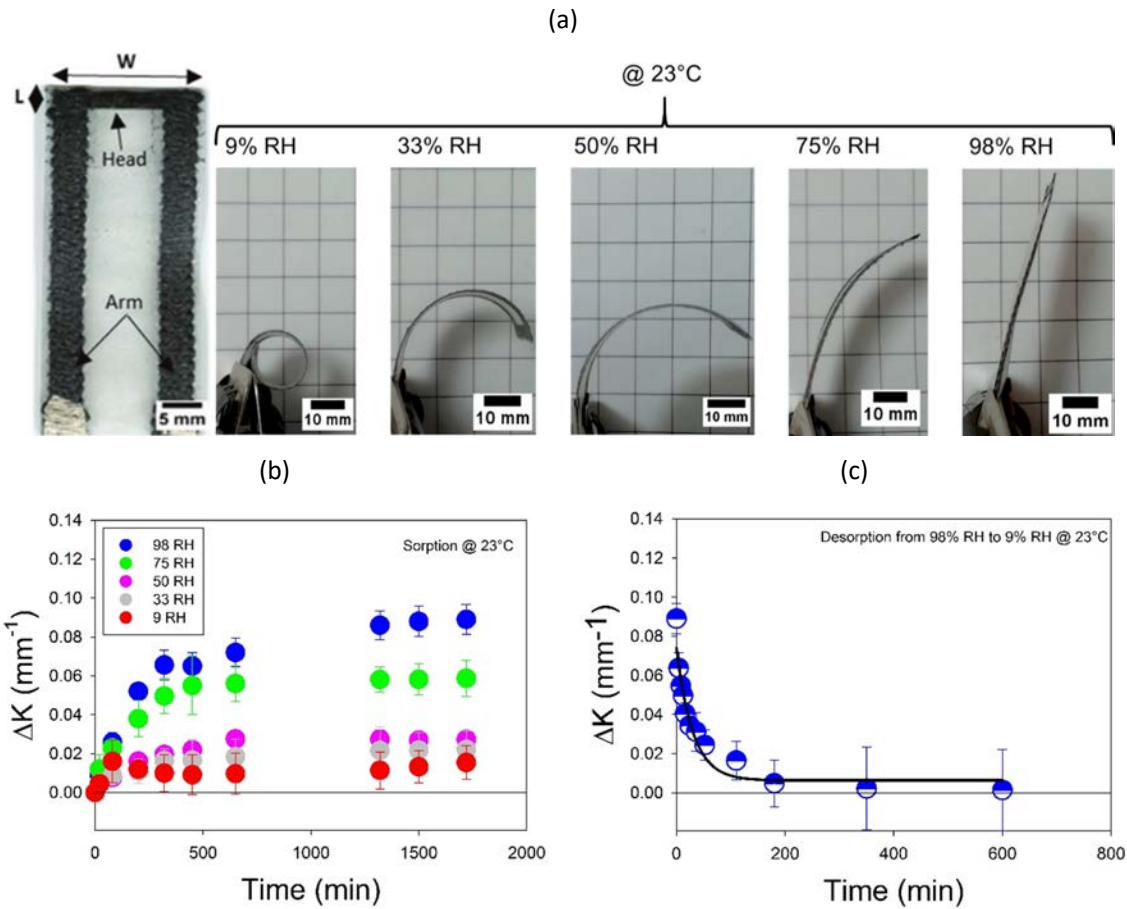
The application of an electrical field to the moisture saturated sample (RH = 98 % in Figure 87.b) leads to an electrical Joule effect-induced heating and a rise of the temperature that may vary versus the input voltage and the electrical conductivity of the composite layer. The variation of the temperature also leads to a change of the moisture content. The increase in temperature, potentially combined with the thermal expansion of the polymeric material would contribute to a thermal actuation similarly observed by Wang et al. [31]. Contrary to the water diffusion within a polymer or a composite, the thermal diffusion induced by the electro-heating effect is a fast kinetics phenomenon [184]. Moisture-driven actuation could be therefore accelerated through the desorption of the moisture out of the composite material. The stiffness and the hygroscopic shrinkage of each layer is altered by the presence of this mechanism. Once the electrical field is switched off, the autonomous moisture sorption drives back the morphing behavior. In the present concept, the hygroscopic behavior of the bilayer is used for actuation responsiveness, while the electrical stimulus allows to trigger and enhance the speed of the actuation.

2. cCF/PA6-I:PA6 bilayers as hygromorphic actuators

Continuous carbon fiber reinforced polyamide based composites have been manufactured with a rectangular shape (L = 70 mm and w = 20 mm) based on an optimal bilayer architecture designed using an equivalent bimetallic beam model (see section 4.1 of Chapter 1). The cCF/PA6-I layer has an overall thickness of 0.125 mm and is printed transversally to the length of the sample. The conductive network (not triggered during this step) has a rectangular-type U-shape pattern (Figure 88.a) with a ratio L/W of 0.25. When exposed to various humid environments (0 %, 9 %, 33 %, 50 %, 75 %, and 98 % RH) the cCF/PA6-I:PA6 bilayers show a very pronounced actuation authority (Figure 88.a). Dried samples exhibit a high curvature value at low RH values, then straighten in a humid environment. From image analysis it is possible to measure the relative curvature ΔK , which is the difference between the initial curvature $K_{initial}$ and the final one K_t . The actuated curvature evolves nonlinearly with the sorption time (Figure 88.b). A quick reactivity is observed during the initial time of sorption and once the saturation is reached the relative curvature has its maximum.

A maximum relative curvature of $0.088 \pm 0.011 \text{ mm}^{-1}$ (Figure 88.b) is recorded for samples stored at 98 % RH and 23 °C; this value is comparable to the one exhibited by natural fibers, paper or hydrogel based hygromorphic materials with similar thickness [177], [318], [319]. The maximum curvature depends on the moisture content (Figure 88.b, c). The higher the content, the larger the actuation responsiveness (Figure 88.b)). The reactivity however appears not to be affected by the moisture

content, and circa 12 h have been necessary for the full and autonomous actuation of the cCF/PA6-I:PA6 bilayers. This timeline corresponds to the moisture sorption, diffusion and complete saturation within the material itself. After reaching a stable value of the curvature at 98 % RH, the cCF/PA6-I:PA6 bilayers are placed in a dry environment (RH = 9 %) at room temperature ($T = 23\text{ }^{\circ}\text{C}$). During the drying step, the final value of ΔK is reached even faster (350 min) than in the case of sorption (1000 min—see Figure 88.c). Compared to the initial weight of the sample stabilized at 9 % RH, a close value is observed meaning a reversible moisture transport (Figure 88.d).



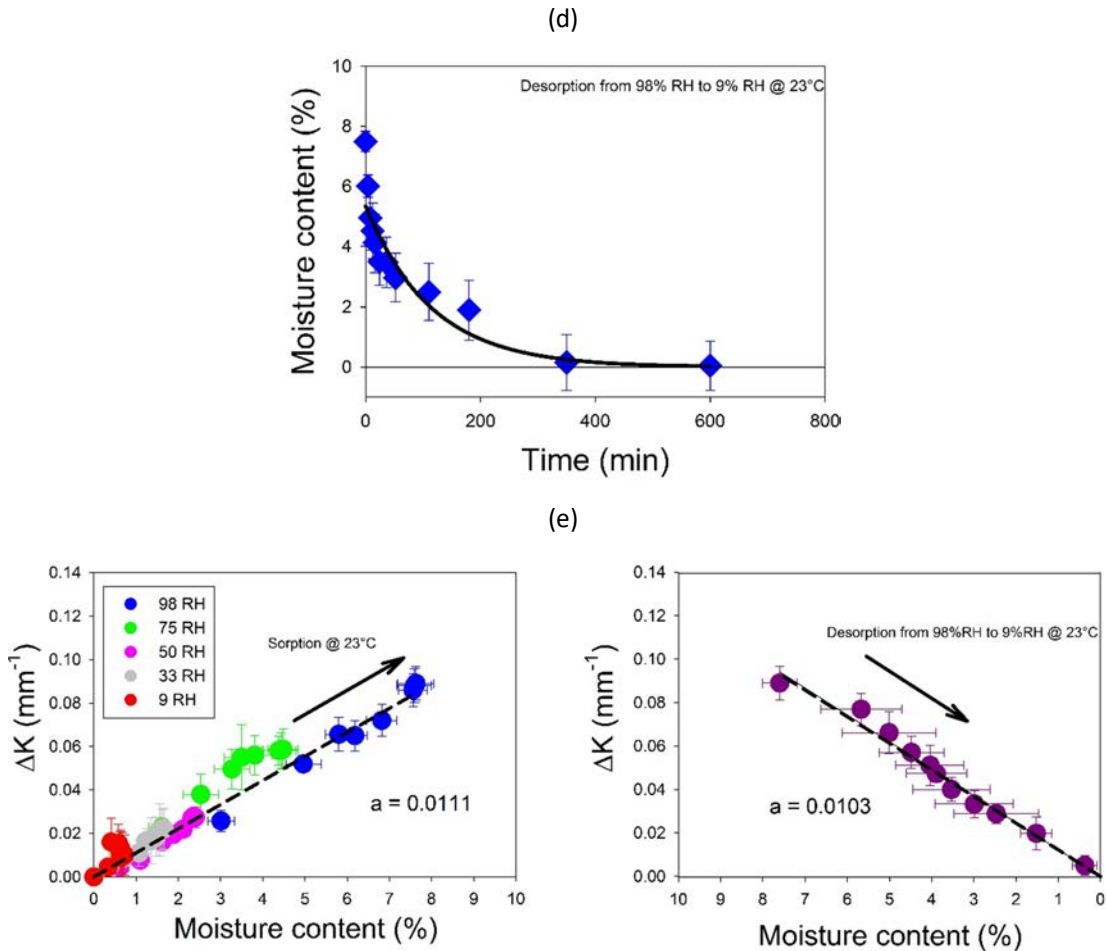


Figure 88 : a) Bilayer cCF:PA6-I/PA6 U-shape sample with transverse printed pattern and its shape evolution when the relative humidity is increased from dry (9 % RH) to a wet environment (98 % RH) at 23 °C. b) The evolution of the relative curvature actuation for different humidity levels shows the increase in actuation reactivity and responsiveness with the moisture content during sorption. c) The evolution of the relative curvature of the printed cCF:PA6-I during passive desorption from 98% RH to 9 % RH (exponential decay fit of $R^2 = 0.960$) at 23 °C shows the reversibility of the actuation. d) Evolution of the moisture content during desorption from 98 % RH to 9 % RH fitted with an exponential decay fit ($R^2 = 0.884$). e) Evolution of the relative curvature ΔK over a variation of moisture content during sorption at several RH levels (left) and desorption from 98% RH to 9% RH (right) at 23 °C. The changes of curvature due to sorption and desorption versus the moisture show a linear behavior ($R^2 = 0.99$ for sorption and $R^2 = 0.98$ for desorption) that allows to track the maximum amplitude of the induced curvature knowing the moisture content.

The faster achievement of the ΔK value also clearly shows that the mechanisms associated with moisture transport and autonomous responsiveness are fully reversible, but that the reactivity is different between the sorption and desorption phases. This actuation asymmetry has also been

observed on natural fiber based hygromorphic actuators, whose active and passive layers are based on similar materials [212], [269]. The hygromechanical effects within the passive layer are, however, different in the case of sorption or desorption. During sorption, the bilayers tend to straighten and the passive layer (cCF/PA6-I) is transversally loaded in compressive mode. On the contrary, during desorption the bilayers tend to bend and the passive layer is transversally loaded in tension. Since the transverse compressive stiffness of unidirectional laminates is generally higher than the transverse tensile one, the passive layer is easier to bend than to straighten, which affects the actuation speed.

The global hygromorphic behavior (sorption/desorption) is illustrated by the evolution of the relative curvature versus the moisture content for several moist and desorption conditions (from 98 % RH to 9 % RH—Figure 88.e). The relative curvature shows almost linear trends for what it concerns the moisture content over the sorption/desorption processes ($R^2 = 0.99$ for sorption step and $R^2 = 0.98$ for desorption step). The slopes of the curves are also almost identical in magnitude (0.011 for sorption and 0.010 for desorption), and that indicates that the same mechanisms are very likely to be involved in the two processes. The amplitude of the radius of curvature generated by the actuation of the hygromorphic composite materials can be therefore predicted by tracking the relative humidity. This feature also suggests that these smart materials could also be used as moisture sensors.

3. cCF/PA6-I:PA6 bilayers as electro-thermo-hygromorphic actuators

Printed cCF:PA6-I composites are used here as a load-bearing layer with an electrical circuit. The multifunctional composite material provides a passive moisture-induced morphing shape capability and an active electrically-controlled phase. Two input voltages (10 and 15 V) are applied thanks to the U-shaped printed pattern to control the moisture content. Those voltages are chosen to use a low input electric power (0.1 and 0.6 W for 10 and 15 V, respectively), and they are also compatible with analogous values for soft actuators reported in open literature [212], [213], [375]. Electro-heating leads to a heterogeneous temperature field (Figure 89.a). With an input of 15 V, the cCF/PA6-I area reaches an average temperature of 40.0 ± 1.8 °C. A similar but less pronounced behavior is observed at the lower applied voltage of 10 V, with an average temperature of 29.2 ± 1.3 °C. (Figure 89.b). The current circulates through the shortest pathway and prevents in this case the formation of a homogeneous heating field. Furthermore, at the end of one of the arms near the head zone an unusual temperature peak of 65 °C has been observed for the five replicates (yellow spot in

Figure 89.a). This high value of local temperature is due to printing-induced defects which cause a weak contact and therefore a high resistance between one arm and the head. Those high values of temperature can lead to temperature-induced damages (Figure 89.c). The zone of pure PA6 in the middle of the U-shape layer is hardly affected by the electro-heating and this restrains to the area where the carbon fibers are located. In this work a commercial printer has been used to make the case for the feasibility study, however printing parameters such as the fiber trajectory have not been fully customized.

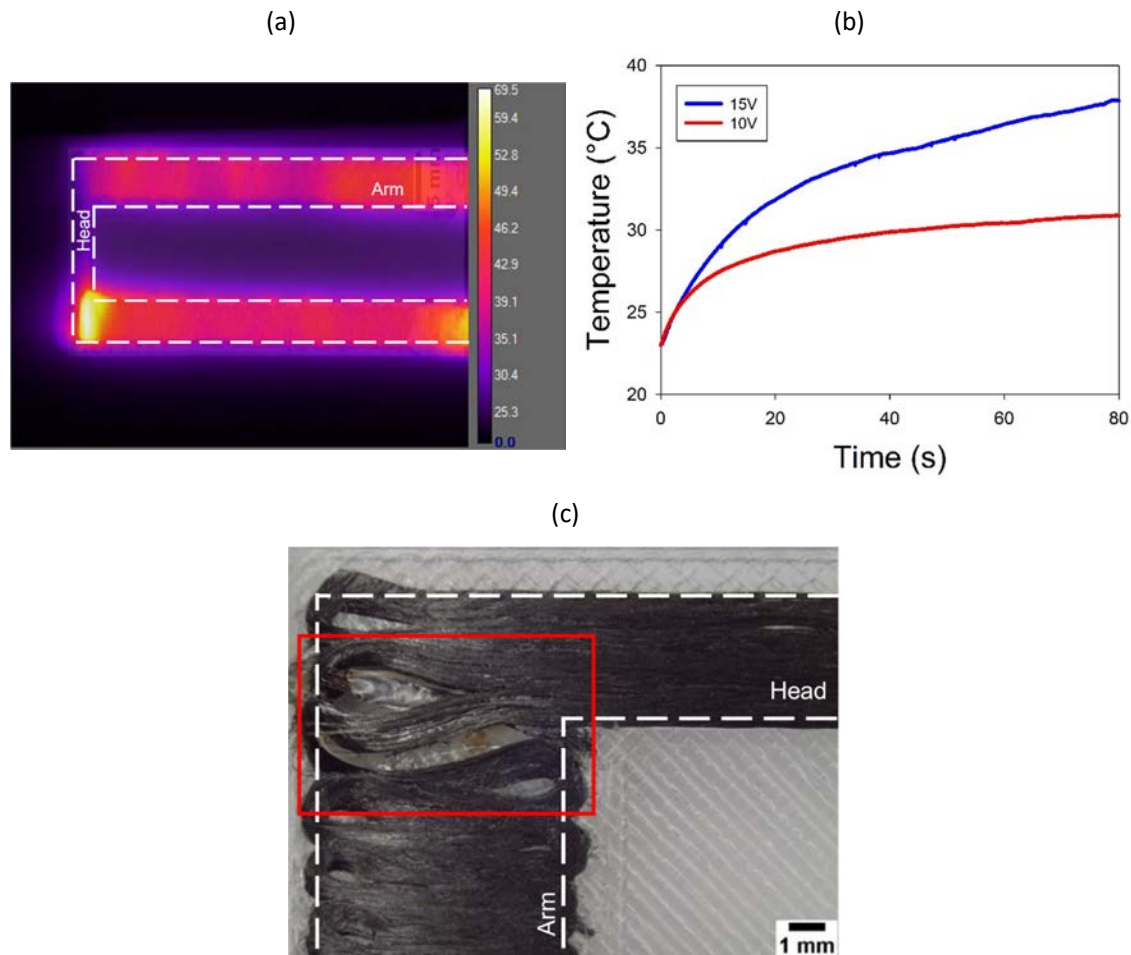


Figure 89 : a) Infrared thermography image of the hygromorphic material with the printed electric circuit at steady state and 15 V. The image shows the heterogeneity of the heating linked with printing defects. b) Evolution of the average temperature in the arm and in the head of the cCF:PA6-I layers at 10 and 15 V. c) Example of a damage related to hot spot that is induced by the printing process (affecting the electrical conductivity of the sample).

The cCF/PA6-I:PA6 bilayers printed with this pattern nevertheless feature lower peak temperatures than those measured by Amjadi et al. [213] (approx. 70 °C) and Hamed et al. [212] (approximately

80–100 °C) on thin electro-active papers. The electro-heating of these hygromorphic composite materials did not cause to overcome the glass transition temperature (T_g) of the PA6 (50 °C) of the thermally active layer, nor the one of the PA6-I (135 °C) belonging to the cCF/PA6-I layer. High chain mobility, high free volume variation of the glassy polymer and therefore a high thermal expansion is observed when a polymer is close or crosses the T_g [376]. During the first actuation step thermal strains are very small, and therefore the contribution of a thermally-induced actuation is negligible. The elastic properties of the composite laminates do evolve with temperature, but only significantly above 60 °C for the transverse cCF/PA6-I, and beyond 80 °C for the longitudinally printed cCF/PA6-I patterns (Figure 90). Therefore, during the electrical stimulus, the elastic properties of the composite could be considered as constant.

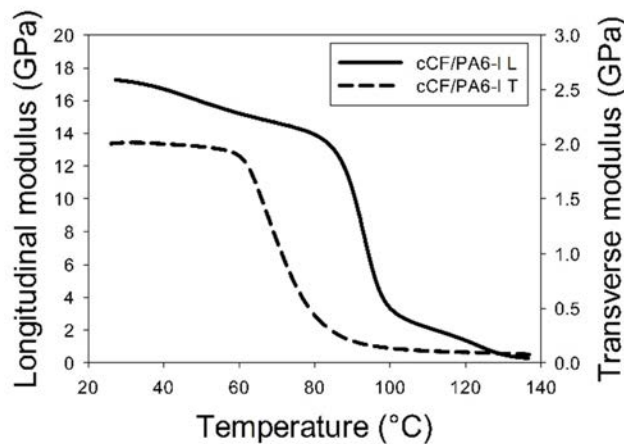


Figure 90 : Evolution of cCF/PA6-I transverse and longitudinal modulus over temperature measured through DMA analysis.

The moisture content within the hygromorphic materials after the electrical stimulus and the increase of temperature has been quantified with reference to an initial wet state of 98 % RH. The moisture content has been decreased exponentially to 9 % RH during the electrical heating while the desorption time has been drastically reduced (10 times) from 300 min in environmental conditions to 30 min when the samples have been electroactivated (Figure 91.a, b). Higher input voltage (15 V) leads to a higher desorption rate as well as an increase of moisture loss (7.1 ± 1.3 % for 15 V and 4.2 ± 0.8 % for 10 V—Figure 91.a, b). Higher water content at 10 V has been observed after actuation and that is due to a lower temperature reached upon the electrical stimulation (Figure 91.b). As a consequence, a slower desorption rate occurs with a pseudo-plateau reached after 30 min (Figure 91.b). The desorption rate is close to zero and would lead to a full desorption if the samples were subjected to a higher actuation time. Within the range of moisture content considered in this work,

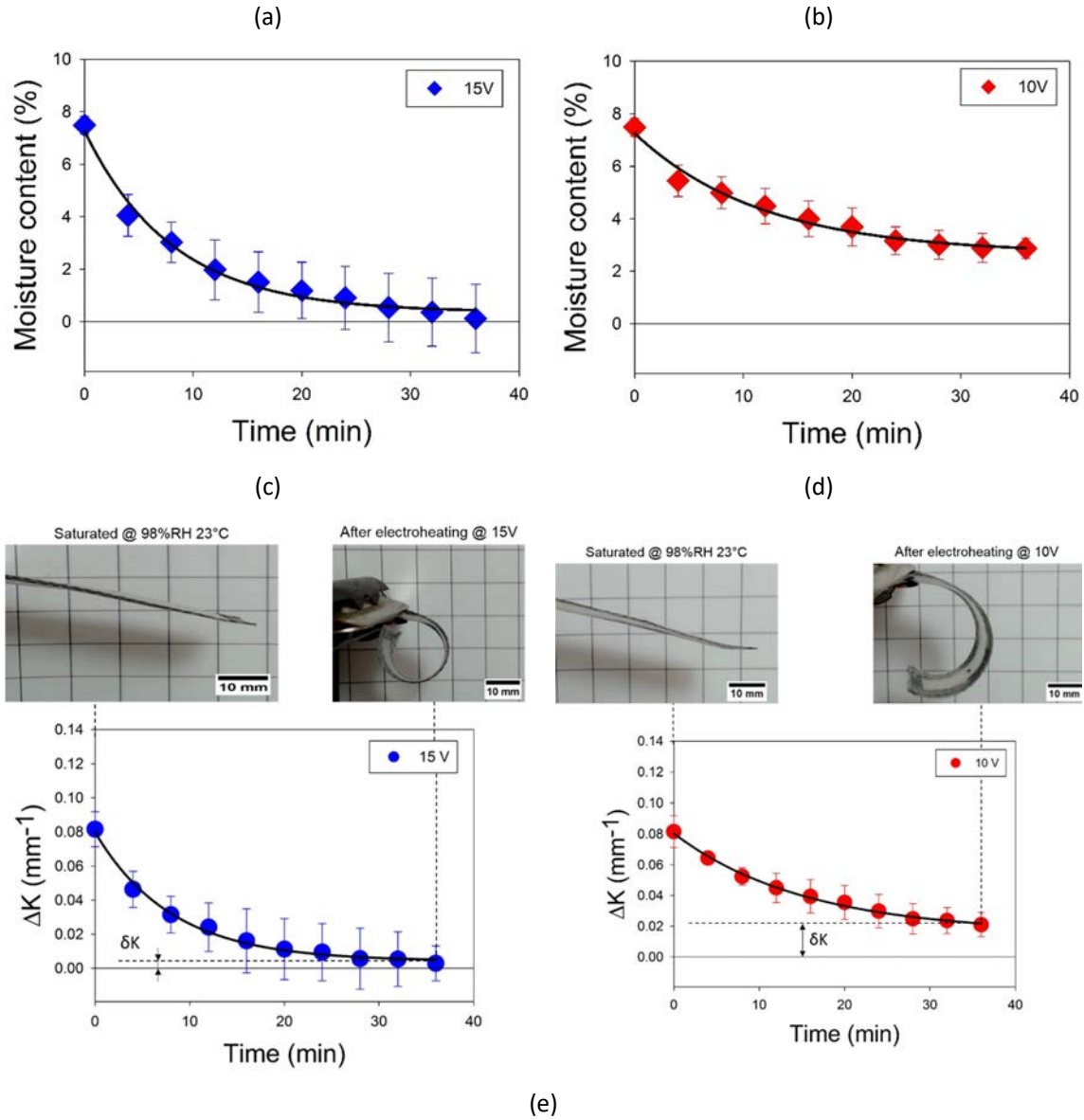
both the PA6 and the cCF/PA6-I layers undergo some important hygroscopic expansions/shrinkages ($\epsilon_z = 2.8\%$ $\epsilon_y = 1.1\%$) and a significant variation of stiffness (between 20 % and 40 %) (see section 3.1 of Chapter 3).

Nevertheless, the lowest stiffness values observed here are larger than those belonging to the previous hygromorphic hydrogel and paper-based actuators. The thermal strain (ϵ_T) of the active layer is 0.2 % for a temperature variation (ΔT) of 21.6 °C (Figure 89.b), while the hygroscopic strain (ϵ^h) reaches 2.4 % for a moisture content variation (ΔM) of only 7.1 %. The hygroscopic strain is 13 times higher than the thermal one in samples subjected to a voltage of 15 V. As a consequence, the hygroscopic functionality of the cCF/PA6-I:PA6 bilayers is more important than the thermal capability for the printed multifunctional material.

The overall electro-thermo-hygroscopic bending actuation of 4D hygromorphic composite materials (Figure 91.a and b) has been verified. The actuation authority shows a similar trend for the two levels of voltage used, with a rapid shape-change followed by a stabilization of the curvature. A slight twisting is observed for any voltage due to process-induced defects which prevent the sample symmetry (Figure 91.c, d). With 15 V of input, the samples transition from a straight configuration at 98 % RH (left in Figure 91.a) to a curved one ($0.079 \pm 0.010 \text{ mm}^{-1}$) similar to those observed in autonomous hygromorphs in dry state ($0.083 \pm 0.017 \text{ mm}^{-1}$). At 10 V, a residual curvature ΔK of $0.021 \pm 0.008 \text{ mm}^{-1}$ is observed because of an incomplete desorption ($2.9 \pm 0.4\%$ after 10 V actuation) caused by the lower value of the electrically-induced temperature. These results show the possibility of using voltage to monitor temperature, moisture content and therefore the change in shape of the material.

The relative curvature versus the moisture content (Figure 91.e) during the desorption and subsequent sorption at 98 % RH and 23 °C after complete drying with the 15 V actuation clearly show—again—the full reversibility of the process. A linear fit between change in curvature and moisture content is also observed in this case, both during electro-heating and passive sorption ($R^2 = 0.99$ and $R^2 = 0.96$, respectively). The magnitudes of the slopes between electric drying and resorption are quite similar ($a = 0.103$ and $a = 0.107$ for electrical drying and re-sorption steps, respectively). This confirms that passive and active electro-thermo-hygromorphic actuators with the current circuit architecture are based on similar actuation principles, although the slope coefficients for the electro-heating case are an order of magnitude higher than for the autonomous case. After one electro-thermo-hygro-actuation and a subsequent storage at 98 % RH and 23 °C the samples recover the shape previously observed during the sorption step ($0.093 \pm 0.012 \text{ mm}^{-1}$) (Figure 88.b).

One can therefore assume that no or negligible damage occurs during the electro-heating phase. The 4D printed configuration of the cCF/PA6-I:PA6 hygromorphic composite bilayers with the embedded electrical functionality demonstrates therefore the capability of speeding up the desorption of water and the change of shape. The variation of the electric input enables to control the morphing.



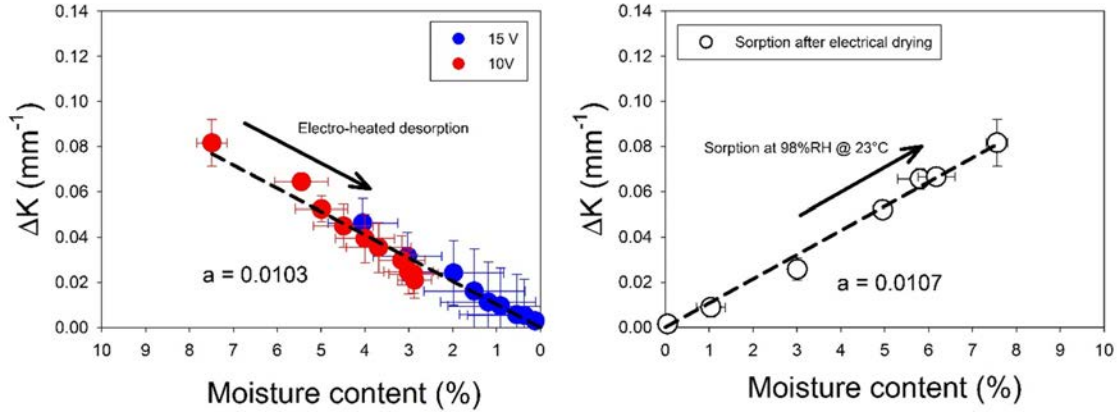


Figure 91 : Evolution of the moisture content of the samples saturated at 98 % RH and 23 °C subjected to 15 V a) and 10 V b). The behavior fits an exponential decay with $R^2 = 0.993$ and $R^2 = 0.979$ for the 15 and 10 V cases. Evolution of the relative curvature electrothermally activated at 15 V c) and 10 V d) with exponential decay fit ($R^2 = 0.987$ and $R^2 = 0.996$ for 15 and 10 V, respectively). The coupled pictures show the sample in saturated state at 98 % RH and 23 °C (left) and after electrothermally activated desorption (right) at c) 15 V and d) 10 V. e) The relative curvature versus the moisture content for (left) both electroheating actuation, i.e., 10 and 15 V ($R^2 = 0.99$) and for (right) samples undergoing another sorption step at 98 % RH and 23 °C after electrical drying ($R^2 = 0.96$).

To underline the potential of this novel class of smart materials made of electro-thermo-hygro-morph over pure passive thermally-actuated morphing structures, similar campaign of tests has been carried out on dried cCF/PA6-I:PA6 bilayers at 9 % RH instead that at 98 % RH saturated (Figure 92). The initial moisture content in the sample is close to zero to cancel the contribution of the moisture-induced actuation during the electro-thermo-hygro-morphing. Once the electrical stimulus is applied (10 or 15 V), a rapid change of curvature is observed during the first 60 s; this confirms the rapidity of the thermal actuation (Figure 92). The responsiveness (curvature) remains however significantly lower (four times reduced) compared to the electro-thermo-hygro-morphing case. This confirms that the novel electro-thermo-hygro-morphic materials possess a higher degree of hygroexpansion than pure thermal one (Table 10). Once the electrical stimulus is switched off, the initial curvature is attained with no variation of moisture content.

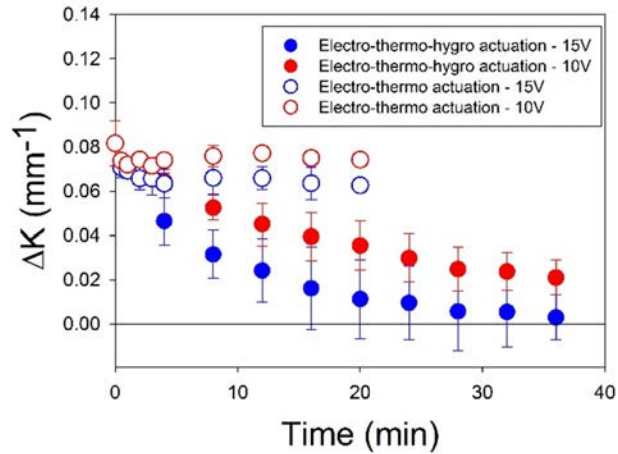


Figure 92 : Evolution of the relative curvature of the electrothermally hygromorphs saturated at 9 % RH at 23 °C activated at 15 and 10 V for initially 98 % RH/23 °C saturated samples and dried samples. The moisture saturated samples show a higher actuation potential in terms of responsiveness (relative curvature) due to the higher hygroexpansion compared to the pure thermal one.

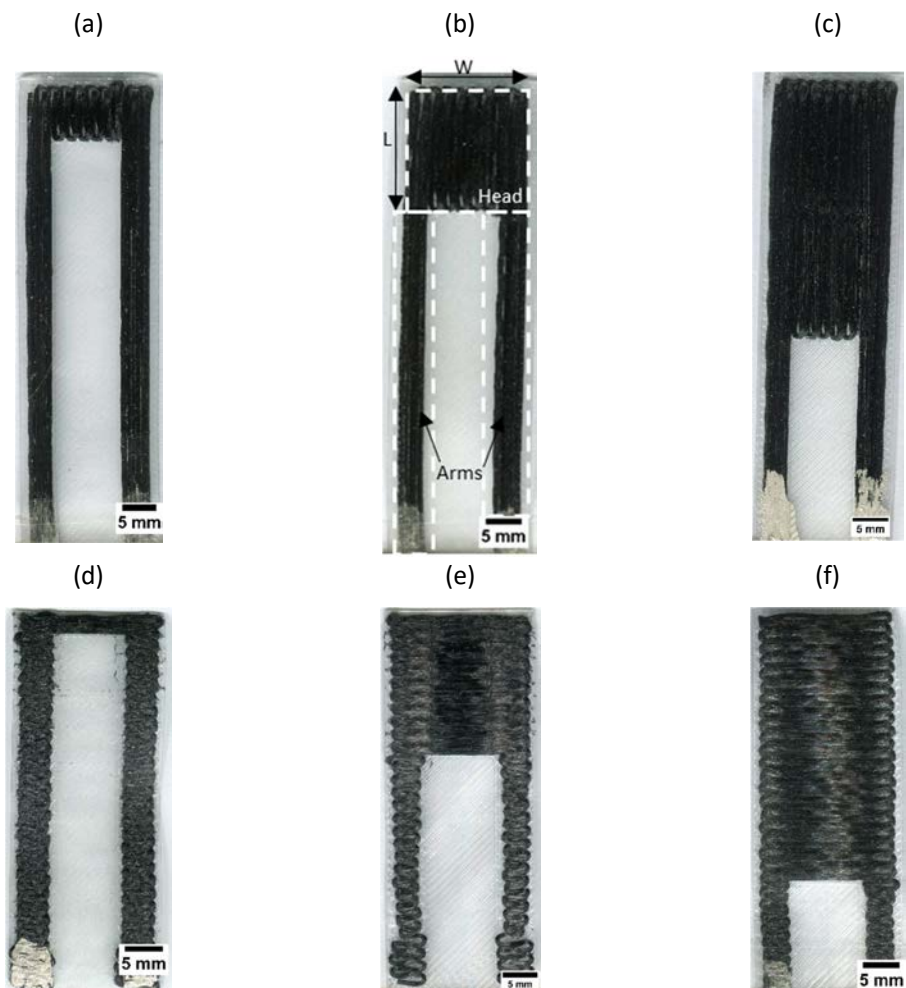
4. Influence of the print pattern on the electro-thermo-hygro actuation of the cCF/PA6-I:PA6 bilayers

In order to better understand the mode of actuation, the electro-thermo-hygro actuation has been transposed to various patterns which have been tailored thanks to FFF. The printed pattern, i.e. the orientation and distribution of the conductive filaments, is supposed to influence the electrical, thermal, hygroscopic and mechanical properties of the composite laminates.

Therefore, two categories of architectures were investigated to evaluate the influence of structural stiffness on actuation response, i.e. longitudinal (Figure 93.a, b, c) and transverse (Figure 93.d, e, f) patterns. Different head sizes were investigated with a L/W ratio of 0.25, 0.5, 1 and 2 due to their influence on the transverse curvature [377]. Figure 93.b exhibits the surface area of the arms and head and the L and W considered in the L/W ratio. In the following section, the samples with transverse patterns and a L/W ratio of 0.25, 1 and 2 are referred as L/W = 0.25 T, L/W = 1 T and L/W = 2T, respectively while the samples with longitudinal patterns and a L/W ratio of 0.5, 1 and 2 are referred as L/W = 0.5 L, L/W = 1 L and L/W = 2 L, respectively.

Another architecture is proposed (Figure 93.g) with a contour of cCF/PA6-I printed on a layer of PA6 in order to optimize heat distribution and achieve high maximal temperatures. Each architecture is a

bilayer designed following bimetallic theory and Timoshenko equations (see section 4.1 in Chapter 1). The influence of architecture on electrical conductivity, temperature distribution, moisture desorption ability and bending curvature is investigated in order to better understand the influence of architecture design on actuation.



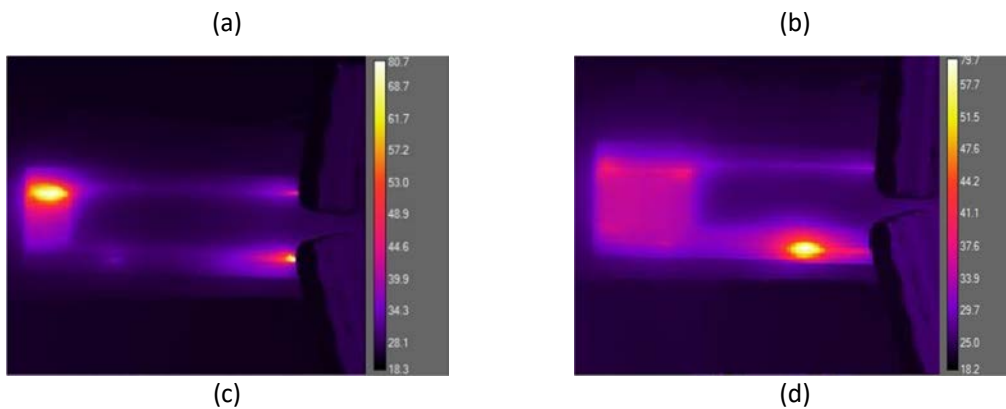
(g)



Figure 93 : Configurations of printed patterns. Two pattern families of patterns were investigated; the longitudinal pattern, with several L/W ratios, i.e 0.5 (a); 1 (b) and 2 (c); and the transverse pattern with 0.25 (d), 1 (e) and 2 (f) L/W ratios. A contouring strategy with a minimum of carbon fibers was also studied (g).

4.1. Influence of the printed pattern on the electro-heating

It is clear that the print pattern of the conductive layer influences the maximum temperature and its distribution on the electrically active layer and consequently the thermal actuation of the composite. The heat distribution after stabilization (tests performed at 50 % RH at 23 °C) in the conductive layer for samples submitted to a 15 V power supply is shown in Figure 94.



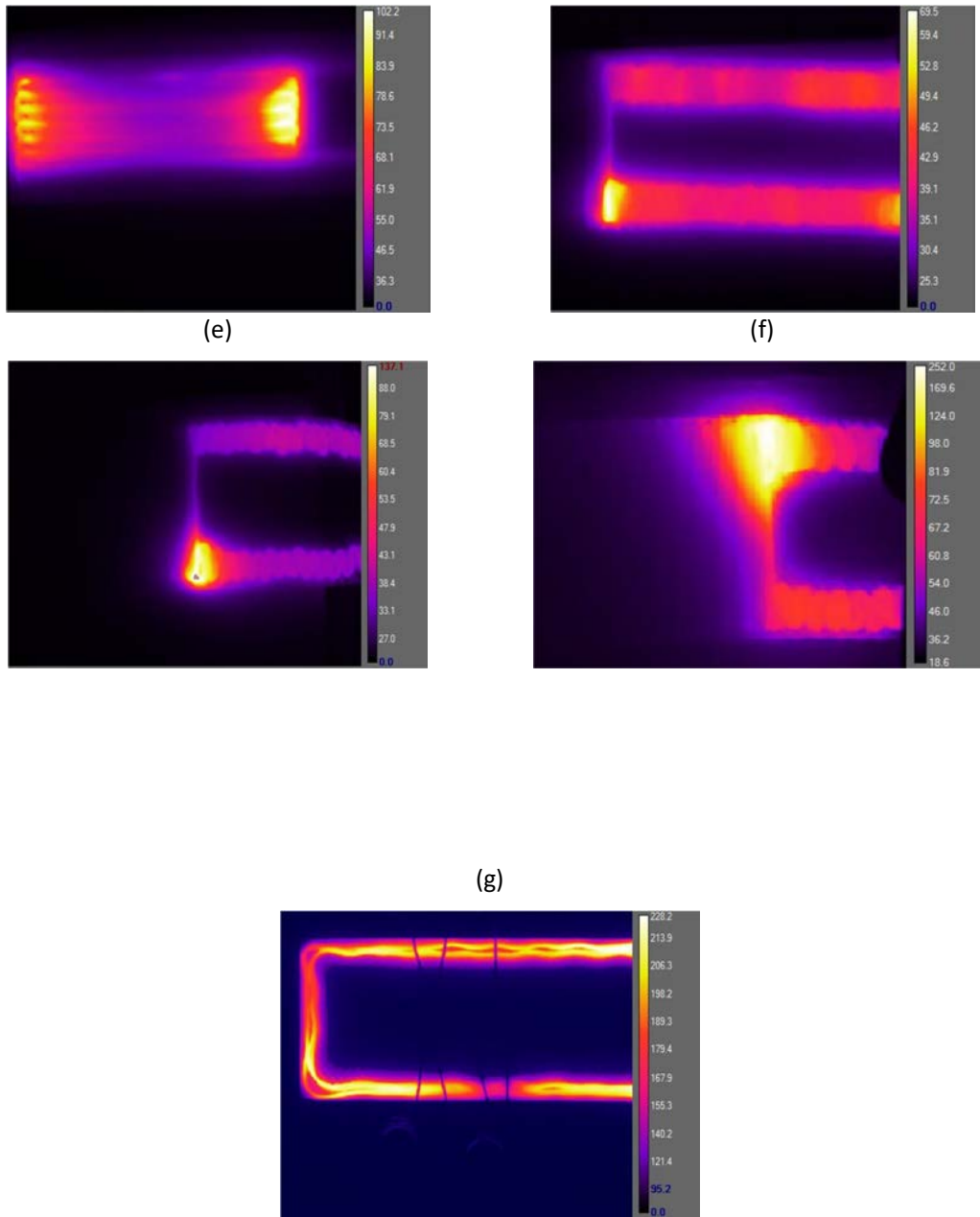


Figure 94 : Thermography images for longitudinally printed cCF/PA6-I with $L/W = 0.5$ (a); $L/W = 1$ (b); $L/W = 2$ and $t_p/t_a \approx 0.4$ (c); Transversally printed cCF/PA6-I with $L/W = 0.25$ (d); $L/W = 1$ (e); $L/W = 2$ (f) and $t_p/t_a \approx 1$. Printed sample with a contour of cCF/PA6-I over with $t_p/t_a \approx 0.3$ (g).

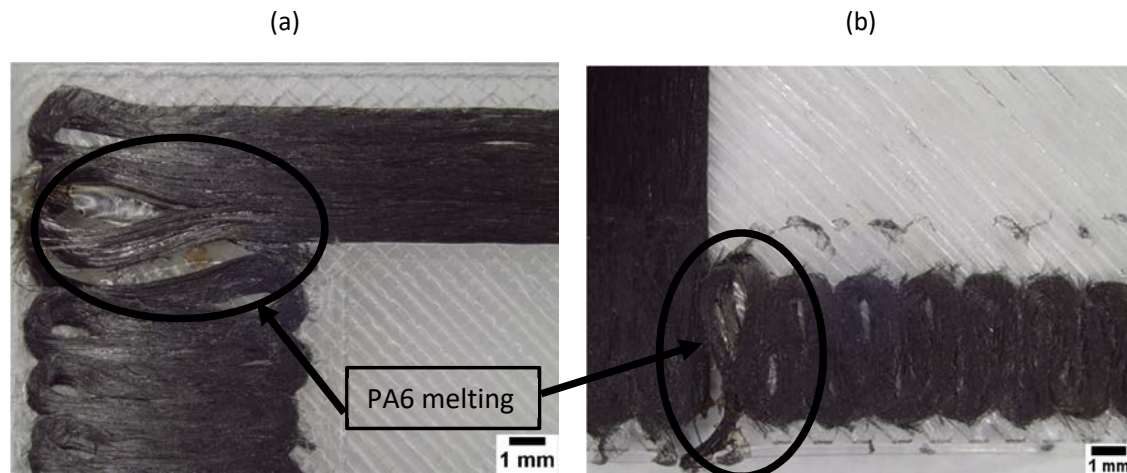
Analysis of the infrared thermography shows that the electro-heating is not perfectly distributed in each pattern where hot spots are observed, with the exception of the contour pattern (Figure 94.g). This local heating is due to higher local resistance caused by discontinuities in filament deposition, as observed in section 1.3 of Chapter 3. Among the singularities, filaments loop (Figure 94.c) caused by the printed-head's back and forth motion are one of the main singularities that leads to hot spots.

These process-dependent defects imply local damaging in the longitudinal and transverse structures (Figure 94.a, b) due to local heating above the melting temperature of PA6 ($T = 200\text{ }^{\circ}\text{C}$) which leads to degradation of the polyamide matrix, fiber breakage and even bead spacing.

For longitudinal samples, the electrically-induced heating is fairly evenly dispersed in the conductive layer despite the presence of high local heating. The average temperature reached appears to be only slightly affected by the aspect ratio L/W ($40.8 \pm 5.4\text{ }^{\circ}\text{C}$ for $L/W = 0.5$; $40.2 \pm 1.9\text{ }^{\circ}\text{C}$ for $L/W = 1$ and $47.4 \pm 2.5\text{ }^{\circ}\text{C}$ for $L/W = 2$) despite a higher electrical resistance for a higher L/W ratio due to a longer conductive network.

The transverse samples show a lack of continuity between the arm and head areas (Figure 94.d, e, f) and no electrical heating is observed in the head areas for both $L/W = 1$ and 2 transverse samples. Indeed, the electric current always follows the shortest pathway and therefore the bead nearest to the arm area. For $L/W = 1$ transverse pattern, the non-heated area represents 33 % of the total surface of the sample whereas it represents 66 % of the surface for $L/W = 2$ transverse pattern. For $L/W = 2$ transverse structures, slight heating is observed in the head area due to a heat conduction. With regard to the surface of the arm, there is an increase in the average temperature in this area when the L/W ratio becomes higher ($40.0 \pm 1.8\text{ }^{\circ}\text{C}$ for $L/W = 0.25$; $43.1 \pm 7.4\text{ }^{\circ}\text{C}$ for $L/W = 1$ and $65.4 \pm 4.8\text{ }^{\circ}\text{C}$ for $L/W = 2$) due to the shortening of the arm leading to a shorter conductive network and therefore a higher electrical current.

Due to the shorter electric pathway caused by the lack of electro-heating in the head area, transverse cCF/PA6-I conductive patterns reach a higher temperature than longitudinal patterns, especially in the case of high L/W patterns.



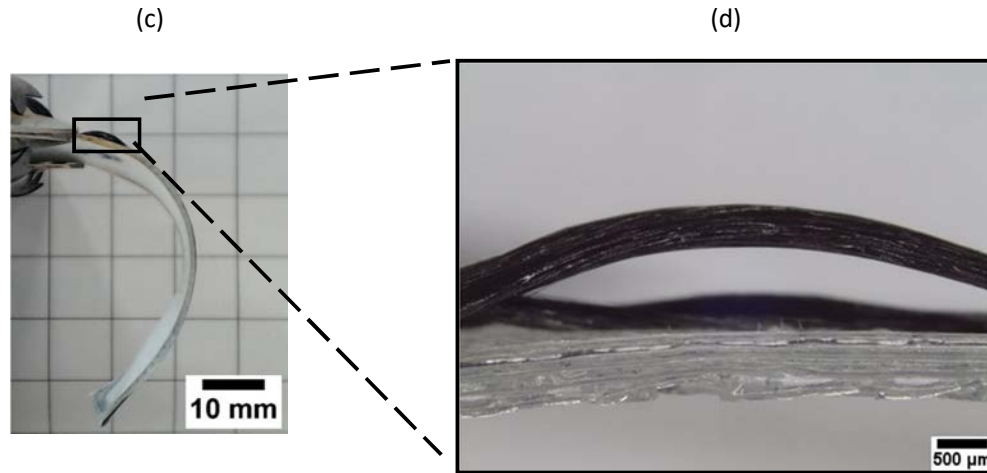


Figure 95 : Observed damages for the longitudinal (a) and transverse (b) patterns showing filament loops caused by printer-head round-trip. In this area, hot spots appear and lead to thermal degradation of the surrounding Polyamide matrix, fiber breakage and even bead spacing. Observed damages for the contour printing pattern (magnification $\times 1$) (c) and magnified contour damage ($\times 20$) (d) showing the delamination between the electrically-active cCF/PA6-I phase and the PA6 layer after a full electro-thermo-hygro actuation cycle.

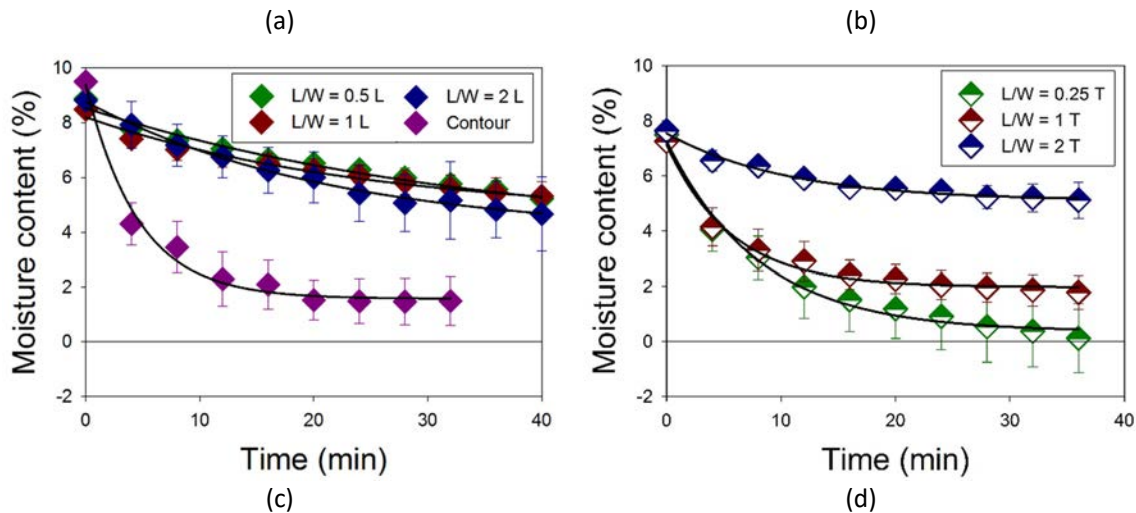
The contour patterns have a well-dispersed electro-heating and allow to reach a high average temperature (178 ± 7 °C) thanks to its optimized architecture slightly affected by the printing singularities (porosity, gap and beads overlap). However, contour electro-heating leads to thermal degradation of the PA6 and debonding between the active and passive layers caused by heterogeneous thermal and hygroscopic deformation between these layers (Figure 95.c, d).

4.2. Influence of the printed pattern on the electro-thermo-hygro-morphic actuation

As a consequence of the electrical heating, the bending actuation of 4D printed samples by water desorption seems to be adapted by the distribution of the stiffness. First of all, there is a difference between the longitudinal, contour and transverse patterns with respect to the amplitude of curvature, even though the optimal stacking sequence was chosen according to the bimetallic theory. For example, longitudinal samples achieve a responsiveness of approx. 0.01 mm^{-1} , while the contour pattern allows the actuating amplitude to be tripled with an amplitude curvature of approx. 0.03 mm^{-1} . Transverse printing achieves greater responsiveness with a curvature amplitude range between 0.03 and 0.08 mm^{-1} (Figure 96.d).

Thanks to the higher temperatures reached for transverse specimens than for longitudinal patterns, a higher desorption rate is observed (Figure 96.a, b) which affects the thermal and hygroscopic deformation and the resulting actuation response. However, the stiffness of the hygroscopically passive layer (CCF/PA6-I) is the key to controlling bending actuation responsiveness. Indeed, stiffer samples, i.e. longitudinal patterns, have a lower curvature responsiveness (Figure 96.c) than transverse structures (Figure 96.d) with equivalent water content. This is highlighted by the evolution of the relative amplitude of the curvature as a function of moisture content (Figure 96.e, f), which follows a linear trend regardless of the pattern. The transverse patterns show a slope four times higher ($a = 0.011$) than the longitudinal patterns ($a = 0.003$) due to the greater stiffness of the electrically-active layer in the longitudinal patterns which limits their ability to bend. Hence, transverse specimens display a better bending capacity but a lower stiffness (see section 2.1 of Chapter 3) which could limit their applications.

The contour pattern offers an intermediate solution and combines a relatively high rigidity and variation in curvature. The contour structures exhibit the highest average temperature reached compared to the other printing patterns, which drastically alters the stiffness of both layers (0.2 GPa at 180 °C; 17 GPa at 25 °C for the passive layer, Figure 90) and changes how the electro-thermo-hygro actuator works. In addition, with electro-thermal heating, contour specimens lose 8 % of their water content while other longitudinal counterparts show a water loss of about 4 %.



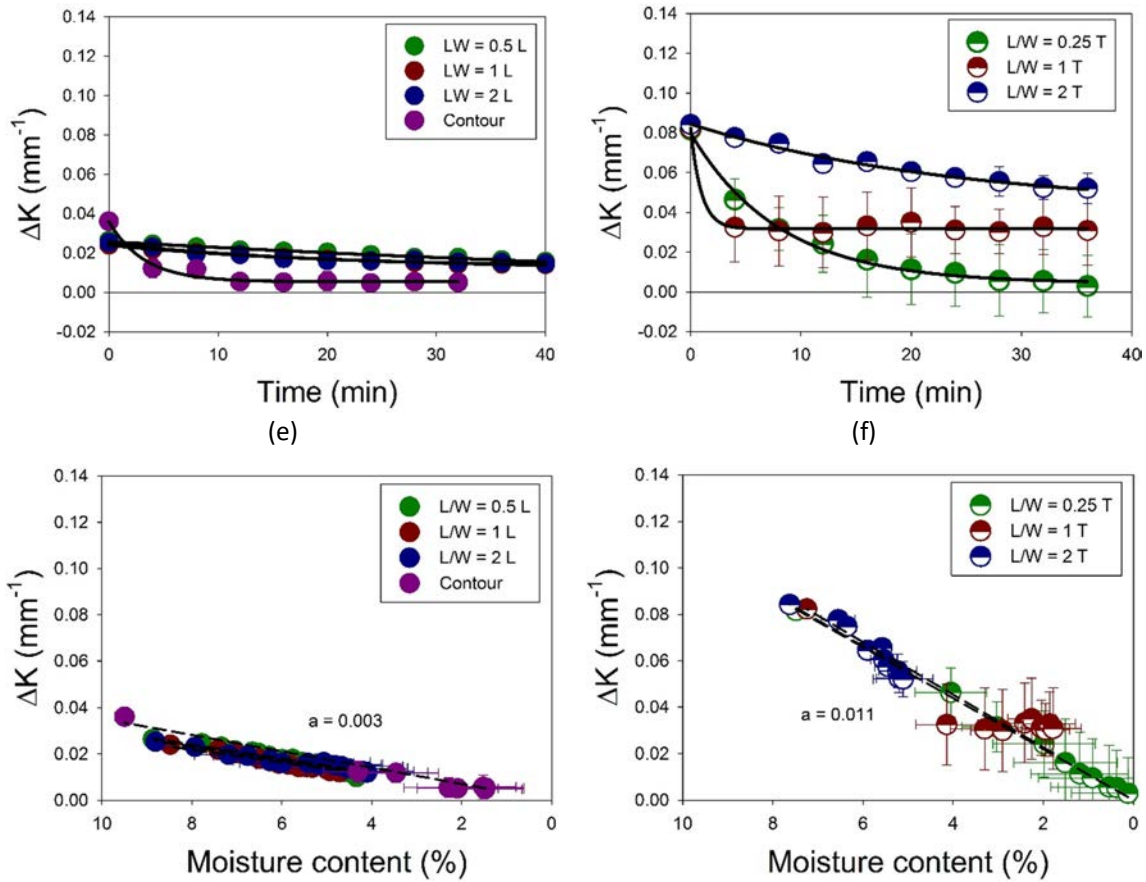


Figure 96 : Evolution of moisture content for longitudinal geometries (including contour pattern) (a) and transverse patterns (b) submitted at 15 V fitted with an exponential decay fit ($R^2 = 0.984$ for $L/W = 0.5 L$; $R^2 = 0.985$ for $L/W = 1 L$; $R^2 = 0.996$ for $L/W = 2 L$; $R^2 = 0.987$ for contour; $R^2 = 0.987$ for $L/W = 0.25 T$; $R^2 = 0.986$ for $L/W = 1 T$ and $R^2 = 0.983$ for $L/W = 2 T$) and evolution of relative curvature induced by electro-thermo-hygro actuation for longitudinal structures (c) and transverse geometries (d) fitted with an exponential decay fit ($R^2 = 0.992$ for $L/W = 0.5 L$; $R^2 = 0.992$ for $L/W = 1 L$; $R^2 = 0.995$ for $L/W = 2 L$; $R^2 = 0.979$ for contour; $R^2 = 0.990$ for $L/W = 0.25 T$; $R^2 = 0.991$ for $L/W = 1 T$ and $R^2 = 0.988$ for $L/W = 2 T$). Evolution of relative curvature over water content for longitudinal (e) and transverse (f) specimens which highlights a linear shape for all geometries ($R^2 = 0.993$ for $L/W = 0.5 L$; $R^2 = 0.997$ for $L/W = 1 L$; $R^2 = 0.965$ for $L/W = 2 L$; $R^2 = 0.976$ for contour; $R^2 = 0.993$ for $L/W = 0.25 T$; $R^2 = 0.991$ for $L/W = 1 T$ and $R^2 = 0.982$ for $L/W = 2 T$) and highlight a slope didn't affect by L/W ratios but rather by pattern stiffness.

In addition to higher thermal strains, higher hygroscopic strains are reached. The reactivity (actuation speed) of the actuators can also be tuned by printing the pattern. Higher electrical conductivity and higher average temperature of the contour pattern result in higher reactivity with full actuation over 10 minutes compared to over 60 minutes for other longitudinal counterparts. With regard to

transverse patterns, full desorption and actuation occurs after 30 minutes for $L/W = 0.25$ and $L/W = 2$ while $L/W = 1$ patterns show very fast actuation (less than 4 minutes). With regard to longitudinal patterns, the L/W ratio of the conductive network appears to have a slight influence on water desorption and the amplitude of the induced curvature (Figure 96.a, c). It is explained by the heat distribution and the maximum temperature induced by the electrical actuation. However, a high residual water content (6 %) remains in the structure after stabilization due to insufficient electro-heating which does not provide enough energy to desorb all water molecules throughout the thickness of the sample. This incomplete desorption of water does not allow the structure to return to its initial dry curvature ($\Delta K = 0 \text{ mm}^{-1}$). For contour structures, a high actuation temperature allows more water molecules to be desorbed, but residual moisture ΔM remains after actuation ($\Delta M = 1.49 \pm 0.88 \%$). The remaining water could be due to the low thermal conductivity of the PA6, which limits temperature homogenization in the PA6 area. Another explanation for the residual water can be found in the diffusion of water in to the polyamide matrix. During water sorption, several diffusion mechanisms lead to two types of water: free water that has diffused into the matrix defects (free volumes, micro-porosities) by capillarity and bonded water that has been chemically absorbed by the polyamide surface. Hence, it can be supposed that the thermal energy provided by the electrical heating was not high enough to break the chemical bonds of the bonded water throughout the thickness of the sample, but was high enough to desorb all the free water.

The L/W ratio seems to have a strong influence on the transverse structures. The higher the L/W ratio, the lower the amount of water desorbed (Figure 96.b) and consequently the smaller the variation in curvature (Figure 96.d). The influence of the L/W ratio on water desorption for transverse structures is explained by temperature distribution described below. For high L/W ratios, actuation is limited to the area of the arm which becomes smaller as the L/W ratio increases (Figure 96.d, e, f) and thus affects the overall change in water content. Heterogeneous electro-heating also leads to an incomplete desorption of water at ratios $L/W = 1$ and 2 where the bonded water located in the non-heated area is assumed not to be desorbed after actuation while the free water in this area is passively desorbed. This difference in moisture content therefore leads to a smaller curvature variation at high L/W ratios (Figure 96.d) and an anisotropic bending which is limited to the surface of the arms.

<i>Transverse structures</i>		<i>Longitudinal structures</i>	
$L/W=0.25$		$L/W=0.5$	
(a)	(b)	(c)	(d)

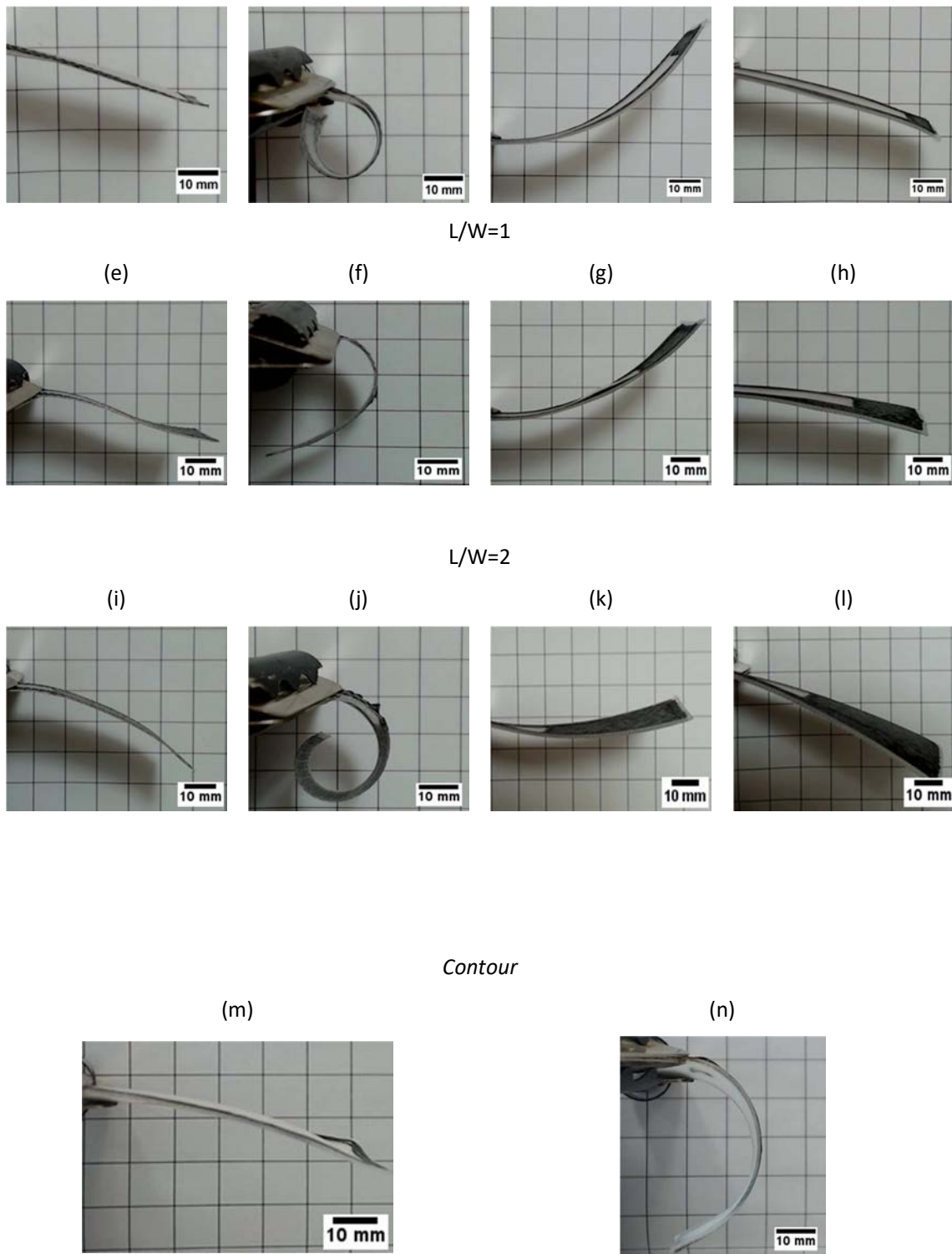


Figure 97 : Evolution of the shape of the actuators between the initial saturated state at 98 % RH at 23 °C (a,c,e,g,i,k,m) and the final actuated state at 15 V and 50 % RH at 23 °C (b,d,f,h,j,l,n) for transversal (a,b,e,f,l,j) and longitudinal (c,d,g,h,k,l) patterns with different L/W ratios, i.e. 0.25 (a,b): 0.5 (c,d); 1 (e-h); 2 (i-l) and for longitudinal contour structures (m,n).

High L/W ratios, however, result in higher bending stiffness due to an increase in the moment of inertia of the cCF/PA6-I section, which diminishes the structure's ability to bend at high L/W ratios. The evolution of curvature for different prints is reported in Figure 97 for samples stored at 98 % RH at 23 °C and dried at 15 V at 50 % RH at 23 °C. First, the shape of the fully saturated samples differs from the longitudinal and transverse structure. For transverse structures, the samples are almost straight with a slight positive curvature value while the longitudinal samples display a negative curvature in the fully saturated state. This difference is explained by the difference between longitudinal and transverse stiffness of the cCF/PA6-I composite and also by the higher difference in CHE between longitudinal cCF/PA6-I and PA6 compared to the difference in CHE between transverse cCF/PA6-I and PA6. As a result, when absorbing water, the longitudinal structures undergo a higher strain gradient, resulting in a greater amplitude of curvature.

After electro-heating, the transverse patterns display a large variation in curvature (Figure 96.d) located all along the sample for L/W = 0.25 (Figure 97.b) while the curvature is mainly located in the arm area for L/W = 1 (Figure 97.i) and a difference in variation in curvature is observed between the arm and the head area for L/W = 2. This difference is explained by the variation in actuation speed between the arm and head areas. The arm areas are subjected to electro-thermo-hygro desorption (Figure 94.e) while the head area is submitted only to passive desorption at 50 % RH at 23 °C. With regard to the longitudinal and contour pattern, the homogeneous temperature distribution makes it possible to achieve a more homogeneous curvature variation for all L/W ratios compared to the transverse patterns.

Hence, the longitudinal structures have an interesting actuation potential due to the large difference in stiffness between the active and passive layers, combined with the highly asymmetrical hygroscopic expansion between these layers. Moreover, these structures allow negative curvature values to be achieved, in contrast to transverse patterns which are limited to positive curvature values. However, these structures are limited by their low desorption rate caused by a low electro-induced temperature. Transverse patterns exhibit a greater amplitude of curvature than longitudinal ones thanks to a higher desorption rate, but suffer from heterogeneous electro-heating which causes local damage and incomplete water desorption. Finally, the contour patterns display high a high amplitude of curvature thanks to a well-distributed electrical heating, but local damage occurs in the form of delamination between the electrically-active cCF/PA6-I phase and the PA6 layer. Hence, depending on the actuation specification (reactivity or responsiveness), the selection and

optimization of printing patterns by means of stiffness/electrical conductivity/Expansion objectives can be achieved.

Conclusion

Hygromorphs are a class of smart materials that are constantly being developed due to their significant potential for autonomous actuation and high responsiveness. The present chapter has proposed a novel class of smart multi-stimuli-responsive 4D printed hygromorphic composite materials that overcome the significant limitations of current hygromorphs (lack of effective actuation control and slow response). This new class of smart materials also possess intrinsic load-bearing capabilities and control functionalities through the embedded electro-thermal actuation. The moisture content within the novel materials presented here could either vary autonomously and thus provide a purely hygromorphic actuation, or be controlled by an electro-thermal stimulus to monitor and control the moisture content, and the resulting curvature. A bilayer microstructure inspired by biological hydraulic actuators such as pine cones was used to optimize out-of-plane displacement. A commercial printer with filaments conventional materials was used in this work to produce the smart hygromorphic materials. Aside from the moisture-sensitive PA6 polymer, cCF/PA6-I composites have been used that can maximize the anisotropy of the resulting hygromorphic material.

In this work, hygromorphic composites were designed using bimetallic-type beam model theory adapted to moisture activation. These materials have shown an autonomous response, with a relatively high variation in bending curvature, sensitive to the variation in relative humidity between dry and wet state (98 % RH). Another class of active hygromorphic materials has been developed, based on the use of an electro-thermal stimulus to control the moisture content within the materials and the curvature. The induced electrical heating of the cCF/PA6-I conductive layer generates a heterogeneous temperature field due to the features of the 4D printing process. The maximum temperatures recorded in the samples do not exceed the glass transition of the cCF/PA6-I and PA6 layers, so the thermal strains are low. In these materials, it can therefore be said that humidity variation and hygroscopic strains dominate the actuating response. When actuated, multi-stimuli-responsive hygromorphic composite materials show a very remarkable tenfold increase in actuation speed during desorption compared to autonomous (passive) hygromorphic samples; the responsiveness of the two classes of materials remains the same. The control of the moisture content by means of various electrical voltage inputs is self-evident, and the hygroscopic actuation

can therefore be triggered and actively controlled. When the electric current is switched off, the hygromorphic materials become autonomous (passive) actuators again, and cooling and ambient moisture cause a fully reversible actuation. When applying electro-heating to an initially dried sample, rapid actuation with very low responsiveness can be observed; this once again confirms the potential of this novel electro-thermo-hygromorphic material as a new and interesting class of smart solids to be used for ambient sensing, but also as architectural and deployable structures and mechanical metamaterials by 4D printing with load-bearing capabilities.

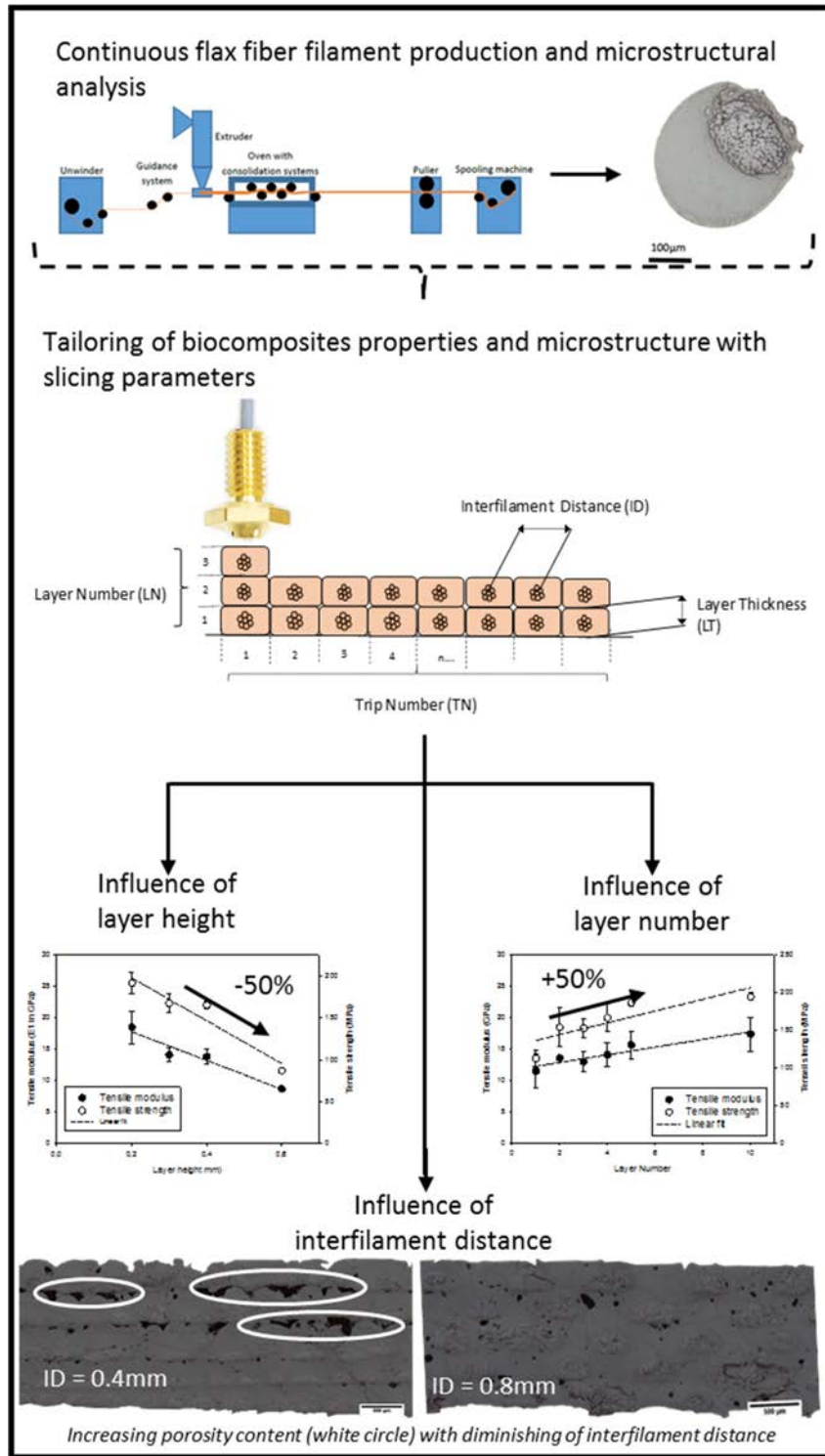
Finally, 4D printed smart composites are printed with different patterns (longitudinal, transverse and contour) and different L/W ratios (distribution of conductive pattern) leading to a combination of temperature, hygroscopic expansion and stiffness distribution over the sample. It's another key to tune the multi-responsive composite. Indeed, the actuation speed has been accelerated by the contour geometry because the electrical conductivity, the maximal temperature reached and therefore the desorption rate is improved. Responsiveness is greatly altered by the pattern. The longitudinal stiffness of the carbon fiber could limit the bending ability, while the transverse patterns exhibit a high responsiveness with a large amplitude of curvature. Moreover, longitudinal patterns lead to a slight "negative" curvature in the saturated wet state and a slight "positive" curvature in the dry state; while transverse patterns display only a positive curvature but with a higher amplitude of curvature. Consequently, a wide dispersion of design possibilities is possible with the control of fibers orientation in 4D printed actuators thanks to the very high fiber orientation in continuous filaments and the control of fibers orientation provided by the 3D printing process.

The modification of the L/W ratio has no influence on the actuation but could create structural rigidity (synclastic curvature) which may open novel research on multistimulable bistable 4D printed composites. However, the printing process has induced local defects that result in high local heating and local damage that prevent several actuation cycles from being carried out. Indeed, in this study, a commercial printer was used without the possibility of modifying the G-code or the printing parameters. Therefore, further research should be conducted on open printing devices to consider active structures: 4D printed shape morphing metamaterial.

Moreover, the reactivity of the material could be further improved by maximizing the hygroscopic expansion gradient between the active and passive layers in the sample, for instance by adding highly moisture-sensitive materials such as natural fibers found in hygromorphic biocomposites. Additionally, the distribution of stiffness in the material could also be adjusted through 4D printing of anisotropic components (fibrous materials) to develop programmable bioinspired structures. Finally,

mechanical instabilities encountered in biological systems (*Dioanea muscipula* for instance) could be used in 4D printed structures.

Chapter 5: Tailoring the mechanical properties of 3D printed continuous flax/PLA biocomposites with slicing parameters



Recently, the addition of continuous fibers to 3D printing composites have gained interest as it offers high mechanical performance for structural applications. Moreover, due to environmental concerns, natural fiber composites are also increasingly being investigated. Although the development of biocomposites is still in its infancy in terms of technological maturity, 3D printing is an incredible opportunity for biocomposites to develop for the first time on the same time scale as their synthetic counterparts. However, due to recent developments, there is a lack of knowledge on the understanding of the relationship between the printing parameter (nozzle and bed temperature, printing speed, printing trajectory,...), the slicing parameters (layer height, interfilament distance, raster angle,...) and the resulting architecture and mechanical properties, especially for continuous natural fiber printed composites.

In this fifth chapter, an investigation between several slicing parameters such as Layer Height (LH), Interfilament Distance (ID), Trip Number (TN), Layer Number (LN) and raster angle on the sample geometry (printing accuracy), microstructure and tensile properties of continuous flax fibers/PLA biocomposites (cFF/PLA) is presented. The aim of this work is to control the microstructure and mechanical performance of composites through slicing parameters in order to target applications in terms of design or variable stiffness composites for morphing applications.

First of all, a description of the filament manufacturing process is done as well as a microstructural analysis of the printable filaments. Then, the influence of the Layer Height (LH) on the microstructure and mechanical performance was investigated. Layer thickness induced by Layer Height is a crucial parameter that dictates filament compaction during the printing and its influence on porosity content, sample geometry and mechanical performances has been investigated.

Then, the influence of the Trip Number (TN) and Interfilament Distance (ID) was studied. These parameters are closely related and dictate the space available for the filament between the nozzle and adjacent filament and thus the compaction of the composite.

An investigation of the printed Layer Number (LN) to assess its influence on the out-of-plane compaction of composites and thus on the microstructure and mechanical performance of composites. Finally, the influence of the raster angle was studied to evaluate the anisotropy of continuous flax fiber composites.

1. Production of continuous filaments of flax/PLA biocomposites and description of the microstructure

1.1. Production of continuous filament of flax/PLA biocomposites by co-extrusion process

Continuous flax/PLA biocomposites filaments were elaborated thanks to the co-extrusion process described in section 1.2 of Chapter 2. In the literature, continuous filaments reinforced with synthetic fibers are commonly manufactured by extrusion of filaments [91], [93]–[95], pultrusion of commingled yarn [92], [96] or by impregnation of fibers in a resin solution [130].

Processing parameters such as temperature, extrusion rate line speed and oven temperature has been optimized to manufacture filaments with reduced porosity content and diameter in the same range as coated continuous synthetic fibers (400-500 μm). For this purpose, yarns with low TEX (68 tex) and low twist (320 turn/meter) were selected to obtain a filament of small diameter and a good impregnation of the fiber/matrix. Work on the optimization of processing parameters was carried out as a part of an internship project by Antoine Barbé, and this study made it possible to determine a set of optimized process parameters summarized in Table 11.

Consequently, the study identified a set of optimized process parameters, summarized in Table 11.

Table 11 : Extrusion parameters to produce continuous flax/PLA filaments.

Process parameters	
Die size (mm)	0.6 (diameter) x 20 (length)
Extruder temperature ($^{\circ}\text{C}$)	180
Die temperature ($^{\circ}\text{C}$)	190
Oven temperature ($^{\circ}\text{C}$)	120
Guidance furnace temperature ($^{\circ}\text{C}$)	125
Consolidating system (mm)	40 x 7
Puller speed (m/min)	1
Extrusion speed (rpm)	5

1.2. Microstructure of the continuous filament of flax/PLA biocomposites prior to printing

Continuous filaments of flax/PLA biocomposites (cFF/PLA) exhibit irregularities on their surface which have led to imperfectly circular filaments (Figure 98), mainly due to the co-extrusion process and the twisted architecture of the fiber bundles.

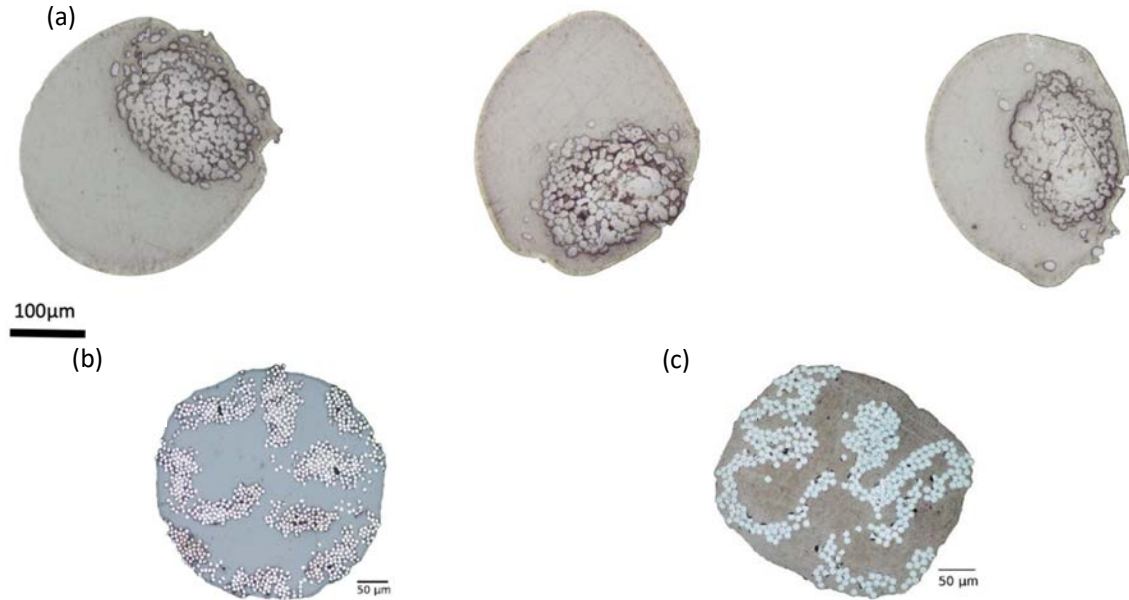


Figure 98 : Cross-section of continuous flax/PLA biocomposites filaments made by co-extrusion process (a) and cross-section of continuous carbon (b) and glass (c) fiber based filaments.

The co-extrusion process allows to develop cFF/PLA filaments of small diameter ($503 \pm 47 \mu\text{m}$) similar to those previously published by Le Duigou et al. [298] and slightly larger than commercial continuous glass or carbon/polyamide filaments [90]. Some limitations still need to be overcome with regard to this manufacturing process:

- The diameter of the filament shows a variation (Figure 98) with maximal values around $800 \mu\text{m}$ and minimal values around $300 \mu\text{m}$. Changes in diameter may affect filament compaction, the reproducibility of 3D printing and the microstructure of the composite and possibly induce nozzle clogging. By comparison, filaments reinforced with continuous synthetic fibers show a lower coefficient of variation (2.8 % and 6.8 % for carbon and glass fibers, respectively against 9.3 % for cFF/PLA).

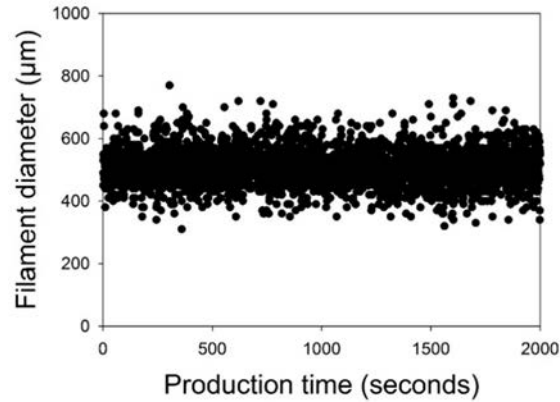


Figure 99 : Typical evolution of filament diameter during filament production by extrusion process (time scale of 2000 seconds)

- The low dispersion of flax yarns in the PLA matrix is shown by the deviation of the matrix and the fiber-rich areas (Figure 98) from the centre of the filament. This seems to be due to the co-extrusion die geometry. This is explained by co-extrusion process where the coating matrix comes into flax yarn on one side only (Figure 98).

- The porosities are mainly located in the flax yarn, giving a porosity v_p of 2.2 ± 0.8 %. This value is low compared to filaments that are produced from short natural fibers ($8.4 < v_p < 47$ %) [256], [269], or in the range of polyamide filaments reinforced with continuous glass ($v_p = 1.34 \pm 0.13$ %) or carbon ($v_p = 1.85 \pm 0.30$ %) (see section 1.1 of Chapter 3).

- The low efficiency and yield of the co-extrusion process which is currently limited to 1 m/min. To this end, several improvements should be investigated, such as the design of the co-extrusion die, the development of commingled yarn, the use of flax tape instead of flax yarns, the use of thicker flax yarn and bigger die size to raise filament tensile resistance and thus puller speed, the modification of polymer nature with lower viscosity, etc...

2. Influence of Layer Height (LH) on the mechanical properties of printed cFF/PLA composites

As shown in section 1.2 of Chapter 1, Layer Height (LH) is a slicing parameter that refers to the distance between the nozzle and the building platform as defined in the G-code. The resulting thickness of a printed ply due to the compression of the nozzle on the heated bed is noted Layer

Thickness (LT) (Figure 100). Here, a flat-head nozzle with an aperture diameter about 1.4 mm was used to promote compaction and drive filament during printing.

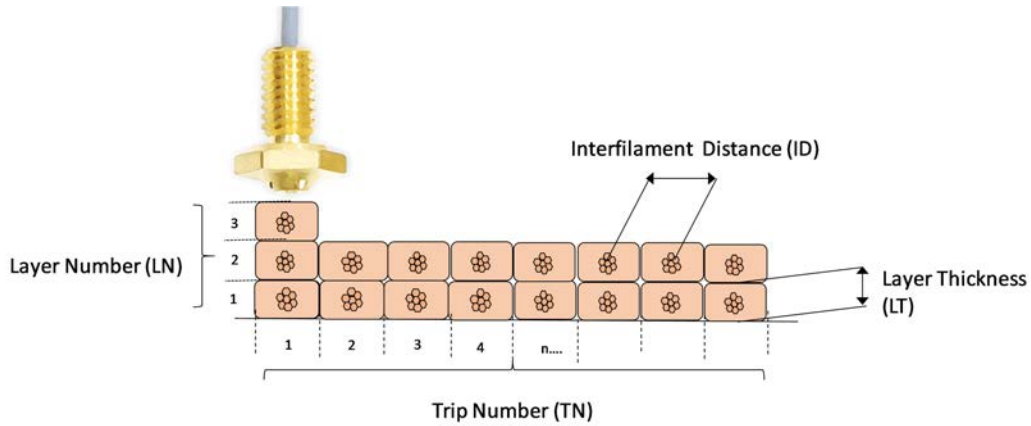


Figure 100 : Schematic view of the printing process for continuous flax/PLA biocomposites and the corresponding test parameters.

A wide range of Layer Height (LH) is investigated and the corresponding Layer Thickness (LT) is measured on a single printed layer (Figure 101.b black solid symbols)). The relationship between these quantities is quasi-linear ($R^2 = 0.96$ with a slope $a = 0.52$) but there is a difference between the programmed Layer Height and the actual Layer Thickness. Two regimes may be observed: Below $LH = 0.3$ mm, the actual Layer Thickness is always greater than the programmed thickness. This leads to overcompaction of the material, as evidenced by the value of the compression ratio around 2. The latter is defined as the ratio of the initial filament diameter ($503 \pm 47 \mu\text{m}$) to the measured ply thickness (Figure 101.a white symbols). Overcompaction can be explained by the twisted structure of the continuous flax yarn, which prevents complete compaction of the filament by the nozzle during printing. It can be argued that printing many layers whose actual thickness is greater than LH can result in the printing nozzle to be crushed when the actual thickness of layer n exceeds the LH of layer $n+1$. This will be discussed in more detail in the section 3.6. of this chapter.

Above the threshold of 0.3 mm, there is a monotonic increase in the actual thickness with LH until the filament can no longer be printed. An LH of 0.7 mm is the maximum value that was successfully printed. Within this range, the actual thickness is always slightly less than the preset values, which means that undercompaction occurs.

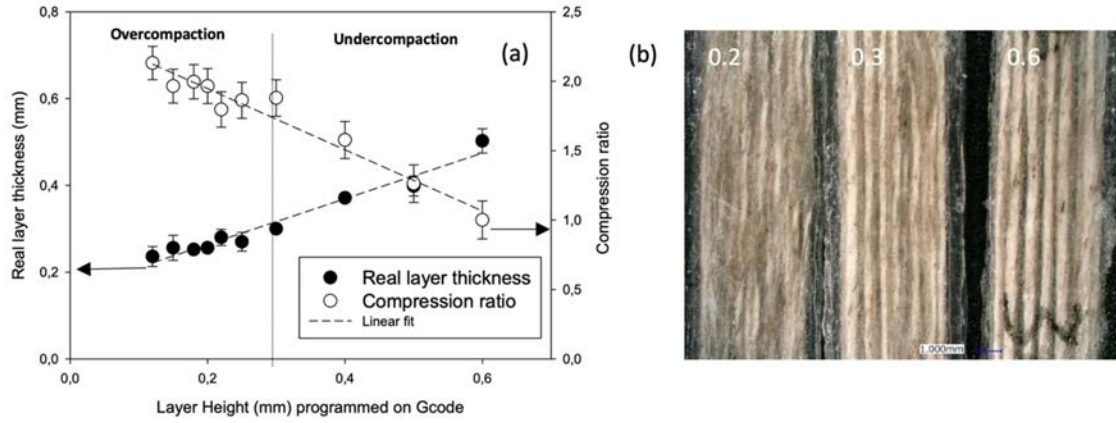


Figure 101 : Evolution of the measurement of the actual layer thickness on a layer after the printing process as a function of the programmed layer height (LH) for cFF/PLA composites (a). Photograph of the cFF/PLA composites surface with different LHs (b) (Interfilament Distance (ID) = 0.6 mm, Trip Number (TN) = 25 and Layer Number (LN) = 1).

Figure 101.b evidences that for a low LH (e.g. 0.2 mm) where there is overcompaction, a misalignment of the flax fibers is observed (Figure 101.b). The increase in LH allows the yarn to be less compacted, which is clearly observed on the surface of the samples and the fiber reinforcement appears to be more rectilinear.

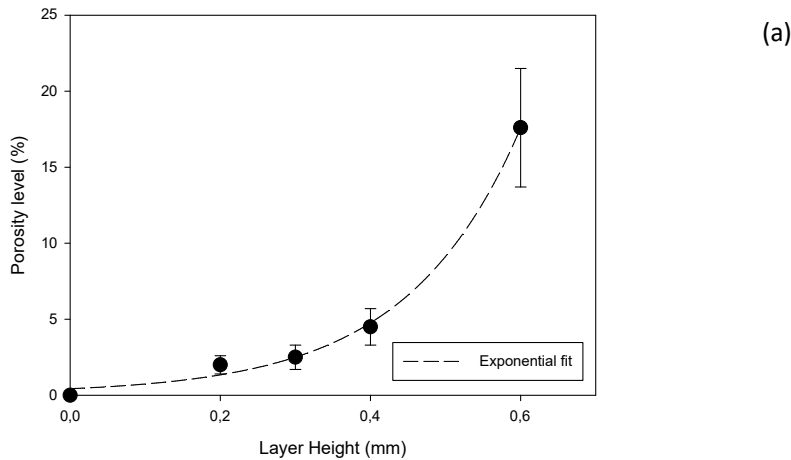


Figure 102 : Evolution of the porosity level (V_p) as a function of the layer height of cFF/PLA composites (a), the dotted line represents an exponential raise fit of the experimental data. Micrographic section of cFF/PLA composites with different LH (from 0.2 to 0.6mm) (b) (ID = 0.6mm, TN = 25 and LN = 5).

The porosity content has been evaluated on samples with three different LHs, 0.2, 0.3 and 0.6 mm (Figure 102.a). The porosity level follows an exponential increase with Layer Height from $V_p = 2.0 \pm 0.6 \%$ for LH = 0.2 mm to $17.6 \pm 3.9 \%$ for LH = 0.6 mm. Thus, a smaller LH creates a smaller space between the layers where the bonding and interdiffusion mechanism have apparently been triggered (Figure 102.b) due to a higher compression ratio (Figure 101.a white symbols). A LH of 0.6 mm results in very high porosity, mainly located in the interlayer zone. The modification of LH also induces a linear reduction in both the E1 stiffness and strength of continuous flax fiber/PLA composites (Figure 102.a). This confirms that the compression ratio, which represents the pressure applied to the filament during printing, can modulate the microstructure and mechanical properties by influencing the bonding mechanism between the printed layers. The results are gathered in Table 12.

Table 12 : The tensile properties of cFF/PLA composites for different layer heights (LH) (ID = 0.6mm, TN = 25 and LN = 5).

LH (mm)	E1 (GPa)	σ (MPa)	ε (%)
0.2	17.6 ± 3.1	183 ± 22	1.5 ± 0.2
0.3	14.1 ± 4.2	166 ± 31	1.9 ± 0.1
0.4	13.8 ± 1.2	163 ± 5	1.7 ± 0.1
0.6	8.4 ± 0.6	87 ± 1	1.4 ± 0.1

The highest tensile properties found for LH = 0.2 mm are in the same range than those previously published considering the slight difference of fiber volume fraction ($26.4 \pm 1.1 \%$ vol. against 30.5 % vol.) [298]. By comparison, similar materials (Flax/PLA with $W_f = 30 \%$ wt.) manufactured with thermocompression exhibited a more brittle behavior with a sudden rupture around 0.8 % of strain [378]. The twisted yarn architecture of continuous flax/PLA may contribute to tougher tensile properties which may be advantageous for structural design.

A Rule of Mixture (RoM) is applied to estimate the flax fiber reinforcement properties by back calculation (with $E_m = 3.5$ GPa [379] and $V_f = 26.5 \%$ vol.). A fiber stiffness of 60 GPa is calculated, which is relevant for the properties of flax fibers [380] and other work on conventional manufacture of flax fiber composites [309], [381]. As a result, the FFF of continuous flax fiber biocomposites retained the reinforcement potential of flax fibers even if thermal cycles were applied (co-extrusion and printing processes).

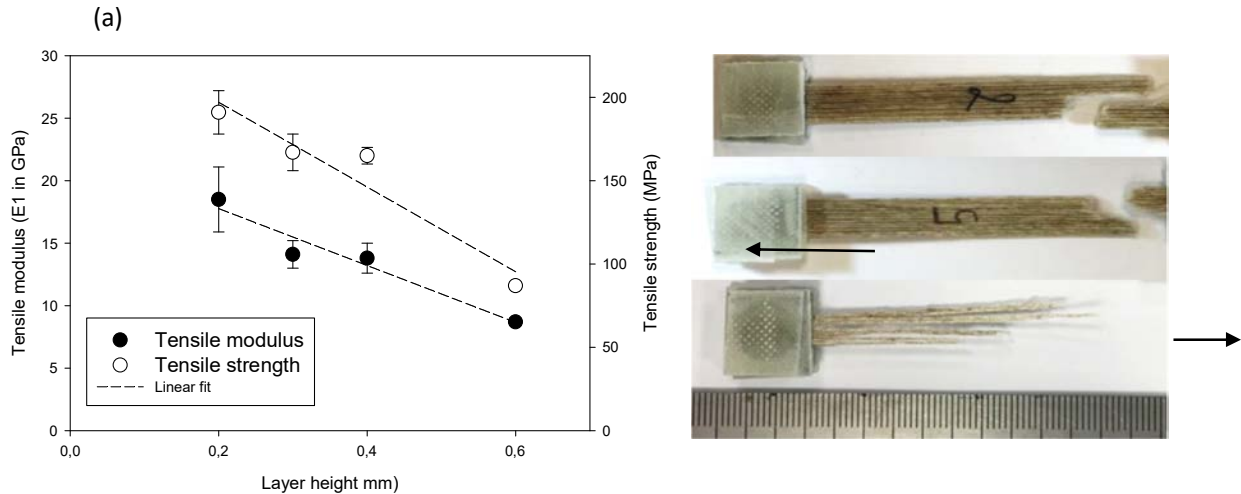


Figure 103 : Evolution of tensile modulus ($E1$) and tensile strength as a function of layer height of cFF/PLA composites (a). Fracture surface microscope observation of cFF/PLA composites (a). Fractured surface microscope observation of cFF/PLA composites with various LH (from 0.2 to 0.6mm) ($ID = 0.6\text{mm}$, $TN = 25$ and $LN = 5$).

Analysis of fractures analysis of longitudinal cFF/PLA revealed changes with LH. For $LH = 0.2\text{ mm}$, there is an initial transverse crack followed by propagation along the tensile axis (Figure 103.b). There are numerous fiber pull-outs. This effect is less pronounced for printed samples with an LH of 0.3 mm. When LH reaches 0.6 mm, the fracture mechanism is radically modified by the delamination caused by a lower compression ratio and explained by a higher porosity content located at the inter-layer interface.

Hence, the control of LH allows the microstructure of cFF/PLA printed biocomposites and the resulting mechanical properties to be checked. This change in microstructure is expected to accelerate the moisture sorption mechanism, as has been evidenced elsewhere in printed short-wood-fiber/PLA biocomposites [269], [305], while maintaining constant hygroexpansion [363].

3. Influence of Trip Number (TN) and Interfilament Distance (ID) on the mechanical properties of printed cFF/PLA composites

The Trip Number (TN) represents the number of individual paths taken by the printer to draw the parallelepiped sample (Figure 100). A single printed filament has a TN of 1 and two adjacent printed filaments correspond to a $TN = 2$. Figure 104.a shows the evolution of layer thickness with the Trip Number.

The Trip Number and thus the effect of neighboring filaments influences the thickness of the printed layers. For trip numbers greater than 6, the sample thickness is almost constant and then depends on the LH values, as evidenced in Figure 101.a. Below TN = 6, there is a drastic reduction in the thickness of the layer, the limit of which is given by the thickness and compressibility of the flax yarn (Figure 98).

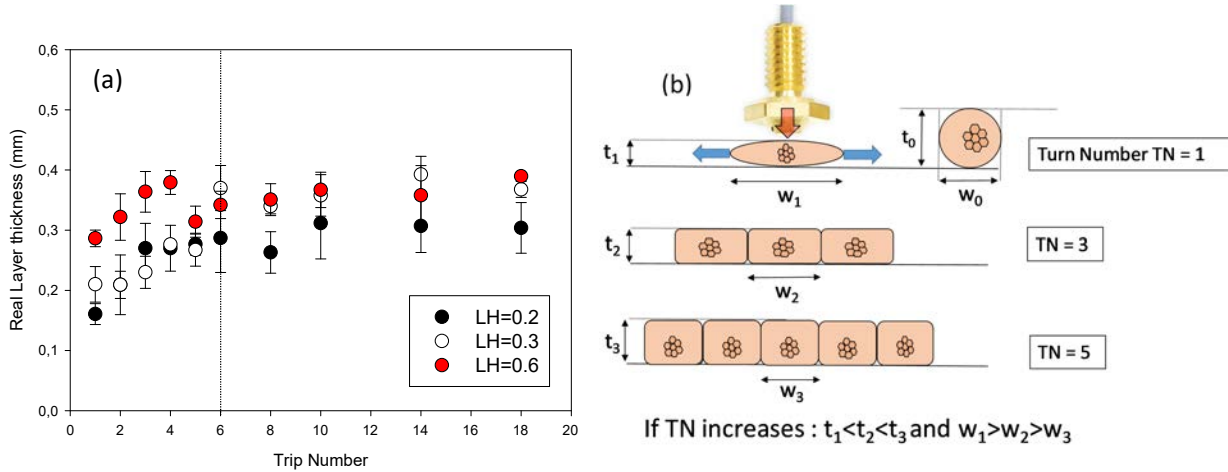


Figure 104 :Evolution of the actual layer thickness (measured on one layer) as a function of the trip number for different layer height (0.2, 0.3 and 0.6mm) (a) (ID = 0.6mm, LN = 1). Schematic view of the effect of TN on the thickness and width of printed cFF/PLA composites (b).

This highlights the constraining effect of the neighboring filaments during compression by the nozzle, which prevents the polymer from spreading. Indeed, during printing, the nozzle compresses the filament on the bed or on the previous composite layer, but the volume of the printed filament must be constant (considering the reduction in the volume of porosity due to the compression ratio). Thus, due to the constraining effect of the neighboring filament, the polymer matrix will not be able to flow in a lateral direction and will spread in an out-of-plane direction and a greater thickness will be achieved. LH is also changing this situation. A schematic view is proposed to reproduce the phenomenon in Figure 104.b. The Trip Number follows an exponential decay with filament width (Figure 104.b and Figure 105.a). The latter is calculated by dividing the total width of the sample by the Trip Number. One should keep in mind that the width of the filament is fundamentally different from the Interfilament Distance (Figure 98 and section 1.2 of Chapter 1). ID focuses on the distance between the center of printed beads (center of flax yarns), while the width of the sample takes into account the overall geometry and the polymer flowing over the edge. Without an adjacent filament, the polymer matrix can migrate freely (Figure 104.b). Indeed, the printing of a filament shows that a width of 1.764 ± 0.071 mm is obtained (Figure 105.b) while the increase of the Trip Number drastically reduces the average width between the filaments to an almost constant value of 0.6 mm after TN = 10. The choice of the Trip Number will affect the accuracy of the sample geometry.

Actually, this value is close to the preset value of Interfilament Distance. A lower Layer Height of 0.2 or 0.3 logically increases the filament width at higher compression (Figure 104.b and Figure 105.a) than LH = 0.6 mm.

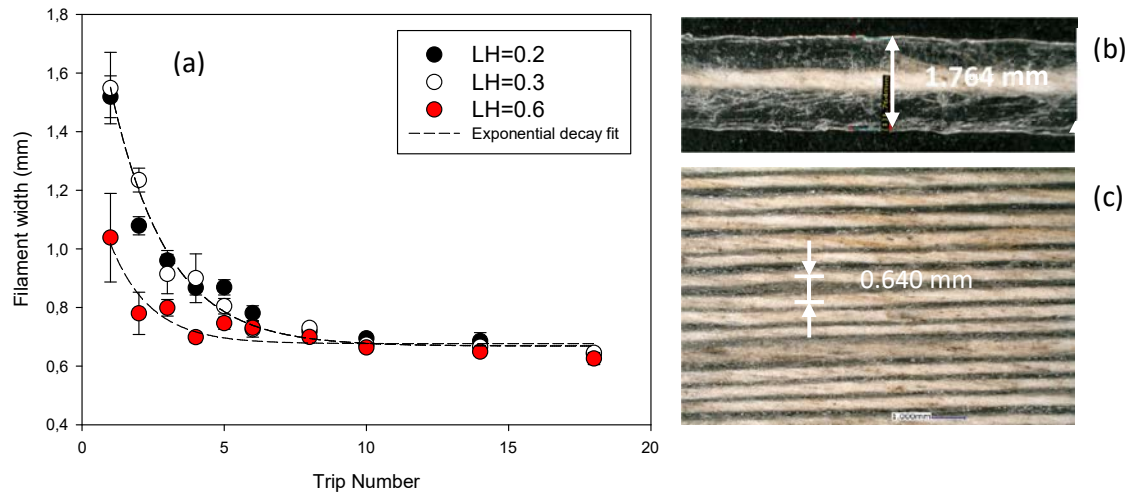


Figure 105 : Evolution of filament width as a function of the Trip Number (TN) for different Layer Heights (LH) (0.2, 0.3 and 0.6 mm) (a) (ID = 0.6 mm, LN = 1). Micrograph of a single printed filament (b) and several printed filaments (c) showing the effect of the trip number on the filament width.

Figure 106.a, b present a similar experiment but with different Interfilament Distance (ID) of 0.4, 0.6 and 0.8 mm while keeping a constant Layer Height (LH = 0.3 mm) during printing. The Interfilament Distance ID enables to control the gap between the printed beads which should influence the internal cohesion of the sample, the fiber content for a constant sample width but also the mechanical properties [35]. The tested values have been selected because they allow the printing of high quality material. Above ID = 0.8 mm, there is a lack of cohesion between the filaments, making it impossible to carry out mechanical tests.

The sigmoid trend in layer thickness with Trip Number is broadly similar to Figure 104.a with an increase in composite thickness with TN until stabilization occurs around TN = 10. This is observed regardless of the ID. However, the Interfilament Distance considerably influences the variation in layer thickness between low and high Trip Number (Figure 106.a). High ID (ID = 0.8 mm) that are greater than the initial filament diameter ($503 \pm 47 \mu\text{m}$) flatten the curve with a reduction in the thickness of the final layer. On the contrary, a low ID of 0.4 mm, which is smaller than the filament diameter, drastically increases the thickness of the composite and leads to a deviation from the

preset thickness given by the Layer Height (LH = 0.3 mm) and also on the compression ratio (real thickness/initial filament diameter) because of flax yarn overlapping.

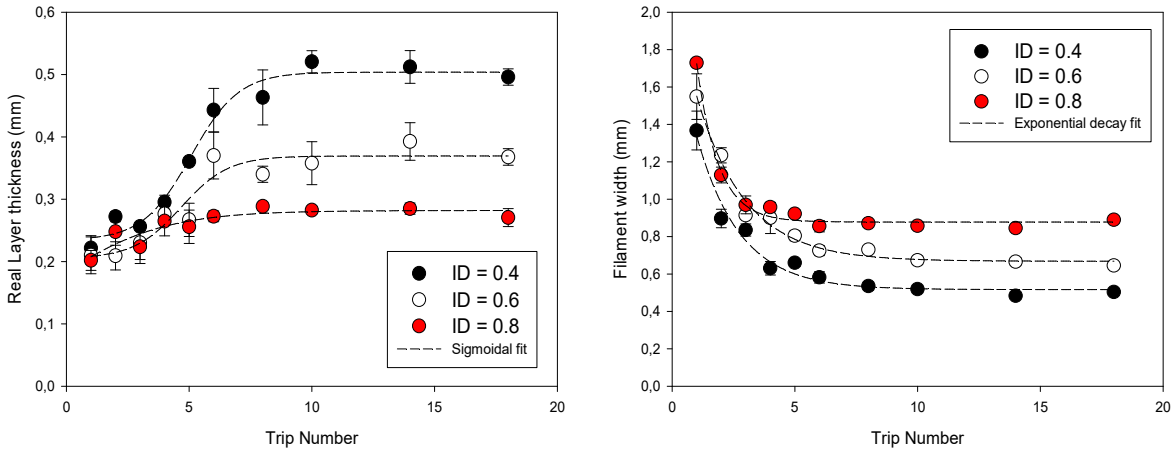


Figure 106 : Evolution of the real thickness of the layer (on one layer) as a function of the Trip Number (TN) for different Interfilament Distances (0.4, 0.6 and 0.8 mm) (a) (LH = 0.3 mm, LN = 1). Evolution of the filament width as a function of Trip Numbers (TN) for different Interfilament Distances (0.4, 0.6 and 0.8 mm) for a cFF/PLA composite. (LH = 0.3 mm, LN = 1).

Figure 106.b confirms that the Trip Number has a dramatic effect on sample width and average filament width. Above TN = 10, the average filament width reaches values in the same range than the preset Interfilament Distance (0.4, 0.6 and 0.8 mm) due to the reduced flow of the polymer matrix. Here, the space available for the printed filament is slaved to the distance between neighboring filaments (ID) (Figure 106). Reducing the lateral space between the filaments, and keeping the volume of the material implies a flow of the polymer in the direction of thickness.

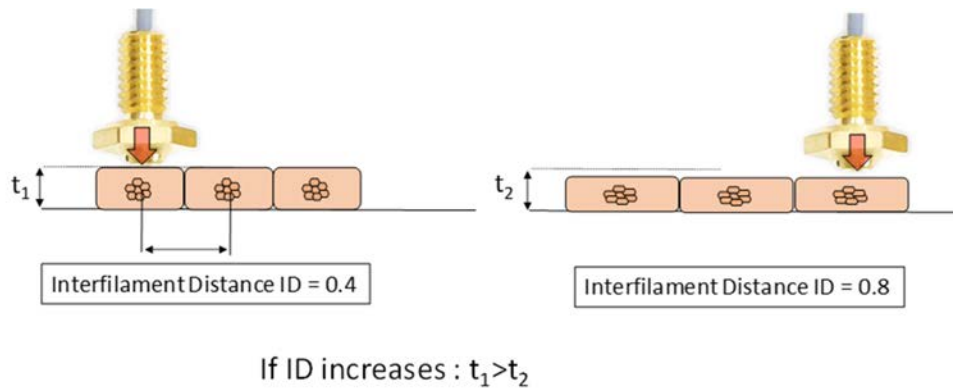


Figure 107 : Schematic view of the effect of Interfilament Distance (ID) during the variation of Trip Number as a function of the thickness of the layer. The LH is kept constant.

The consequences of the Trip Number and the Interfilament Distance on the tensile properties are evidenced in Table 13. Optimal tensile properties are found for ID = 0.6 mm. The lower stiffness and strength observed for ID = 0.4 mm are due the microstructure and associated defects due to filament overlapping, mis-alignments and porosity. Indeed, the variation of ID also implies a slight modification of the microstructure with a higher porosity for ID = 0.4 mm ($V_p (ID = 0.4 \text{ mm}) = 5.4 \pm 0.8 \%$; $V_p (ID = 0.6 \text{ mm}) = 3.2 \pm 0.7 \%$; $V_p (ID = 0.8 \text{ mm}) = 2.3 \pm 0.9 \%$ which may be due to the overlapping of filaments.

As observed in Figure 108, for ID = 0.4 mm, higher porosity content appears in the last layers. This phenomenon is explained by the overlapping of the flax yarns on a layer N leading to an irregular surface for the deposition of the layer $N+1$.

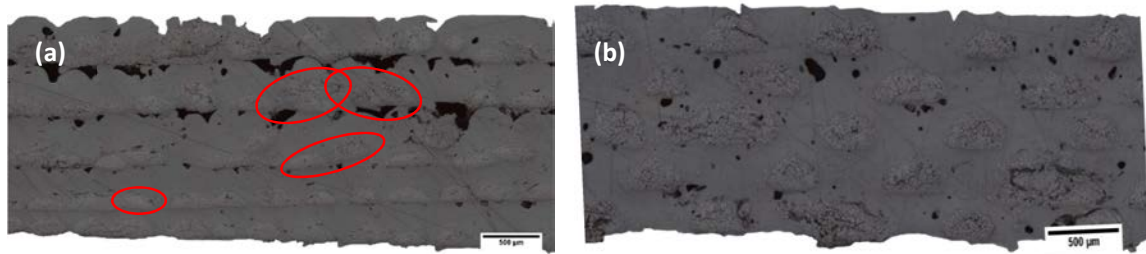


Figure 108 : Cross-section of cFF/PLA composite with ID = 0.4 mm (a) and 0.8 mm (b). Red circle shows the filament overlapping. (LH = 0.3 mm, TN = 37 and 19 for ID = 0.4 and 0.8 mm respectively, LN = 5).

The Trip Number does not affect the stiffness of the printed samples as standard deviations overlap. However, the strength is altered with a decrease as the TN increases. This may be due to a statistically uncertain number of defects due the larger sample size (fiber overlap, cracks on sample edge,...).

Table 13 : Tensile modulus, tensile strength and strain for various Interfilament distances (0.4, 0.6, 0.8mm) and Trip Numbers (5, 10 and 25) for cFF/PLA printed composite. The tests were performed on one sample with a Layer Number = 5 for interfilament distances variation and Layer number = 1 for Trip Numbers.

ID (mm)	E1 (GPa)	σ (MPa)	ϵ (%)
0.4	12.8 ± 1.5	135 ± 10	1.4 ± 0.1
0.6	15.6 ± 2.2	186 ± 4	1.9 ± 0.2
0.8	16.4 ± 2.4	147 ± 16	1.6 ± 0.3
TN	E1 (GPa)	σ (MPa)	ϵ (%)
5	10.3 ± 1.9	130 ± 19	1.7 ± 0.2

10	9.6 ± 2.2	132 ± 14	1.6 ± 0.3
25 (full sample)	11.4 ± 2.7	112 ± 11	1.6 ± 0.2

4. Influence of Layer Number (LN) on the mechanical properties of printed cFF/PLA composites

The Layer Number (LN) represents the number of printed layers (Figure 98). Figure 109.b shows that the printing of several layers induces, for a LH = 0.2 or 0.3 mm, a linear reduction of the average thickness of the layers from 0.3 to 0.2 mm. The average layer thickness is calculated by dividing the total thickness by the Layer Number.

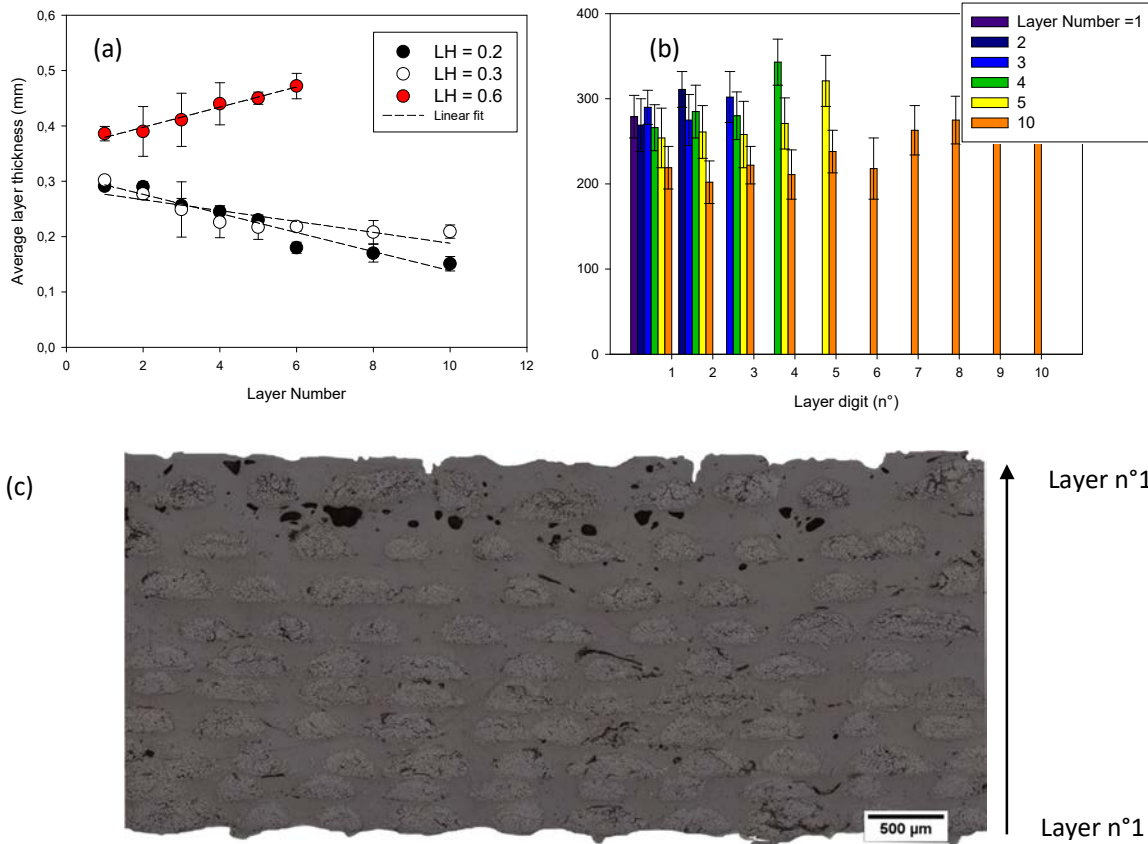


Figure 109 : Evolution of the average layer thickness as a function of the Layer Number (LN) for different Layer Heights (0.2, 0.3 and 0.6 mm) (ID = 0.6 mm, TN = 25) (a). Evolution

of the actual layer thickness as a function of layer digit ($n^{\circ}1$ to 10), (b) ($ID = 0.6$ mm, $LH = 0.3$ mm, $TN = 25$). Micrographic cross section of 10 layers of cFF/PLA showing the difference in architecture through the laminate (c) ($ID = 0.6$ mm, $LH = 0.3$ mm, $TN = 25$, $LN = 10$).

The trend is radically different when the LH is set at 0.6 mm with a thickness that increases slightly with the Layer Number (Figure 109.b). In addition, beyond 6 printed layers, the increase in the distance between the nozzle and the surface is such that compaction is considerably reduced and the printing process with adhesion to the previous layer could not take place. Increasing the Layer Number from 1 to 10 does not generate a homogeneous distribution of layer thickness and compression ratio across all plies. Figure 109.b, c evidence the evolution of the actual thickness of each layer as a function of the layer digit, i.e. the position of each layer in the sample (1 is the layer nearest building plate and 10 the last printed layer).

The increase in the Layer Number induces a continuous increase in the actual layer thickness through the laminate with a thinner layer for the first layer compared to the last printed layers (Figure 109.b, c). Thus, printing an N layer affects the previous N-1 layer by providing additional compressive pressure on the molten composite. The more LN, the greater the compression on the previous layers.

Therefore, in order to achieve a constant compression ratio throughout the printing process, a function of the LH values should be proposed rather than a constant value. Work should also be done on the effect of the yarn on the compressibility of the filament.

The Layer Number (LN) has only a small effect on the overall sample width and the average filament width (Figure 110) with a slight linear increase with the Layer Number for LH of 0.2 and 0.3 mm. This is caused by the additional compression when printing many layers. Thus, the almost constant value of the filament width with LN increasing at a fixed value of $LH = 0.6$ mm confirms the relationship between additional layer, compression and filaments width.

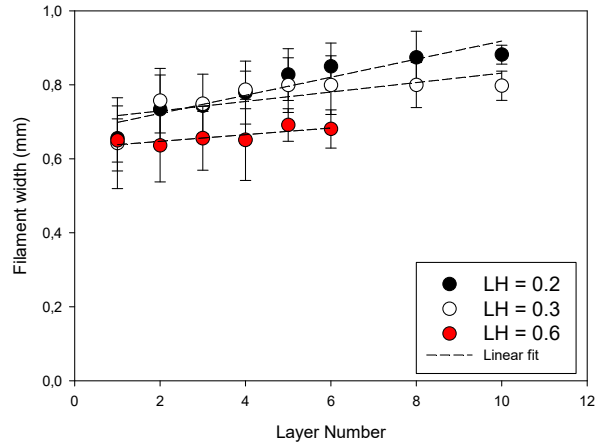
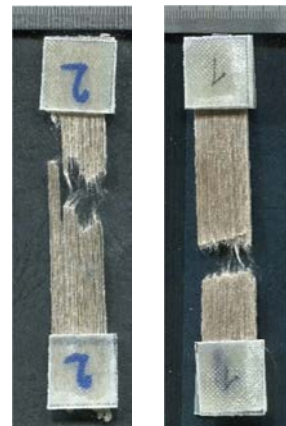
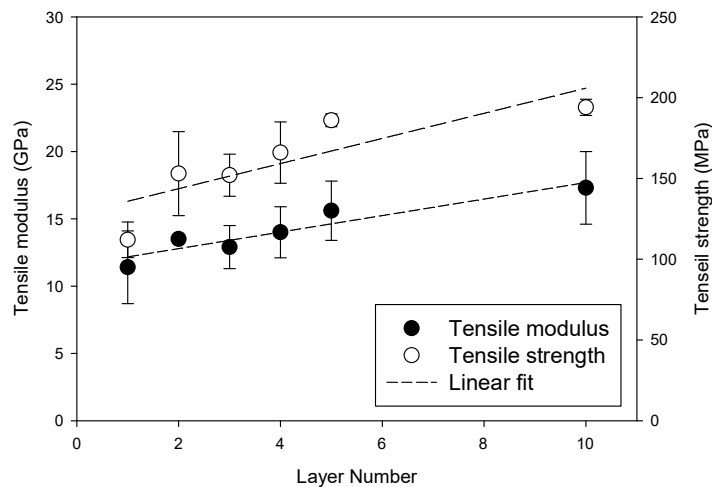


Figure 110 : Evolution of the average filament width as a function of the Layer Number (LN) for different Layer Heights (0.2, 0.3 and 0.6 mm) (ID = 0.6mm, TN = 25) for a cFF/PLA composite.

The consequence of various Layer Numbers (LN) on the tensile properties and fracture behavior of cFF/PLA composite is evidenced in Figure 111.a,b. The mechanical data are gathered in Table 14. The increase in LN from one layer to ten layers implies a linear increase in tensile modulus (+ 50 %) which is due to the greater compaction of the printed filament as shown by average layer thickness diminishing as seen in Figure 109.a.

Higher tensile strength (+ 73 %) and similar strain at break are also measured when five layers are printed (Table 14). This confirms that the load transfer between the PLA matrix and the flax yarn reinforcement is more efficient with a higher Layer Number, as highlighted by observation of the fracture surface (Figure 111.b). In fact, a reduced number of dry yarns is observed for LN = 10 compared to biocomposite with LN = 1 due to the compacting effect on the impregnation of the flax yarns.



(a)

Figure 111 : Evolution of tensile modulus and tensile strength as a function of Layer Number (LN) (ID = 0.6 mm, LH = 0.3 mm, TN = 25) (a), fracture surface of cFF/PLA composite with Layer Number of 1 and 10 (b) (ID = 0.6 mm, LH = 0.3 mm, TN = 25, LN = 10).

In a similar way than observed in Chapter 3 (but for different reason), the evolution of cFF/PLA printed biocomposite properties with their geometry has to be carefully taken into account in the design process.

Table 14 : Tensile properties of cFF/PLA composite for different Layer Numbers (LN) (ID = 0.6 mm, LH = 0.3 mm, TN = 25).

LN	E_1 (GPa)	σ (MPa)	ϵ (%)
1	11.4 ± 2.7	112 ± 11	1.6 ± 0.2
2	13.5 ± 0.2	153 ± 26	1.6 ± 0.2
3	12.9 ± 1.6	152 ± 13	1.7 ± 0.3
4	14 ± 1.9	166 ± 19	1.8 ± 0.3
5	15.6 ± 2.2	186 ± 4	1.9 ± 0.2
10	17.3 ± 2.7	194 ± 8	1.7 ± 0.1

Figure 112.a,b and c bring together all the mechanical results of this work and compare them to short natural fiber printed composites (Figure 112.a), continuous natural fiber reinforced printed composites (Figure 112.a) and biocomposite manufactured using conventional processes (Figure 112.b, c). Overall, the mechanical properties are always considerably higher than for printed short natural fiber composites. This emphasizes their potential for semi-structural applications in the same range as continuous glass/PA composites (see Chapter 3). The dispersion of stiffness and strength is important and shows that for a similar Flax/PLA material, with a similar fiber volume fraction, the 3D printing process can interestingly give a wide range of tensile properties (from single to double for strength and from single to triple for stiffness) depending on the slicing parameters (LH, ID, TN and NL) which opens the design space for biocomposites parts.

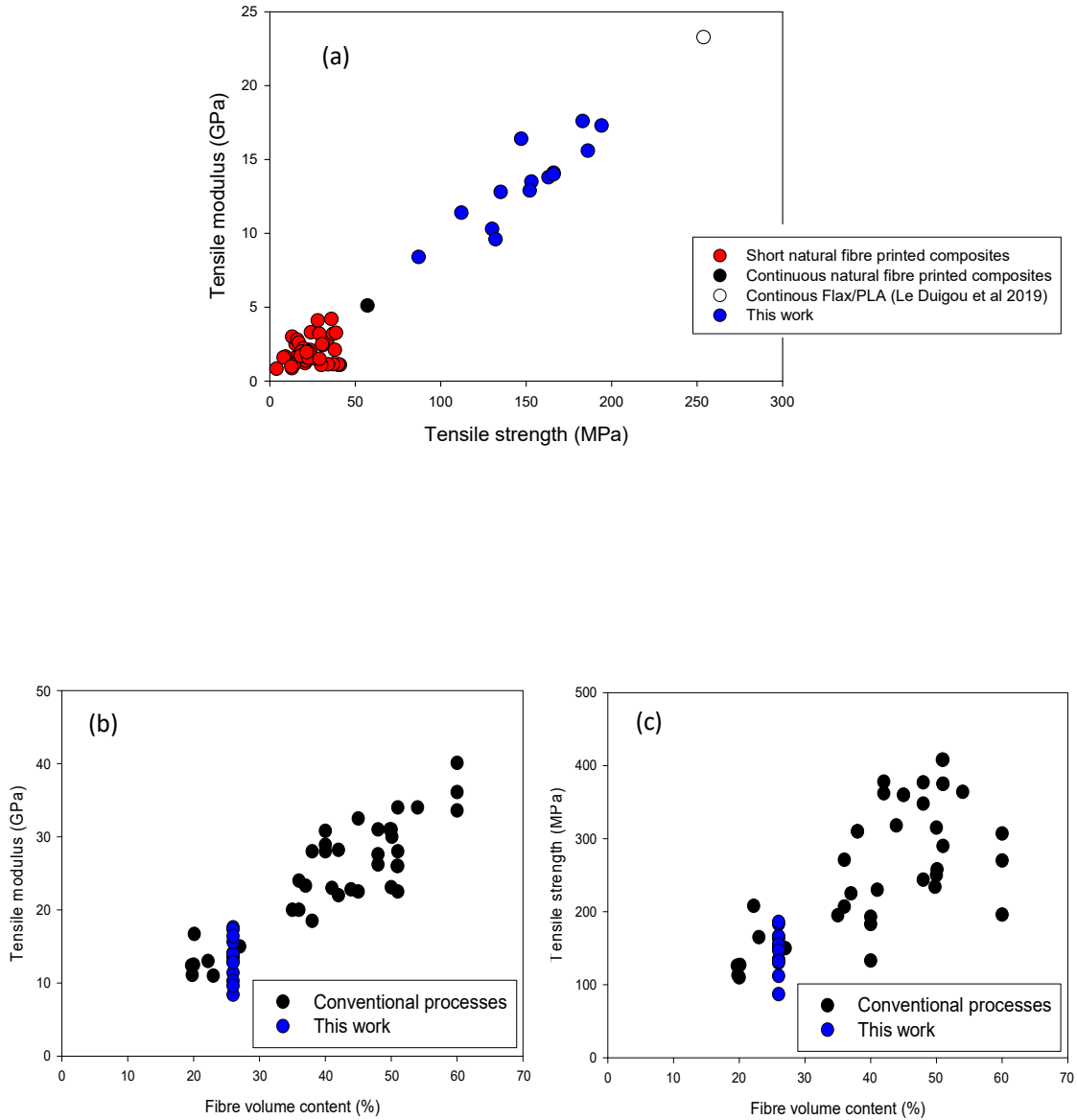


Figure 112 : Graph of tensile modulus and tensile strength (a) [85], [266], [268], [275], [282], [292], [302], [308]. Evolution of Tensile modulus (b) and tensile strength (b) as a function of fiber volume fraction for cFF/PLA in relation to the literature values for the conventional manufacture of natural long fiber composites [237], [259], [309], [310], [382]–[387].

Compared to the work of Matsuzaki et al. [85] on continuous Jute/PLA, the current work exceeds both the tensile modulus and strength. The reasons can be the difference in fiber quality, linear yarn weight, fiber impregnation and fiber content. Previous work carried out in the same laboratory on a similar continuous Flax/PLA composite [298] resulted in tensile properties superior to those presented here ($\approx + 30\%$).

5. Influence of raster angle / fiber orientation on the mechanical properties of printed cFF/PLA composites

As observed in Chapter 3, transversally printed continuous fiber composite exhibit mechanical behavior and properties that are very sensitive to sample geometry and edge effect as evidenced on synthetic composites. Here, two batches are evaluated, one with cut edges (Figure 113.b) and the other left as printed (Figure 113.a) in order to evaluate transverse properties of the 3D printed cFF/PLA in-situ.

On the edge of the samples, loops are created due to turning-back of the print head with a curvature radius which depends on the interfilament distance, filament diameter and filament stiffness. Here, cFF/PLA has a radius of curvature of 0.28 ± 0.03 mm, which is three times smaller than the 3D printed composites reinforced with synthetic fibers (see section 1.1 of Chapter 3). This is explained by a higher interfilament distance (0.6 mm here and 0.9 mm for Markforged® composites) and lower stiffness for cFF/PLA (between 11.3 ± 2.7 GPa for cFF/PLA, 60.1 ± 6.9 GPa for continuous carbon based composites, 28.9 ± 2.2 GPa for continuous glass fibers based composites). These loops are specific to 3D printing of continuous fiber composites and induce an original microstructure with the creation of very rich fiber zone and resin-rich regions within the loop.



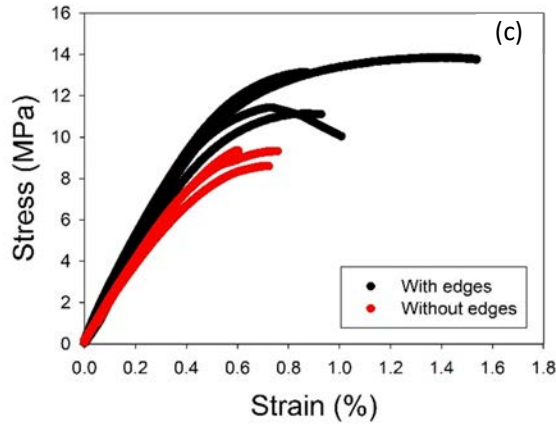


Figure 113 : Photograph of cFF/composites with raster angle of 90° with edged (a) and without edges (b). Tensile stress vs train of cFF/PLA printed parts tested in transverse direction with and without edges (c). (ID = 0.6 mm, LH = 0.3 mm, TN = 166, LN = 5).

Typical tensile stress as a function of strain of transverse cFF/PLA with and without edges is presented in Figure 113.c. For the nature of the two samples, the stress increases up to 0.6 and 0.9 % for samples with and without edges, respectively, followed by plastic deformation and sample rupture around 0.7 % for samples without edges and between 1 and 1.8 % for samples with edges. In the literature, flax fibers composites elaborated by thermocompression exhibit a more brittle behavior with a sudden rupture at around 0.8 % of strain [378].

Indeed, the loop induces a pre-crack at the edges of the sample and, during tensile test characterization, the crack propagates between the detached printed beads, leading to unwinding and breakage (Figure 114), as observed in section 2.1 of Chapter 3 for 3D printed composites reinforced with synthetic fibers. Consequently, the transverse properties are influenced by the inter-bead cohesion, the interface between flax yarn and the matrix and the microstructure of the edges (fiber rich and matrix rich areas, cracks induced by 3D printing) which explain its ductile behavior and moderate mechanical performance.

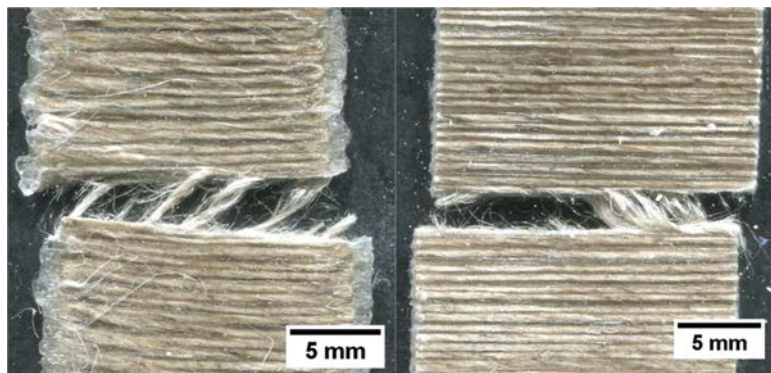


Figure 114: Fracture images of transverse specimen with edges (left) and without edges (right).

Mechanical properties of transverse parts are summarized in Table 15. First, a strong anisotropy is observed for cFF/PLA samples. Tensile Moduli exhibit an Anisotropic Ratio (AR ratio longitudinal to transverse properties) between 6.2 and 7.8 for samples with and without edges. AR for strength is between 15 and 20 for parts with and without edges, respectively. The edged of the part appears to influence the mechanical properties of transverse parts with transverse modulus and strength 25 % and 35 % higher for transverse parts with edges. This difference can be explained by several factors:

- The PLA matrix at the edges of the specimen (Figure 113.a) removed in samples without edges (Figure 113.b) act as a gangue-like coating and contributes to the transverse tensile properties.
- The loops on the edges of the samples lead to fiber-rich areas but also to a small amount of flax fibers that can contribute to energy dissipation during transverse loading.

Compared to continuous synthetic fiber composites, the transverse stiffness has been improved (between 0.2 and 1.2 GPa for carbon and glass fiber reinforced composites) while a similar range of transverse strength is observed (between 5 and 12 MPa for carbon and glass fiber reinforced composites).

Actually, the transverse properties of natural and synthetic fiber reinforced printed composites depend mainly on the inter-bead interface as well as edge defects (resin-rich areas and cracks located between the loops).

Table 15 : Mechanical properties of transverse cFF/PLA samples compared with longitudinal ones. (ID = 0.6mm, LH = 0.3mm, TN = 166 for transverse and TN = 25 for longitudinal, LN = 5).

	E1 (GPa)	σ (MPa)	ϵ (%)
90° with edges	2.5 ± 0.1	12.3 ± 1.4	1.1 ± 0.3
90° without edges	2.0 ± 0.1	9.1 ± 0.4	0.7 ± 0.01
0°	15.6 ± 2.2	186 ± 4	1.9 ± 0.2

Moreover, the higher stiffness for cFF/PLA can be attributed to the higher stiffness of PLA compared to polyamide (E = 3.6 GPa and E = 1.7 GPa for PLA and PA respectively [379], [388]).

Compared to flax fiber composites manufactured by thermocompression with a similar fiber content ($W_f = 30\%$ wt.), cFF/PLA exhibit drastically lower transverse strength ($E_T = 4.15 \pm 0.35$ GPa and $\sigma_T = 27 \pm 3$ MPa for conventionally manufactured biocomposites) [298]. Lower properties are attributed to the printing induced microstructure with inter-bead interfaces and low intra bead transverse cohesion due to incomplete impregnation of the yarn.

Conclusion

Additive manufacturing is an emerging technology to produce the next generation of composite materials that is currently limited by the lack of applied materials. In the context of current environmental concerns, it is becoming necessary to develop biobased and material with lower environmental footprint. Most natural fiber composites used for 3D printing include short natural fibers with moderate mechanical properties. One alternative is the development of continuous natural reinforced polymer to improve the mechanical properties.

The purpose of this chapter was to present the manufacturing and 3D printing of cFF/PLA and to deeper investigate the relationship between several slicing parameters such as the Layer Height (LH), the Interfilament Distance (ID), the Trip Number (TN), the Layer Number (LN) and the raster angle on the final sample geometry (printing accuracy), the microstructure and the tensile properties in order to envisage the tailoring of 3D printed continuous flax/PLA biocomposites.

First of all, the co-extrusion allowed to create thin cFF/PLA filaments, which is very promising for designing small-scale structure of parts with a very intricate design. However, this manufacturing process exhibit some limitations, especially with regard to its reproducibility and the rate of filament production.

Layer Height is a crucial parameter to control the compaction of filament during printing. Decreasing LH from 0.6 to 0.2 mm induced a reduction in layer thickness, a decrease in porosity content and an increase in tensile properties (+210 % for stiffness and strength).

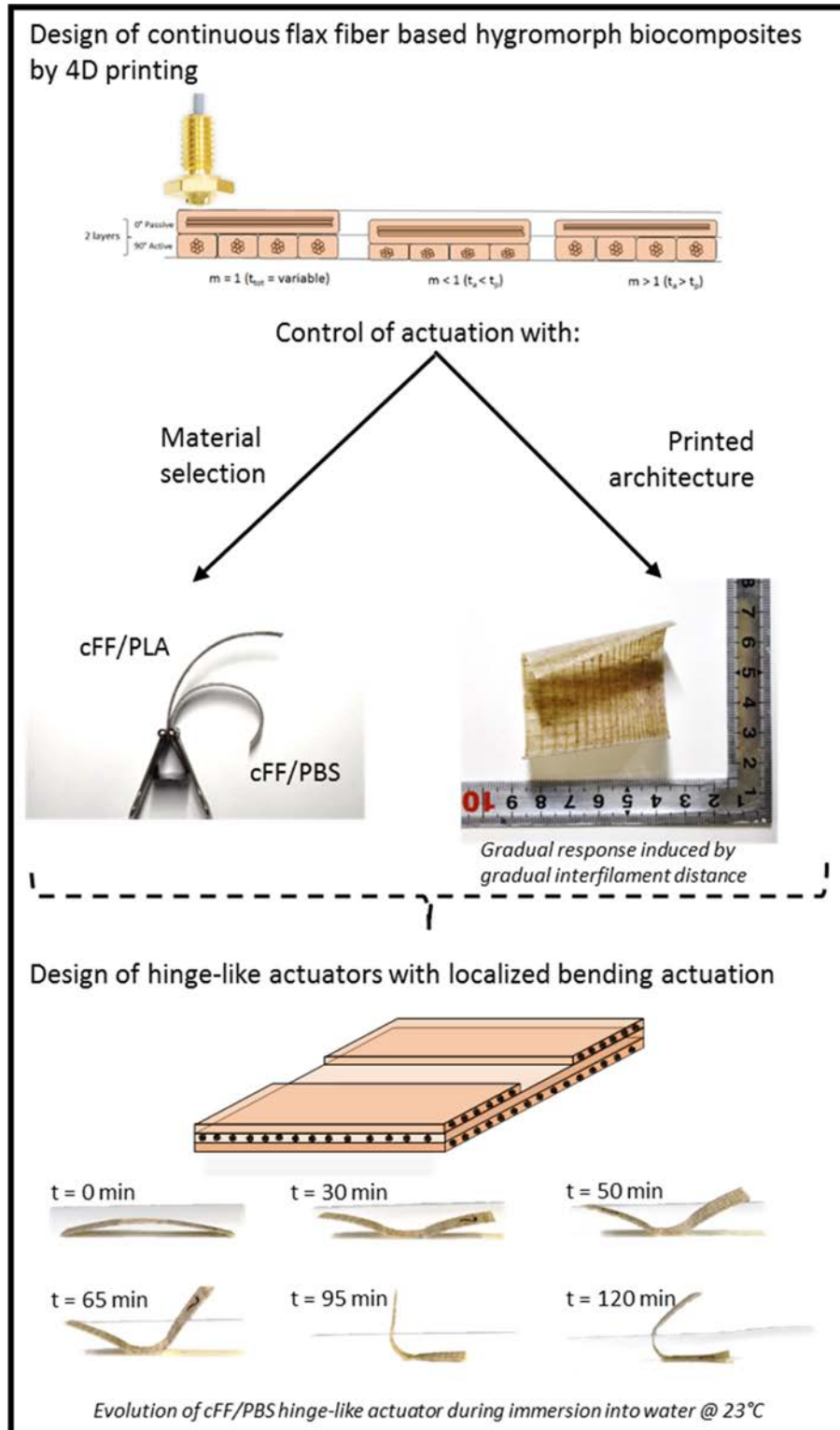
Layer thickness was limited by the compressibility of the twisted flax yarn while the relation between LH and the actual layer thickness was linear. Over and under-compaction were noticed in low to high LH. This implied that when printing many layers, the compaction ratio (initial filament diameter/real layer thickness) varied. Increasing Layer Number from 1 to 10 brought higher compaction ratio and

higher tensile properties (+ 50 % in modulus and + 73 % in strength). Compaction varied along the cross section, with the first plies being the most compressed. Trip Number (TN) and Interfilament Distance (ID) acted as “neighboring filaments” that influenced the polymer matrix flowing during the printing process by controlling the space available for the filament between the nozzle and the adjacent filaments. This considerably affected the average layer thickness as well as the overall geometry of the sample. Increasing Trip Number from 1 to 18 reduced the space available for the polymer matrix to flow for each filament. Thus, the sample geometry is more accurate and the average filament width (total width/ Trip Number) followed the preset Interfilament Distance. A decrease of ID from 0.8 to 0.4 emphasized this effect.

cFF/PLA composites exhibit a strong anisotropy with longitudinal properties between 6 and 8 times higher than those of transverse ones. This difference is explained by the high sensitivity of the transverse properties to printing defects (such inter-bead porosities) as well as the lower transverse properties of the flax fibers compared to the longitudinal properties.

Overall, the 3D printing process presented here with continuous flax/PLA composites yielded to a wide range of tensile properties that have always been considerably higher than the current published values on short natural fiber printed composites. The tensile properties are of the same order as those of continuous glass/PA printed composites. This confirms the potential of continuous flax fiber reinforced printed composites as high performance composite materials with the added-value of a versatile and disruptive manufacturing process.

Chapter 6: 4D printing of hygromorphic biocomposites with continuous flax fiber/PLA: toward compliant mechanism



Hygromorphic BioComposites (HBC) are a recent trend that is of great interest due to the high water sensitivity of natural fibers and their greater stiffness compared to pure polymers. Moreover, 4D printing allows to fine-tune their material architecture and thus their responsiveness and reactivity. Thus, 4D printing of HBC is a new promising new trend in the development of actionable structures. Moreover, the addition of continuous fibers should help control actuation by anisotropy.

The purpose of this chapter is to assess the potential of 4D-printed bioinspired Hygromorphic BioComposites (HBC) made from a biopolymer (PLA) reinforced with continuous flax fibers (cFF). Timoschenko's equations and parameters, which are usually used for the prediction of the bilayer curvature are discussed in the context of 4D printing.

The selection of materials is first analyzed with the characterization of hygro-elastic properties related to the formulation of two types of HBC, i.e. a stiff polylactic acid (PLA) and a ductile PolyButylene Succinate (PBS) matrix-based composites, named cFF/PLA and cFF/PBS, respectively. cFF/PBS, whose hygroscopic expansion is higher than that of the cFF/PLA, boosts the actuating properties.

Then, the local and gradual architecture of the cFF/PBS is investigated following the bending responsiveness and the reactivity given by changing Interfilament Distance (ID). This slicing parameter influences the HBC architecture and its programming in the 4D printing process.

Finally, compliant mechanism via a localized bending actuation is performed with the design and printing of hinge-like structures. Again, microstructural effects such as hinge gap and interfilament distance (ID) variation imply a wide range of responses, paving the way for the design of complex 4D printed HBC structures based on a compliant mechanism with sequential response

1. Design of hygromorphic biocomposites

To design the hygromorphic biocomposites, the analytical solution given by Timoshenko [320] of the curvature variation $\Delta\kappa$ of a beam subjected to bending due to the difference $\Delta\beta$ of the coefficients of hygroscopic expansion and the moisture content ΔM (see section 4.1 of Chapter 1) was selected. To achieve the highest curvature, the total thickness of the bilayer sample should be kept as small as possible in order to reduce the bending stiffness. Therefore, the minimum number of layers was selected, i.e. two layers. Then, an optimal thickness ratio $m = \frac{t_p}{t_a}$, where t_p is the thickness of passive layer and t_a the thickness of active layer (Figure 115.a) corresponding to the highest value of curvature (Figure 116.a). As observed in the section 2 of Chapter 5, the specificity of FFF compared to the conventional process is the ability to control the compression ratio (diameter of initial filament/real layer thickness) uniformly or not on each layer thanks to the parameter “Layer Height” (LH). Thus, by maintaining a constant number of layers, it may be possible to adjust the thickness ratio m (Figure 115).

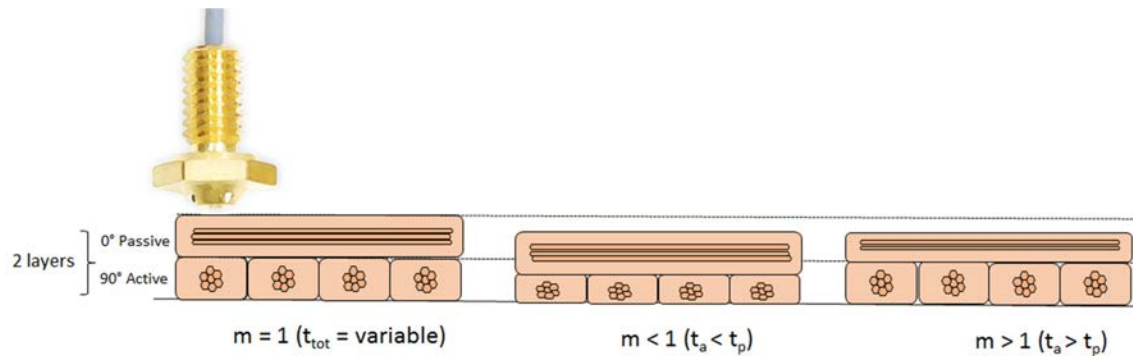


Figure 115 : Schematic view of the concept of different compression ratios allowing a multiple combination of the m ratio with only two printed layers. t_{tot} is the total thickness of the laminate, t_a and t_p are the thickness of the active and passive layers respectively.

Table 16 gathers the theoretical ratio m , the total sample thickness t_{tot} , the passive layer thickness t_p , the active layer thickness t_a , the real m ratio, the compression ratio and the responsiveness of cFF/PLA biocomposites as a function of the Layer Height.

The total thickness differs variably from the preset Layer Height depending on the LH values selected. Maintaining a similar LH between the first and second layer does not allow a ratio m of 1 to be achieved. m ratio varies from 0.87 to 1.19 with an increase in LH from 0.2 to 0.4 mm and *in fine* modifies the responsiveness of HBC. The best correspondence between the theoretical m and the

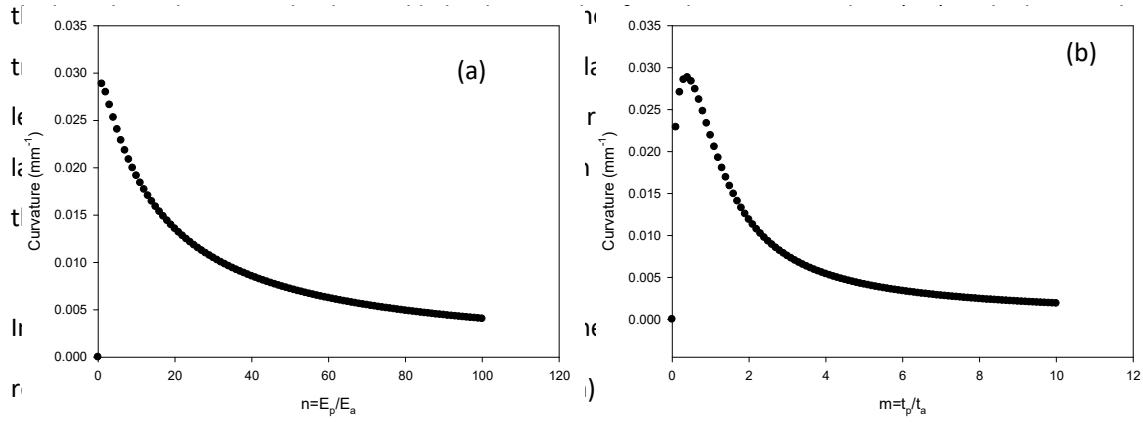
measured m is observed for a Layer Height of 0.3 mm, that confirms the results of the previous chapter on the compaction behavior of cFF/PLA. Section 2 of Chapter 5 showed that while varying the compression rate in a single layer, there are three regimes, namely overcompaction, compaction and undercompaction. Actually, a threshold could be observed around 0.3 mm. Thus, programming a Layer Height of less than 0.3 mm always results in an overcompaction and a layer thickness of approx. 0.2-0.25 mm. This has been attributed to the architecture of the yarn which prevents the reduction of the compressibility of the filament but also to the effect of the compaction of the second layer that influences the compaction of the first layer.

Table 16 : The ratio m , the ratio of each layer height, the global compression ratio and the responsiveness of cFF/PLA hygromorphic biocomposites. The basic printing sequence is $[90/0^\circ]$. * means a printing sequence of $[0/90^\circ]$.

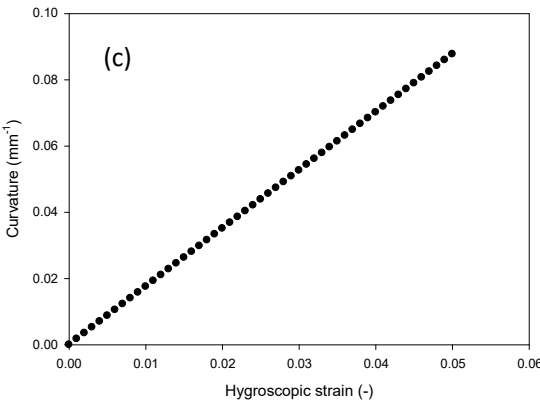
Theoretical 90° and 0° Layer Height (mm / mm)	m _{theoretical ratio}	Total thickness (μm)	Passive layer thickness (μm)	Active layer thickness (μm)	m _{real} ratio	Compression ratio (-)	Responsiveness (10^{-3} mm^{-1})
0.2 / 0.2	1	562 ± 17	269 ± 24	310 ± 12	0.83 ± 0.02	1.80	26.2 ± 3.0
0.3 / 0.3	1	602 ± 14	284 ± 12	316 ± 5	0.90 ± 0.04	1.66	27.5 ± 2.0
0.4 / 0.4	1	719 ± 13	400 ± 12	335 ± 5	1.19 ± 0.02	1.40	15.3 ± 1.0
0.2 / 0.1	0.5	553 ± 34	281 ± 33	296 ± 21	0.93 ± 0.06	1.80	15.3 ± 2.0
0.2 / 0.4	2	651 ± 18	354 ± 22	306 ± 16	1.15 ± 0.07	1.54	13.2 ± 1.0
0.2 / 0.2 *	1	598 ± 44	293 ± 23	300 ± 14	0.98 ± 0.06	1.70	10.0 ± 2.0

Increasing LH towards undercompaction (LH = 0.4 mm) decreases the compression ratio from 1.8 to 1.4 and increases the porosity content. A change in LH from 0.2 to 0.4 mm implies an increase in porosity from $2.1 \pm 0.9 \%$ to $4.5 \pm 1 \%$ which has a negative effect on elastic properties, hygroexpansion and responsiveness [269]

Changing LH between the first and second layer modifies the ratio m from 0.87 to 1.16 and almost doubles the responsiveness according to Timoshenko's equations (Figure 116.a). Changing the printing sequence from $[90/0^\circ]$ to $[0/90^\circ]$ ((0.2 / 0.2)) modifies the ratio m from 0.87 to 0.98 and consequently the actuation. Material compressibility, slicing and printing parameters can control the architecture of the HBC. Contrary to section 4 of Chapter 5, in this study the first layer is always



increase of n leads to a reduction in the tensile moduli of the passive layers. Here again, the printing parameters such as layer heights and interfilament distances of the hygromorphic biocomposite depend on the layer height and layer thickness, which affect the composite responsiveness. For the design of actuators based



would allow us to lower the thickness of the passive layer at a high level. Through different layer thicknesses, the design window of the composite depends on layer thickness ratio and thus in the design of actuators based on hygromorphic biocomposites should be taken into account for

The differential coefficients of hygroscopic expansion in the beam direction between the active β_a and passive β_p layers is represented by $\Delta\beta$ in Equation 2. The term ΔM represents the change in moisture content in the HBC with a variation of the moisture condition. The curvature evolves linearly with hygroexpansion (Figure 116.b) which emphasizes the predominant role of this parameter on the ratio n or m . Previous work has evidenced that porosity has a negative effect on the hygroscopic expansion of 3D printed biocomposites [269], while the tensile modulus of the matrix has a constraining effect on the fibers during hygroscopic expansion [389].

Figure 116 : Evolution of the curvature as a function of the ratio m (t_p/t_a) with $n = 7.05$ (a), of the ratio n ratio (E_p/E_a) with $m = 1$ (b) and of the hygroscopic strain (c) for cFF/PLA hygromorphic biocomposites.

2. Material selection

Compared to hygromorphic wood-based materials, hygromorphic biocomposites often result in a longer levelling time or slower responsiveness as they do not have the vascular capacity of wood tissue. In addition, the thermoplastic material may have a theoretical thickness threshold that limits moisture absorption [390]. Therefore, the formulation of materials is of great importance. This is one major advantage of hygromorphic biocomposites compared to the wood-based hygromorph. Thus, besides the cFF/PLA hygromorphs where the matrix is considered stiff, the cFF/PBS counterparts exhibit drastically different tensile properties due to soft matrix ($E_{PLA} = 3.6$ GPa ; $\epsilon_{PLA} = 3$ % [379] and $E_{PBS} = 0.64$ GPa ; $\epsilon_{PBS} = 264$ % [391]). The soft polymer should be able to withstand larger hygroscopic strain and reduce the constraining effect over fibers.

The mechanical, hygroscopic and actuating properties of the hygromorphic biocomposites cFF/PLA and cFF/PBS are gathered in Table 17 . Due to continuous reinforcement combined with a low linear

weight (68 Tex) and the selection of flax fibers, the tensile properties of biocomposites have evidenced high values compared to the literature data on 3D-printed short-fiber biocomposites [392].

Table 17: Mechanical, hygroscopic and actuation properties of cFF/PLA and cFF/PBS hygromorphic biocomposites.

Materials	Longitudinal		Transverse		Anisotropic	Responsiveness (mm ⁻¹)	Reactivity (10 ⁻⁴ mm ⁻¹ min ⁻¹)
	Modulus (GPa)	E ₁	stiffness (MPa)		ratio ($n = E_p/E_a$)		
cFF/PLA	15.6 ± 2.2		2.5 ± 0.1		6.24	0.028 ± 0.002	1.2 ± 0.4
cFF/PBS	10.3 ± 0.7		0.43 ± 0.04		24	0.054 ± 0.003	7.2 ± 0.9

Printing the bilayer with LH = 0.1 mm has not been possible due to overcompaction and technical failure. Here, the Layer Height applied to the tensile test specimens (0 or 90°) are the same as those used for the bilayer, i.e. 0.2 mm.

As noticed in section 5 of Chapter 5, the transverse modulus is low and mainly influenced by those of the PLA matrix, the microstructure heterogeneities and the printing-induced defects. The anisotropic ratio (or the ratio $n = E_p/E_a = 6.24$) is considerably higher than that of 3D-printed short-wood-fibers ($V_f = 15$ % vol.) reinforced PLA biocomposites ($n = 1.5$ [269]) but lower than that of continuous flax fiber ($V_f = 60$ % vol.) reinforced maleic-anhydride-grafted-polypropylene (MAPP/Flax) biocomposite ($n = 17.3$ [319]).

Although increasing the ratio n reduces the actuation potential (Figure 115.b), controlling the anisotropic properties allows better control of the directionality of shape-changing and improves the building potential of the multi-curvature system, creating constraints for the longitudinally oriented fibers and swelling for the transverse ones [390]. As evidenced by Wang et al. [215] on continuous carbon fibers/PA6, the final direction of curvature is the angular bisection line of the acute angle between the crossing fiber bundles. Hygroexpansion is driven by the architecture of the natural fibers (via the microfibrillar angle, MFA) and their content within the matrix. Thus, the results obtained for 3D-printed cFF/PLA are in the same range as those observed for MAPP/Flax with a similar fiber fraction [176] but obviously lower than those of MAPP/Flax biocomposites containing 60 % vol. [319].

The production of filaments with continuous natural fibers is still in its early stages and several optimizations should be made as the volume fraction of the fiber is currently limited to $V_f = 30\%$ vol.

Substitution of PBS for the PLA matrix reduces longitudinal and transverse stiffness by 30 % and 75 % respectively due to the high contribution of the matrix (Table 17) in composites having moderate fiber content. Interestingly, the anisotropic ratio and hygroscopic strains are drastically improved compared to cFF/PLA counterparts. Then, cFF/PBS shows a 250 % increase in hygroscopic strain compared to cFF/PLA biocomposites. Free flax fibers can exhibit a radial hygroscopic expansion of about $21 \pm 3\%$ [274], thus a low stiffness matrix such as PBS seems to reduce the constraining effect on the flax fibers during the sorption, which allows a higher hygroexpansion of fibers.

Actuation measurements were carried out on cFF/PLA and cFF/PBS samples whose stacking sequence was set to a total number of two layers (Table 17). Comparison of the theoretical curvature with those obtained experimentally confirms that the use of Timoschenko's equations to design hygromorphic biocomposites with a slender geometry is fairly reliable (error rates of 9 % and 7 % for cFF/PLA and cFF/PBS, respectively). Figure 117.a, b and c show the microstructure of cFF/PLA HBC after printing, cFF/PLA and cFF/PBS HBC before and after immersion in water, respectively.

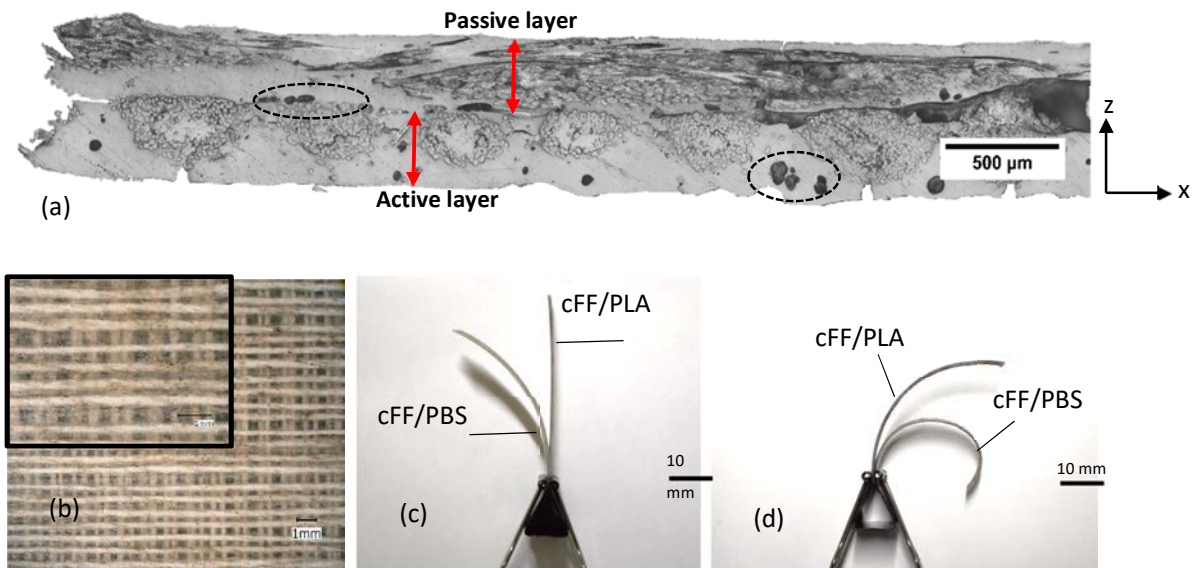


Figure 117 : Microscopic observation of cFF/PLA cross section showing bilayer microstructure and interlaminar defects (a), in-plane microstructure with a higher magnification insert showing local misalignment and variation of interfilament distance (b), comparison of the initial state of the hygromorphic biocomposites cFF/PLA and cFF/PBS taken after printing (c) and after immersion in water (d).

Microscopic observations of the HBC microstructure highlight the quality of the microstructure control even though some interlaminar and matrix porosities (Figure 117.a), local misalignment of the yarn and local variation of the interfilament distance may be noticed (Figure 117.b). Overall, 4D-printing of hygromorphic biocomposites with continuous flax fibers offers a much better actuating performance than that observed with short-natural-fibers-reinforced HBC. For example, short-wood-fibers/PLA-PHA (blend) hygromorphic biocomposites have a maximal curvature of $0.012 \pm 0.003 \text{ mm}^{-1}$ [269]. This is mainly attributed to the higher fiber content, the different biochemistry of the fibers (lignin content) and better control of fiber orientation. However, a higher maximal curvature is achieved with 4D printed continuous carbon fiber/polyamide based actuators operated at 98 % RH at 23 °C (see Chapter 4), i.e. $0.088 \pm 0.011 \text{ mm}^{-1}$. This difference is explained by a higher $\beta_T \Delta M$ for continuous carbon fiber/polyamide based actuators (6.4 for continuous carbon fiber/polyamide based actuators instead of 3.8 for cFF/PBS actuators).

The curvature analysis was performed by the difference between the initial curvature (50 % RH at 23 °C) and the final curvature (immersion at 23 °C). Hygromorphic cFF/PBS biocomposites show an increase in responsiveness by a factor 2 compared to cFF/PLA. This can be directly attributed to the higher transverse hygroexpansion of cFF/PBS (Table 17).

To better understand the link between hygroexpansion, matrix stiffness and curvature actuation, the radial residual stresses generated within asymmetrical laminates by moisture sorption are estimated using Equation 15 [393]:

$$\sigma_{22} = \sigma_{radial} = \frac{E_{11} \cdot E_{22} \cdot t}{E_{11} + E_{22} \Delta \rho} \left(\frac{1}{2} + \frac{1}{24} \left(2 + \frac{E_{11}}{G_{12}} + \frac{E_{22}}{G_{12}} \right) \right) \quad \text{Equation 15}$$

With t the total thickness of the sample ($t = 0.650 \text{ mm}$), $\Delta \rho$ the differential curvature radius ($\Delta \rho = \rho$ after printing - ρ after actuation), E_{11} and E_{22} are the values of longitudinal and transverse modulus, G_{12} is the in-plane shear modulus of the laminate estimated by the rule of mixture using $G_{flt} = 2500 \text{ MPa}$ [394] and $G_m = \frac{Em}{2(1+\nu)}$. We obtained a range of radial compressive stresses of 31 and 17 MPa for cFF/PLA and cFF/PBS respectively, confirming the lower constraining effect of PBS on flax fibers. Although it may affect the load transfer between the fiber and the matrix as proposed elsewhere [274], the curvature is enhanced, underlining the predominant effect of the differential expansion between the layers on the differential expansion between the fiber and the matrix.

The initial state observed after printing is radically different between the two biocomposites. While cFF/PLA has a flat shape after printing (Figure 117.b) showing a state of almost zero-stress, cFF/PBS already has a curvature in the opposite direction to the curvature induced by moisture (Figure 117.c).

This may be due to the difference in glass transition temperature between PLA and PBS ($T_{g \text{ PLA}} = 56 \text{ }^\circ\text{C}$ and $T_{g \text{ PBS}} = -28 \text{ }^\circ\text{C}$) that explains the different states of thermal stress. The difference in curvature between the initial state (after printing) and the zero-curvature state of cFF/PBS represents about 15 % of their total curvature variation and is due to a combination of thermal stress release and hygroscopic stresses. Further work should be carried out to decorrelate the contribution of thermal and hygroscopic strains on the actuation.

The reactivity of cFF/PLA and cFF/PBS, evaluated as the actuation speed (i.e. the slope of the curvature curve as a function of time) is also drastically higher than for hygromorphic biocomposites reinforced with short fibers for a similar reason to responsiveness [269]. cFF/PBS exhibits a 6-fold higher reactivity than the composites based on the PLA matrix (Table 17). Reducing the matrix constraining effect on the fiber improves transient and stationary sorption by increasing the free volume of the polymer [395]. In addition, PBS ($M = 0.9 \text{ \%}$ at $20 \text{ }^\circ\text{C}$) is more sensitive to moisture than PLA ($M = 0.3 \text{ \%}$ at $20 \text{ }^\circ\text{C}$) [396], [397].

After sorption and desorption, the hygromorphic biocomposite does not return to its initial position. cFF/PLA and cFF/PBS lose 51 % and 30 % of their actuation amplitude, respectively (Table 17). This point has already been observed also for thermally compressed cFF/PP HBC [318], 4D-printed short-wood-fibers/PLA-PHA blend HBC [269] and Wood/PLA-PHA blend with additional layers of PA [216]. Several explanations can be proposed, such as the high internal stresses in the transverse direction that can promote crack propagation [395]. The higher the moisture gradient, the higher the internal hygroscopic stresses [398]. These immersion tests represent a severe environment that can trigger an additional degradation mechanism through the leaching of pectin-based polysaccharides as well as hornification; i.e. the reconfiguration of the cellulose which occurs after the wet/dry cycle and which leads to an irreversible loss of the sensitivity of the fibers to water and therefore of their swelling capacity. [238], [318], [399], [400].

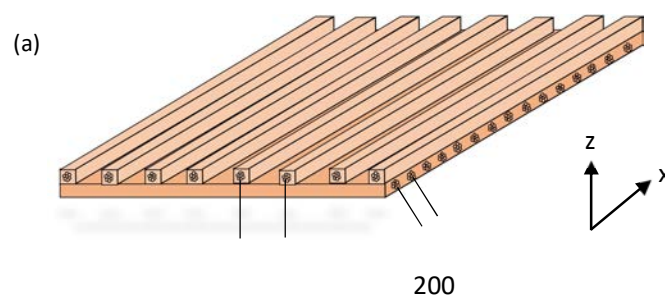
Improvement in actuation reliability has been evidenced by grafting the matrix with a coupling agent [318], using unidirectional fiber tapes with untwisted fiber bundles to promote interfacial load transfer capability [309] and the selection of moisture-resistant fibers such as jute [319].

Finally, the stiffness of the matrix is a key criterion that reinforces the hygromorphic feature of the continuous natural fiber, which is currently technically limited by the fiber fraction. This confirms the superiority of 4D-printed hygromorphic biocomposites with continuous fibers and especially cFF/PBS over current discontinuous fibers-based HBC and wood bilayer hygromorphs for their customized performance. The next section will therefore focus on the potential of cFF/PBS HBC.

3. Control of the stiffness with variation of the architecture by controlling the interfilament distance

Stiffness control of composite laminates can usually be done by adjusting component selection, fiber content, or orientation. Unlike conventional manufacturing processes, additive manufacturing such as FFF offers a new dimension by customizing the mesoscale architecture of materials and their related properties. Section 3 Chapter 5 showed that the distance between the filaments (or the nozzle diameter or hatching space Figure 100) can influence the stiffness of a continuous-flax reinforced biocomposite. Equation 2 and 3, described above, point out that the ratio n (E_p/E_a) is another key parameter to control the responsiveness of bilayer actuators.

Figure 118 shows a schematic diagram of the hygromorphic biocomposite composed of two layers, where each layer has a different interfilament distances ($ID_a = 0.6$ mm and $ID_p = 3$ mm,) and the curvature in the x-axis is targeted thanks to the slender geometry (Length \gg Width). To decrease the ratio n , E_p should be reduced or E_a should be increased. (The "a" and "p" indices stand for active and passive respectively).



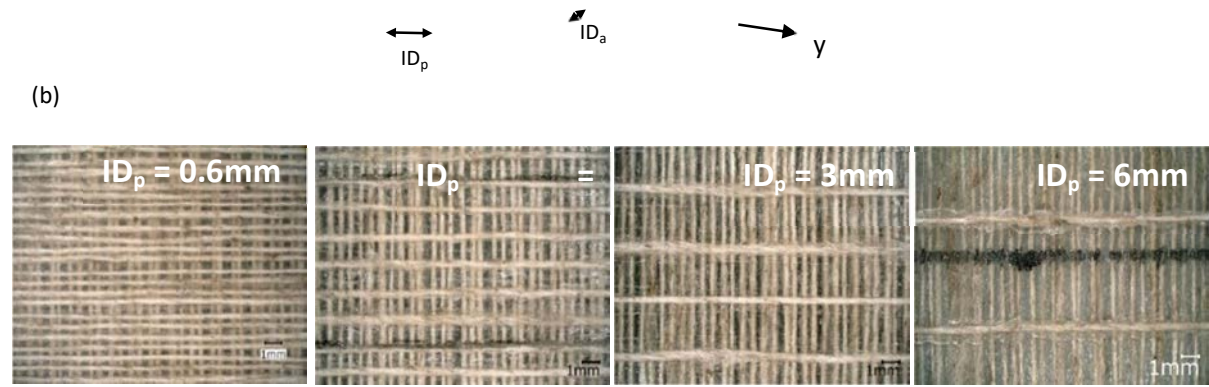


Figure 118 : Schematic drawing of the HBC showing the interfilament parameters ID_p and ID_a for passive and active layer respectively (a), micrograph pictures of the mesoscale architecture of cFF/PBS as a function of the interfilament distance in the passive layer ID_p (b).

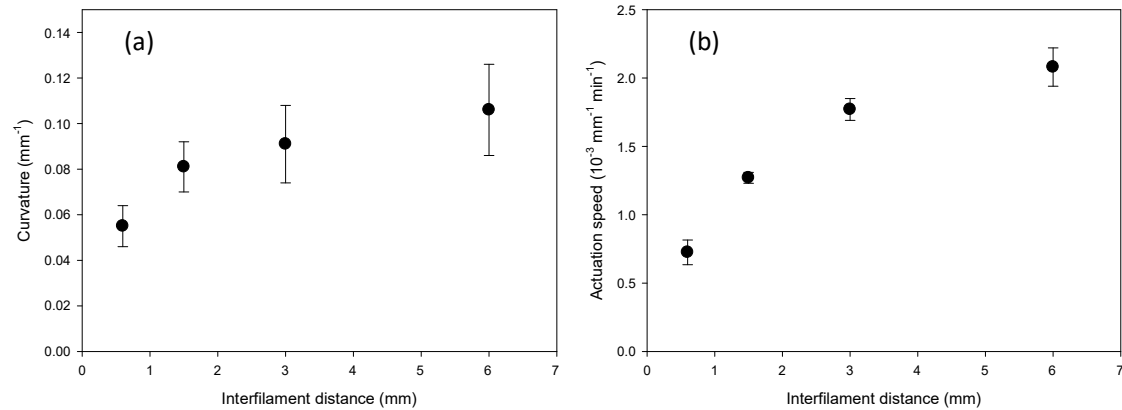
The choice of changing the interfilament distance on the active or passive layer greatly affects the actuation behavior of the HBC, not only the amplitude of curvature but also the direction of actuation.

Indeed, if one considers that the targeted curvature lies along the x-axis and is determined by the transverse expansion of the active layer, a change in the spatial distribution within the passive layer with an increase of ID_p from 0.6 to 6 mm will more than double the responsiveness of the HBC (c). The variation of the Interfilament distance considerably opens up the design envelope for 4D-printed HBC.

This is corroborated by several achievements on different systems. For example, on an actuation system opposite to HBC, *i.e.* with a responsive matrix and a passive fiber, Wang et al. [215] has evidenced a 25 % thermally induced change in curvature on the carbon/PA bilayer when the distance between the filaments varies from 2 to 12 mm. Gladman et al. [207] also observed this phenomenon in their hydrogel/cellulose nanofibrills systems and claimed that the distance between filaments acts as an indicator of thickness and therefore of the flexural rigidity and curvature. Zhao et al. [401] evidenced that the change in stiffness of the passive fiber of their poly N-isopropylacrylamide (PNIPAAm) reinforced with 3D-printed polymeric fiber scaffold affects the bending actuation of the bilayer.

Changing ID_a while keeping ID_p constant leads to the opposite result, because an increasing interfilament distance reduces the hygroexpansion of a hygromorphic composite [207]. In addition, on the basis of a balanced asymmetrical laminate and depending on the slenderness of the sample,

the transverse swelling of the passive layer may overcome the transverse swelling of the active layer and lead to transversal curvature. This point deserves to be further investigated in future work as it opens the way for new multidirectional actuation.



The interfilament distance ID also plays a major role on the reactivity of cFF/PBS HBC with a 300 % increase in the transient mechanism with a ID_p increased from 0.6 to 6 mm (Figure 119.b). The open voids left by the distance between the filaments increase the surface-to-volume ratio of the sample and thus make the material more accessible to moisture interactions. This could be compared to the vascular capacity of the wood tissue, which promotes moisture exchange through a controlled porosity architecture [390]. This strategy has already been successfully used in holed hydrogel bilayers actuators [402] and milled-in grooves on wood bilayer [327] to accelerate the moisture uptake and response.

Interestingly, this means that being able to design HBCs with different reactivity by controlling the architecture can transform a simple HBC actuation into a potential complex sequential actuation for complex structure morphing. The different actuation time scales embedded into the HBC architecture allow for a non-uniform response to a uniform stimulus.

The reliability of these 4D-printed cFF/PBS also depends on the interfilament distance (Figure 120.a).

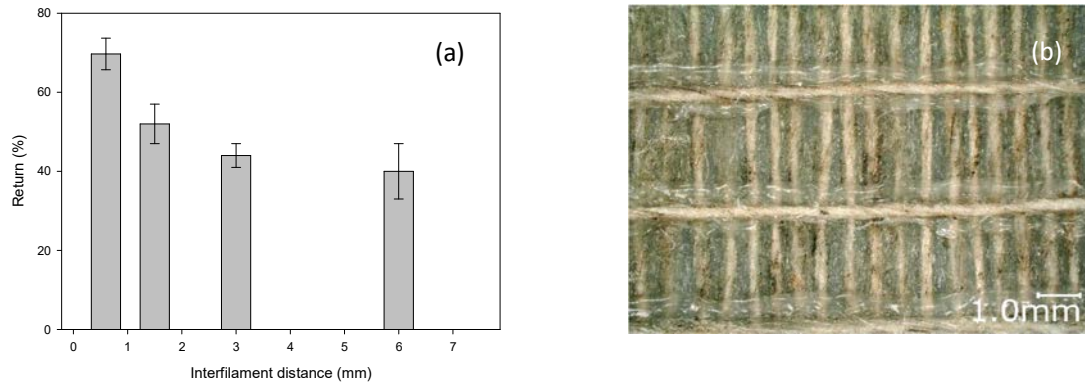


Figure 120 : Evolution of the position of cFF/PBS HBC after one sorption/desorption cycle as a function of interfilament distance, ID_p (a). In-plane observation of cFF/PBS HBC with $ID_p = 3$ mm showing the interfacial and interlaminar regions (b).

Higher ID_p reduces the capacity of HBC to be fully reversible even if a stabilization around 40 % of the mechanism is observed above 3 mm. As already discussed, the degradation induced by immersion in water is severe but the increase in ID_p leads to a greater reduction which should be due to the reduction of the interfacial area (fiber/matrix and interlaminar areas) to transfer the loads. Printing cFF/PBS HBC with orthogonally oriented layers leads to a complex bonding zone. Figure 120.b shows that due to the absence of neighboring filaments in the passive layer, the flowing area of the polymer on the previous layer is larger. This point was discussed in the section 3 of Chapter 5 on unidirectional samples. This may affect local stress state and should be investigated in more depth in the future.

Instead of printing the layers with a constant interfilament distance, it is possible to complexify the spatial distribution of flax yarns to obtain in-plane gradient of stiffness and a non-uniform actuation. Figure 121.a presents the distribution of flax yarns within the passive layer of a cFF/PBS HBC where variation of ID follows a power law.

Figure 121.b shows the results when this power law distribution is applied to the passive layer of the HBC. Since an increase in ID_p implies an increase of the curvature (Figure 121.a), the sample has a curvature gradient along its width, from edge to edge (Figure 121.a). Since HBC evidence high anisotropic properties (Table 17), this strategy can be combined with the geometric effect to underline enhanced and complex bistability. Similar proposals have been made by Ge et al. [189] on SMP composites, which showed a sculpted surface with a complex non-uniform curvature obtained by controlling the in-plane architecture of the laminate. Generally speaking, the concept of gradual in-plane actuation could withstand a reconfigurable surface. Momeni et al. [403] proposed a plant

leaf-mimetic smart wind turbine blades, whose gradual in-plane curvature allows to tailor the aeroelasticity. This wind turbine blade eliminates the need for traditional electromechanical systems and moving parts.

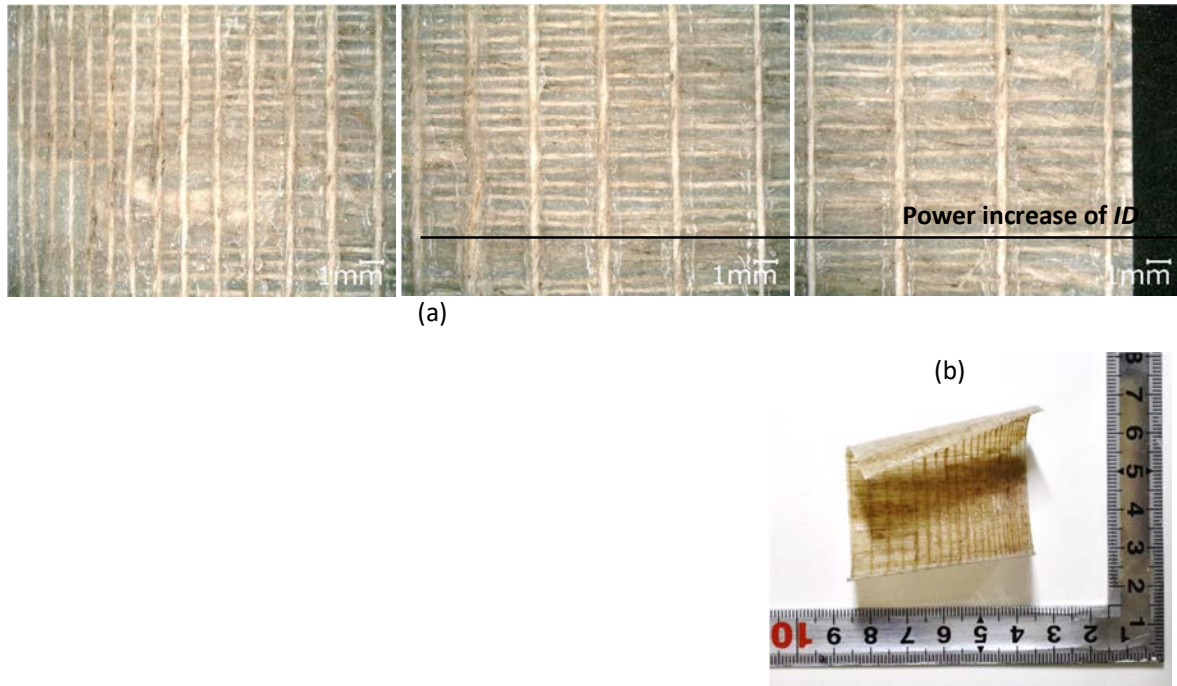


Figure 121 : Gradient distribution (power law) of filament within the passive layer of cFF/PBS HBC (a) and its response to water immersion (b) showing gradual surface response depending on the location.

Parallel to interfilament distance, the local variation in thickness may give rise to similar observation in terms of responsiveness and reactivity. Indeed, as the bending stiffness of laminates is directly linked to the thickness through inertia, the latter controls the amplitude of curvature. This is confirmed by equations 2 and 3 as well as Figure 116.a . As the transient mechanism (moisture sorption or temperature change) also depends on the geometry, the local variation of thickness controls the reactivity. Van Manen et al. [183] proposed a sequential shape shifting where they adjust the delays of each active PLA part by locally controlling the thickness.

4. Compliant mechanism with localized bending actuation

By programming heterogeneities in the spatial distribution of 4D-printed materials, a structure with a predefined and accurate shape could be obtained [197]. Asymmetric lay-up leads to a curvature induced by the differential hygroexpansion between the active and passive layers. The creation of a

localized area can be designed in different ways: a localized bilayer zone where the rigid links are only one layer of material or a balanced trilayer with a gap leaving free curvature.

As HBCs are anisotropic materials, upon actuation, the rigid link composed of a single biocomposite layer will be constrained by the bilayer and an out-of-plane bending will be generated. Thus, the second solution is adopted. Figure 122.a shows a schematic view of the hinge-like compliant mechanism designed and tested here. Parameter a represents the hinge gap, the area where the bilayer can actuate.

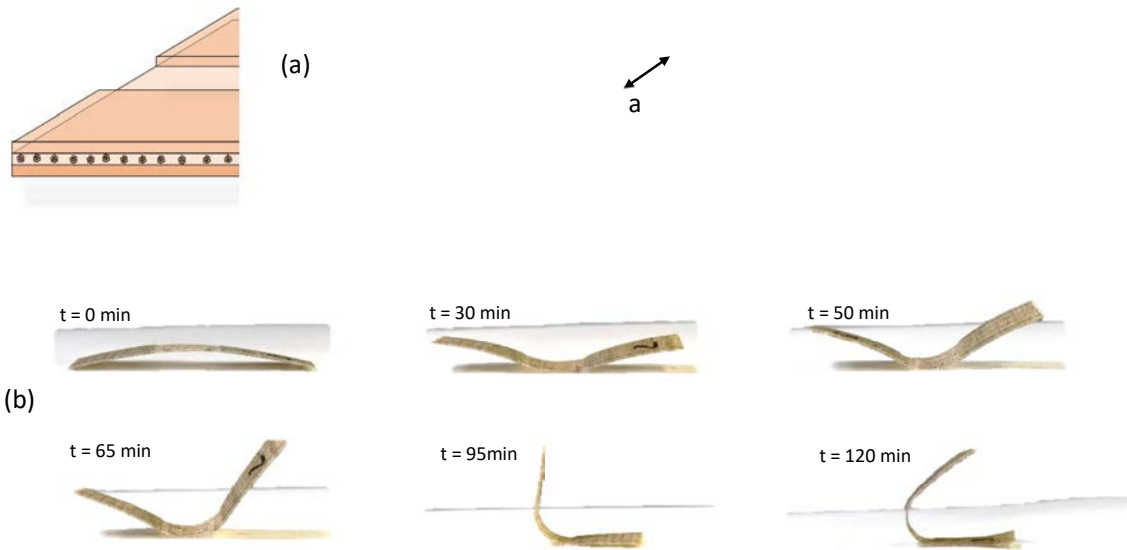


Figure 122 : Schematic view of the compliant hinge-like mechanism made of cFF/PBS. Parameter a represents the hinge gap where the actuation is located (a). Photograph of the cFF/PBS during actuation ($a = 20$ mm and $d_p = 3$ mm).

The orientation of the flax yarn is similar to those previously evaluated, $0/90^\circ$. This area has been considered by Baker et al. [204] as a “valley” or “mountain” fold line for designing complex adaptive origami structures. Figure 122.b shows an example of the result obtained for a 20 mm hinge. Compared to a simple bilayer (Figure 116.b and c), the actuation motion provided by the compliant hinge is clearly localized, enabling better control of the final shape (Figure 121.b). Thus, the actuation curvature becomes an actuation angle. Increasing the length of the hinge from 10 to 30 mm doubles the actuation angle for a sample where ID_p is equal to 0.6 mm (Figure 123.a).

For comparison, the equivalent actuation angle of the entire bilayer sample (70 mm) is shown on the same graph (Figure 123.a). The design of a compliant hinge system lowers the total movement of the bilayer through the constraining effect of the rigid links and the reduction of the bending moment. This has already been observed with SMP smart hinges [191] or hydrogel trilayer hinges [204]. Based on the previous section on the effect of the interfilament distance, the compliant hinges have been optimized.

By increasing ID_p , the interfilament distance in the passive layer of the bilayer implies a drastic increase of the actuation angle by a factor of 2 for a similar hinge length.

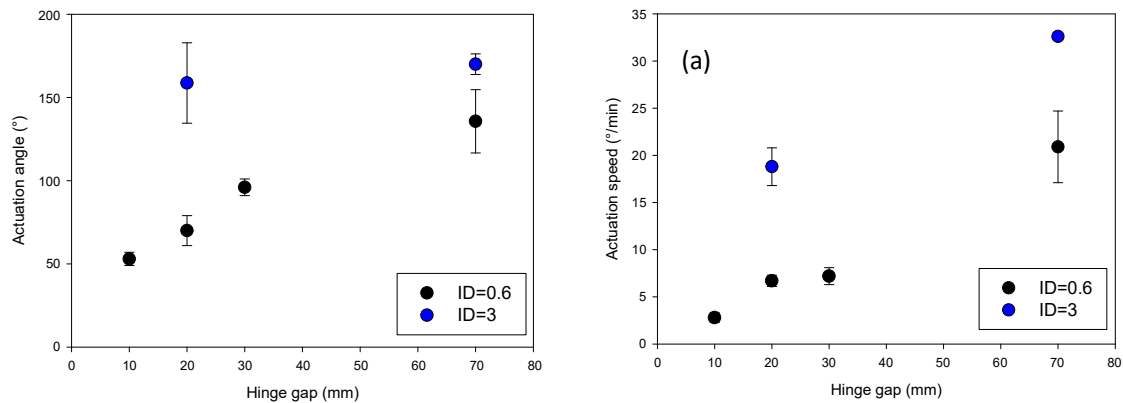


Figure 123 : Evolution of actuation angle (a) and speed (b) with hinge gap for different interfilament spacing of cFF/PBS HBC.

Hence, the combination of hinge gap and interfilament distance allows better control of the architecture of 4D-printed HBC and consequently widen their potential through a sharp actuation. In order to confirm this trend, further investigation should be carried out by increasing the distance between the filaments and the gap in the hinges. After drying, the sample with the hinge gap of 10 to 30 mm and the complete sample (70 mm) exhibit a curvature of 85 to 70 % of their initial position. Once again, the increase of ID_p reduces the reliability with a return capacity of only 30 %.

The actuating speed is changed according to the hinge gap. Increasing the hinge gap from 10 to 30 mm can double the response speed, although it is still drastically lower than for the full 70 mm long sample. A change in the hygroscopic stress state within the sample could be argued.

Similarly, according to the results shown in Figure 119.b, increasing the interfilament distance can speed up the actuation by more than 300 %. The potential of designing compliant hinges with a wide range of temporal response is evidenced, paving the way for multi sequential folding structures.

Conclusion

4D-printing of shape changing material today rarely focuses on continuous fiber composites, even though it offers better elastic properties and anisotropy control. In this way, biocomposites based on continuous flax fiber with biobased and biodegradable matrices (PLA and PBS) were proposed and tested as their properties drastically overcome those of biocomposites with short natural fibers.

The architecture of biocomposites were inspired by that of the pine cone with an asymmetrical lay-up (bilayer), which has given rise to Hygromorphic BioComposites (HBC) that are capable of changing shape according to variations in humidity. The design of HBC can be achieved following Timoschenko's model. Each parameter was discussed in the framework of 4D printing. The ratio m describing the ratio between the passive layer and the active layer shows an optimum leading to the highest curvature. 4D printing enables the control of this ratio within the same number of layers independently controlling the compression ratio between printed layers. The ratio n or the anisotropic ratio (E_p/E_a) also influences the final curvature. Control of the tensile modulus of each layer can also be achieved by 4D printing, either by changing the interfilament distance, the local thickness and the orientation of printing. The last and most influential parameter is the difference in hygroexpansion between layers.

Again, the microstructure induced by printing can influence this parameter, but the material is a limiting factor due to the moderate fiber fraction.

Material selection has been discussed with the characterization of the hygro-elastic properties of the matrix with a rigid cFF/PLA and a ductile cFF/PBS. These two materials overcome the mechanical, hygroscopic and actuating properties of short-natural-fiber based hygromorphic biocomposites, confirming the relevance of the development of continuous natural fiber biocomposites HBC. A great improvement in actuation potential (responsiveness, reactivity and reliability) was observed for PBS-based HBC compared to PLA-based counterparts. Low stiffness reduces the internal stresses that lead to a reduction in the constraining effect of the matrix on the matrix and probably on the hygroexpansion of the fibers. Thus, matrix selection can compensate for the low fiber content encountered in the 4D printing process. This point needs to be further investigated in future work.

Then, the local and gradual architecture of the 4D-printed cFF/PBS was studied following the bending responsiveness and reactivity given by the different interfilament distance. Increasing this parameter improved both the amplitude and speed of actuation by reducing the bending modulus and providing a higher surface-to-volume ratio for moisture sorption. Controlling the actuation kinetics with the same material but with a different architecture opens up the design of HBCs to multi-step shape changing materials. A combination of sample geometry and gradual interfilament distance (in the active or passive layer) provides a complex actuation pattern with surface morphing. Further work on this relationship should be done to maximize the design envelope through mesoscale bilayer architectures with programmable anisotropy.

Finally, the compliant mechanism (hinge) was printed and tested to highlight the microstructural effect, such as the hinge gap and the various interfilament distances, on the spatio-temporal response range. Compliant hinges allowed a more precise displacement from bending to folding. By extrapolation, the hinge can be considered as the folding pattern for origami structures. Shorter hinges result in a smaller actuation angle and a longer actuation time. The combination of meso- (interfilament distance) and macro- (hinge) architecture by 4D printing opens up the accessible range of HBC performance.

General conclusion

3D/4D printing with Fused Filament Fabrication (FFF) is a disruptive technology that enables the manufacture of intricate final parts with reduced processing costs and without the use of additional tooling. However, due to their moderate mechanical properties, 3D printing of continuous fiber composites has started to emerge and is now a growing area of research.

The aim of this thesis work was to better understand 3D and 4D printing of continuous fiber composites by studying the relationship between the printing process, the resulting microstructure, and the mechanical and hygromechanical behaviors. To this end, this work has been carried out on off-the-shelf composites based on continuous synthetic fiber (carbon and glass fiber) and on novel flax fiber composites developed in the laboratory. This work therefore aims to target structural or semi-structural applications as well as morphing and self-deploying structures using 4D printing of continuous fiber composites.

The literature review highlighted the main achievements in 3D/4D printing by Fused Filament Fabrication (FFF) with an emphasis on 3D printing of continuous fiber composites. This technology enables structural performance to be achieved and would appear to be a complementary technology to other continuous fiber additive manufacturing processes such as Automated Fiber Placement (AFP) or Automated Tape Laying (ATL). However, high porosity content, lack of interfacial adhesion between fiber and matrix lead to lower mechanical performance than conventionally manufactured composites. In addition, the environmental durability of these materials was unknown. In this literature study, further emphasis has been spotted on 4D printing, in particular on biomimicry paradigm as well as smart materials (thermally actuated Shape Memory Polymers (SMPs) and moisture actuated hydrogels). The study of the literature shown that actuation with moisture variation led to a higher amplitude (responsiveness) than thermal actuation, but also highlighted the lack of control and the low mechanical performance of 4D printed hydrogels in a wet environment. Finally, 3D/4D printing of natural fiber reinforced composites that offer interesting specific mechanical performances and a moderate environmental impact has been described. Here again, the potential of continuous natural fibers was evidenced for both mechanical and morphing purposes, due to their high water sensitivity and their anisotropy.

A study of the relationship between the 3D printing process, microstructure and mechanical performance was carried out for continuous carbon and glass fiber reinforced composites

manufactured with a commercial 3D printer (MarkTwo® from Markforged®). In addition, to target outdoor and marine engineering applications (one of the IRDL Pillar), a complementary study on the accelerated seawater aging on mechanical performance has been carried out in collaboration with Ifremer. First of all, the analysis of the 3D printed composites revealed several process-related defects, such as a high porosity mainly located between the printed beads and a heterogeneous fiber distribution. The turning back of the filaments on the edge of the part also induced a singular microstructure which causes defects that could affect the transverse properties. Moreover, this study has shown that the fiber content of 3D printed structures is related to the geometry of the structure and therefore the mechanical properties of composite are not intrinsic. The printing process with this commercial 3D printer has other drawbacks such as the lack of control over the fiber trajectory, the absence of modifiable slicing parameters that prevent optimization of the printing process and the lack of material selection.

The mechanical performance survey was divided into three tests: a tensile test on the longitudinal and transverse parts and double cantilever beam tests to evaluate the interlaminar strength of 3D printed composites. Characterization of the tensile tests showed that the longitudinal properties are only slightly affected by the printing process. The addition of continuous fiber allowed a great improvement in mechanical properties compared to short-fiber composites and had similar mechanical properties and lower density compare to aluminum (between 1.1 and 1.4 for 3D printed composite, 2.7 for aluminum). However, the tensile strength remained lower than that of conventionally manufactured composites because of a limited fiber volume fraction and the inherent microstructure (porosity, heterogeneity). However, transverse properties were significantly inferior to the longitudinal ones and very sensitive to print defects and are nowadays a limiting factor in the design of 3D printed structures. The study of the interlaminar fracture of continuous carbon / polyamide 3D printed composites by mean of a double cantilever beam showed that the samples tested have interlaminar properties as high as those of conventionally manufactured polyamide-based composites.

To evaluate the durability of 3D printed composites in relation to moisture sorption, two studies were carried out, i.e. under various moisture environments (9-98 % RH) and also under a 6-months seawater aging at 40 °C. A relatively high sensitivity to water has been observed for 3D printed polyamide composites reinforced with continuous carbon or glass fibers, as well as hygroscopic expansion influenced by the original microstructure. This should be considered in the design of the structure. A reduction in longitudinal and transverse tensile properties as well as in flexural properties was observed in relation to water sorption but, as far as the environmental study is

concerned, full reversibility is observed, whereas seawater aging at 40 °C induced irreversible damage. However, for both types of composites, the mechanical performance remains sufficiently high for structural outdoor and marine engineering applications.

The hygro-sensitivity of polyamide composite based on continuous carbon fibers as well as the electrical conductivity of the carbon fibers have been used to develop new hygromorphic, multi-responsive and smart 4D printed composites. These actuators had a bilayer microstructure inspired by the pine cone scale, consisting of one layer of continuous carbon fiber coated with Polyhexamethylene isophthalamide (PA6-I) transversally printed and one layer of pure polyamide 6. Under the effect of environmental variations, the hygroscopic strain gradient between these layers led to a passive hygromorphic actuation. Thanks to the electrical conductivity of the carbon fibers, electro-heating was induced towards the actuator in order to control the moisture content and speed-up water desorption, overcoming the current limitations of hygromorphs, i.e. the lack of control of the actuation (which depends on the environmental conditions) and the slow response due to the slow sorption of water. In this work, the electro-thermo-hygromorphic actuation pathway accelerated the desorption of water from the sample stored at 98 % RH at 23 °C by a factor 10 with full reversibility and with a water content and amplitude of curvature that depend on the electrical input power. This actuation pathway was applied to various patterns (longitudinal and transverse) with different aspect ratios, leading to a combination of temperature, hygroscopic expansion and stiffness distribution. The responsiveness of the sample was strongly altered by the printed pattern; longitudinal samples show low responsiveness (due to the high stiffness of the carbon) while transverse samples exhibit high responsiveness. Hence, a wide scatter of designs is possible thanks to the control of the electrical input power, the initial water content and also the fibers orientation brought by the printing process.

In order to improve the response of the actuation and also because of the interest regarding their low environmental impact and the management of their end-of-life, the development of a new flax fiber composite elaborated by 3D printing has been investigated. A study on the influence of several slicing parameters (layer height, interfilament distance, trip number, number of layer and raster angle) on the microstructure, geometry and mechanical performance of the parts was carried out in order to be able to tune the stiffness of the composite for structural and actuation applications. First of all, the height of the layer made it possible to control the compaction of the filaments in relation to the printing and its reduction made it possible to reduce the thickness of the layer, the porosity content and, finally, to enhance the stiffness of the composite. Moreover, increasing the number of layers improved the compaction ratio and enhanced the stiffness of the composite. The Interfilament

distance induced several microstructural defects (fibers overlap, porosities) which negatively affected the tensile stiffness when it was too low, while too high a distance between the filaments resulted in a lower cohesion and tensile strength. The Trip number considerably affected the accuracy of the sample geometry with a considerably higher average filament size for a low number of turns compared to a high number of trips and a sample thickness that depends on the number of trips. Finally, such as 3D printed composites based on synthetic fibers, 3D printed biocomposites exhibited a high anisotropy between longitudinal and transverse properties, the transverse properties being strongly affected by manufacturing (process) defects. Hence, it appeared that accurate control of slicing parameters allowed a large scale of composite stiffness to be achieved (from 1 GPa to 18 GPa) and had a great potential for controlling the microstructure for several applications such as acoustic or actuation applications.

Finally, 3D-printed flax fiber composites were used to develop hygromorphic biocomposites produced by 4D printing. The hygromorphic biocomposite actuators were designed as bilayer and used biobased and biodegradable matrices (polylactic acid and polybutylene succinate). The purpose of this chapter was to assess the influence of material selection and sample architecture on the response to actuation. A higher actuation potential (higher responsiveness, reactivity and reliability) was observed for flax fibers reinforced composite based on polybutylene succinate. Thus, this material was selected to evaluate the influence of architecture on bending responsiveness and reactivity. A first study focused on the interfilament distance, and, increasing this parameter improves the speed and amplitude of actuation thanks to a lower bending modulus. Finally, hinge-like structures were printed and tested to assess the influence of hinge gap and interfilament distance on actuation. The hinge-like design allows precise control of the bending response. Shorter hinges result in a smaller actuation angle and longer actuation time. Finally, the combination of meso-(interfilament distance) and macro-(hinge) architecture allows control of actuation speed and responsiveness and opens up many possibilities in terms of design capability.

Perspectives

In the following part, perspectives and ongoing works on 3D printing of continuous fiber based composites are divided into 4 categories: work on filament production, on material functionality for 3D and 4D printing and regarding 3D printing process.

Filament production

With regard to the manufacture of continuous flax fiber filaments, the flax fibers are heterogeneously distributed, whereas perfect impregnation of the yarn was not reached and the fiber content is currently limited.

As observed in chapter 5, there is a discrepancy between the layer height (distance between printed nozzle and build plate during 3D printing) and the layer thickness (real thickness of printed layer), especially for low layer height (below 0.3 mm) due to the yarn architecture.

Thus, the filament manufacturing process needs to be improved and deeper investigated.

There are several possibilities for the initial modification of the flax yarn to improve the performance of the composite. For example, the use of flax/polymer commingled yarn or flax slits instead of flax yarns must be studied. This should reduce the difficulty of polymer migration within the flax yarn, improve the distribution of fiber in the filament and potentially increase their compressibility and their content.

Then, the production rate and filament reproducibility should be also deeper investigated. Working with a larger extrusion die would make possible to obtain a thicker flax yarn, less sensitive to process variations and with a higher tensile breaking load, thus accelerating the speed of the extrusion line. However, this process change would result in a decrease in fiber content and printing accuracy. Besides the co-extrusion process, other manufacturing processes such as pultrusion could be proposed but economical issue must be raised.

Last point would be to convince flax yarn producers about the technical potential of 3D and 4D printing but also about the future market with end-users. Investments should be done in R&D to produce industrial high quality filaments in large quantities.

Similar work must be done with synthetic materials as their availability is sorely lacking.

Material functionality for 3D printing of synthetic and natural fiber composites

For outdoor and marine engineering applications, the use of a less moisture-sensitive matrix would result in less water uptake, less hygro-sensitive swelling and, consequently, better durability of the composite. To broaden the scope of applications, a wider range of coating matrices should be developed. For example, high temperature matrix (PEEK, PEKK, PEI...), tough matrix with large deformability (Thermoplastic Elastomer) and bio based matrix (outside PLA) are rarely investigated despite their large potential to enhance the design range of 3D printed composites.

Deeper insights should be performed to understand multiple interfaces (fiber/matrix, bead/bead, layer/layer), their formation and performance with printing parameters. The reduction of defects such as porosity, overlapping, gap and fiber waviness must be addressed to democratize the use of 3D printed continuous fiber composites. Thus, their formation during printing have to be well-understood taking into account the multi-scale adhesion mechanism (wetting, interdiffusion) associated with the thermal and hygroscopic phenomenon and the slicing/printing parameters. The post-consolidation step should also be evaluated.

In-life performance, such as fatigue and creep properties, are still unknown in the literature and need to be realized in various thermal and moist environments to better understand and estimate the life time span of 3D printed composites.

Because biocomposites are known to be sensitive to moisture variations, deeper investigations are required on the hygromechanical properties of 3D printed biocomposites, focusing on the influence of slicing parameters, and the resulting microstructure, on moisture diffusion in the composite and the resulting hygromechanical properties. Similarly, a study of seawater aging shall be carried out on 3D printed biocomposites to target marine engineering applications for these materials.

Moreover, 3D printing can be used to develop very complex cellular structures as well as complete sandwich structures. The latter are composed of two skins and a cellular core and makes it possible to achieve high stiffness with a low density of parts. Thus, deeper researches should be performed on the feasibility, mechanical performances and durability of these structures. The combination of topological/parametric optimization and continuous fiber composite printing should open the door to a new generation of high-performance recyclable structures. In the same direction, metamaterials are periodic cellular structures whose properties are not found in nature due to their original

architecture. Because 3D printing allows to precisely tune the architecture of the parts, this technology is today the best solution for manufacturing metamaterials with intricate architecture. There are significant examples of metamaterials such as auxetic structures with a negative Poisson's ratio (i.e. materials which expand transversally when longitudinally stretched), structures with a shear modulus close to zero or structures with negative refractive index. Hence, 3D printing of metamaterials could bring new original functionality to 3D printed structures and widen the scope of application. For example, auxetic structures display enhanced mechanical properties and a high ability to mitigate vibrations, which is very interesting for acoustic applications such as aircraft nacelles.

Finally, 3D printing of composite materials allows to manufacture structures whose properties are controlled locally according to the nature of the material or the trajectory of the fibers. Thus, it is possible to introduce a gradient of properties within the structure (in a same layer or in the thickness) thanks to a hierarchical architecture as a function of solicitations undergone by the printed structure.

Material scale for 4D printing

Natural fibers-based filaments could be enhanced with synthetic fibers to create hybrid fiber formulations. The addition of continuous carbon fibers in the flax yarn or the addition of short carbon fibers in the polymer matrix is an interesting way to bring multi-functional actuation and trigger electro-thermo-hygromorphic actuation and thus to speed up and control the curvature response of 4D printed hygromorphic biocomposites and should be investigated to develop multi-stimulable hygromorphic biocomposites elaborated by 4D printing. Other additional stimulation, such as temperature or light, can be used to control water desorption in 4D printed hygromorphic actuators. Thus, further studies should be performed on the influences of the formulation of 4D printed multi-stimulable biocomposite on the responsiveness and speed of actuation for various stimuli.

In addition, there is a need for more knowledge on the quality of the interface between the flax yarn and the coated matrix and to improve the mechanical properties of the composites as well as the durability of the 4D printed actuators. Finally, further research should be carried out on the manufacture of continuous flax fibers coated with a smooth polymer or a highly water-sensitive polymer matrix, such as a hydrogel, in order to enhance and accelerate the actuation response of 4D printed hygromorphic biocomposites.

If the reversibility of synthetic fiber-based actuators has been demonstrated in Chapter 4, further research should be done on the durability of the actuators after several sorption/desorption cycles and the resulting damage induced by electro-thermo-hygro actuation and differential swelling on the microstructure of the actuators. Similar work shall be performed on 4D printed hygromorphic biocomposites to better understand the actuation pathway and the role of the microstructure and fiber/matrix interface on actuator durability.

As observed in Chapters 4 and 6, actuator design has a major influence on the actuation response of 4D printed actuators. Consequently, a wide range of studies is possible in order to enhance the amplitude and speed of actuation and to generate an original swelling behavior. Hence, future studies on 4D printing of actuators based on synthetic and natural fibers will need to investigate in more detail the influence of printed bio-inspired architectures on final shape, actuation speed and responsiveness.

In Chapter 4, the length/width ratio of the 4D printed actuator does not significantly influence the actuator response, but it may be used to induce synclastic bioinspired curvature of the 4D Printed actuators. In the 4D printed hygromorphic biocomposites elaborated in this study, depending on the slenderness of the sample, the passive layer may undergo greater transverse swelling than the active one and have opposite curvature. These capabilities should be further investigated in order to develop new multidirectional actuators. For example, in the literature, bio-mimetic robots have been developed with a non-symmetrically laminated carbon fiber prepreg to mimic the *Venus Flytrap*. Thanks to 4D printing, bi-stable composites with tuned asymmetrical architecture could be developed to trigger a very fast actuation.

Another parameter such as the interfilament distance reduced the flexural stiffness and increased the surface area in contact with the water, thus accelerating the actuation. Moreover, since it is possible to monitor the porosity content with slicing parameters such as layer height, a parametric study could be done to enhance water sorption kinetics in 4D printed hygromorphic composites with a biomimetic microstructure made of porosity networks in order to fully control the actuation cycle. The orientation of the fibers allows to control the distribution of stiffness of the composite and to orient amplitude the curvature. For example, a 0/90° stacking of layers results in a bending response while a 45/-45° stacking results in a twisting response. Consequently, 4D printing shall be used to precisely control the fiber orientation through the raster angle to create programmable bio-inspired structures. As evidenced in Chapters 5 and 6, the slicing parameters play a major role on the stiffness of the composite as well as on the composite layer, so both m and n (equation 2 and 3), the ratios

depend on the slicing parameters. Consequently, further work shall be carried out to better understand the relationship between m and n ratios in 4D printed hygromorphic biocomposites and its effect on biocomposites actuation. Moreover, in a same composite, the control of slicing parameter and architecture in 4D printing allows to introduce a gradient of properties (stiffness, coefficient of thermal and hygroscopic expansions, thickness, etc...) and shall be considered in further studies to develop actuators with multi-directional shape orientation.

Finally, another improvement of this preliminary works is the use of hygromorphic materials developed to create complex structures with a high response such as shape-changing metamaterials, i.e. structures whose properties are not found in nature due to their architecture and composition, thanks to 4D printing.

Manufacturing and printing processes

As regards the 3D printing process for continuous synthetic fiber reinforced composites, further studies should be carried out on open 3D printers and open slicers in order to precisely control the trajectory of the fibers and to optimize these properties of the composite, in particular with regard to the transverse properties which are today the weak point of 3D printing of continuous fibers based composites. Precise fiber trajectory could also be achieved thanks to a nozzle head with thinner aperture which might reduce filament waviness during printing. Deeper investigations on the influence of printing and slicing parameters on the microstructure and mechanical performances of composites should also be performed.

As stated in the literature, internal stresses develop in the printed parts during 3D printing and cooling of the parts due to high temperature gradient inside the part, which may cause warping or delamination. Further work is needed to evaluate the internal stress state of 3D printed composites as a function of printing and slicing parameters and its influence on composite performance and damage. Thus, several solutions should be investigated to reduce these internal stresses thanks to post curing. The use of a heated chamber would allow better control of the temperature field.

The future of the 3D printing process with continuous fiber composites involves several issues. The first is the combination of Automated Fiber Placement with 3D printing, as pioneered by Fibertech in China and Arevo[®], to develop 3D printing using a robotic arm with multiple degree of freedom to print structures with unlimited design capability. The second way to improve 3D printing of continuous fiber composites is large scale parts printing to bridge the gap with Automated Fiber

Placement and make possible one-way printing of large parts without restrictions on part design. Finally, in order to fine-tune the properties of the structure and print in one-way full structure or to develop hybrid composites, it is necessary to study working with several printing nozzles mounted on a printing head.

Another promising way of study for 3D printing of composites is to combine predictive mechanical models with slicers software that could fully automate the composite manufacturing process. This concept aims to model the solicitations experienced by the desired printed structures and, in response, to adjust globally and locally the printing and slicing parameters (fiber orientation, layer thickness, etc...) to suit the mechanical requirements of the desired structure.

References

- [1] S. M. F. Kabir, K. Mathur, and A. M. Seyam, "A critical review on 3D printed continuous fiber-reinforced composites: history, mechanism, materials and properties," *Compos. Struct.*, 2019.
- [2] J. R. C. Dizon, A. H. Espera, Q. Chen, and R. C. Advincula, "Mechanical characterization of 3D-printed polymers," *Addit. Manuf.*, vol. 20, pp. 44–67, 2018.
- [3] O. A. Mohamed, S. H. Masood, and J. L. Bhowmik, "Optimization of fused deposition modeling process parameters: a review of current research and future prospects," *Adv. Manuf.*, vol. 3, no. 1, pp. 42–53, 2015.
- [4] J. Le Boterff, "Thesis report in french: Compréhension des phénomènes physico-chimiques impliqués dans la réalisation de pièces polyoléfinés par fabrication additive," 2019.
- [5] G. D. Goh, Y. L. Yap, S. Agarwala, and W. Y. Yeong, "Recent Progress in Additive Manufacturing of Fiber Reinforced Polymer Composite," *Adv. Mater. Technol.*, vol. 1800271, pp. 1–22, 2018.
- [6] S. Crump, "Apparatus and method for creating three-dimensional objects Available at: <https://patents.google.com/patent/US5121329A/en>," 1992.
- [7] Z. Liu, Y. Wang, B. Wu, C. Cui, Y. Guo, and C. Yan, "A critical review of fused deposition modeling 3D printing technology in manufacturing polylactic acid parts," *Int. J. Adv. Manuf. Technol.*, 2019.
- [8] X. Wang, M. Jiang, Z. Zhou, J. Gou, and D. Hui, "3D printing of polymer matrix composites: A review and prospective," *Compos. Part B Eng.*, vol. 110, pp. 442–458, 2017.
- [9] L. Li, Q. Sun, C. Bellehumeur, and P. Gu, "Composite Modeling and Analysis for Fabrication of FDM Prototypes with Locally Controlled Properties," *J. Manuf. Process.*, vol. 4, pp. 129–141, 2002.
- [10] Q. Sun, G. M. Rizvi, C. T. Bellehumeur, and P. Gu, "Effect of processing conditions on the bonding quality of FDM polymer filaments," *Rapid Prototyp. J.*, vol. 14, no. 2, pp. 72–80, 2008.
- [11] S. Ahn, M. Montero, D. Odell, S. Roundy, and P. K. Wright, "Anisotropic material properties of fused deposition modeling ABS," *Rapid Prototyp. J.*, vol. 8, no. 4, pp. 248–257, 2002.
- [12] S. H. Masood, K. Mau, and W. Q. Song, "Tensile Properties of Processed FDM Polycarbonate Material," *Mater. Sci. Forum*, vol. 656, pp. 2556–2559, 2010.
- [13] G. D. Goh *et al.*, "Process – Structure – Properties in Polymer Additive Manufacturing via Material Extrusion : A Review Process – Structure – Properties in Polymer Additive Manufacturing via Material," *Crit. Rev. Solid State Mater. Sci.*, vol. 0, no. 0, pp. 1–21, 2019.
- [14] B. Brenken, E. Barocio, A. Favaloro, R. B. Pipes, and V. Kunc, "Fused filament fabrication of fiber-reinforced polymers : A review," *Addit. Manuf.*, vol. 21, no. October 2017, pp. 1–16, 2018.
- [15] R. P. Wool, B. L. Yuan, and O. J. McGarel, "Welding of Polymer Interfaces," *Polym. Eng. Sci.*, vol. 29, no. 19, pp. 1340–1367, 1989.
- [16] C. Bellehumeur, L. Li, Q. Sun, and P. Gu, "Modeling of Bond Formation Between Polymer Filaments in the Fused Deposition Modeling Process," *J. Manuf. Process.*, vol. 6, pp. 170–178, 2004.
- [17] D. Popescu, A. Zapciu, C. Amza, F. Baci, and R. Marinescu, "FDM process parameters in fl uence over the mechanical properties of polymer specimens : A review," *Polym. Test.*, vol. 69, no. May, pp. 157–166, 2018.
- [18] P. K. Gurralla and S. P. Regalla, "Part strength evolution with bonding between filaments in fused deposition modelling," *Virtual Phys. Prototyp.*, vol. 9, pp. 141–149, 2014.
- [19] L. G. Blok, M. L. Longana, H. Yu, and B. K. S. Woods, "An investigation into 3D printing of fi bre reinforced thermoplastic composites," *Addit. Manuf.*, vol. 22, no. May, pp. 176–186, 2018.
- [20] X. Zhao *et al.*, "Poplar as biofiber reinforcement in composites for large-scale 3D printing," *ACS Appl. Bio Mater.*, 2019.
- [21] A. Lanzotti, M. Grasso, G. Staiano, and M. Martorelli, "The impact of process parameters on mechanical properties of parts fabricated in PLA with an open-source 3-D printer," *Rapid Prototyp. J.*, vol. 21/5, pp. 604–617, 2015.
- [22] S. F. Costa, F. M. Duarte, and J. A. Covas, "Thermal conditions affecting heat transfer in FDM / FFE : a contribution towards the numerical modelling of the process," *Virtual Phys. Prototyp.*, pp. 35–46, 2014.
- [23] N. Aliheidari, R. Tripuraneni, A. Ameli, and S. Nadimpalli, "Fracture resistance measurement of fused deposition modeling 3D printed polymers," *Polym. Test.*, vol. 60, no. March, pp. 94–101, 2017.
- [24] X. Deng, Z. Zeng, B. Peng, S. Yan, and W. Ke, "Mechanical Properties Optimization of Poly-Ether-Ether-Ketone via Fused," *Materials (Basel)*, 2018.
- [25] A. Kantaros and D. Karalekas, "Fiber Bragg grating based investigation of residual strains in ABS parts

- fabricated by fused deposition modeling process," *Mater. Des.*, vol. 50, pp. 44–50, 2013.
- [26] M. A. Yardimci and S. Güçeri, "Conceptual framework for the thermal process modelling of fused deposition," *Rapid Prototyp. J.*, vol. 2, no. 2, pp. 26–31, 1996.
- [27] A. Bellini and S. Güçeri, "Mechanical characterization of parts fabricated using fused deposition modeling," *Rapid Prototyp. J.*, vol. 9, no. 4, pp. 252–264, 2003.
- [28] J. F. Rodriguez, J. P. Thomas, and J. E. Renaud, "Design of Fused-Deposition ABS Components for Stiffness," *J. Mech. Des.*, vol. 125, pp. 545–551, 2003.
- [29] S. F. Costa, F. M. Duarte, and J. A. Covas, "Estimation of filament temperature and adhesion development in fused deposition techniques," *J. Mater. Process. Tech.*, vol. 245, pp. 167–179, 2017.
- [30] K. G. Jaya Christiyar, U. Chandrasekhar, and K. Vankateswarlu, "A study on the influence of process parameters on the Mechanical Properties of 3D printed ABS composite," *IOP Conf. Ser. Mater. Sci. Eng.*, vol. 114, 2016.
- [31] F. Ning, W. Cong, Y. Hu, and H. Wang, "Additive manufacturing of carbon fiber-reinforced plastic composites using fused deposition modeling: Effects of process parameters on tensile properties," *J. Compos. Mater.*, vol. 51, no. 4, pp. 451–462, 2017.
- [32] A. W. Fatimatuzahraa, B. Farahaina, and W. A. Y. Yusoff, "The effect of employing different raster orientations on the mechanical properties and microstructure of Fused Deposition Modeling parts," in *IEEE Symposium on Business, Engineerin and Industrial Applications*, 2011, pp. 22–27.
- [33] T. Letcher, B. Rankouhi, and S. Javadpour, "Experimental Study of Mechanical Properties of Additively Manufactured ABS Plastic as a Function of Layer Parameters," in *International Mechanical Engineering Congress and Exposition*, 2015, no. December.
- [34] B. M. Tymrak, M. Kreiger, and J. M. Pearce, "Mechanical properties of components fabricated with open-source 3-D printers under realistic environmental conditions," *Mater. Des.*, vol. 58, pp. 242–246, 2014.
- [35] O. S. Es-Said, J. Foyos, R. Noorani, M. Mendelson, and R. Marloth, "Effect of Layer Orientation on Mechanical Properties of Rapid Prototyped Samples," *Mater. Manuf. Process.*, vol. 15, no. 1, pp. 107–122, 2000.
- [36] J. F. Rodriguez, J. P. Thomas, and J. E. Renaud, "Mechanical behavior of acrylonitrile butadiene styrene (ABS) fused deposition materials. Experimental investigation," *Rapid Prototyp. J.*, vol. 7, no. 3, pp. 148–158, 2001.
- [37] G. C. Onwubolu and F. Rayegani, "Characterization and Optimization of Mechanical Properties of ABS Parts Manufactured by the Fused Deposition Modelling Process," *Int. J. Manuf. Eng.*, vol. 2014, 2014.
- [38] A. P. Gordon, J. Torres, M. Cole, A. Owji, and Z. Demastry, "An approach for mechanical property optimization of fused deposition modeling with polylactic acid via design of experiments," *Rapid Prototyp. J.*, vol. 2, no. January 2015, 2016.
- [39] M. A. Caminero, J. M. Chacon, E. Garcia-Plaza, P. J. Nuñez, J. M. Reverte, and J.-P. Becar, "Additive Manufacturing of PLA-Based Composites Using Fused Filament Fabrication : Effect of Graphene Nanoplatelet Reinforcement on Mechanical Properties , Dimensional Accuracy and Texture," *Polymers (Basel)*, vol. 11, no. 799, 2019.
- [40] A. K. Sood, R. K. Ohdar, and S. S. Mahapatra, "Parametric appraisal of mechanical property of fused deposition modelling processed parts," *Mater. Des.*, vol. 31, no. 1, pp. 287–295, 2010.
- [41] Y. Zhang and K. Chou, "A parametric study of part distortions in fused deposition modelling using three-dimensional finite element analysis," *Proc. Inst. Mech. Eng. Part B J. Eng. Manuf.*, vol. 222, pp. 959–967, 2008.
- [42] M. Fernandez-Vicente, W. Calle, S. Ferrandiz, and A. Conejero, "Effect of Infill Parameters on Tensile Mechanical Behavior in Desktop 3D Printing," *3D Print. Addit. Manuf.*, vol. 3, no. 3, pp. 183–192, 2016.
- [43] S. Charlon and J. Soulestin, "Thermal and geometry impacts on the structure and mechanical properties of part produced by polymer additive manufacturing," *J. Appl. Polym. Sci.*, no. January, pp. 1–23, 2020.
- [44] W. Zhong, F. Li, Z. Zhang, L. Song, and Z. Li, "Short fiber reinforced composites for fused deposition modeling," *Mater. Sci. Eng. A301*, vol. 301, pp. 125–130, 2001.
- [45] M. L. Shofner, K. Lozano, F. J. Rodríguez-Macias, and E. V. Barrera, "Nanofiber-reinforced polymers prepared by fused deposition modeling," *J. Appl. Polym. Sci.*, vol. 89, no. 11, pp. 3081–3090, 2003.
- [46] M. L. Shofner, F. J. Rodríguez-Macias, R. Vaidyanathan, and E. V. Barrera, "Single wall nanotube and vapor grown carbon fiber reinforced polymers processed by extrusion freeform fabrication," *Compos. Part A Appl. Sci. Manuf.*, vol. 34, pp. 1207–1217, 2003.
- [47] X. Wei, D. Li, W. Jiang, Z. Gu, X. Wang, and Z. Zhang, "3D Printable Graphene Composite," *Sci. Rep.*, pp. 1–7, 2015.

- [48] A. Plymill, R. Minneci, D. A. Greeley, and J. Gritton, "Graphene and Carbon Nanotube PLA Composite Feedstock Development for Fused Deposition Modeling Graphene and Carbon Nanotube PLA Composite Feedstock," 2016.
- [49] F. Ning, W. Cong, J. Qiu, J. Wei, and S. Wang, "Additive manufacturing of carbon fiber reinforced thermoplastic composites using fused deposition modeling," *Compos. Part B Eng.*, vol. 80, pp. 369–378, 2015.
- [50] H. L. Tekinalp *et al.*, "Highly oriented carbon fiber-polymer composites via additive manufacturing," *Compos. Sci. Technol.*, vol. 105, pp. 144–150, 2014.
- [51] L. J. Love *et al.*, "The importance of carbon fiber to polymer additive manufacturing," *J. Mater. Res.*, vol. 29, no. 17, pp. 1893–1898, 2014.
- [52] D. Jiang and D. E. Smith, "Anisotropic mechanical properties of oriented carbon fiber filled polymer composites produced with fused filament fabrication," *Addit. Manuf.*, vol. 18, pp. 84–94, 2017.
- [53] O. S. Carneiro, A. F. Silva, and R. Gomes, "Fused deposition modeling with polypropylene," *Mater. Des.*, vol. 83, pp. 768–776, 2015.
- [54] B. P. Heller, D. E. Smith, and D. A. Jack, "Effects of extrudate swell and nozzle geometry on fiber orientation in Fused Filament Fabrication nozzle flow," *Addit. Manuf.*, vol. 12, pp. 252–264, 2016.
- [55] A. A. Hassen *et al.*, "The durability of large-scale additive manufacturing composite molds," in *CAMX Conference Proceedings. Anahim, CA, 2016*, 2016, no. April 2018.
- [56] C. E. Duty *et al.*, "Structure and Mechanical Behavior of Big Area Additive Manufacturing (BAAM) Materials," *Rapid Prototyp. J.*, vol. 23, no. 1, p. , 2017.
- [57] University of Maine, "UMaine Composites Center receives three Guinness World Records related to largest 3D printer. URL: www.umaine.edu. Consulted on April 2020th," 2020. .
- [58] R. S. Bay and C. L. Tucker, "Stereological measurement and error estimates for three-dimensional fiber orientation," vol. 32, no. 4, 1992.
- [59] T. Mulholland and N. Rudolph, "Process-Induced Fiber Orientation in Fused Filament Fabrication," *J. Compos. Sci.*, vol. 2, no. 45, pp. 1–14, 2018.
- [60] A. Garcia, "Nozzle geometry effects on exit orientation of short fiber composites," 2017.
- [61] R. T. L. Ferreira and I. A. Ashcroft, "Optimal orientation of fibre composites for strength based on Hashin ' s criteria optimality conditions," *Struct. Multidiscip. Optim.*, no. 2009, 2020.
- [62] S. Fu and B. Lauke, "Effects of fiber length and fiber orientation distributions on the tensile strength of short-fiber reinforced polymers," *Compos. Sci. Technol.*, vol. 56, no. 2, pp. 1179–1190, 1996.
- [63] S. Mortazavian and A. Fatemi, "Effects of fiber orientation and anisotropy on tensile strength and elastic modulus of short fiber reinforced polymer composites," *Compos. Part B*, vol. 72, pp. 116–129, 2015.
- [64] S.-Y. Fu, B. Lauke, E. Mäder, C.-Y. Yue, and X. Hu, "Tensile properties of short-glass-fiber- and short-carbon-fiber-reinforced polypropylene composites," *Compos. Part A Appl. Sci. Manuf.*, vol. 31, pp. 1117–1125, 2000.
- [65] S.-Y. Fu, X. Hu, and C.-Y. Yue, "Effect of fiber length and orientation distributions on the mechanical properties of short-fiber-reinforced polymers: A Review," *Mater. Sci. Res. Int.*, vol. 5, no. 2, 1999.
- [66] G. Liao *et al.*, "Properties of oriented carbon fiber / polyamide 12 composite parts fabricated by fused deposition modeling," *Mater. Des.*, vol. 139, pp. 283–292, 2018.
- [67] C. Mahajan and D. Cormier, "3D Printing of Carbon Fiber Composites With Preferentially Aligned Fibers," *Proc. 2015 Ind. Syst. Eng. Res. Conf.*, 2015.
- [68] M. Somireddy, C. V Singh, and A. Czekanski, "Mechanical behaviour of 3D printed composite parts with short carbon fiber reinforcements," *Eng. Fail. Anal.*, vol. 107, no. June 2019, p. 104232, 2020.
- [69] M. Spoerk, C. Savandaiah, F. Arbeiter, G. Traxler, C. Holzer, and J. Sapkota, "Anisotropic properties of oriented short carbon fibre filled polypropylene parts fabricated by extrusion-based additive manufacturing," *Compos. Part A*, 2018.
- [70] J. Yu *et al.*, "Printing direction dependence of mechanical behavior of additively manufactured 3D preforms and composites," *Compos. Struct.*, vol. 184, no. November, pp. 917–923, 2018.
- [71] M. F. Afrose, S. H. Masood, M. Nikzad, and P. Iovenitti, "Effects of Build Orientations on Tensile Properties of PLA Material Processed by FDM," *Adv. Mater. Res.*, vol. 1045, pp. 31–34, 2014.
- [72] N. G. Karsli and A. Aytac, "Tensile and thermomechanical properties of short carbon fiber reinforced polyamide 6 composites," *Compos. Part B*, vol. 51, pp. 270–275, 2013.
- [73] D. Lee, "On Studies of Tensile Properties in Injection Molded Short Carbon Fiber Reinforced PEEK Composite," *KSME J.*, vol. 10, no. 3, pp. 362–371, 1996.
- [74] Z. A. M. Ishak and J. P. Berry, "Hygrothermal Aging Studies of Short Carbon Fiber reinforced nylon 6.6,"

- J. Appl. Polym. Sci.*, vol. 51, pp. 2145–2155, 1994.
- [75] M. Knight and H. T. Hahn, "Strength and elastic modulus of a randomly-distributed short fiber composite," *J. Compos. Mater.*, vol. 9, 1975.
- [76] J. Denault and B. Foster, "Tensile Properties of Injection Molded Long Fiber Thermoplastic Composites," *Polym. Comp.*, vol. 10, no. 5, 1989.
- [77] T. D. Ngo, A. Kashani, G. Imbalzano, K. T. Q. Nguyen, and D. Hui, "Additive manufacturing (3D printing): A review of materials, methods, applications and challenges," *Compos. Part B Eng.*, vol. 143, no. February, pp. 172–196, 2018.
- [78] P. Parandoush and D. Lin, "A review on additive manufacturing of polymer-fiber composites," *Compos. Struct.*, vol. 182, no. September, pp. 36–53, 2017.
- [79] G. Marsh, "Automatin aerospace composites production with fibre placement," *Reinf. Plast.*, vol. 55, no. 3, pp. 32–37, 2011.
- [80] M. Lan, "Thesis report in french: Etude de l'influence des singularites créées par la technique de placement de fibres automatisé sur les performances des matériaux composites," 2016.
- [81] A. W. Blom, "Structural Performance of Fiber-Placed, Variable-Stiffness Composite Conical and Cylindrical Shells A.W. Blom," 2010.
- [82] M. Lan, D. Cartié, P. Davies, and C. Baley, "Influence of embedded gap and overlap fiber placement defects on the microstructure and shear and compression properties of carbon – epoxy laminates," *Compos. Part A*, vol. 82, pp. 198–207, 2016.
- [83] M. Lan, D. Cartié, P. Davies, and C. Baley, "Microstructure and tensile properties of carbon-epoxy laminates produced by automated fibre placement: Influence of a caul plate on the effects of gap and overlap embedded defects," *Compos. Part A Appl. Sci. Manuf.*, vol. 78, pp. 124–134, 2015.
- [84] R. Matsuzaki *et al.*, "Effects of set curvature and fiber bundle size on the printed radius of curvature by a continuous carbon fiber composite 3D printer," *Addit. Manuf.*, vol. 24, pp. 93–102, 2018.
- [85] R. Matsuzaki *et al.*, "Three-dimensional printing of continuous-fiber composites by in-nozzle impregnation," *Sci. Rep.*, vol. 6, no. 1, p. 23058, 2016.
- [86] X. Tian, T. Liu, C. Yang, Q. Wang, and D. Li, "Interface and performance of 3D printed continuous carbon fiber reinforced PLA composites," *Compos. Part A Appl. Sci. Manuf.*, vol. 88, pp. 198–205, 2016.
- [87] Y. Yamanaka, A. Todoroki, M. Ueda, Y. Hirano, and R. Matsuzaki, "Fiber Line Optimization in Single Ply for 3D Printed Composites," *Open J. Compos. Mater.*, vol. 6, no. 4, pp. 121–131, 2016.
- [88] C. Yang *et al.*, "3D printing for continuous fiber reinforced thermoplastic composites : mechanism and performance," *Rapid Prototyp. J.*, vol. 23, no. 1, pp. 209–215, 2017.
- [89] P. Bettini, G. Alitta, G. Sala, L. Di Landro, and L. Di Landro, "Fused Deposition Technique for Continuous Fiber Reinforced Thermoplastic," *J. Mater. Eng. Perform.*, vol. 26, no. 2, pp. 843–848, 2017.
- [90] G. L. D. Goh *et al.*, "Characterization of mechanical properties and fracture mode of additively manufactured carbon fiber and glass fiber reinforced thermoplastics," *Mater. Des.*, vol. 137, pp. 79–89, 2017.
- [91] M. Yamawaki and Y. Kouno, "Fabrication and mechanical characterization of continuous carbon fiber-reinforced thermoplastic using a preform by three-dimensional printing and via hot-press molding," *Adv. Compos. Mater.*, vol. 3046, no. September, pp. 1–11, 2017.
- [92] T. H. J. J. Vaneker, "Material Extrusion of Continuous Fiber Reinforced Plastics Using Commingled Yarn," *Procedia CIRP*, vol. 66, pp. 317–322, 2017.
- [93] Q. Hu, Y. Duan, H. Zhang, D. Liu, B. Yan, and F. Peng, "Manufacturing and 3D printing of continuous carbon fiber prepreg filament," *J. Mater. Sci.*, vol. 53, no. 3, pp. 1887–1898, 2018.
- [94] M. Eichenhofer, J. C. H. Wong, and P. Ermanni, "Continuous lattice fabrication of ultra-lightweight composite structures," *Addit. Manuf.*, 2017.
- [95] T. Liu, X. Tian, M. Zhang, D. Abliz, D. Li, and G. Ziegmann, "Interfacial performance and fracture patterns of 3D printed continuous carbon fiber with sizing reinforced PA6 composites," *Compos. Part A Appl. Sci. Manuf.*, vol. 114, no. July, pp. 368–376, 2018.
- [96] J. Pu, E. Saleh, I. Ashcroft, and A. Jones, "Technique for processing of continuous carbon fibre reinforced PEEK for fused filament fabrication," 2019.
- [97] H. Mei, Z. Ali, Y. Yan, I. Ali, and L. Cheng, "Influence of mixed isotropic fiber angles and hot press on the mechanical properties of 3D printed composites," *Addit. Manufacturing*, vol. 27, no. February, pp. 150–158, 2019.
- [98] F. Van der Klift, Y. Koga, A. Todoroki, M. Ueda, Y. Hirano, and R. Matsuzaki, "3D Printing of Continuous Carbon Fibre Reinforced Thermo-Plastic (CFRTP) Tensile Test Specimens," *Open J. Compos. Mater.*, vol. 6, no. 1, pp. 18–27, 2016.

- [99] A. N. Dickson, J. N. Barry, K. A. McDonnell, and D. P. Dowling, "Fabrication of continuous carbon, glass and Kevlar fibre reinforced polymer composites using additive manufacturing," *Addit. Manuf.*, vol. 16, pp. 146–152, 2017.
- [100] J. Justo, L. Távora, L. García-Guzmán, and F. París, "Characterization of 3D printed long fibre reinforced composites," *Compos. Struct.*, vol. 185, pp. 537–548, 2018.
- [101] M. Iragi, C. Pascual-gonzález, A. Esnaola, C. S. Lopes, and L. Aretxabaleta, "Ply and interlaminar behaviours of 3D printed continuous carbon fibre- reinforced thermoplastic laminates ; effects of processing conditions and microstructure," *Addit. Manuf.*, vol. 30, no. September, p. 100884, 2019.
- [102] A. Todoroki, T. Oasada, Y. Mizutani, and Y. Suzuki, "Tensile property evaluations of 3D printed continuous carbon fiber reinforced thermoplastic composites," *Adv. Compos. Mater.*, vol. 0, no. 0, pp. 1–16, 2019.
- [103] A. D. Pertuz, S. Díaz-cardona, and O. A. González-estrada, "Static and fatigue behaviour of continuous fibre reinforced thermoplastic composites manufactured by fused deposition modelling technique," *Int. J. Fatigue*, vol. 130, no. July 2019, p. 105275, 2020.
- [104] G. W. Melenka, B. K. O. O. Cheung, J. S. Schofield, M. R. Dawson, and J. P. Carey, "Evaluation and prediction of the tensile properties of continuous fiber-reinforced 3D printed structures," *Compos. Struct.*, vol. 153, pp. 866–875, 2016.
- [105] F. Wang, Z. Zhang, F. Ning, G. Wang, and C. Dong, "A mechanistic model for tensile property of continuous carbon fiber reinforced plastic composites built by fused filament fabrication," *Addit. Manuf.*, vol. 32, no. November 2019, p. 100967, 2020.
- [106] N. Li, Y. Li, and S. Liu, "Rapid prototyping of continuous carbon fiber reinforced polylactic acid composites by 3D printing," *J. Mater. Process. Technol.*, vol. 238, pp. 218–225, 2016.
- [107] Q. He, H. Wang, K. Fu, and L. Ye, "3D printed continuous CF / PA6 composites : Effect of microscopic voids on mechanical performance," *Compos. Sci. Technol.*, vol. 191, no. December 2019, p. 108077, 2020.
- [108] B. Akhoundi, A. H. Behraves, and A. B. Saed, "Improving mechanical properties of continuous fiber-reinforced thermoplastic composites produced by FDM 3D printer," 2018.
- [109] M. Heidari-Rarani, M. Rafiee-Afarani, and A. M. Zahedi, "Mechanical characterization of FDM 3D printing of continuous carbon fiber reinforced PLA composites," *Compos. Part B*, vol. 175, no. October 2018, p. 107147, 2019.
- [110] R. Omuro, M. Ueda, R. Matsuzaki, A. Todoroki, and Y. Hirano, "Three-dimensional printing of continuous carbon fiber reinforced thermoplastics by in-nozzle impregnation with compaction roller," in *21st International Conference on Composite Materials*, 2017, no. August, pp. 20–25.
- [111] C. Oztan, R. Karkkainen, M. Fittipaldi, G. Nygren, L. Roberson, and M. Lane, "Microstructure and mechanical properties of three dimensional-printed continuous fiber composites," *J. Compos. Mater.*, pp. 1–10, 2018.
- [112] R. T. L. Ferreira *et al.*, "Experimental characterization and micrography of 3D printed PLA and PLA reinforced with short carbon fibers," *Compos. Part B Eng.*, vol. 124, no. September, pp. 88–100, 2017.
- [113] M. Arhant, P.-Y. Y. Le Gac, M. Le Gall, C. Burtin, C. Briançon, and P. Davies, "Effect of Sea Water and Humidity on the Tensile and Compressive Properties of Carbon-Polyamide 6 Laminates," *Compos. Part A Appl. Sci. Manuf.*, vol. 91, pp. 250–261, 2016.
- [114] E. C. Botelho, Figiel, M. C. Rezende, and B. Lauke, "Mechanical behavior of carbon fiber reinforced polyamide composites," *Compos. Sci. Technol.*, vol. 63, no. 13, pp. 1843–1855, 2003.
- [115] M. Araya-Calvo *et al.*, "Evaluation of compressive and flexural properties of continuous fiber fabrication additive manufacturing technology," *Addit. Manuf.*, vol. 22, no. May, pp. 157–164, 2018.
- [116] P. Zhuo, S. Li, I. Ashcroft, A. Jones, and J. Pu, "3D Printing of Continuous Fibre Reinforced Thermoplastic Composites," *21st Int. Conf. Compos. Mater.*, no. August, pp. 20–25, 2017.
- [117] X. Tian, T. Liu, Q. Wang, A. Dilmurat, D. Li, and G. Ziegmann, "Recycling and remanufacturing of 3D printed continuous carbon fiber reinforced PLA composites," *J. Clean. Prod.*, vol. 142, pp. 1609–1618, 2017.
- [118] J. Zhang, Z. Zhou, F. Zhang, Y. Tan, and R. Yi, "Molding process and properties of continuous carbon fiber three- dimensional printing," *Adv. Mech. Eng.*, vol. 11, no. 3, pp. 1–11, 2019.
- [119] T. N. A. T. Rahim, A. M. Abdullah, H. Akil, D. Mohamad, and Z. A. Rajion, "The improvement of mechanical and thermal properties of polyamide 12 3D printed parts by fused deposition modelling," vol. 11, no. 12, pp. 963–982, 2017.
- [120] C. Ziemian, M. Sharma, and S. Ziemian, "Anisotropic mechanical properties of ABS parts fabricated by fused deposition modelling," *Mech. Eng.*, pp. 159–180, 2012.

- [121] A. Nugroho, R. Ardiansyah, L. Rusita, and I. Larasati, "Effect of layer thickness on flexural properties of PLA (PolyLactid Acid) by 3D printing Effect of layer thickness on flexural properties of PLA (PolyLactid Acid) by 3D printing," 2018.
- [122] T. Ohsawa, M. Miwa, and M. Kawade, "Axial Compressive Strength of Carbon Fiber," *J. Appl. Polym. Sci.*, vol. 39, pp. 1733–1743, 1990.
- [123] M. A. Caminero, J. M. Chacón, I. García-moreno, J. M. Reverte, and G. P. Rodríguez, "Interlaminar bonding performance of 3D printed continuous fi bre reinforced thermoplastic composites using fused deposition modelling," *Polym. Test.*, vol. 68, no. March, pp. 415–423, 2018.
- [124] J. M. Whitney and C. E. Browning, "On short-beam shear tests for composite materials," *Exp. Mech.*, vol. 25, no. 3, pp. 294–300, 1985.
- [125] J.-K. Kim and Y.-W. Mai, *Engineered interfaces in fiber reinforced composites*, Elsevier, 1998.
- [126] J. P. Reis, M. F. S. F. de Moura, R. D. F. Moreira, and F. G. A. Silva, "Pure mode I and II interlaminar fracture characterization of carbon- fi bre reinforced polyamide composite," *Compos. Part B*, vol. 169, no. January, pp. 126–132, 2019.
- [127] H. Shiratori, A. Todoroki, M. Ueda, and R. Matsuzaki, "Mechanism of folding a fiber bundle in the curved section of 3D printed carbon fiber reinforced plastics," *Adv. Compos. Mater.*, vol. 0, no. 0, pp. 1–11, 2019.
- [128] M. Such, C. Ward, and K. Potter, "Aligned Discontinuous Fibre Composites : A Short History," *J. Multifunct. Compos.*, vol. 3, no. 2014, pp. 155–168, 2014.
- [129] P. Parandoush, L. Tucker, C. Zhou, and D. Lin, "Laser assisted additive manufacturing of continuous fiber reinforced thermoplastic composites," *Mater. Des.*, vol. 131, no. August, pp. 186–195, 2017.
- [130] J. Qiao, Y. Li, and L. Li, "Ultrasound-Assisted 3D printing of continuous fiber-reinforced thermoplastic (FRTP) composites," *Addit. Manuf.*, p. 100926, 2019.
- [131] N. Li, G. Link, and J. Jelonnek, "3D microwave printing temperature control of continuous carbon fiber reinforced composites," *Compos. Sci. Technol.*, vol. 187, no. November 2019, p. 107939, 2020.
- [132] T. Liu, X. Tian, Y. Zhang, Y. Cao, and D. Li, "High-pressure interfacial impregnation by micro-screw in-situ extrusion for 3D printed continuous carbon fi ber reinforced nylon composites," *Compos. Part A*, vol. 130, no. January, p. 105770, 2020.
- [133] W. Hao, Y. Liu, H. Zhou, H. Chen, and D. Fang, "Preparation and characterization of 3D printed continuous carbon fiber reinforced thermosetting composites," *Polym. Test.*, vol. 65, no. November 2017, pp. 29–34, 2018.
- [134] A. V. Azarov, F. K. Antonov, M. V. Golubev, A. R. Khaziev, and S. A. Ushanov, "Composite 3D printing for the small size unmanned aerial vehicle structure," *Compos. Part B*, 2019.
- [135] A. V. Azarov *et al.*, "Development of a two-matrix composite material fabricated by 3D printing," *Polym. Sci. Ser. D*, vol. 10, no. 1, pp. 87–90, 2017.
- [136] "Fiber™ from Dekstop Metal. URL available at: <https://www.desktopmetal.com/products/fiber>. Consulted on April 2020."
- [137] "Red Series™ from 9T Labs. URL available at: <https://www.9tllabs.com/product>. Consulted on April 2020."
- [138] "Arevo. URL available at: <https://arevo.com/>. Consulted on April 2020."
- [139] "Continuous Composites. URL available at: <https://www.continuouscomposites.com/technology>. Consulted on April 2020."
- [140] "Atropos from +lab. URL available at: <http://www.piulab.it/projects/atropos-redefine-manufacturing>. Consulted on April 2020."
- [141] A. A. Stepashkin, D. I. Chukov, F. S. Senatov, A. I. Salimon, A. M. Korsunsky, and S. D. Kaloshkin, "3D-printed PEEK-carbon fiber (CF) composites : Structure and thermal properties," *Compos. Sci. Technol.*, vol. 164, pp. 319–326, 2018.
- [142] L. Meng, T. Xiaoyong, S. Junfan, Z. Weijun, L. Dichen, and Q. Yingjie, "Impregnation and interlayer bonding behaviours of 3D-printed continuous carbon- fiber-reinforced poly-ether-ether-ketone composites," *Compos. Part A*, vol. 121, no. December 2018, pp. 130–138, 2019.
- [143] H. Al Abadi, H. Thai, V. Paton-cole, and V. I. Patel, "Elastic properties of 3D printed fibre-reinforced structures," *Compos. Struct.*, vol. 193, no. March, pp. 8–18, 2018.
- [144] H. Brooks and S. Molony, "Design and evaluation of additively manufactured parts with three dimensional continuous fibre reinforcement," *Mater. Des.*, vol. 90, pp. 276–283, 2016.
- [145] N. Li *et al.*, "Path-designed 3D printing for topological optimized continuous carbon fibre reinforced composite structures," *Compos. Part B*, vol. 182, no. July 2019, p. 107612, 2020.
- [146] J. Huang and R. T. Haftka, "Optimization of fiber orientations near a hole for increased load-carrying

- capacity of composite laminates," *Struct. Multidiscip. Optim.*, vol. 30, pp. 335–341, 2005.
- [147] M. W. Tosh and D. W. Kelly, "On the design , manufacture and testing of trajectorial fibre steering for carbon fibre composite laminates &," *Compos. Part A*, vol. 31, pp. 1047–1060, 2000.
- [148] A. N. Dickson, K. Ross, and D. P. Dowling, "Additive Manufacturing of Woven Carbon Fibre Polymer Composites," *Compos. Struct.*, no. August, 2018.
- [149] T. Shafighfard, E. Demir, and M. Yildiz, "Design of fiber-reinforced variable-stiffness composites for different open- hole geometries with fiber continuity and curvature constraints," *Compos. Struct.*, vol. 226, pp. 1–14, 2019.
- [150] N. V. Banichuk, V. V. Saurin, and A. A. Barsuk, "Optimal orientation of orthotropic materials for plates designed against buckling," *Struct. Optim.*, vol. 10, no. 1890, pp. 191–196, 1995.
- [151] H. K. Cho and R. E. Rowlands, "Optimizing Fiber Direction in Perforated Orthotropic Media to Reduce Stress Concentration," *J. Compos. Mater.*, vol. 43, no. 10, pp. 1177–1198, 2015.
- [152] A. V Malakhov and A. N. Polilov, "Design of composite structures reinforced curvilinear fibres using FEM," *Compos. Part A*, vol. 87, pp. 23–28, 2016.
- [153] K. Sugiyama *et al.*, "3D printing of optimized composites with variable fiber volume fraction and stiffness using continuous fiber," *Compos. Sci. Technol.*, vol. 186, no. November 2019, p. 107905, 2020.
- [154] G. McKnight and C. Henry, "Variable Stiffness Materials for Reconfigurable Surface Applications," vol. 5761, pp. 119–126, 2005.
- [155] W. Wang and S. Ahn, "Shape Memory Alloy-Based Soft Gripper with Variable Stiffness for Compliant and Effective Grasping," *Soft Robot.*, vol. 0, no. 0, pp. 1–11, 2017.
- [156] M. A. McEvoy and N. Correll, "Thermoplastic variable stiffness composites with embedded, networked sensing, actuation, and control," *J. Compos. Mater.*, no. March, pp. 1–10, 2014.
- [157] S. Tibbits, "4D printing: multi-material shape change," *Archit. Des.*, pp. 116–121, 2014.
- [158] E. Pei, "4D printing – revolution or fad ?," 2015.
- [159] Z. X. Khoo, J. Ee, M. Teoh, Y. Liu, and C. K. Chua, "3D printing of smart materials : A review on recent progresses in 4D printing," vol. 2759, 2015.
- [160] F. Momeni, S. M. Mehdi Hassani, X. Liu, and J. Ni, "A review of 4D printing," *Mater. Des.*, vol. 122, pp. 42–79, 2017.
- [161] T. Chen, O. R. Bilal, R. Lang, C. Daraio, and K. Shea, "Autonomous Deployment of a Solar Panel Using Elastic Origami and Distributed Shape-Memory-Polymer Actuators," *Phys. Rev. Appl.*, vol. 10, no. 1, p. 1, 2019.
- [162] W. Wang, N.-G. Kim, H. Rodrigue, and S. Ahn, "Modular assembly of soft deployable structures and robots," *Mater. Horizons*, 2017.
- [163] S. Reichert, A. Menges, and D. Correa, "Meteorosensitive architecture: Biomimetic building skins based on materially embedded and hygroscopically enabled responsiveness," *Comput. Des.*, vol. 60, pp. 50–69, Mar. 2015.
- [164] G. N. Levy, R. Schindel, and J. P. Kruth, "Rapid manufacturing and rapid tooling with layer manufacturing (LM) technologies, state of the art and future perspectives," *CIRP Ann. - Manuf. Technol.*, vol. 52, no. 2, pp. 589–609, 2003.
- [165] L. Sun *et al.*, "Stimulus-responsive shape memory materials: A review," *Mater. Des.*, vol. 33, no. 1, pp. 577–640, 2012.
- [166] M. Zarek, N. Mansour, S. Shapira, and D. Cohn, "4D Printing of Shape Memory-Based Personalized Endoluminal Medical Devices," *Macromol. Rapid Commun.*, 2017.
- [167] J. K. H. Lin and H. Fang, "Concept Study of a 35-m Spherical Reflector System for NEXRAD in Space Application," in *American Institute of Aeronautics and Astronautics*, 2006, no. May, pp. 1–12.
- [168] S. Poppinga *et al.*, "Toward a New Generation of Smart Biomimetic Actuators for Architecture," *Adv. Mater.*, vol. 30, no. 19, pp. 1–10, 2018.
- [169] J. M. Benyus, *Biomimicry : Innovation Inspired by Nature*. 1997.
- [170] W. Barthlott, C. Neinhuis, H. Verlot, and C. L. Schott, "Purity of the sacred lotus , or escape from contamination in biological surfaces," *Planta*, pp. 1–8, 1997.
- [171] J. Lienhard, S. Schleicher, S. Poppinga, and T. Masselter, "Flectofin : a hingeless flapping mechanism," vol. 45001.
- [172] M. S. Aziz and A. Y. El, "Biomimicry as an approach for bio-inspired structure with the aid of computation," *Alexandria Eng. J.*, vol. 55, no. 1, pp. 707–714, 2016.
- [173] Y. Forterre, J. M. Skotheim, J. Dumais, and L. Mahadevan, "How the Venus flytrap snaps," *Nature*, vol. 433, no. January, pp. 421–425, 2005.
- [174] T. Sibaoka, "Rapid Plant Movements Triggered by Action Potentials," *Bot. Mag. Tokyo*, pp. 73–95, 1991.

- [175] A. Le Duigou and M. Castro, "Moisture-induced self-shaping flax-reinforced polypropylene biocomposite actuator," *Ind. Crop. Prod.*, vol. 71, pp. 1–6, 2015.
- [176] A. Le Duigou and M. Castro, "Evaluation of force generation mechanisms in natural, passive hydraulic actuators," *Sci. Rep.*, vol. 6, no. January, 2016.
- [177] E. Reysat and L. Mahadevan, "Hygromorphs: from pine cones to biomimetic bilayers," *J. R. Soc. Interface*, vol. 6, no. 39, pp. 951–957, 2009.
- [178] R. Elbaum and Y. Abraham, "Insights into the microstructures of hygrosopic movement in plant seed dispersal," *Plant Sci.*, vol. 223, pp. 124–33, Jun. 2014.
- [179] C. Dawson, J. F. V. Vincent, and A.-M. Rocca, "How pine cones open," *Nature*, vol. 390, pp. 18–25, 1997.
- [180] N. J. Kanu, E. Gupta, U. K. Vates, and G. K. Singh, "An insight into biomimetic 4D printing," *RSC Adv.*, pp. 38209–38226, 2019.
- [181] P. Fratzl and F. G. Barth, "Biomaterial systems for mechanosensing and actuation," vol. 462, no. November, 2009.
- [182] A. Holstov, B. Bridgens, and G. Farmer, "Hygromorphic materials for sustainable responsive architecture," *Constr. Build. Mater.*, vol. 98, pp. 570–582, 2015.
- [183] T. van Manen, S. Janbazz, and A. A. Zadpoor, "Programming 2D/3D shape-shifting with hobbyist 3D printers," vol. 4, no. 6, 2017.
- [184] C. Yang, B. Wang, D. Li, and X. Tian, "Modelling and characterisation for the responsive performance of CF/PLA and CF/PEEK smart materials fabricated by 4D printing," *Virtual Phys. Prototyp.*, vol. 12, no. 1, pp. 69–76, 2017.
- [185] J. N. Rodriguez, C. Zhu, E. B. Duoss, T. S. Wilson, C. M. Spadaccini, and J. P. Lewicki, "Shape-morphing composites with designed micro-architectures," *Sci. Rep.*, vol. 6, no. June, 2016.
- [186] A. I. Salimon, F. S. Senatov, V. A. Kalyaev, and A. M. Korsunsky, *Shape memory polymer blends and composites for 3D and 4D printing applications*. Elsevier Inc., 2020.
- [187] W. Zhang *et al.*, "Shape memory behavior and recovery force of 4D printed textile functional composites," *Compos. Sci. Technol.*, vol. 160, no. March, pp. 224–230, 2018.
- [188] Y. Mao, K. Yu, M. S. Isakov, J. Wu, M. L. Dunn, and H. J. Qi, "Sequential Self-Folding Structures by 3D Printed Digital Shape Memory Polymers," *Nat. Publ. Gr.*, pp. 1–12, 2015.
- [189] Q. Ge, H. J. Qi, M. L. Dunn, Q. Ge, H. J. Qi, and M. L. Dunn, "Active materials by four-dimension printing," *Appl. Phys. Lett.*, vol. 103, no. 13, 2013.
- [190] Q. Ge, C. K. Dunn, H. J. Qi, and M. L. Dunn, "Active origami by 4D printing," *Smart Mater. Struct.*, vol. 23, no. 9, p. 94007, 2014.
- [191] S. Akbari *et al.*, "Enhanced Multimaterial 4D Printing with Active Hinges," *Smart Mater. Struct.*, 2018.
- [192] Q. Ge, A. H. Sakhaei, H. Lee, C. K. Dunn, N. X. Fang, and M. L. Dunn, "Multimaterial 4D Printing with Tailorable Shape Memory Polymers," *Sci. Rep.*, vol. 6, no. July, pp. 1–11, 2016.
- [193] H. Yang *et al.*, "3D Printed Photoresponsive Devices Based on Shape Memory Composites," *Adv. Mater.*, vol. 1701627, pp. 1–7, 2017.
- [194] A. M. Hubbard, R. W. Mailen, M. A. Zikry, M. D. Dickey, and J. Genzer, "Controllable curvature from planar polymer sheets in response to light," *Soft Matter*, vol. 13, no. 12, pp. 2299–2308, 2017.
- [195] L. Ionov, "Hydrogel-based actuators : possibilities and limitations," *Mater. Today*, vol. 17, no. 10, pp. 494–503, 2014.
- [196] M. C. Mulakkal, R. S. Trask, V. P. Ting, and A. M. Seddon, "Responsive cellulose-hydrogel composite ink for 4D printing," *Mater. Des.*, vol. 160, pp. 108–118, 2018.
- [197] D. Raviv *et al.*, "Active Printed Materials for Complex Self-Evolving Deformations," *Sci. Rep.*, vol. 4, no. 7422, pp. 1–8, 2014.
- [198] S. Tibbits, C. McKnelly, C. Olguin, D. Dikovskiy, and S. Hirsch, "4D Printing and universal transformation," *ACADIA 2014 Des. AGENCY*, pp. 539–548, 2013.
- [199] S. Liu, X. Chen, and Y. Zhang, *Hydrogels and hydrogel composites for 3D and 4D printing applications*. Elsevier Inc., 2020.
- [200] A. Kirillova, R. Maxson, G. Stoychev, C. T. Gomillion, and L. Ionov, "4D Biofabrication Using Shape-Morphing Hydrogels," *Adv. Mater.*, vol. 1703443, pp. 1–8, 2017.
- [201] L. Huang *et al.*, "Ultrafast Digital Printing toward 4D Shape Changing Materials," *Adv. Mater.*, pp. 1–6, 2017.
- [202] S. Naficy, R. Gatelly, R. G. Iii, H. Xin, and G. M. Spinks, "4D Printing of Reversible Shape Morphing Hydrogel Structures," *Macromol. Mater. Eng.*, pp. 1–9, 2016.
- [203] S. Y. Zheng, Y. Shen, F. Zhu, J. Yin, J. Qian, and J. Fu, "Programmed Deformations of 3D-Printed Tough Physical Hydrogels with High Response Speed and Large Output Force," *Adv. Funct. Mater.*, vol.

- 1803366, pp. 1–8, 2018.
- [204] A. B. Baker, S. R. G. Bates, T. M. Llewellyn-jones, L. P. B. Valori, M. P. M. Dicker, and R. S. Trask, “4D printing with robust thermoplastic polyurethane hydrogel-elastomer trilayers,” *Mater. Des.*, vol. 163, p. 107544, 2019.
- [205] Y. Mao *et al.*, “3D Printed Reversible Shape Changing Components with Stimuli Responsive Materials,” *Sci. Rep.*, vol. 6, no. 1, p. 24761, 2016.
- [206] Z. Liang, Y. Liu, F. Zhang, Y. Ai, and Q. Liang, “Dehydration-triggered shape morphing based on asymmetric bubble hydrogel microfibers,” *Soft Matter*, 2018.
- [207] A. Sydney Gladman, E. A. Matsumoto, R. G. Nuzzo, L. Mahadevan, and J. A. Lewis, “Biomimetic 4D printing,” *Nat. Mater.*, vol. 15, no. 4, pp. 413–418, 2016.
- [208] I. Burgert and P. Fratzl, “Actuation systems in plants as prototypes for bioinspired devices,” *Philos. Trans. R. Soc. A Math. Phys. Eng. Sci.*, vol. 367, no. 1893, pp. 1541–1557, 2009.
- [209] G. V. Laivins and A. M. Scallan, “The mechanism of hornification of wood pulps,” *Prod. Papermak.*, pp. 1235–1260, 1993.
- [210] L. Chen, M. Weng, F. Huang, and W. Zhang, “Light-and humidity-driven actuators with programmable complex shape-deformations,” *Sensors Actuators B. Chem.*, vol. 282, no. November 2018, pp. 384–390, 2019.
- [211] L. Chen, M. Weng, P. Zhou, L. Zhang, Z. Huang, and W. Zhang, “Multi-responsive actuators based on a graphene oxide composite: intelligent robot and bioinspired applications,” *Nanoscale*, no. DOI: 10.1039/c7nr01913k, 2017.
- [212] M. M. Hamed *et al.*, “Electrically Activated Paper Actuators,” *Adv. Funct. Mater.*, vol. 26, no. 15, pp. 2446–2453, 2016.
- [213] M. Amjadi and M. Sitti, “High-Performance Multiresponsive Paper Actuators,” *ACS Nano*, vol. 10, no. 11, pp. 10202–10210, 2016.
- [214] X. Lan, Y. Liu, H. Lv, X. Wang, J. Leng, and S. Du, “Fiber reinforced shape-memory polymer composite and its application in a deployable hinge,” *Smart Mater. Struct.*, vol. 18, no. 24002, p. 6pp, 2009.
- [215] Q. Wang *et al.*, “Programmable morphing composites with embedded continuous fibers by 4D printing,” *Mater. Des.*, vol. 155, pp. 404–413, 2018.
- [216] D. Correa *et al.*, “3D printing wood :Programming hygroscopic material transformations,” *3D Print. Addit. Manuf.*, vol. 2, no. 3, pp. 106–116, 2015.
- [217] J. U. Schmied, H. Le Ferrand, P. Ermanni, A. R. Studart, and A. F. Arrieta, “Programmable snapping composites with bio-inspired architecture,” *Bioinspiration and Biomimetics*, vol. 12, no. 2, 2017.
- [218] R. M. Erb, J. S. Sander, R. Grisch, and A. R. Studart, “Self-shaping composites with programmable bioinspired microstructures,” *Nature*, pp. 1–8, 2013.
- [219] X. Tian, Q. Wang, and D. Li, “Design of a continuous fiber trajectory for 4D printing of thermally stimulated composite structures,” 2020.
- [220] S. Van Hoa, “Development of composite springs using 4D printing method,” *Compos. Struct.*, vol. 210, no. April 2018, pp. 869–876, 2019.
- [221] S. V Hoa and X. Cai, “Twisted composite structures made by 4D printing method,” *Compos. Struct.*, vol. 238, no. January, p. 111883, 2020.
- [222] A. Bourmaud, J. Beaugrand, D. U. Shah, V. Placet, and C. Baley, “Towards the design of high-performance plant fibre composites,” *Prog. Mater. Sci.*, vol. 97, no. July 2017, pp. 347–408, 2018.
- [223] D. U. Shah, P. J. Schubel, and M. J. Clifford, “Can flax replace E-glass in structural composites ? A small wind turbine blade case study,” *Compos. Part B*, vol. 52, pp. 172–181, 2013.
- [224] A. Le Duigou and C. Baley, “Coupled micromechanical analysis and life cycle assessment as an integrated tool for natural fibre composites development,” *J. Clean. Prod.*, vol. 83, pp. 61–69, 2014.
- [225] N. Defoirdt *et al.*, “Assessment of the tensile properties of coir, bamboo and jute fibre,” *Compos. Part A Appl. Sci. Manuf.*, vol. 41, no. 5, pp. 588–595, 2010.
- [226] P. Fratzl, R. Elbaum, and I. Burgert, “Cellulose fibrils direct plant organ movements,” *Faraday Discuss*, vol. 139, pp. 275–282, 2008.
- [227] T. Joffre, R. C. Neagu, S. L. Bardage, and E. K. Gamstedt, “Modelling of the hygroelastic behaviour of normal and compression wood tracheids,” *J. Struct. Biol.*, vol. 185, no. 1, pp. 89–98, Jan. 2014.
- [228] A. Lefeuvre, A. Le Duigou, A. Bourmaud, A. Kervoelen, C. Morvan, and C. Baley, “Analysis of the role of the main constitutive polysaccharides in the flax fibre mechanical behaviour,” *Ind. Crops Prod.*, vol. 76, pp. 1039–1048, Dec. 2015.
- [229] A. Lefeuvre, A. Bourmaud, C. Morvan, and C. Baley, “Elementary flax fibre tensile properties: Correlation between stress–strain behaviour and fibre composition,” *Ind. Crops Prod.*, vol. 52, pp. 762–

- 769, Jan. 2014.
- [230] A. le Duigou, A. Bourmaud, E. Balnois, P. Davies, and C. Baley, "Improving the interfacial properties between flax fibres and PLLA by a water fibre treatment and drying cycle," *Ind. Crops Prod.*, vol. 39, pp. 31–39, Sep. 2012.
- [231] C. Baley, Y. Perrot, F. Busnel, H. Guezenoc, and P. Davies, "Transverse tensile behaviour of unidirectional plies reinforced with flax fibres," *Mater. Lett.*, vol. 60, no. 24, pp. 2984–2987, Oct. 2006.
- [232] C. Baley, "Analysis of the flax fibres tensile behaviour and analysis of the tensile stiffness increase," vol. 33, pp. 939–948, 2002.
- [233] V. Placet, O. Cissé, and M. Lamine Boubakar, "Nonlinear tensile behaviour of elementary hemp fibres. Part I: Investigation of the possible origins using repeated progressive loading with in situ microscopic observations," *Compos. Part A Appl. Sci. Manuf.*, vol. 56, pp. 319–327, Jan. 2014.
- [234] D. U. Shah, "Damage in biocomposites: Stiffness evolution of aligned plant fibre composites during monotonic and cyclic fatigue loading," *Compos. Part A Appl. Sci. Manuf.*, Sep. 2015.
- [235] D. Shah, P. Schubel, M. Clifford, and P. Licence, "The Tensile Behavior of Off-Axis Loaded Plant Fiber Composites: An Insight on the Nonlinear Stress–Strain Response," *Polymer Compos.*, vol. 1454–1504, 2012.
- [236] Z. E. Cherif, C. Poilâne, A. Vivet, B. Ben Doudou, and J. Chen, "About optimal architecture of plant fibre textile composite for mechanical and sorption properties," *Compos. Struct.*, vol. 140, pp. 240–251, Apr. 2016.
- [237] A. Bourmaud, A. Le Duigou, C. Gourier, and C. Baley, "Influence of processing temperature on mechanical performance of unidirectional polyamide 11 – flax fibre composites," *Ind. Crop. Prod.*, vol. 84, pp. 151–165, 2016.
- [238] C. A. S. Hill, A. Norton, and G. Newman, "The Water Vapor Sorption Behavior of Natural Fibers," *J. Appl. Polym. Sci.*, vol. 112, no. 3, pp. 1524–1537, 2009.
- [239] D. L. Bismarck A, Mishra S, Lampke T. Mohanty AK, Mishra M, "Plant fibers as reinforcement for green composites," *Nat. fibers, Biopolym. biocomposites. Boca Rat. CRC Press.*, 2005.
- [240] K. Pickering, "Properties and Performance of Natural-Fibre Composites," *Woodhead Publ.*, vol. 1st ed, p. 576, Jun. 2008.
- [241] A. Monti and E. Alexopoulou, Eds., *Kenaf: A Multi-Purpose Crop for Several Industrial Applications*. London: Springer London, 2013.
- [242] A. K. Bledzki and J. Gassan, "Composites Reinforced with Cellulose Based Fibres," *Prog. Polym. Sci.*, vol. 24, pp. 221–274, 1999.
- [243] N. Dayakar, "'Effective Properties of Randomly Oriented Kenaf Short Fiber Reinforced' by Dayakar Naik L.," *Thesis report*, 2015. .
- [244] H. M. Akil, M. F. Omar, A. Mazuki, S. Safiee, Z. Ishak, and A. Abu Bakar, "Kenaf fiber reinforced composites: A review," *Mater. Des.*, vol. 32, no. 8–9, pp. 4107–4121, Sep. 2011.
- [245] R. Mahjoub, J. Yatim, A. Sam, and S. Hashemi, "Tensile properties of kenaf fiber due to various conditions of chemical fiber surface modifications," *Constr. Build. Mater.*, vol. 55, pp. 103–113, 2014.
- [246] O. Faruk, A. K. Bledzki, H.-P. Fink, and M. Sain, "Biocomposites reinforced with natural fibers: 2000–2010," *Prog. Polym. Sci.*, vol. 37, no. 11, pp. 1552–1596, Nov. 2012.
- [247] A. Bourmaud, A. Le Duigou, and C. Baley, *Mechanical performance of flax-based biocomposites*. 2015.
- [248] A. Komuraiah, N. Kumar, and B. Prasad, "Chemical Composition of Natural Fibers and its Influence on their Mechanical Properties," *Mech. Compos. Mater.*, vol. 50, no. 3, 2014.
- [249] M. Eder, O. Arnould, J. Dunlop, J. Hornatowska, and L. Salmen, "Experimental micromechanical characterisation of wood cell walls.," *Wood Sci. Technol.*, vol. 43, no. 163–182, 2013.
- [250] A. Boumaud, J. Beaugrand, D. Shah, V. Placet, and C. Baley, "Towards the design of high performance biocomposites," *Prog. Mater. Sci.*, vol. 97, pp. 347–408, 2018.
- [251] K. L. Pickering, M. G. A. Efendy, and T. M. Le, "A review of recent developments in natural fibre composites and their mechanical performance," *Compos. Part A Appl. Sci. Manuf.*, vol. 83, pp. 98–112, 2016.
- [252] L. Marrot, A. Lefevre, B. Pontoire, A. Bourmaud, and C. Baley, "Analysis of the hemp fiber mechanical properties and their scattering (Fedora 17)," *Ind. Crops Prod.*, vol. 51, pp. 317–327, Nov. 2013.
- [253] V. Placet, O. Cisse, and M. L. Boubakar, "Influence of environmental relative humidity on the tensile and rotational behaviour of hemp fibres," *J. Mater. Sci.*, vol. 47, no. 7, pp. 3435–3446, Dec. 2011.
- [254] S. Eichhorn and R. Young, "Composite micromechanics of hemp fibres and epoxy resin microdroplets," *Compos Sci Technol*, pp. 767–772, 2004.
- [255] C. Baley *et al.*, "Specific features of flax fibres used to manufacture composite materials," *Int. J. Mater.*

- Form.*, 2018.
- [256] D. Filgueira, S. Holmen, J. K. Melbø, D. Moldes, A. T. Echtermeyer, and G. Chinga-carrasco, "3D Printable Filaments Made of Biobased Polyethylene Biocomposites," *Polymers (Basel)*, vol. 10, no. 314, 2018.
- [257] A. Bourmaud and C. Baley, "Investigations on the recycling of hemp and sisal fibre reinforced polypropylene composites," *Polym. Degrad. Stab.*, vol. 92, no. 6, pp. 1034–1045, Jun. 2007.
- [258] A. Bourmaud, G. Ausias, G. Lebrun, M. L. Tachon, and C. Baley, "Observation of the structure of a composite polypropylene/flax and damage mechanisms under stress," *Ind. Crops Prod.*, vol. 43, pp. 225–236, 2013.
- [259] G. Coroller *et al.*, "Effect of flax fibres individualisation on tensile failure of flax/epoxy unidirectional composite," *Compos. Part A Appl. Sci. Manuf.*, vol. 51, pp. 62–70, 2013.
- [260] B. Madsen, A. Thygesen, and H. Lilholt, "Plant fibre composites – porosity and volumetric interaction," *Compos. Sci. Technol.*, vol. 67, no. 7–8, pp. 1584–1600, Jun. 2007.
- [261] A. Bourmaud and C. Baley, "Effects of thermo mechanical processing on the mechanical properties of biocomposite flax fibers evaluated by nanoindentation," *Polym. Degrad. Stab.*, vol. 95, no. 9, pp. 1488–1494, 2010.
- [262] C. Baley, A. Le Duigou, A. Bourmaud, and P. Davies, "Influence of drying on the mechanical behaviour of flax fibres and their unidirectional composites," *Compos. Part A*, vol. 43, no. 8, pp. 1226–1233, 2012.
- [263] T. Yang, "Effect of Extrusion Temperature on the Fiber-Reinforced Polylactic Acid Composite (WFRPC)," *Polymers (Basel)*, 2018.
- [264] S. Guessasma, S. Belhabib, and H. Nouri, "Understanding the microstructural role of bio-sourced 3D printed structures on the tensile performance," *Polym. Test.*, vol. 77, no. June, 2019.
- [265] M. Kariz, M. Sernek, M. Obućina, and M. K. Kuzman, "Effect of wood content in FDM filament on properties of 3D printed parts," *Mater. Today Commun.*, 2017.
- [266] D. Stoof and K. Pickering, "Fused Deposition Modelling of Natural Fibre/Polylactic Acid Composites," *J. Compos. Sci.*, vol. 1, no. 1, p. 8, 2017.
- [267] G. Xie, Y. Zhang, and W. Lin, "Plasticizer combinations and performance of wood flour-poly(lactic acid) 3D printing filaments," *BioResources*, vol. 12, no. 3, pp. 6736–6748, 2017.
- [268] A. R. Torrado Perez, D. A. Roberson, and R. B. Wicker, "Fracture surface analysis of 3D-printed tensile specimens of novel ABS-based materials," *J. Fail. Anal. Prev.*, vol. 14, no. 3, pp. 343–353, 2014.
- [269] A. Le Duigou, M. Castro, R. Bevan, and N. Martin, "3D printing of wood fibre biocomposites: From mechanical to actuation functionality," *Mater. Des.*, vol. 96, pp. 106–114, 2016.
- [270] T. N. Tran *et al.*, "Cocoa Shell Waste Biofilaments for 3D Printing Applications," *Macromol. Mater. Eng.*, vol. 1700219, p. 1700219, 2017.
- [271] F. Gentles, J. Anderson, and J. L. Thomason, "Characterisation of the transverse thermoelastic properties of natural fibres used in composites," in *14th European Conference on Composite Materials, ECCM14, 7-10 June 2010, Budapest*, 2010.
- [272] F. R. Cichocki Jr. and J. L. Thomason, "Thermoelastic anisotropy of a natural fiber," *Compos. Sci. Technol.*, vol. 62, no. 5, pp. 669–678, 2002.
- [273] J. Thomason, "Dependence of interfacial strength on the anisotropic fiber properties of jute reinforced composites," *Polym. Compos.*, vol. 31, no. 9, pp. 1525–1534, 2009.
- [274] A. Le Duigou, J. Merotte, A. Bourmaud, P. Davies, K. Belhouli, and C. Baley, "Hygroscopic expansion : A key point to describe natural fibre / polymer matrix interface bond strength," *Compos. Sci. Technol.*, vol. 151, pp. 228–233, 2017.
- [275] M. Milosevic, D. Stoof, and K. L. Pickering, "Characterizing the Mechanical Properties of Fused Deposition Modelling Natural Fiber Recycled Polypropylene Composites," *J. Compos. Sci.*, vol. 1, no. 1, p. 7, 2017.
- [276] D. Stoof and K. Pickering, "Sustainable composite fused deposition modelling filament using recycled pre-consumer polypropylene," *Compos. Part B*, 2017.
- [277] B. Coppola, E. Garofalo, L. Di Maio, P. Scarfato, and L. Incarnato, "Investigation on the use of PLA / hemp composites for the fused deposition modelling (FDM) 3D printing," *AIP Conf. Proc.*, vol. 20086, pp. 1–5, 2018.
- [278] X. Xiao, V. S. Chevali, P. Song, D. He, and H. Wang, "Polylactide/hemp hurd biocomposites as sustainable 3D printing feedstock," *Compos. Sci. Technol.*, p. 107887, 2019.
- [279] D. Depuydt *et al.*, "Production and Characterization of Bamboo and Flax Fiber Reinforced Polylactic Acid Filaments for Fused Deposition Modeling (FDM)," *Polym. Compos.*, 2018.
- [280] D. X. Zhao, X. Cai, G. Z. Shou, Y. Q. Gu, and P. X. Wang, "Study on the Preparation of Bamboo Plastic Composite Intend for Additive Manufacturing," *Key Eng. Mater.*, vol. 667, pp. 250–258, 2015.

- [281] M. A. Pop *et al.*, "Structural changes during 3D printing of bioderived and synthetic thermoplastic materials t a," *J. Appl. Polym. Sci.*, vol. 47382, pp. 1–11, 2018.
- [282] J. Safka, M. Ackerann, J. Borek, S. Martin, J. Habr, and L. Behalek, "Use of composite materials for FDM 3D print technology," *Mater. Sci. Forum*, vol. 862, pp. 174–181, 2016.
- [283] A. Kearns, "Cotton Cellulose Fibers for 3D Print Material," 2017.
- [284] Y. Tao, H. Wang, Z. Li, P. Li, and S. Q. Shi, "Development and application of wood flour-filled polylactic acid composite filament for 3d printing," *Materials (Basel)*, vol. 10, no. 4, pp. 1–6, 2017.
- [285] D. Filgueira, S. Holmen, J. K. Melbø, D. Moldes, A. T. Echtermeyer, and G. Chinga-carrasco, "Enzymatic-Assisted Modification of Thermomechanical Pulp Fibers To Improve the Interfacial Adhesion with Poly(lactic acid) for 3D Printing," *ACS Sustain. Chem. Eng.*, 2017.
- [286] J. I. Montalvo Navarrete, M. A. Hidalgo-Salazar, E. Escobar Nunez, and A. J. Rojas Arciniegas, "Thermal and mechanical behavior of biocomposites using additive manufacturing," *Int. J. Interact. Des. Manuf.*, no. May, 2017.
- [287] M. A. Montalvo Navarrete, Jorge I.; Hidalgo-Salazar, "3D Printing with natural fiber reinforced filament," pp. 0–12.
- [288] Y. Tao, L. Pan, D. Liu, and P. Li, "A case study : Mechanical modeling optimization of cellular structure fabricated using wood flour- filled polylactic acid composites with fused deposition modeling," *Compos. Struct.*, vol. 216, no. January, pp. 360–365, 2019.
- [289] N. E. N. Zander, J. J. H. Park, Z. Z. R. Boelter, and M. A. Gillan, "Recycled Cellulose Polypropylene Composite Feedstocks for Material Extrusion Additive Manufacturing," *ACS Omega*, vol. 4, pp. 13879–13888, 2019.
- [290] J. Girdis, L. Gaudion, S. L. O. Schke, and A. Dong, "Rethinking Timber : Investigation into the Use of Waste Macadamia Nut Shells for Additive Manufacturing," *JOM*, pp. 2–6, 2016.
- [291] Torrado Perez AR, Roberson DA, Wicker RB, "Fracture surface analysis of 3D printed tensiles specimens of novel ABS based materials," *J Fail Anal. Preven*, vol. 14, pp. 343–353, 2014.
- [292] D. Stoof and K. Pickering, "Sustainable composite fused deposition modeling filament using recycled pre-consumer polypropylene," *Compos. Part B Eng.*, vol. 135, pp. 110–118, 2018.
- [293] H. Bi, Z. Ren, R. Guo, M. Xu, and Y. Song, "Fabrication of flexible wood flour/thermoplastic polyurethane elastomer composites using fused deposition molding," *Ind. Crops Prod.*, vol. 122, pp. 76–84, 2018.
- [294] H. Liu, H. He, X. Peng, B. Huang, and J. Li, "Three-dimensional printing of poly(lactic acid) bio-based composites with sugarcane bagasse fiber: Effect of printing orientation on tensile performance.," *Polym. Adv. Technol.*, vol. 30, pp. 910–922, 2019.
- [295] F. Daver, K. Peng, M. Lee, M. Brandt, and R. Shanks, "Cork-PLA composite filaments for fused deposition modelling," *Compos. Sci. Technol.*, no. 10.1016/j.compscitech.2018.10.008, 2018.
- [296] J. Girdis, L. Gaudion, G. Proust, S. Loschke, and A. Dong, "Rethinking Timber: Investigation into the Use of Waste Macadamia Nut Shells for Additive Manufacturing," *JOM*, vol. 69, no. 3, pp. 575–579, 2017.
- [297] R. Guo, Z. Ren, H. Bi, Y. Song, and M. Xu, "Effect of toughening agents on the properties of poplar wood flour/poly(lactic acid) composites fabricated with fused deposition modeling.," *Eur. Polym. J.*, vol. 107, pp. 34–45, 2018.
- [298] A. Le Duigou, A. Barbé, E. Guillou, and M. Castro, "3D printing of continuous flax fibre reinforced biocomposite for structural applications," *Mater. Des.*, vol. 180, p. 107884, 2019.
- [299] C. Badouard, F. Traon, C. Denoual, C. Mayer-Laigle, G. Paës, and A. Bourmaud, "Exploring mechanical properties of fully compostable flax reinforced composite filaments for 3D printing applications," *Ind. Crops Prod.*, vol. 135, pp. 246–250, 2019.
- [300] Y. Dong, J. Milentis, and A. Pramanik, "Additive manufacturing of mechanical testing samples based on virgin poly (lactic acid) (PLA) and PLA/wood fibre composites," *Adv. manuf.*, no. <https://doi.org/10.1007/s40436-018-0211-3>, 2018.
- [301] M. Osman and M. Atia, "Investigation of ABS-rice straw composite feedstock filament for FDM," *Rapid Prototyp. Journal*, vol. 24, no. 6, pp. 1067–1075, 2018.
- [302] Q. Tarrés, J. K. Melbø, M. Delgado-Aguilar, F. X. Espinach, P. Mutjé, and G. Chinga-Carrasco, "Bio-polyethylene reinforced with thermomechanical pulp fibers: Mechanical and micromechanical characterization and its application in 3D-printing by fused deposition modelling," *Compos. Part B Eng.*, vol. 153, pp. 10–17, 2018.
- [303] S. Guessasma, S. Belhabib, and H. Nouri, "Microstructure and Mechanical Performance of 3D Printed Wood-PLA/PHA Using Fused Deposition Modelling: Effect of Printing Temperature," *Polymers (Basel)*, vol. 11, no. 1778, 2019.

- [304] K. Vigneshwaran and N. Venkateshwaran, "Statistical analysis of mechanical properties of wood-PLA composites prepared via additive manufacturing," *Int. J. Polym. Anal. Charact.*, 2019.
- [305] N. Ayrimis, M. Kariz, J. Kwon, and M. Kuzman, "Effect of printing layer thickness on water absorption and mechanical properties of 3D-printed wood/PLA composite materials," *Int. J. Adv. Manuf. Technol.*, vol. 102, pp. 2195–2200, 2019.
- [306] D. Stoof and K. Pickering, "3D Printing of Natural Fibre Reinforced Recycled Polypropylene," *Process. Fabr. Adv. Mater.*, pp. 668–691, 2017.
- [307] A. Kelly and W. R. Tyson, "Tensile properties of fibre-reinforced metals: copper/tungsten and copper/molybdenum," *J. Mech. Phys. Solids*, vol. 13, 1965.
- [308] T. Yang, "Effect of extrusion temperature on the physico-mechanical properties of unidirectional wood fiber reinforced polylactic acid composite (WFRPC) components using fused deposition modeling," *Polymers (Basel)*, vol. 10, no. 976, pp. 1–11, 2018.
- [309] J. Baets, D. Plastria, J. Ivens, and I. Verpoest, "Determination of the optimal flax fibre preparation for use in unidirectional flax-epoxy composites," *J. Reinf. Plast. Compos.*, vol. 33, pp. 493–502, 2014.
- [310] C. Baley *et al.*, "Flax/PP manufacture by automated fibre placement (AFP)," *Mater. Des.*, vol. 94, 2016.
- [311] N. Sanandiyaa, Y. Vijay, M. Dimopoulou, S. Dritsas, and J. Fernandez, "Large-scale additive manufacturing with bioinspired cellulosic materials," *Sci. Reports*, vol. 8, no. 1, p. 8642., 2018.
- [312] M. Rüggeberg and I. Burgert, "Bio-Inspired Wooden Actuators for Large Scale Applications," *PLoS One*, vol. 10, no. 4, p. e0120718, 2015.
- [313] G. Holstov, G. Farmer, and B. Bridgens, "Sustainable Materialisation of Responsive Architecture," *Sustainability*, vol. 9, no. 435, pp. 1–20, 2017.
- [314] C. Vailati, E. Bachtiar, P. Hass, I. Burgert, and R. M., "An autonomous shading system based on coupled wood bilayer elements," *Energy Build.*, 2017.
- [315] L. Guiducci *et al.*, "Honeycomb actuators inspired by the unfolding of ice plant seed capsules," *PLoS One*, vol. 11, no. 11, pp. 1–21, 2016.
- [316] L. Yao *et al.*, "bioPrint: A Liquid Deposition Printing System for Natural Actuators," *3D Print. Addit. Manuf.*, vol. 2, no. 4, pp. 168–179, 2015.
- [317] X. Chen, L. Mahadevan, A. Driks, and O. Sahin, "Bacillus spores as a building blocks for stimuli-responsive materials and nanogenerators," *Nat. Nanotechnol. Lett.*, vol. 9, pp. 137–141, 2014.
- [318] A. Le Duigou and M. Castro, "Hygromorph BioComposites: Effect of fibre content and interfacial strength on the actuation performances," *Ind. Crops Prod.*, vol. 99, pp. 142–149, 2017.
- [319] A. Le Duigou, S. Requile, J. Beaugrand, F. Scarpa, and M. Castro, "Natural fibres actuators for smart bio-inspired hygromorph biocomposites," *Smart Mater. Struct.*, vol. 26, no. 12, 2017.
- [320] S. Timoshenko, "Analysis of bi-metal thermostats," *J. Opt. Soc. Am.*, vol. 11, no. 3, pp. 233–255, 1925.
- [321] T. T. Demaine. ED, ML. Demaine, D Koschitz, "Curved Crease Folding a Review on Art, Design and Mathematics," *Proc. IABSE-IASS Symp.*, 2011.
- [322] and P. H. Neville. RM, Chen. J, Guo. X, Zhang. F, Wang. W, Dobah.Y, Scarpa.F, Leng. J, "A kirigami shape memory polymer honeycomb concept for deployment," *Smart Mater. Struct.*, vol. 5, p. 05LT03, 2017.
- [323] S. S. Rossiter. J, "Kirigami design and fabrication for biomimetic robotics," *Bioinspiration, Biomimetics, Bioreplication, proc SPIE*, vol. 9055, 2014.
- [324] Sareh. S and J Rossiter, "Kirigami artificial muscles with complex biologically inspired morphologies," *Smart Mater. Struct.*, vol. 22, p. 14004, 2013.
- [325] P. Zhang, P. Chen, B. Wang, R. Yu, H. Pan, and B. Wang, "Evaluating the hierarchical, hygroscopic deformation of the *Daucus carota umbel* through structural characterization and mechanical analysis," *Acta Biomater.*, vol. 99, pp. 457–468, 2019.
- [326] D. Van Opdenbosch, G. Fritz-Popovski, W. Wagermaier, O. Paris, and C. Zollfrank, "Moisture-Driven Ceramic Bilayer Actuators from a Biotemplating Approach," *Adv. Mater.*, vol. 28, pp. 5235–5240, 2016.
- [327] C. Vailati, P. Hass, I. Burgert, and M. Rüggeberg, "Upscaling of wood bilayers: design principles for controlling shape change and increasing moisture change rate," *Mater. Struct.*, vol. 50, no. 250, p. <https://doi.org/10.1617/s11527-017-1117-4>, 2017.
- [328] E. Vazquez, B. Gursoy, and J. Duarte, "Designing for shape change : A Case study on 3D Printing Composite Materials for Responsive Architectures," *Conference*, pp. 391–400, 2019.
- [329] D. Correa and A. Menges, "Fused filament fabrication for multi kinetic state climate responsive aperture," *Rethink. Des. Constr. [Proceedings Fabr. Conf. 2017]*, vol. (ISBN: 978, pp. 190–195, 2017.
- [330] R. Lincoln, F. Scarpa, V. Ting, and R. Trask, "Multifunctional composites: a metamaterial perspective," *Multifunc Mater*, 2019.
- [331] M. Wagner, T. Chen, and K. Shea, "Large Shape Transforming 4D Auxetic Structures," *3D Print. Addit.*

- Manuf.*, no. September 2017, p. 3dp.2017.0027, 2017.
- [332] S. Turcaud, L. Guiducci, P. Fratzl, Y. Bréchet, and J. Dunlop, "An excursion into the design space of biomimetic architected biphasic actuator," *Int. J. Mater. Res.*, vol. 102, no. 6, 2011.
- [333] E. Vazquez, B. Gürsoy, and J. Duarte, "Formalizing Shape-Change: Three-Dimensional Printed Shapes and Hygroscopic Material Transformations," *Int. J. Archit. Comput.*, pp. 1–17, 2019.
- [334] L. Guiducci, Weaver, Y. Bréchet, P. Fratzl, and J. Dunlop, "The Geometric Design and Fabrication of Actuating Cellular Structures," *Adv. Mater. Interfaces*, vol. 2, no. 11, p. 1500011, 2015.
- [335] L. Cheng, A. Dwan, and C. C. Gryte, "Isothermal phase behavior of nylon-6,-66, and -610 polyamides in formic acid water systems," *J. Polym. Sci. Part B Polym. Phys.*, vol. 32, pp. 1183–1190, 1994.
- [336] P. Davies, B. R. Blackman, and A. J. Brunner, "Standard test methods for delamination resistance of composite materials: Current status," *Appl. Compos. Mater.*, vol. 5, no. 1, pp. 345–364, 1998.
- [337] J. G. Williams, "On the calculation of energy release rates for cracked laminates with residual stresses," *Int. J. Fract.*, vol. 36, no. 2, pp. 101–119, 1988.
- [338] K. Kageyama, T. Kobayashi, and T. W. Chou, "Analytical compliance method for Mode I interlaminar fracture toughness testing of composites," *Composites*, vol. 18, no. 5, pp. 393–399, 1987.
- [339] S. Hashemi, A. J. Kinloch, and J. G. Williams, "The Analysis of Interlaminar Fracture in Uniaxial Fibre-Polymer Composites," *Proc. R. Soc. A Math. Phys. Eng. Sci.*, vol. 427, no. 1872, pp. 173–199, 1990.
- [340] A. Berthereau and E. Dallies, "Fibres de verre de renforcement," *Tech. l'ingénieur*, vol. 33, no. 0, 2008.
- [341] M. F. Ashby, "The Mechanical Properties of Cellular Solids," *Metall. Trans. A*, vol. 14A, pp. 1755–1769, 1983.
- [342] P. Olivier, J. P. Cottu, and B. Ferret, "Effects of cure cycle pressure and voids on some mechanical properties of carbon/epoxy laminates," *Composites*, vol. 26, no. 7, pp. 509–515, 1995.
- [343] L. Liu, B. M. Zhang, D. F. Wang, and Z. J. Wu, "Effects of cure cycles on void content and mechanical properties of composite laminates," *Compos. Struct.*, vol. 73, no. 3, pp. 303–309, 2006.
- [344] H. Zhu, B. Wu, D. Li, D. Zhang, and Y. Chen, "Influence of Voids on the Tensile Performance of Carbon/epoxy Fabric Laminates," *J. Mater. Sci. Technol.*, vol. 27, no. 1, pp. 69–73, 2011.
- [345] J. Varna, R. Joffe, L. A. Berglund, and T. S. Lundström, "Effect of voids on failure mechanisms in RTM laminates," *Compos. Sci. Technol.*, vol. 53, no. 2, pp. 241–249, 1995.
- [346] L. P. Canal, J. Segurado, and J. Llorca, "Failure surface of epoxy-modified fiber-reinforced composites under transverse tension and out-of-plane shear," *Int. J. Solids Struct.*, vol. 46, no. 11–12, pp. 2265–2274, 2009.
- [347] R. Maurin, P. Davies, and N. Baral, "Transverse Properties of Carbon Fibres by Nano-Indentation and Micro-mechanics," *Appl. Compos. Mater.*, no. 15, pp. 61–73, 2008.
- [348] D. Treber, B. Haspel, P. Elsner, and K. A. Weidenmann, "Delamination fracture toughness of continuous glass-fiber / epoxy composites for structural applications," *Int. J. Plast. Technol.*, 2016.
- [349] P. Davies, W. Cantwell, C. Moulin, and H. H. Kausch, "A study of the delamination resistance of IM6/PEEK composites," *Compos. Sci. Technol.*, vol. 36, no. 2, pp. 153–166, 1989.
- [350] N. Baral, P. Davies, C. Baley, and B. Bigourdan, "Delamination behaviour of very high modulus carbon/epoxy marine composites," *Compos. Sci. Technol.*, vol. 68, no. 3–4, pp. 995–1007, 2008.
- [351] V. Tamuzs, S. Tarasovs, and U. Vilks, "Progressive delamination and fiber bridging modeling in double cantilever beam composite specimens," *Eng. Fract. Mech.*, vol. 68, pp. 513–525, 2001.
- [352] P. Davies and D. R. Moore, "Glass/nylon-6.6 composites: Delamination resistance testing," *Compos. Sci. Technol.*, vol. 38, no. 3, pp. 211–227, 1990.
- [353] A. J. Kinloch, G. K. Kodokian, and J. F. Watts, "The adhesion of thermoplastic fibre composites," *Philos. Trans. R. Soc. A Math. Phys. Eng. Sci.*, vol. 338, pp. 83–112, 1992.
- [354] M. Arhant, "Thesis report: Composites thermoplastiques pour enceintes sous-marines," 2016.
- [355] X. Yao, C. Luan, D. Zhang, L. Lan, and J. Fu, "Evaluation of carbon fiber-embedded 3D printed structures for strengthening and structural-health monitoring," *Mater. Des.*, 2016.
- [356] P. Davies, F. Mazéas, and P. Casari, "Sea Water Aging of Glass Reinforced Composites: Shear Behaviour and Damage Modelling," *J. Compos. Mater.*, vol. 35, pp. 1343–1372, 2001.
- [357] G. S. Park, "Transport Principles—Solution, Diffusion and Permeation in Polymer Membranes," *Synth. Membr. Sci. Eng. Appl.*, pp. 57–107, 1986.
- [358] H. F. Mark, N. M. Bikales, C. G. Oberberger, G. Menges, and J. I. Kroschwitz, *Encyclopedia of Polymer Science and Engineering - 2nd edition*, vol. 11. 1990.
- [359] J. L. Thomasson and G. Porteus, "Swelling of glass-fiber reinforced polyamide 66 during conditioning in water, ethylene glycol and antifreeze mixture," *Polym. Polym. Compos.*, vol. 16, no. 2, pp. 101–113, 2008.

- [360] E. Stellrecht, B. Han, and M. G. Pecht, "Characterization of Hygroscopic Swelling Behavior of Mold Compounds and Plastic Packages," *IEEE Trans. components Packag. Technol.*, vol. 27, no. 3, pp. 499–506, 2004.
- [361] E. Pérez-Pacheco, J. I. Cauich-Cupul, A. Valadez-González, and P. J. Herrera-Franco, "Effect of moisture absorption on the mechanical behavior of carbon fiber/epoxy matrix composites," *J. Mater. Sci.*, vol. 48, no. 5, pp. 1873–1882, 2013.
- [362] J. Crank, *The mathematics of diffusion*. 1975.
- [363] V. Gager, A. Le Duigou, A. Bourmaud, F. Pierre, K. Behlouli, and C. Baley, "Understanding the effect of moisture variation on the hygromechanical properties of porosity-controlled nonwoven biocomposites?," *Polym Test.*, vol. 78, no. 105944, 2019.
- [364] K. A. Downes and J. L. Thomason, "A method to measure the influence of humidity and temperature on the interfacial adhesion in polyamide composites," *Compos. Interfaces*, vol. 22, no. 8, pp. 757–766, 2015.
- [365] R. T. D. Prabhakaran and H. Toftegaard, "Environmental effect on the mechanical properties of commingled-yarn-based carbon fibre/polyamide 6 composites," *J. Compos. Mater.*, pp. 1–15, 2014.
- [366] L. Sang, C. Wang, Y. Wang, and W. Hou, "Effects of hydrothermal aging on moisture absorption and property prediction of short carbon fiber reinforced polyamide 6 composites," *Compos. Part B*, vol. 153, no. August, pp. 306–314, 2018.
- [367] R. Taktak, N. Guermazi, J. Derbeli, and N. Haddar, "Effect of hygrothermal aging on the mechanical properties and ductile fracture of polyamide 6 : Experimental and numerical approaches," vol. 148, pp. 122–133, 2015.
- [368] E. Sarlin, R. Sironen, T. Pärnänen, M. Lindgren, M. Kanerva, and J. Vuorinen, "The effect of matrix type on ageing of thick vinyl ester glass-fibre- reinforced laminates," *Compos. Struct.*, vol. 168, pp. 840–850, 2017.
- [369] N. Tual *et al.*, "Characterization of Sea Water Ageing Effects on Mechanical Properties of Carbon/Epoxy Composites for Tidal Turbine Blades," *Compos. Part A*, vol. 78, pp. 380–389, 2015.
- [370] I. Kafodya, G. Xian, and H. Li, "Durability study of pultruded CFRP plates immersed in water and seawater under sustained bending : Water uptake and effects on the mechanical properties," *Compos. Part B*, vol. 70, pp. 138–148, 2015.
- [371] X. Jiang, J. Song, X. Qiang, H. Kolstein, and F. Bijlaard, "Moisture Absorption / Desorption Effects on Flexural Property of Glass-Fiber-Reinforced Polyester Laminates : Three-Point Bending Test and Coupled Hygro-Mechanical Finite Element Analysis," *Polymers (Basel)*, vol. 290, no. 8, 2016.
- [372] M. Eftekhari and A. Fatemi, "Tensile behavior of thermoplastic composites including temperature, moisture, and hygrothermal effects," *Polym. Test.*, vol. 51, pp. 151–164, 2016.
- [373] J. M. Skotheim and L. Mahadevan, "Physical Limits and Design Principles for Plant and Fungal Movements," *Science (80-)*, vol. 308, pp. 1308–1310, 2005.
- [374] L. Lim, I. A. N. J. Britt, and M. A. Tung, "Sorption and Transport of Water Vapor in Nylon 6 , 6 Film," *J. Appl. Polym. Sci.*, vol. 71, pp. 197–206, 1998.
- [375] J. Ru, Z. Zhu, Y. Wang, and H. Chen, "A moisture and electric coupling stimulated ionic polymer-metal composite actuator with controllable deformation behavior," 2018.
- [376] P. Z. J.A. Nairn, "Matrix solidification and the resulting residual thermal stresses in composites," *J Mater Sci*, vol. 20, no. 1, pp. 355–367, 1985.
- [377] G. Stoychev, S. Zakharchenko, S. Turcaud, J. W. C. Dunlop, and L. Ionov, "Shape-programmed folding of stimuli-responsive polymer bilayers," *ACS Nano*, vol. 6, no. 5, pp. 3925–3934, 2012.
- [378] A. Le Duigou *et al.*, "A multi-scale study of the interface between natural fibres and a biopolymer," *Compos. PART A*, vol. 65, pp. 161–168, 2014.
- [379] Naturworks, "Ingeo™ Biopolymer 3260HP Technical Data Sheet," https://www.natureworksllc.com/~media/Files/NatureWorks/Technical-Documents/Technical-Data-Sheets/TechnicalDataSheet_3260HP_injection-molding_pdf.pdf?la=en.
- [380] C. Baley and A. Bourmaud, "Average tensile properties of French elementary flax fibers," *Mater. Lett.*, vol. 122, pp. 159–161, 2014.
- [381] F. Bensadoun *et al.*, "Impregnated Fibre Bundle Test for Natural Fibres used in Composites," *J. Reinf. Plast. Compos.*, vol. 36, no. 13, pp. 942–957, 2017.
- [382] C. Baley, M. Lan, A. Bourmaud, and A. Le Duigou, "Compressive and tensile behaviour of unidirectional composites reinforced by natural fibres: Influence of fibres (flax and jute), matrix and fibre volume fraction," *Mater. today Commun.*, 2018.
- [383] A. Monti, A. El Mahi, Z. Jendli, and L. Guillaumat, "Mechanical behaviour and damage mechanisms

- analysis of a flax-fibre reinforced composite by acoustic emission," *Compos. Part A Appl. Sci. Manuf.*, vol. 90, pp. 100–110, 2016.
- [384] S. Liang, P.-B. Gning, and L. Guillaumat, "Quasi-static behaviour and damage assessment of flax/epoxy composites," *Mater. Des.*, vol. 67, pp. 344–353, Feb. 2015.
- [385] A. Lefeuvre, A. Bourmaud, and C. Baley, "Optimization of the mechanical performance of UD flax/epoxy composites by selection of fibres along the stem," *Compos. Part A Appl. Sci. Manuf.*, vol. 77, pp. 204–208, Oct. 2015.
- [386] T. Cadu *et al.*, "What are the key parameters to produce a high-grade bio-based composite? Application to flax/epoxy UD laminates produced by thermocompression," *Compos. Part B Eng.*, vol. 150, pp. 36–46, 2018.
- [387] I. Van de Weyenberg, J. Ivens, A. De Coster, B. Kino, E. Baetens, and I. Verpoest, "Influence of processing and chemical treatment of flax fibres on their composites," *Compos. Sci. Technol.*, vol. 63, no. 9, pp. 1241–1246, Jul. 2003.
- [388] Markforged, "https://www.markforged.com/materials (Acces." [Online]. Available: www.markforged.com.
- [389] T. Joffre, E. L. G. Wernersson, A. Miettinen, C. L. Luengo Hendriks, and E. K. Gamstedt, "Swelling of cellulose fibres in composite materials: Constraint effects of the surrounding matrix," *Compos. Sci. Technol.*, vol. 74, pp. 52–59, Jan. 2013.
- [390] D. Correa *et al.*, "4D Pine Scale: Biomimetic 4D Printed Autonomous Scale and Flap Structures Capable of Multi-Phase Movement," *Philos. Trans. A. Math. Phys. Eng. Sci.*, vol. 378, no. 2167, p. 20190445, 2020.
- [391] A. Bourmaud, D. Åkesson, J. Beaugrand, A. Le Duigou, M. Skrifvars, and C. Baley, "Recycling of L-Poly-(lactide)-Poly-(butylene-succinate)-flax biocomposite," *Polym. Degrad. Stab.*, vol. 128, 2016.
- [392] A. Le Duigou, D. Correa, M. Ueda, R. Matsuzaki, and M. Castro, "A Review of 3D and 4D printing of natural fibres biocomposites," *Submitt. to Mater. Des.*, 2020.
- [393] P. Parlevliet, H. Bersee, and A. Beukers, "Residual stresses in thermoplastic composites—A study of the literature—Part II: Experimental techniques," *Comp. Part A Appl. Sci. Manuf.*, vol. 38, no. 3, pp. 651–655, 2007.
- [394] Baley C Kervoëlen A Le Duigou A Goudenhooff C Bourmaud A, "Is the low shear modulus of flax fibres an advantage for polymer reinforcement?," *Mater. Lett.*, vol. 185, pp. 534–536, 2016.
- [395] M. Péron, A. Céline, M. Castro, F. Jacquemin, and A. Le Duigou, "Study of hygroscopic stresses in asymmetric biocomposite laminates," *Compos. Sci. Technol.*, vol. 169, no. October 2018, pp. 7–15, 2019.
- [396] A. Le Duigou, P. Davies, and C. Baley, "Seawater ageing of flax/poly(lactic acid) biocomposites," *Polym. Degrad. Stab.*, vol. 94, no. 7, 2009.
- [397] S. Charlon, N. Follain, J. Soulestin, M. Sclavons, and S. Marais, "Water Transport Properties of Poly(butylene succinate) and Poly[(butylene succinate)-co-(butylene adipate)] Nanocomposite Films: Influence of the Water-Assisted Extrusion Process," *J. Phys. Chem. C*, vol. 121, pp. 918–930, 2017.
- [398] M. Péron, A. Céline, F. Jacquemin, and A. Le Duigou, "Hygroscopic stresses in asymmetric biocomposite laminates submitted to various relative humidity conditions," *Comp. Part A Appl. Sci. Manuf.*, 2020.
- [399] A. Le Duigou, V. Keryvin, J. Beaugrand, M. Pernes, F. Scarpa, and M. Castro, "Humidity responsive actuation of bioinspired hygromorph biocomposites (HBC) for adaptive structures," *Compos. Part A*, vol. 116, no. July 2018, pp. 36–45, 2019.
- [400] A. Le Duigou, A. Bourmaud, and C. Baley, "In-situ evaluation of flax fibre degradation during water ageing," *Ind. Crops Prod.*, vol. 70, pp. 204–210, Aug. 2015.
- [401] C. Zhao, L. Ren, Z. Song, L. Deng, and Q. Liu, "Structure-driven biomimetic self-morphing composites fabricated by multi-process 3D printing," *Comp. Part A Appl. Sci. Manuf.*, vol. 123, pp. 1–9, 2019.
- [402] G. Stoychev, L. Guiducci, S. Turcaud, J. Dunlop, and L. Ionov, "Hole programmed superfast multistep folding of hydrogel bilayers," *Adv. Funct. Mater.*, pp. 1–7, 2016.
- [403] F. Momeni, S. Sabzpooshan, R. Valizadeh, M. Morad, X. Liu, and J. Ni, "Plant leaf-mimetic smart wind turbine blades by 4D printing," *Renew. energy*, vol. 130, 2018.

Titre : Impression 3D et 4D de composites à hautes performances renforcés par des fibres continues synthétiques ou naturelles pour des applications structurelles ou de morphing.

Mots clés : Impression 3D, Fibre continue, Propriétés mécaniques, Impression 4D, Biocomposite, Hygromorphes, Biomimétisme

Résumé : L'impression 3D et plus spécifiquement la technique de Fused Filament Fabrication (FFF) de matériaux composites à renforts continus est un domaine d'étude en plein essor visant à pallier les faibles performances mécaniques rencontrées par les composites élaborés en impression 3D et ainsi ouvrir les champs d'applications (aéronautique, course au large...). Autre tendance, l'impression 4D qui permet de développer des matériaux stimulables (capteurs et/ou actionneurs) et d'envisager des structures architecturées complexes se déformant sous l'action de divers stimuli (humidité, électricité, température, pression...). Le travail de thèse s'inscrit dans ce contexte pluriel et vise à développer de nouveaux matériaux multifonctionnels par impression 3D et 4D. Dans un premier temps, le travail de thèse a pour objectif scientifique de comprendre les

relations entre le procédé, la microstructure induite, les performances mécaniques et hygromécaniques en vue d'applications structurelles (aéronautique, course au large ...) sur des matériaux composites renforcés de fibres synthétiques (carbone et verre) et naturelles (lin). La deuxième partie des travaux de thèse vise à développer des matériaux composites hygromorphes renforcés de fibres continues (synthétiques et naturelles) avec une architecture en bilame bio-inspirée de la pomme de pin. Le caractère conducteur des fibres de carbone est utilisé pour développer de nouveaux actionneurs electro-thermo-hygromorphes présentant un actionnement contrôlé et accéléré par rapport aux hygromorphes classiques. Enfin, la liberté de design offerte par l'impression 3D a été utilisée pour contrôler localement la rigidité et l'actionnement d'actionneurs composites renforcés de fibres de lin continues.

Title: 3D and 4D printing of high performance continuous synthetic and natural fiber composites for structural applications and morphing structure

Keywords: 3D Printing, Continuous fibers, Mechanical properties, 4D Printing, Biocomposite, Hygromorph, Biomimicry

Abstract: 3D printing and especially Fused Filament Fabrication (FFF) technology for composite materials reinforced by continuous fibers is an emerging research field which aims to enhance the mechanical performance of 3D printing structures and to widen the field of application (aerospace, sailing...). Another trend, 3D printing allows to develop stimuable materials (sensor and/or actuators) and to consider parts with complex architecture that can be deployed under various stimulation (electricity temperature, pressure...). The present work is therefore part of this context and aims to develop new multi-functional materials elaborated by 4D printing. First, the scientific objective of this work is to better understand the relationship between the process, the induced microstructure, mechanical

and the hygromechanical performances in order to target structural applications (aeronautic, sailing) for composite materials reinforced with synthetic fibers (carbon and glass) and natural fibers (flax). The second part of this work aimed to develop hygromorphic composites reinforced with continuous fibers (synthetic and natural) with a bioinspired bilayer architecture inspired by the pinecone scale. The conductive behavior of carbon fiber was used to create new electro-thermo-hygromorph actuators with controlled and accelerated actuation compared to conventional hygromorphs. Finally, the design freedom provided by 4D printing made it possible to control the local stiffness and actuation of composite actuators reinforced with continuous flax fiber.